THE OBLIQUE SEISMIC EXPERIMENT IN OCEANIC CRUST

by

RALPH ARCHIBALD STEPHEN

Dissertation submitted for the degree of

Doctor of Philosophy

Darwin College
Cambridge

May 1978

Safe upon the solid rock the ugly houses stand:

Come and see my shining palace built upon the sand!

Edna St. Vincent Millay

Frontispiece. The Glomar Challenger at Site 417.

DECLARATION

Much of the work recorded in this dissertation is new. The development of synthetic seismogram theory for the case of the receiver within the reflectivity zone is the only treatment of reflectivity method synthetic seismograms for borehole seismometers (Chapter 2). I designed and built the Cambridge Borehole Preamplifier and supervised the construction of the frame to hold the geophones (Chapter 3). I was completely in charge of the first successful Oblique Seismic Experiment in oceanic crust which was carried out from the D/V Glomar Challenger. This was the first time that seismic signals had been received within oceanic crust. The interpretation and conclusions of this work are entirely my own (Chapters 4 and 5).

As with any first attempt at an experiment I was not successful at accomplishing all of the objectives. However a number of interesting ideas have arisen from this work. One of the most significant is that large fissures in young oceanic crust may cause anisotropy in layer 2. Since there is no evidence for large fissures in the old crust (110 My) where this experiment was carried out, it would appear that either large fissures never formed in old crust or that the fissures have healed.

This dissertation is the result of my own work and includes nothing which is the result of work done in collaboration.

No part of this dissertation has been submitted for any other degree or qualification at any other university.

This dissertation does not exceed 80,000 words.

SUMMARY

The Oblique Seismic Experiment (OSE) is proposed to increase the usefulness of the IPOD crustal borehole as a means of investigating layer 2 of oceanic crust. Specific objectives are: to determine the lateral extent of the structure intersected by the borehole, to analyse the role of cracks in the velocity structure of layer 2, to look for anisotropy which may be caused by large cracks with a preferred orientation, and to measure attenuation in oceanic crust.

Both travel time and amplitude techniques are used to plan the experiment and to interpret the data. The reflectivity method for computing synthetic seismograms is developed for the case of the receiver within the reflectivity zone and ray method results are shown for comparison.

A three-component borehole geophone with discrete variable gain pre-amplifiers was developed for the experiment. The first successful Oblique Seismic Experiment in oceanic crust was carried out in March 1977 in a hole 400 miles north of Puerto Rico.

An adequate study of lateral velocity variations was impossible because the hole was not deep enough, the hole was inadequately logged, and the small scale basement topography was not known.

Wyllie's relation, self-consistent theory, and non-interactive theory are applied to the observed velocity profiles in an attempt to quantitatively determine the crack structure. In general both P-wave and S-wave profiles suggest that the crack density decreases with depth in layer 2. Velocities at the bottom of layer 2 are the same as matrix velocities for basalt implying that crack density may be negligible at this depth.

No convincing evidence for anisotropy in either layer 2 or 3 is found. Since the large fissures observed in the FAMOUS area should produce anisotropy it appears that large fissures are not present in the studied crust (110 My). The results agree with the theory that large fissures are less prevalent in older crust, perhaps sealing with age, and that the density of small cracks decreases with depth.

The hole was not deep enough to measure attenuation from normal incidence shots. Amplitudes were not consistent enough to obtain a measure of attenuation from long range shots.

The Oblique Seismic Experiment in March 1977 was a tenuous operation and a higher priority should be given to the experiment before it is attempted again.

ACKNOWLEDGEMENTS

The Oblique Seismic Experiment required the assistance and co-operation of a large number of people.

Mr. J. Unger and Mr. P. Condren from the Geo Space Corporation helped in the acquisition of the working single component geophone. Dr. R.B. Whitmarsh at the Institute of Oceanographic Sciences arranged for pressure testing of the high pressure hydrophone and the Admiralty Underwater Weapons Establishment pressure tested the modified borehole geophone prior to the second experiment.

I would like to thank Drs. Townsend and Mumford at the Cavendish Laboratory for making their digitizing equipment available and Mr. A. Bunch for his digital data reduction programmes.

Mr. T. Claydon designed and built the 3-component jig for the borehole geophone, expedited shipping and fired the charges in the successful experiment. Mr. R. Theobold and Mr. R. Butler helped in the design and construction of the high pressure hydrophone. Mr. G. Ballard, well equipped with his degree in Sanskrit and Medieval Hindu, offered suggestions and advice, for the design of the electronics.

I would like to thank Dr. J. Heirtzler, Dr. H. Stewart, Jr., Dr. K. Louden, Dr. S. White, Dr. W. Bryan, Dr. P. Robinson, Mr. R. Knapp, Mr. V. Larsen, the drilling personnel of Glomar Challenger for Leg 52, the DSDP marine technicians, Captain Clarke, the crew of the Glomar Challenger, Captain Neill and the crew of the Virginia Key for their co-operation in organizing and running the Oblique Seismic Experiment. Dr. G.M. Purdy, Mr. T. Stetson and Mr. J. Broda helped bridge trans-Atlantic communication difficulties and arranged for the explosives. Drs. Hoskin and Groman graciously provided the Lynch survey

data of Site 417.

I thank Drs. B.L.N. Kennett, C.M.R. Fowler, K. Fuchs, G. Müller, V. Červený, I. Pšenčik and Mr. D. Wright for making their computer programmes available to be modified for the OSE case.

Much of the information used in the discussion of the Oblique Seismic Experiment results (Sections 5b) and 5c)) was provided by the shipboard parties of DSDP Legs 51, 52 and 53. Particular recognition should be given to the physical properties team for the megaleg: Drs. J. Francheteau, M. Salisbury, Y. Hamano and Messrs. M. Hobart and D. Johnson. Specific contributions have been noted in the text.

From time to time discussions with Dr. A.W. Smith, Dr. R.S. White, Dr. J.M. Woodside, Dr. J.A.C. Horsfall, Dr. G. King and Dr. K.E. Louden proved valuable in working out ideas. Mrs. S. Williams and Mrs. M.E. Stephen drew many of the diagrams for the thesis. Dr. R.B. Whitmarsh made recommendations to improve the text of the thesis.

The Glomar Challenger ship time was provided by the International Phase of Ocean Drilling and associated organizations. The Natural Environment Research Council funded the other field work and development. The University of Cambridge computing service supplied computer time for the data reduction. I would like to thank Shell Canada Ltd. for supporting my personal expenses for three and a half years.

Dr. B.L.N. Kennett encouraged the theoretical work. The OSE was originally proposed by my research supervisor Dr. D.H. Matthews and I am indebted to him for his guidance and advice throughout the project.

No words can express my appreciation to my wife, Mary Ellen.

TABLE OF CONTENTS

CHAPTER 1

INTRODUCTION

1-1. OBJECTIVES OF THE OSE

As refraction and reflection experiments are used to look at refracted and reflected rays, so the Oblique Seismic Experiment (OSE) is used to look at "oblique" rays, that is, rays which impinge on the receiver at angles of incidence from 0^{o} to almost 90^{o}. In this study this means receiving shots in a borehole which have been generated at the surface from small to large ranges (Figure 1-1-1). Torpedoing, firing charges in a borehole and receiving on the surface, is a form of OSE.

In the study of layer 2 in oceanic crust the Oblique Seismic Experiment bridges the gap between borehole techniques, such as laboratory analysis of cores and well logging, and conventional seismic refraction which uses sonobuoys, ocean bottom seismometers or ocean bottom hydrophones as receivers. By analysing cores in the laboratory one can study oceanic crust on a scale up to a few centimetres and in situ measurements using logging tools can be used to study the oceanic crust up to a few metres from the borehole. However, there is a big difference between these scales and the scale of a marine refraction experiment which is used to look at crust over a few kilometres. The OSE gives information about oceanic crust around the borehole on the scale of hundreds of metres. (This is demonstrated in Section 2-1b)). Sections 1-2 and 1-3 set the stage for the Oblique Seismic Experiment by reviewing previous borehole seismic work and discussing the

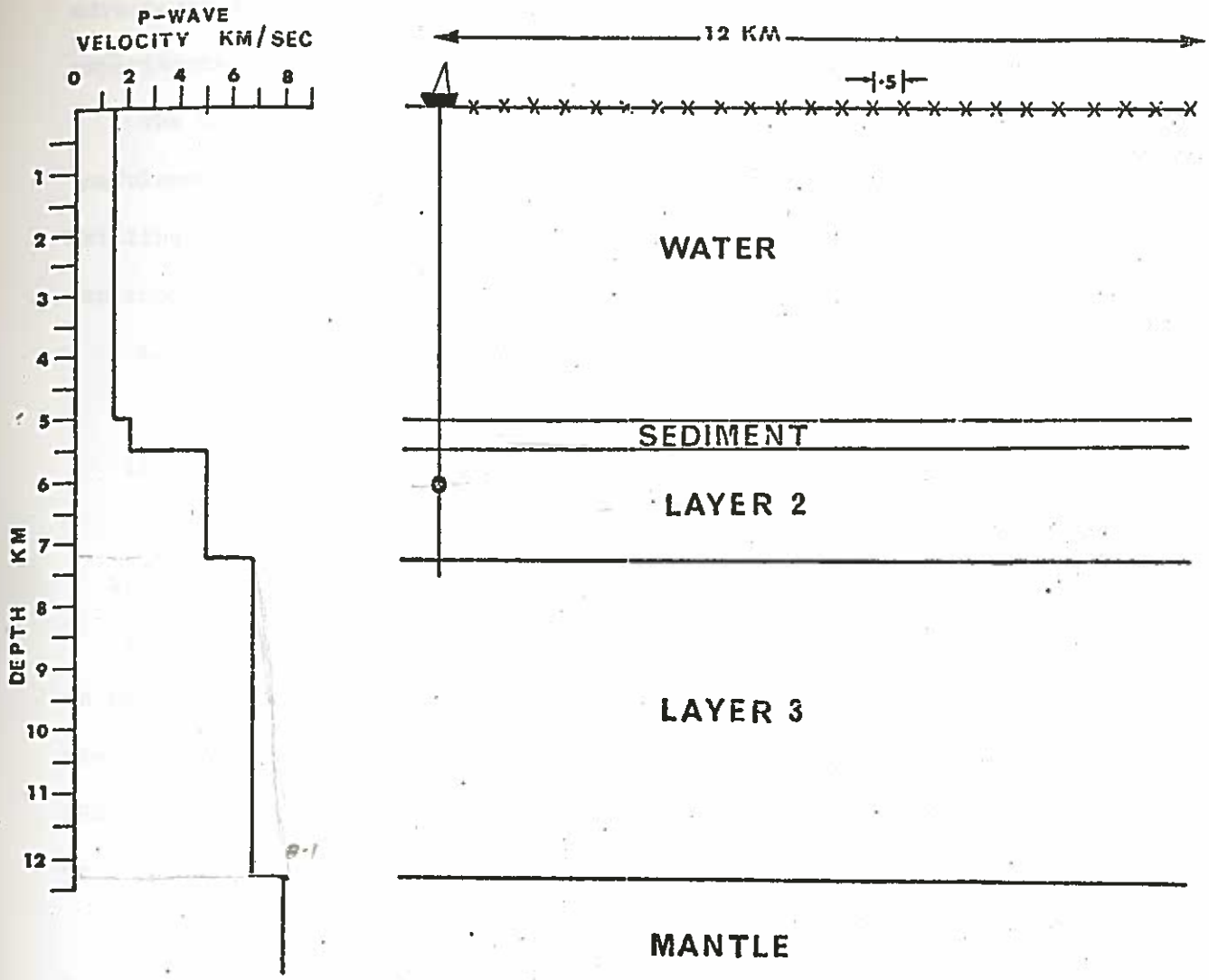

Figure 1-1-1. Layout for the Oblique Seismic Experiment over average oceanic crust (Ludwig, Nafe and Drake, 1970). The dot represents the receiver depth (6 km) for which the synthetic seismogram examples of Section 2-2 are calculated and the crosses indicate the recommended shooting program for the OSE over oceanic crust.

advantages and disadvantages of the OSE over conventional refraction experiments.

The Oblique Seismic Experiment has been proposed to increase the usefulness of IPOD (International Phase of Ocean Drilling) crustal drilling as a means of investigating layer 2 in oceanic crust. The experiment has four objectives:

i. To determine the lateral extent of the structure intersected by the borehole.

ii. To analyse the role of cracks in the velocity structure of oceanic crust.

iii. To look for anisotropy in layer 2.

iv. To measure attenuation in oceanic crust.

In Sections 1-4 to 1-7 these objectives are discussed with a review of previous work by other investigators. The advantages, if any, which the OSE has over other techniques in accomplishing these goals will be pointed out.

1-2. REVIEW OF BOREHOLE SEISMIC WORK

a). Sonic Logging

Two types of sound velocity measurement are used in boreholes: sonic logging and check shooting.

The development of the sonic logging tool was recorded by Vogel (1952), Summers and Broding (1952), Karus and Zuckernik (1958), Khalevin (1958), Tixier et al (1959) and Khalevin and Barykin (1961). Kokesh et al (1965) reported the development of a multiple source and receiver unit which compensates for variable borehole diameter. This method has become standard for sonic logging.

In exploration geophysics, particularly for oil and gas, sonic logs are combined with neutron and gamma-gamma logs to provide estimates of porosity (Section 1-5d)).

b). Check Shooting

The check shooting method measures average velocity between a point in the hole and the surface using explosive or air gun sources and can be divided into work which only considers short range shots (normal incidence) and work which considers long range shots (oblique incidence).

Dix (1939) discussed a method of obtaining velocity-depth profiles from normal incidence check shots and Jolly (1953), Levin and Lynn (1958) and McDonal et al (1958) used normal incidence check shots to study amplitude variation with depth, the nature of reflected and refracted arrivals, and multiples.

Normal incidence shots are routinely used to correct the integrated sonic log so that accurate two-way travel times to reflectors can be obtained for correlation with reflection profiles. As an example, Gretner (1961) analysed discrepancies between sonic log and check shot data and found that integrated sonic log times were less than check shot times by 2% for wells in Western Canada. Strick (1971) attempted to explain Gretner's results in terms of attenuation and dispersion, however, O'Brien and Lucas (1971) performed a more extensive analysis of the discrepancy for wells in the North Sea, Abu Dhabi, Libya and Alaska and found that on average dispersion was not significantly different from zero. O'Brien and Lucas only used data from borehole compensated logging tools whereas Gretner used the less accurate conventional tool.

Oblique incidence check shooting has been used to study anisotropy resulting from horizontal layering (Uhrig and Van Melle, 1955; Dunoyer de Segonzac and Laherrer, 1959; Vanderstoep, 1966), to correlate surface seismic work with stratigraphy (Halperin and Frolova, 1961; Gal'perin, 1974) and to reduce noise caused by scattering in near surface layers (Wuenschel, 1976). Meissner (1965) shot charges in boreholes and received signals at horizontal arrays on the surface to study P and SV travel times and amplitudes.

c). Tube Waves

A common problem to all work using borehole receivers is the complication of tube waves in the well. Papers by Ording and Redding (1953), Riggs (1955), White and Frost (1956) and Gal'perin (1974) show examples of tube waves (Figure 1-2-1). White (1965) reviewed in detail the theory of these waves. He found that "Tube waves are generated when a compressional wave in a surrounding solid passes any major discontinuity in the borehole". The tube wave velocity for a fluid filled borehole in an infinite solid is:

$$c_T = \left[\rho \left(\frac{1}{B} + \frac{1}{\mu}\right)\right]^{-\frac{1}{2}}$$

where ρ is the fluid density, B is the fluid bulk modulus, and μ is the shear modulus of the solid. For a water filled borehole the tube wave velocity is about one quarter of the velocity of a shear wave in the solid.

The effects of tube waves are greatly reduced if a clamped geophone is used rather than a hydrophone and most studies using borehole receivers since the mid-1950's have used clamped geophones.

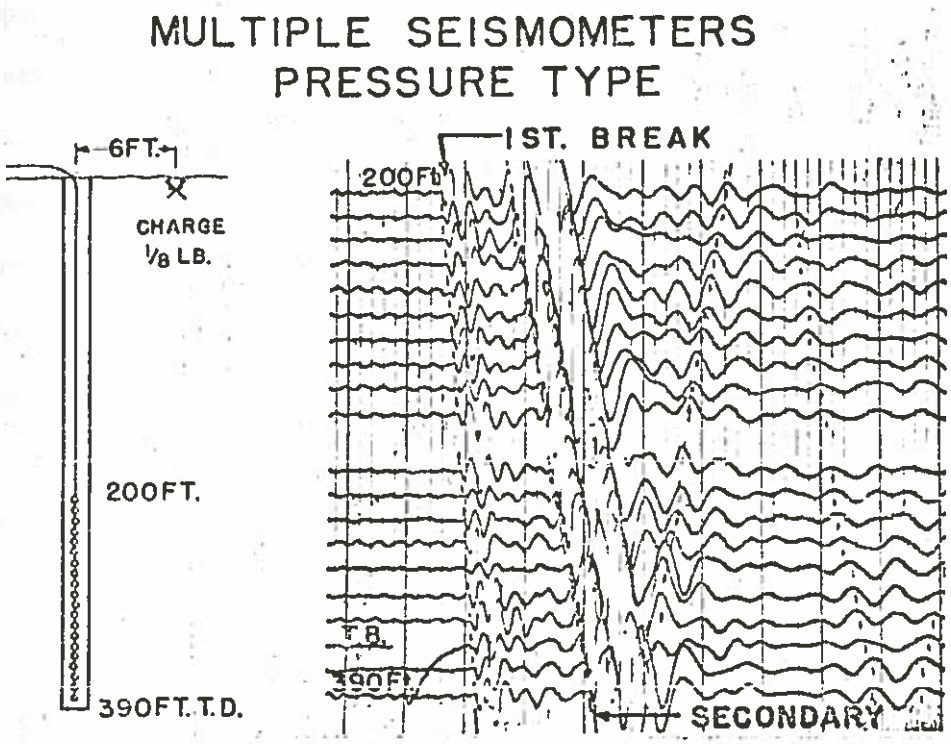

Figure 1-2-1. Example of tube waves in a borehole. The record section displays seismograms from hydrophones at different depths for the same shot. The secondary arrivals are tube waves which travel down the hole and reflect from the bottom. (from Riggs, 1955).

1-3. COMPARISON BETWEEN THE OSE AND CONVENTIONAL REFRACTION WORK

The OSE, which uses a clamped borehole geophone as a receiver, has a number of advantages over conventional seismic refraction techniques, which use ocean bottom seismometers, ocean bottom hydrophones, or sonobuoys. These advantages can be attributed to theoretical factors, which are a result of the different geometries involved in the two experiments and operational factors involved in practical applications.

The principles of marine refraction experiments have been reviewed by Ewing (1963) and Shor (1963), and the use of surface receivers has been discussed by Hill (1963). Sea bottom receivers were proposed to increase the resolution in layer 2 (Shorthouse, 1964; Whitmarsh, 1967) and a number of groups have developed sea bottom seismic recording gear (Whitmarsh, 1970; Francis et al, 1975; Langford and Whitmarsh, 1977; R.V. Johnson et al, 1977; S.H. Johnson et al, 1977; Mattaboni and Solomon, 1977; Prothero, 1977; Francis and Porter, 1977; Sutton et al, 1977; and McDonald et al, 1977). Applications of ocean bottom receivers have been discussed by Whitmarsh (1975), Francis (1976) and Fowler (1976).

The advantages of the OSE which are a result of its unique geometry are:

i. The OSE can give velocities of material near the hole by using near normal incidence shots. This is commonly called check shooting. By comparing travel times from surface shots to geophones at the top and bottom of the hole, the mean velocity of crust within 300 m of the hole can be obtained. The velocity measured by conventional refraction experiments is an average over the range of arrivals and the method requires ranges of 2 km or more to identify the refractor (Raitt, 1963a and Houtz, 1976).

It is inherently impossible for conventional techniques to obtain the same degree of lateral resolution as the OSE or to obtain mean vertical velocities in oceanic layer 2 (also see point v).

ii. The OSE does not rely on the presence of reflecting or refracting horizons in order to obtain a velocity determination. The mean velocity of the material above the geophone can be obtained from direct wave arrivals (Section 2-1b)).

iii. Conventional refraction experiments cannot detect low velocity zones (Ewing, 1963). The OSE can, of course, detect the presence of a low velocity zone above the receiver from velocities obtained from direct wave arrivals. If the low velocity zone is caused by factors on a scale larger than the logging tools can measure (e.g. large vertical fissures), even logging may not detect the zone.

iv. Much better layer 2 velocities can be obtained using the OSE with a receiver within layer 2 because waves which have travelled in layer 2 occur as first arrivals up to ranges of 10 km (Section 2-1b)). This compares with about 4.0 km for conventional refraction work.

v. As will be shown in Section 2-1b), the OSE can be used to look at lateral velocity variations away from the hole. For example, a jump in velocity from 5.0 to 5.5 km/sec at a range of 1.0 km from the hole can be detected. For a refraction experiment using an ocean bottom receiver, layer 2 arrivals may not even occur as first arrivals until a few kilometres from the receiver if sediment is present. For example, Figure 1-3-1 compares conventional refraction experiment geometry, using an ocean bottom receiver, to OSE geometry. For the conventional refraction

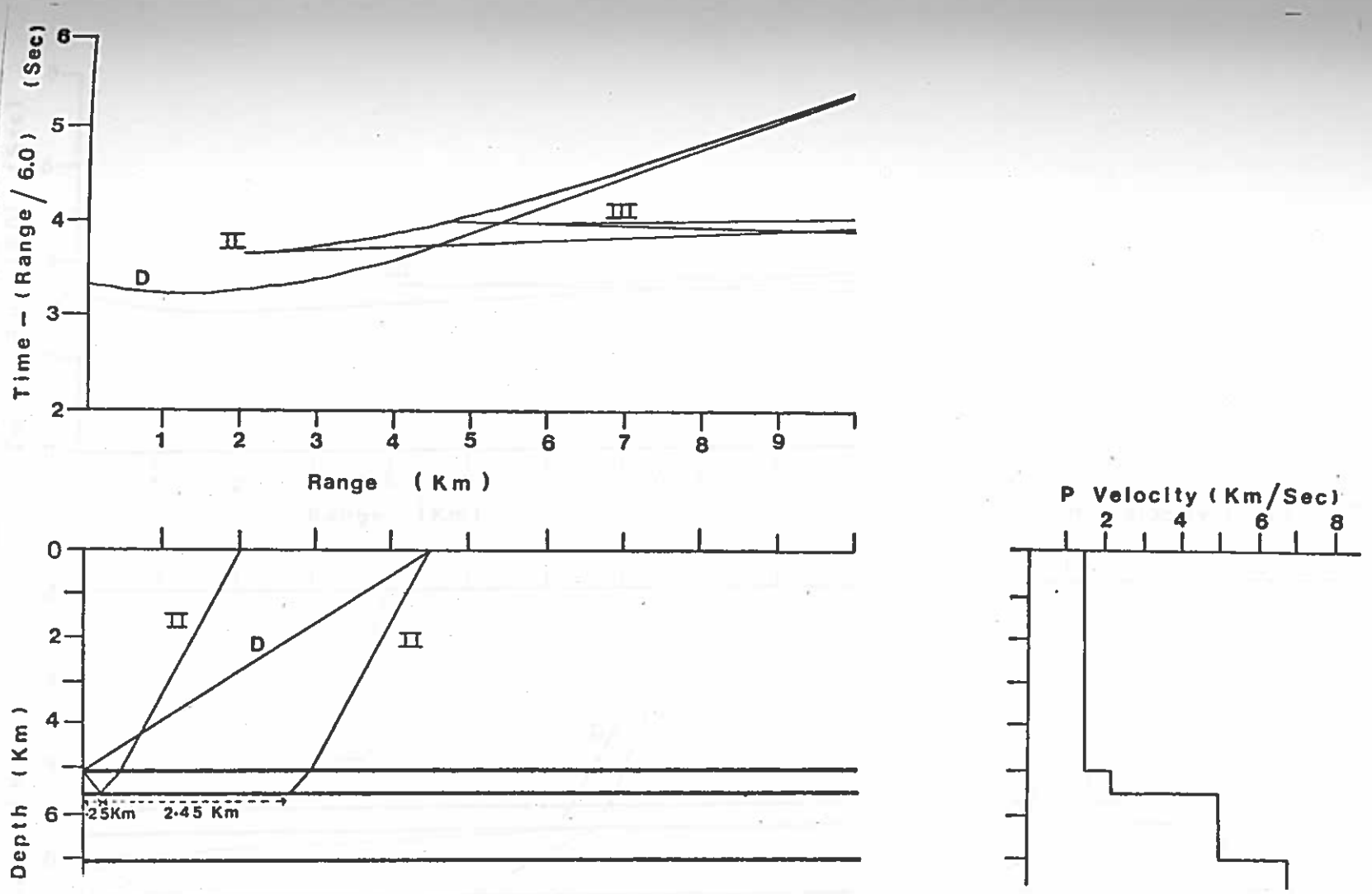

Figure 1-3-1a&b. Comparison between the OSE and a conventional refraction experiment using ocean bottom seismometers. In the conventional refraction case (Figure 1-3-1a) the minimum distance which layer 2 first arrivals have travelled in layer 2 is 2.45 km and the nearest crust sampled is typically 0.25 km away from the receiver. For the OSE geometry (Figure 1-3-1b) layer 2 velocities can be obtained over distances from normal incidence to almost 7 km range in layer 2 and layer 2 is sampled right up to the receiver. In the diagrams D represents the direct arrival and II and III represent the reflected and refracted arrivals for layers 2 and 3 respectively.
The model is the average crust model of Figure 1-1-1.

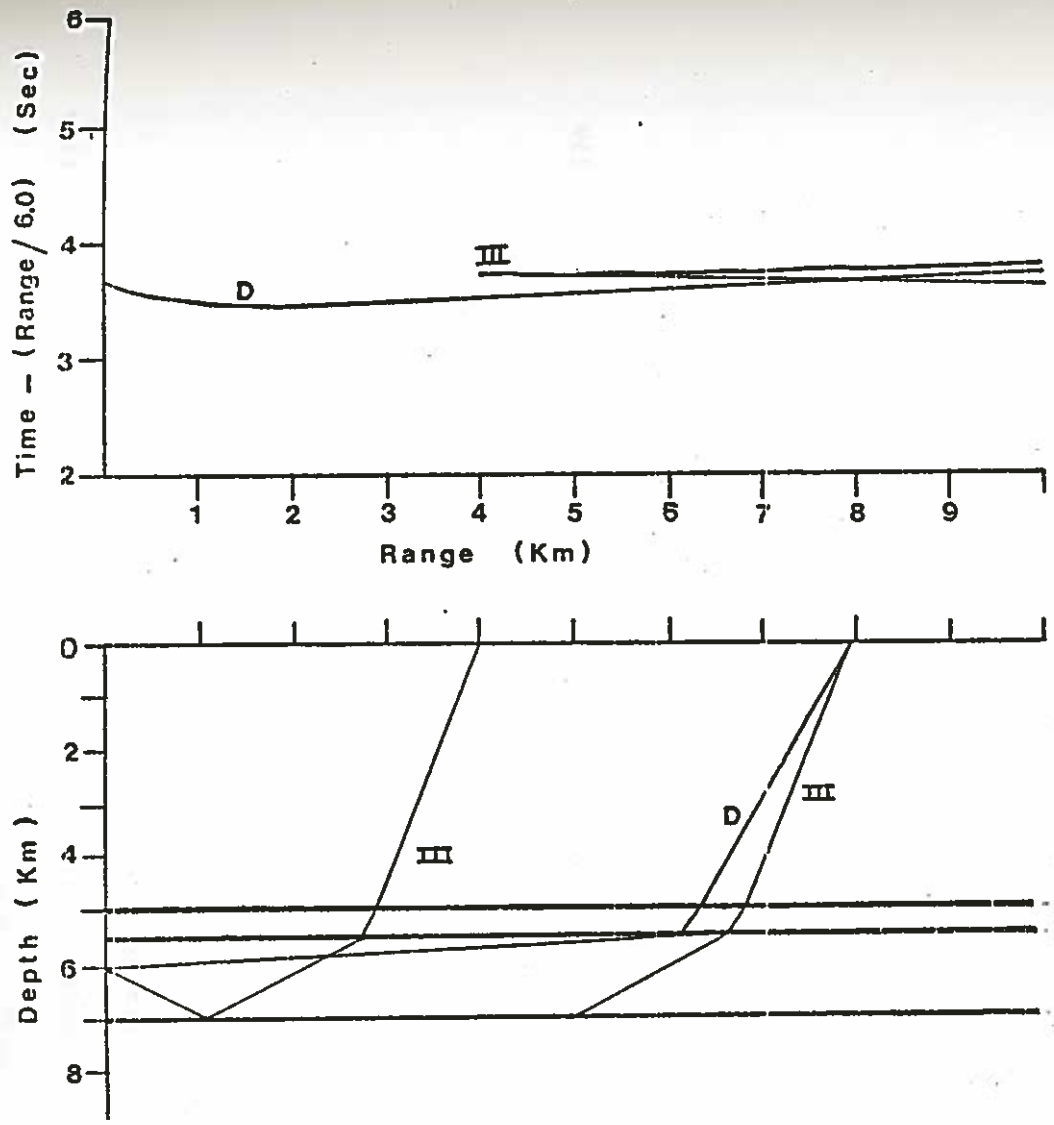
Time - (Range/6.0) (Sec)
6
5
4
3
2
D
III
1
2
3
4
5
6
7
8
9
Range (Km)
Depth (Km)
0
2
4
6
8
III
D
III

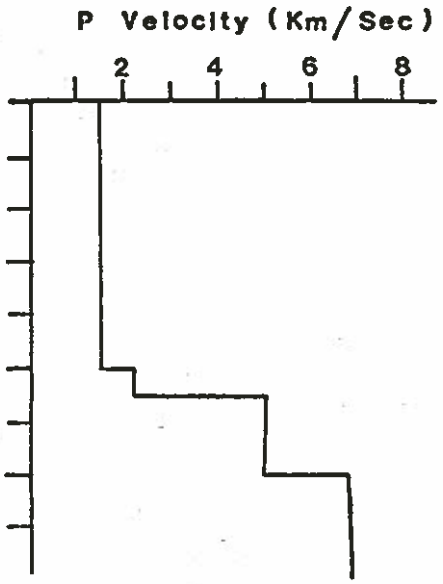
P Velocity (Km/Sec)
2
4
6
8

Figure 1-3-1b

case, with 0.5 km of sediment, layer 2 velocities are not sampled until ranges of 4.5 km and then the velocities are average velocities over at least 2.45 km of layer 2. The OSE samples layer 2 velocities right up to the receiver and is obviously more appropriate for looking at small scale lateral velocity variations than conventional refraction.

vi. Travel times in OSE's are less sensitive to the basement topography correction than travel times in conventional refraction experiments because the ray paths only pass through the basement-sediment interface once. Because of the high contrast in velocity between sediment (~ 2.2 km/sec) and basement (~ 5.0 km/sec) and because this interface is not well resolved by reflection profiling the error introduced into travel time analysis by this correction is significant. For example, if the basement topography is not known to within 50 m an uncertainty of 0.01 sec is introduced into the travel times for each time the ray path crosses the sediment-basement boundary. This problem is discussed further in Section 4-2c).

vii. As will be explained in Section 2-3d), proper attenuation measurements in oceanic crust can be made with the OSE by comparing amplitudes of arrivals at deep and shallow positions in the hole. A correction for the effect of structure between the receivers can be made when the sonic log for the hole is available. It is impossible to obtain satisfactory attenuation measurements from conventional refraction data because the effect of small scale structure cannot be adequately determined.

viii. The OSE is better suited to S-wave velocity studies of layer 2 than conventional refraction work. For example, Figures 2-3-2a

and 2-3-2b show synthetic seismograms for conventional refraction experiments with surface and ocean bottom receivers respectively. The amplitudes of the critically refracted S-waves from layer 2 are either undetectable or confused with other arrivals. In contrast, the corresponding synthetic seismogram for the OSE case (Figure 2-3-6a) shows very strong direct S-waves which appear as first shear wave arrivals for at least 2.0 km. (see also Section 2-3c)). Apparently the velocity contrast between compressional waves in sediment (2.1 km/sec) and shear waves in layer 2 (2.9 km/sec) is not large enough to generate strong shear head waves (Helmberger and Morris, 1970). The transmission coefficients however for P-wave to S-wave conversion at the top of layer 2 are significant particularly at large angles of incidence (Ergin, 1952). Shear wave velocity information is necessary for analysis of cracks (Section 1-5).

The operational advantages of the OSE over conventional refraction experiments are:

ix. The receiver is clamped to the rock wall of the borehole and hence has better coupling than an ocean bottom receiver which has fallen more or less randomly onto the sea bed and may, for example, be sitting on a rubble zone or poorly consolidated sediment. In an OSE, if a sonic log or core description is available, solid sections in the hole can be identified in advance. In addition, one would expect the background noise for a clamped borehole geophone to be less than for a receiver sitting on the sea bed which is exposed to bottom currents (Sutton et al, 1977). One would also expect that the amplitudes of both vertical and horizontal components would be reliable and

directly correlatable.

x. In the OSE case, the receiver is well located with respect to the borehole where in situ conditions have been measured and depths are known most accurately. For free falling bottom receivers the accuracy of emplacement is at best 200 m (Francis et al, 1975; McDonald et al, 1977). Since changes on this scale in basement topography (Section 4-2c) and point vi above) and in internal structure of layer 2 (Aumento et al, 1977) exist, detailed studies where one is interested in crust within a few hundred metres of the borehole are best carried out with an OSE.

The major disadvantage of the OSE is that it is a difficult experiment to carry out. (This is discussed in Sections 3-2 and 5-3d).) The drilling ship time is expensive compared to normal research vessel time and at its present stage of development the experiment requires two ships to rendezvous. This is not a simple task. The OSE is dependent on a borehole and hence is not as flexible as conventional refraction work. At this stage, horizontal arrays of borehole seismometers are out of the question and even reversed profiles are unreasonable.

1-4. STRUCTURE OF LAYER 2

In this section I will discuss the layer 2 velocity structure as measured by refraction experiments. The geological factors which may cause the observed structure will be discussed in Section 1-5a).

The range of refraction velocities for layer 2 is substantially greater than the range for layer 3 or the mantle. Is the greater range

real? Is it caused by velocities changing vertically or horizontally? On what scale are the velocities changing?

Evidence for the greater range of measured layer 2 velocities compared to measured layer 3 and mantle velocities was given by Raitt (1963a). His average layer 2 velocity with standard deviation was 5.05 $\pm$ 0.63 km/sec as opposed to 6.69 $\pm$ 0.26 km/sec and 8.13 $\pm$ 0.24 km/sec for layer 3 and the mantle respectively. These values were based on published marine refraction experiment results up to 1963. Christensen and Salisbury (1975) brought this study up to date. Their values of average layer 2, layer 3 and mantle compressional wave velocities for the main ocean basins with standard deviations were 5.04 $\pm$ 0.69, 6.73 $\pm$ 0.19 and 8.15 $\pm$ 0.31 km/sec respectively. In both studies the standard deviations of the layer 2 velocities (0.63 and 0.69 km/sec) were much greater than the standard deviations of layer 3 velocities (0.26 and 0.19 km/sec). This means that measured layer 2 velocities fall over a greater range than the measured velocities for layer 3 or the mantle.

This greater range for measured layer 2 velocities may be attributed in part to observational errors, caused by the short range over which refractions from layer 2 appear as a first arrival (Raitt, 1963a; Ludwig et al, 1970; Shor et al, 1971; and Kennett, 1977). Placing receivers and/or shots on the sea bed increases the range over which layer 2 arrivals appear as first arrivals (Kennett, 1977; Whitmarsh, 1967; and Shorthouse, 1964). However, no published review of measurements made with ocean bottom receivers exists and it is not yet clear whether such experiments have reduced the range of measured layer 2 velocities.

A number of established authors (Raitt, 1963a; Ludwig et al, 1970; and Shor et al, 1971) feel that at least some of the larger range of

layer 2 velocities is due to real geological factors such as different geology in different regions (Raitt, 1963a) or different geology with depth (Ludwig et al, 1970; Shor et al, 1971). In the latter case layer 2 may consist of two layers, of for example 4.0 and 5.5 km/sec and the velocity which is measured may depend on relative thickness of the layers (Shor et al, 1971). This interpretation is similar to the question of "sampling" a velocity gradient (Whitmarsh, personal communication).

Whitmarsh's suggestion (personal communication) that the wider range of layer 2 refraction velocities may be the result of sampling a velocity gradient at different depths is interesting. Figure 1-4-1 demonstrates the effect of sampling a velocity gradient. Figure 1-4-1a is a travel time diagram for an ocean bottom receiver in a structure with 0.5 km of sediment with a velocity of 2.2 km/sec and a gradient in layer 2 from 3.5 km/sec to 6.0 km/sec over 1.5 km. The sediment arrivals mask most of the low velocity arrivals from layer 2. An estimate of layer 2 velocity based on the first arrivals is 4.5 km/sec. In the travel time diagram of Figure 1-4-1b the sediment is removed and layer 2 is thinner but has the same gradient. In this case an estimate of layer 2 velocity based on travel time analysis is 3.6 km/sec. In these examples the velocity structure of layer 2 is the same but the "measured" velocities differ by almost 1.0 km/sec. Evidence that layer 2 may indeed be a region of gradually increasing velocity has been reported by Helmberger and Morris (1969), Helmberger (1977), Kennett and Orcutt (1976), and Whitmarsh (1978).

In order to sort out the variation in layer 2 velocities with depth and geographical region, Houtz and Ewing (1976) split layer 2 into three layers (based on refraction evidence) and divided observations into three geographical regions (Reykjanes Ridge, Atlantic Ocean and Pacific

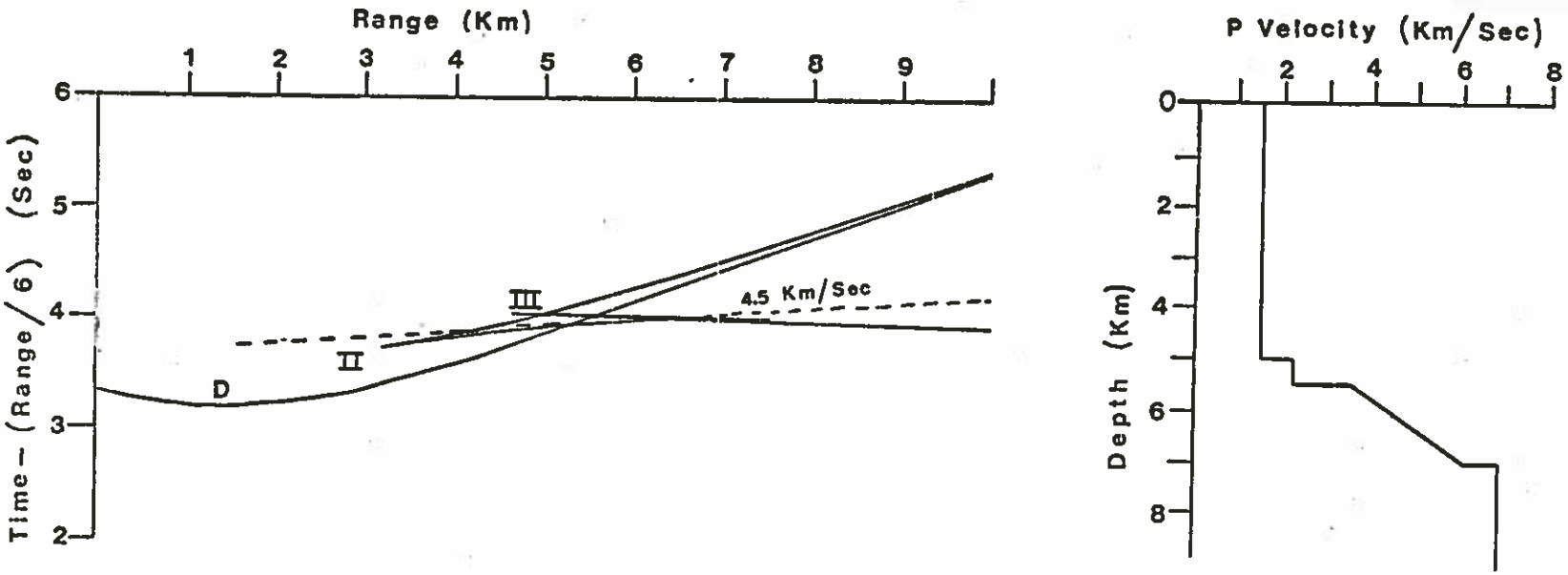

Figure 1-4-1a

Figure 1-4-1a&b. The phenomenon of "sampling" a gradient in layer 2 in an ocean bottom seismometer experiment. Although the velocity structure of layer 2 is the same in both Figures a) and b) the measured refraction velocity changes from 3.6 to 4.5 km/sec because of changes in the thickness of the sediment, the thickness of layer 2 and the depth of layer 2. In the diagrams D represents the direct arrival and II and III represent reflected and refracted arrivals for layers 2 and 3 respectively.

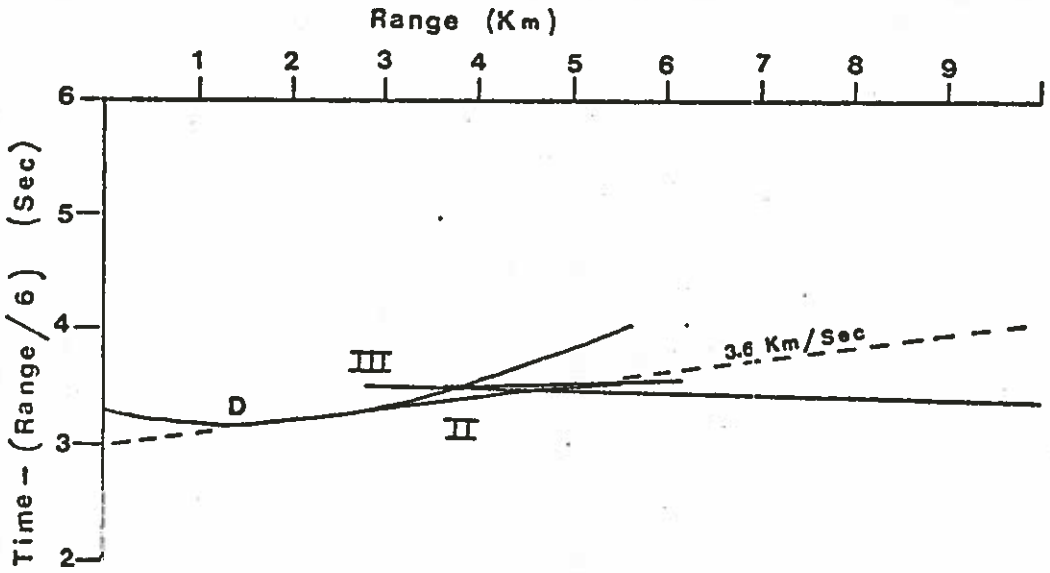
Range (Km)
1
2
3
4
5
6
7
8
9
Time – (Range / 6) (Sec)
6
5
4
3
2
D
III
II
3.6 Km/Sec

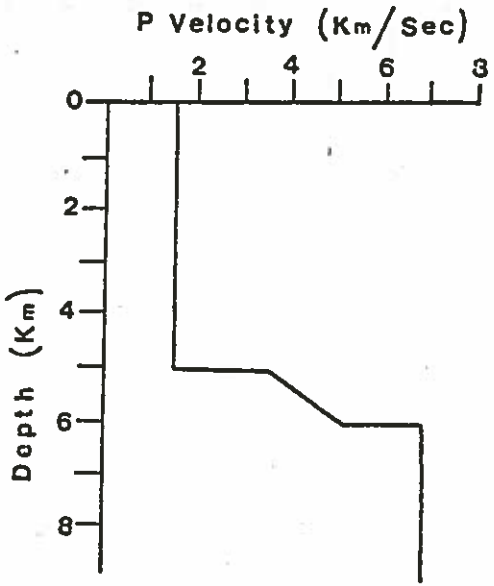
P Velocity (Km/Sec)
2
4
6
8
Depth (Km)
0
2
4
6
8

Figure 1-4-1b

Ocean) at a number of ages of crust. The standard deviations for the top two layers, 2A and 2B (approximately 0.4 km/sec) are still much larger than for layers 2C and 3 (approximately 0.2 km/sec) (Figure 1-4-2). Since the observational problems for layers 2A, 2B and 2C are about the same (ie. short distance over which first arrivals appear) at least some of the discrepancy in the ranges of upper and lower layer 2 velocities is real and reflects geological conditions. The material in upper layer 2 exhibits a greater range of velocity than lower layer 2, layer 3 or the mantle. Conventional seismic analysis to date has not determined whether this range is caused by horizontal changes on a scale smaller than Houtz and Ewing's geographical-age regions or by vertical changes in velocity or both.

Deep sea drilling results show that lithology in layer 2 to a depth of 333m cannot be clearly correlated between holes only 100 m apart (Aumento et al, 1977). It appears that the structure of layer 2 changes laterally on a scale smaller than refraction experiments could resolve. (The limit of this resolution is based on the seismic frequency used and not on the geometry of the experiment). Do these lateral changes in structure exist on a large enough scale to affect seismic velocities and to contribute to the wider range in measured refraction velocities for upper layer 2?

In order to consider the effect of lateral velocity changes I construct a model in which layer 2 consists of blocks of material of effectively constant velocity. These blocks are large enough to resolve at seismic frequencies (at least 0.5 km in lateral extent) and their velocities are typical layer 2 refraction velocities (ranging from 3.5 km/sec to 6.0 km/sec). By drilling into one of these blocks and firing near normal incidence charges into a receiver in the borehole one

Area	Layer 2A			Layer 2B			Layer 2C			Layer 3			
	V,km/s	N	σ	V,km/s	N	σ	V,km/s	N	σ	V,km/s	N	σ	Age, m.y.
Reykjanes	3.61	7	0.52	5.31	7	0.49	6.18	3	0.08	6.80	5	0.23	5
	3.90	5	0.23	4.80	6	0.41	5.80	3	0.26	6.91	4	0.23	12.3
Atlantic	3.33	5	0.67	5.16	4	0.59	6.50	1	...	...	...	...	4
	3.86	4	0.58	5.09	5	0.51	6.00	1	...	6.75	1	...	14
	4.12	3	0.33	5.43	4	0.64	6.25	1	...	...	...	...	27
	4.03	2	0.25	4.93	11	0.29	6.02	6	0.16	...	...	...	52
	...	...	...	5.06	11	0.37	6.10	5	0.21	6.85	5	0.15	73.5
	...	...	...	5.18	14	0.27	6.03	12	0.22	6.74	9	0.22	100
	...	...	...	5.13	19	0.31	6.09	6	0.24	6.78	10	0.20	125.5
	...	...	...	5.22	19	0.37	6.13	11	0.18	6.94	8	0.24	147
	...	...	...	5.09	24	0.32	5.97	12	0.22	6.86	6	0.22	165
Pacific	3.47	12	0.41	5.22	28	0.45	6.16	17	0.21	6.98	15	0.17	1.3
	3.33	3	0.10	5.23	13	0.44	6.19	10	0.16	6.92	6	0.17	5
	3.90	1	...	5.02	11	0.34	5.87	5	0.24	6.83	4	0.24	17
	...	...	...	5.38	6	0.27	6.18	3	0.12	6.73	5	0.21	36
	...	...	...	5.40	10	0.55	5.99	4	0.25	6.78	3	0.28	59.5
	...	...	...	5.33	12	0.22	6.13	7	0.16	6.85	5	0.11	92
	...	...	...	5.63	5	0.44	6.18	3	0.29	6.97	6	0.17	122
	...	...	...	5.43	8	0.36	6.13	4	0.06	6.85	3	0.18	160
Atlantic and Reykjanes	3.74	26	0.50	5.13	124	0.38	6.05	61	0.22	6.83	48	0.21	...
Pacific	3.47	16	0.35	5.28	93	0.39	6.12	53	0.18	6.90	47	0.17	...

Figure 1-4-2. Detailed velocity structure for oceanic crust of different ages in the Atlantic and Pacific Oceans and Reykjanes Ridge. Despite the further breakdown into more layers and into different geographical regions, the spread in upper layer 2 (2A and 2B) velocities is much greater than the spread in lower layer 2 (2C) and layer 3 velocities. (From Houtz and Ewing, 1976).

can determine the velocity of the block (Section 1-3, point i). Also, one can determine the extent of the block by firing lines up to 12 km long in different directions from the hole (Section 1-3, point v and Section 2-1b)).

1-5. CRACKS

a). Significance of Cracks in Oceanic Crust

The nature of cracks in oceanic crust is important for two reasons. First, cracks provide channels in which hydrothermal circulation can flow. The depth and extent of this flow has consequences in oceanic heat flow. Hyndman et al (1977) reported that conductive heat flow near the mid-Atlantic ridge is 0.6 ± 0.1 μcal.cm.$^{-2}$ sec.$^{-1}$ (25 ± 4 mW.m^{-2}) compared to 6.4 μcal.cm.$^{-2}$sec.$^{-1}$ (269 mW.m^{-2}) which is predicted by theoretical models and this discrepancy may be explained by hydrothermal heat transport. Also, an understanding of the formation of mineral concentrations by hydrothermal action would have economic consequences in deep sea mining (Lister, 1974a).

The second reason for studying cracks is to see if they are directly responsible for the seismic discontinuities in oceanic crust. This knowledge would lead to a better understanding of the process of sea-floor spreading and the formation of oceanic crust. Lort and Matthews (1972) performed seismic experiments on the Troodos ophiolite sequence and explained abnormally low velocities in all rock types by the presence of high porosity. They suggested that the layer 2 - layer 3 boundary may represent the depth at which cracks close due to overburden pressure. Poster (1973) reported results from ultrasonic velocity measurements on pressurized samples of the Troodos rocks and concluded that the compositional differences could explain the crustal layering.

The abnormal refraction results were explained by fracturing due to local effects.

To what extent is the large range in upper layer 2 velocities (Section 1-4) caused by variation in rock type (including the effects of weathering and metamorphism) and by variations in the quantity, size or shape of cracks? Whitmarsh (1978) discussed rock types (basalts, meta-basalts and dolerites) and velocities in upper layer 2. His objective was to explain velocity gradients in layer 2 but the same discussion applies to possible lateral velocity variations.

Drilling in the upper portions of layer 2 (up to 0.6 km penetration) has demonstrated that upper layer 2 is primarily basalt (Melson et al, 1974; Rabinowitz et al, 1976; Hyndman, 1977). Schrieber and Fox (1976) measured compressional velocities of laboratory samples of four petrographically different groups of fresh basalt (olivine basalts, plagioclase basalts, plagioclase-olivine basalts and pyroxene basalts). They concluded that there was no correlation between velocity and mineralogy at pressures equivalent to that for layer 2 but that porosity and pore geometry had a significant effect on the measured velocities. Variation in the type of basalt is not a satisfactory explanation for the velocity difference in layer 2.

The velocities of metamorphosed and weathered basalts fall over a broad range from 3.5 to 6.5 km/sec. (Christensen and Salisbury, 1972, 1973; Christensen and Shaw, 1970; Barrett and Aumento, 1970; and Fox et al, 1973). Most of the evidence for metamorphosed basalts, however, comes from dredge hauls of fracture zones and ophiolite sequences on land which may not be typical of oceanic crust. Christensen and Salisbury (1972, 1973) attributed the broad range of velocities in DSDP core material to weathering. Particularly in younger crust, however, the

range in their laboratory measured velocities based only on cores is less than the range for refraction velocities. Cracks on a scale larger than laboratory samples is a possible explanation.

Drilling certainly suggests that there are cracks in oceanic crust on a scale larger than core samples. Using data from Hole 332B, Hyndman (1977) obtained a reasonable refraction velocity from the time-weighted average of basalt velocity from cores and an estimated sediment-rubble velocity. His model for upper layer 2 consisted of fractured basalt with intercalated sediment rubble. Cracks are certainly a significant factor affecting layer 2 refraction velocities.

At this stage it is not clear whether variation in rock type including weathering and metamorphism or variation in crack density is the predominant cause of the wide range of layer 2 refraction velocities. A comparison of rock type and crack density, estimated from coring and logging techniques, with high resolution seismic measurements as close as possible to the hole will be able to differentiate between the two effects. The specific advantages which the OSE has in this type of study are reviewed in Section 1-5g). For the remainder of the dissertation I will assume that cracks are the only cause of significant velocity variation in layer 2.

b). Definitions

For the purpose of investigating the effect of cracks on seismic structure in layer 2 let us define some terms. Cracks and pores are gaps in the rock where no solid phase exists. They may be filled with either liquid or vapour (materials with very low or vanishing shear modulus) or a combination of liquid and vapour. No a priori assumptions are made about the shape or size of a crack or its means of formation. Vesicles

and microcracks are considered to be cracks whose dimensions are smaller than the wavelength of sound used in laboratory sonic velocity measurements ($\sim$ 5 mm, Birch, 1960). Vugs are cracks that are too big to be microcracks, or vesicles but are small compared to the wavelength used in sonic velocity logging (about 250 cm). Their longest dimensions may range from a few millimetres to a few centimetres. Fissures are cracks which are larger than vugs but are small compared to the wavelength of seismic refraction work (which is on the order of a few hundred metres). This approach assumes that cracks affect the bulk properties of the rock and questions of scattering and diffracting of sound around discontinuities on the order of a wavelength are not considered.

In the following sections I will review the background of studies of cracks on the three scales: laboratory studies, well logging work and seismic experiments. Recently, attempts have been made to theoretically predict the velocities of elastic waves in cracked rock and these are also discussed (Section 1-5f)). There will be no loss of continuity if the reader skips these sections.

c). Laboratory Studies of Cracks

Wyllie et al (1956, 1958) conducted one of the first laboratory studies of elastic waves in porous media and demonstrated empirically the validity of the time-average formula:

$$\frac{1}{V^*} = \frac{\phi}{V'} + \frac{(1-\phi)}{V}$$

where V^* is the velocity of the porous rock, V' is the fluid velocity, V is the rock matrix velocity and ϕ is the volumetric porosity. They pointed out that this formula is a good approximation when the rock

is saturated with a high velocity fluid (e.g. water) and is subjected to a high differential pressure. (Differential pressure is the external applied pressure minus the pore pressure.)

A classic laboratory study of P-wave velocity in igneous and metamorphic rocks at pressures up to 10 kbar was performed by Birch (1960, 1961). He discussed the effects of porosity, alteration, anisotropy and composition in detail. An observed increase in velocity with increasing pressure was attributed to pores closing. He explained anisotropy at low pressures by oriented porosity and a much reduced anisotropy at high pressure by crystal alignment. Simmons (1964) supplemented Birch's work by considering S-wave velocities in many of the same samples.

Walsh (1965) and Brace (1965) analysed the effects of cracks on compressibility. The theoretical study of Walsh showed that narrow cracks were almost as effective at increasing compressibility as spherical pores and Brace's laboratory work showed that for most metamorphic and igneous rocks the cracks could be closed by applying pressure but that some pores may stay open at 10 kbar. The work of Wyllie et al, Birch, Simmons, Walsh, Brace and others, established quantitatively that cracks close and velocity increases with increasing pressure. This result led to crack theories to explain aspects of crustal structure.

The dramatic effect of pressure on compressional velocity is greatly reduced if the cracks are saturated with a highly incompressible liquid (Nur and Simmons, 1969a). Flat cracks are necessary for the effect. Shear velocities are not as sensitive as compressional velocities to saturation (Figure 1-5-1). When attempting to determine crack structure from velocity information one must consider the degree

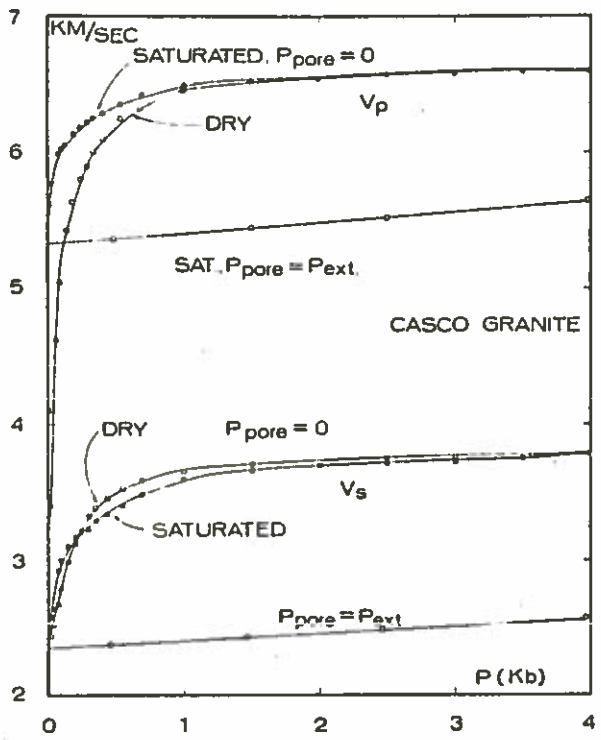

Figure 1-5-1. Compressional and shear wave velocities for dry and saturated rocks as a function of pressure. The decrease in compressional wave velocities with decreased pressure (increased porosity) is less dramatic for saturated rock. (from Nur and Simmons, 1969a)

of saturation.

Hyndman (1977) reviewed the application of laboratory sonic velocity measurements on cored and dredged marine samples to the study of oceanic crust. Laboratory work has demonstrated a relationship between the degree of weathering (from sonic velocities) and age and between degree of weathering and depth (Christensen and Salisbury, 1972, 1973; Hyndman, 1974; Salisbury and Christensen, 1976). From the DSDP Leg 37 results Hyndman attributed the discrepancy between laboratory velocities in fresh cored basalts (approximately 6.0 km/sec) and refraction velocities (approximately 5.0 km/sec) to the effect of large fractures or pockets of intercalated sediment which were indicated by changes in drilling rate. He also gave relationships between compressional velocity and density and between Poisson's ratio and compressional velocity for basalts and gabbros. These relationships can be used in the interpretation of refraction experiments where only P-wave velocity is measured.

d). Investigation of Cracks by Well-Logging

Porosity determinations from well logs are common in petroleum exploration where they are applied to sedimentary rocks. Combinations of sonic logs, gamma-gamma logs, and neutron logs are interpreted using largely empirical relations (Wyllie et al, 1958; Tixier et al, 1959; Geertsma, 1961; Tixier, 1962; Gardner et al, 1974). "Litho-porosity crossplots" display combinations of the logged parameters and facilitate interpretation in areas of complex lithology (Burke et al, 1969; Poupon et al, 1971). The empirical relations are, of course, only well determined for rock types common in oil and gas exploration: sandstone, limestone, dolomite, gypsum, anhydrite, shale, etc.

Sonic logs (Section 1-2a)) measure the velocity of high frequency (20 kHz) sound in the immediate vicinity of the well to penetrations of a metre or less. If the velocity of the matrix is known and it is assumed that water fills the pores then porosity can be calculated from the time-average equation (Section 1-5c)). Pickett (1963), Morris et al (1964) and Bond et al (1971) have discussed the effect of fractures on the amplitudes of sonic logs.

Gamma-gamma logs are based on Compton scattering and measure electron density which is related to the bulk density of the rock depending on the atomic number and atomic weight of the atoms comprising the formation (Tittman and Wahl, 1965). If the matrix density, fluid density and bulk density are known, the total porosity (secondary plus primary) can be calculated.

Neutron logs measure the rate at which high energy neutrons are slowed down due to collisions in the rock (Tittman et al, 1966). Since particles the same size as the neutrons will slow them down most effectively, the log measures the presence of hydrogen. In rocks in which the matrix minerals contain no hydrogen (e.g. basalt) neutron logs measure the quantity of water or oil directly and therefore measure porosity. If the matrix minerals contain hydrogen (e.g. serpentinite, greenstone) the log must be combined with another porosity log to separate the effects of porosity and lithology.

For these logging techniques to be of value in the study of basalts, experience is required. Measurements in basalts of known porosity and composition should be made in order to set up the necessary empirical relations. Continental flood basalt regions (e.g. the Columbia flood basalts) may be suitable. Correlation between logging results and laboratory studies of cores should also be carried out.

e). Field Observations and Cracks in Oceanic Crust

Few attempts have been made to correlate field refraction observations with porosity. The efforts of Lort and Matthews (1972) have already been mentioned (Section 1-5a)). Francis (1976) reported an abnormally high P- to S-velocity ratio (2.08) at the mid-Atlantic ridge from earthquake data which he attributed to high fissure and crack porosity.

Whitmarsh (1978) attempted to obtain upper bounds on a porosity depth function from compressional wave refraction experiments only and his results were consistent with the theory that crack density decreases with depth. The positive velocity gradient at the top of layer 2 was explained by the closing of cracks due to hydrothermal accretion or consolidation as a result of sediment overburden.

f). Theories of the Effects of Cracks on Velocities

The recent interest in dilatancy models of earthquake prediction (Nur, 1972; Whitcomb et al , 1973) generated a number of theoretical studies of the effects of cracks with varying saturation on velocity. Anderson et al (1974) and Kuster and Toksöz (1974) developed theories based on non-interacting, sparse cracks and O'Connell and Budiansky (1974) considered an interactive theory for a system of dense cracks. All theories emphasized the importance of the effect of crack shape on velocity.*

---

* Since this review was written a study of the effect of oriented cracks on P-wave velocity anisotropy has been reported by Crampin (1978) and Crampin et al (1978). For planar and biplanar crack systems, the variation of P-wave velocity is shown to be sufficient to determine the crack densities, the strike of the crack planes, and the shear wave velocities if the dips of the crack planes and the matrix P-wave velocity are assumed.

Anderson et al (1974) considered the orientation of cracks and anisotropy. For liquid filled cracks anisotropy is greater for shear waves than for compressional waves. The opposite is true for gas filled cracks.

The non-interactive theory of Kuster and Toksöz relates porosity (ϕ) and aspect ratio (α) to the bulk moduli (K), shear moduli (μ) and densities (ρ) of the cracked rock (star superscripts), pore fluid (prime superscripts) and matrix (no superscripts). (This notation is used throughout the dissertation). The P- and S-wave velocities are calculated as usual from the moduli and density. Gas, oil and water inclusions are treated by their different moduli (Toksöz et al, 1976). Aspect ratio spectra can be considered.

For spheroidal cracks (a = b > c) the aspect ratio is $^{c}/_{a}$. (The letters a, b and c are the lengths of the principal axes). Observed cracks are connected to theoretical cracks through the concept of the spheroidal crack and Hadley (1976) has reviewed various statistical methods.

The self-consistent theory of O'Connell and Budiansky, on the other hand, relates crack density (ε) and either the saturated fraction (ξ) or the soft-fluid parameter ($\omega = \alpha \frac{K'}{K}$) to the elastic moduli and velocities. The crack density is defined by

$$\varepsilon \equiv \frac{1}{V} \sum a^3$$

where V is volume, a is the long dimension of the crack and the summation is over all of the cracks in the volume. In the simplified case of spheroidal cracks, aspect ratio (α) is related to porosity (ϕ) by:

$$\phi = \frac{4\pi}{3} \alpha \varepsilon .$$

No information about porosity or aspect ratio is obtainable from P- and S-wave velocities if the pore fluids have either very high (e.g. water) or very low (e.g. air) bulk moduli. This theory is best suited to highly fractured, low porosity rocks because interactions are considered but density information is not.

Wyllie's time average formula (Section 1-5c)) based on empirical results is widely used in petroleum exploration. It may be worthwhile to see how it compares with theory. As an example, for a rock with matrix properties, V_p = 6.21 km/sec, V_s = 3.33 km/sec, ρ = 2.95 gm/cc and ϕ = .05, saturated with a fluid of V_p' = 1.55 km/sec and ρ' = 1.0 gm/cc Wyllie's formula gives an effective velocity, V_p^*, of 5.4 km/sec. For the same rock with completely saturated spherical pores the non-interactive theory gives a V_p^* of 6.0 km/sec. An aspect ratio of 0.1 is necessary to give the Wyllie formula result. The self-consistent theory, assuming spheroidal cracks, gives V_p^* of 6.1 km/sec for spheres and again an aspect ratio near 0.1 is required for agreement with Wyllie.

Hadley (1976) compared the self-consistent and non-interactive theories to lab measurements of velocity and observed porosity using a scanning electron microscope. Good agreement between observations and theory was found for hydrostatic loading.

g). Discussion

Ultrasonic measurements on hand samples in the laboratory should be able to predict the effect of microcracks on velocity in situ and sonic logging in oceanic crustal boreholes should determine the effect of vugs on velocity. However, only detailed seismic experiments can tie down the effect of large fractures. The OSE can measure the velocity in the crust at seismic frequencies immediately adjacent to the

hole (Section 1-3, point i). Discrepancies between the integrated sonic log velocities and the seismic velocities may be caused by the presence of large cracks which are not adequately sampled by the drilling. If these large cracks are predominantly vertically oriented there would be a difference between the vertical and horizontal velocities. Cracks and anisotropy are discussed further in Section 1-6d). If the lateral velocity variations discussed in Section 1-4 are caused by cracks, then the studies of cracks and lateral velocity variations are effectively the same. The importance of making seismic velocity measurements in crust where the structure is known by drilling cannot be over emphasized. Because the structure changes on the scale of a few hundred metres, conventional refraction techniques which obtain an average velocity over ranges of 2 km or more (Raitt, 1963a; Houtz, 1976) are inadequate. As explained previously the OSE has better resolution. It is also essential for a proper study of cracks to know the S-wave velocity (Section 1-5f)) and the OSE is more suited to detecting S-wave arrivals than conventional refraction experiments (Section 1-3, point viii).

1-6. ANISOTROPY

a). Outline

Preferred crack orientation may cause seismic anisotropy in layer 2. Before discussing the reasons for this in detail (Section 1-6d)) I will review the theory of anisotropy (Section 1-6b)) and the history of measurements of anisotropy at sea (Section 1-6c)). Section 1-6e) is a review of the OSE and anisotropy.

b). Theory

In an anisotropic medium the elastic parameters vary in general with direction. If the elastic properties are constant in a plane perpendicular to an axis of symmetry then the medium is transversely isotropic. Flat lying sediments may be transversely isotropic with a vertical symmetry axis (Vanderstoep, 1966) and the crystalline structure of the upper mantle may be transversely isotropic with a horizontal symmetry axis in the direction perpendicular to the magnetic lineations (Hess, 1964; Raitt et al, 1969; Morris et al 1969).

Love (1934) developed the theory for elastic wave propagation in a transversely isotropic solid. In general, there are three velocities of propagation and the particle motion cannot be split up into purely compressional or purely shear terms. Stoneley (1949) considered the implications of anisotropy in crustal seismology citing crystal orientation during cooling in a stress system as a possible cause. Appreciating the difficulties in picking travel times he urged the use of three-component seismometers in order to ascertain the plane of polarization of the S-waves. Červený (1972) and Červený and Pšenčik (1972) developed methods for calculating travel-time curves in inhomogeneous, anisotropic media.

Recently, studies of the effects of anisotropy on signal amplitudes and the polarization of body wave arrivals have been reported by Bamford and Crampin (1977) and Crampin (1977). They noted that large quantities of refracted P-wave data are required to separate the effects of anisotropy and lateral inhomogeneities using velocity analysis. Crampin (1977) suggested using polarization anomalies to measure anisotropy although little analysis along these lines for body waves has been attempted. A proper polarization study requires that the orientation

of the horizontal components be known (Crampin, pers. comm.). In the OSE case it may be possible to determine geophone orientation from the direct P-wave arrival at long ranges.

c). Measurements of Anisotropy at Sea

Oceanic crust is formed by a bilaterally symmetric process and any study of oceanic crustal structure should consider the possibility of azimuthal velocity anisotropy. Anisotropy has been measured at sea for the upper mantle and one can obtain a feel for the problem of measuring anisotropy at sea by considering the techniques used. Hess (1964) suggested that there may be transverse isotropy in the upper mantle based on refracted P-wave velocities obtained by Raitt (1963b) and Shor and Pollard (1964). Backus (1965) did an analysis of P-wave and S-wave velocities for the cases of i) a transversely isotropic mantle with horizontal axis of symmetry, ii) crustal and mantle inhomogeneities and iii) a curved and sloping Moho, in order to distinguish possible causes of azimuthal dependence. Crosson and Christensen (1969) adapted the theory of Backus to the case of an unrestricted axis of symmetry. Both studies concluded that the data of Raitt and Shor implied the existence of a transversely isotropic upper mantle.

Raitt et al (1969) and Morris et al (1969) conducted detailed velocity surveys in the Pacific with the expressed intent of determining upper mantle anisotropy. Cross patterns of lines (two receiving ships) and circles around cross patterns (one receiving ship) were shot. The data was analysed using a modified version of the delay-time technique (Gardner, 1939; Scheidegger and Willmore, 1957; Willmore and Bancroft, 1960; Berry and West, 1966; and Smith et al, 1966). The average velocity

was determined to within 0.025 km/sec confidence limits and the anisotropy was 0.3 km/sec in the first case and 0.6 km/sec in the latter. Upper mantle anisotropy in the Atlantic was reported by Keen and Tramontini (1970). In this work the time-term method was necessary to confidently determine anisotropy.

d). Anisotropy in Layer 2

Three causes of anisotropy in the oceanic crust and the upper mantle have been suggested: i) preferred crack orientation (Walsh, 1965), ii) Crystal orientation (Hess, 1964; Christensen, 1972; Johnson and Wenk, 1974) and iii) nonhydrostatic stress on cracked rock (Nur and Simmons, 1969b). The oriented, linear block faulting observed at the Mid-Atlantic Ridge in the FAMOUS (French American Mid-Ocean Undersea Study) area [by the deep sea submersible, Alvin, (Ballard et al, 1975; Ballard and van Andel, 1977) and by a deep tow instrument package (Macdonald and Luyendyk, 1977 and Luyendyk and Macdonald, 1977)] would be expected to give a preferred crack orientation which would be the most likely source of upper layer 2 anisotropy. The standard deviation of crack orientation at one site in the inner floor studied by Macdonald and Luyendyk was only 6^{o}. As the crust moves outward it is uplifted in a series of normal faults to the rift mountains which again are remarkably well oriented.

Estimates of the effect of preferred crack orientation on velocity can be obtained from Anderson et al's theoretical work. Figure 1-6-1 gives shear and compressional wave velocities normal and parallel to cracks of various densities and aspect ratio. For example, an anisotropy of 0.4 km/sec for both P-waves and S-waves is caused by cracks with an aspect ratio of 0.05 and a porosity of only 2%. For spheroidal cracks this

TABLE 2. Vertical Velocities V_{P2} and V_{S2}, Horizontal Velocities V_{P1}, V_{S1}, and V_{S2}, and Velocity Ratios $\zeta = (V_P/V_S - 1)$ as a Function of Aspect Ratio α, Porosity ϕ, and Bulk Modulus of the Fluid Phase κ_f

α	ϕ	κ_f, kbar	V_{P1}, km/s	V_{P2}, km/s	V_{S1}, km/s	V_{S2}, km/s	$\zeta_1^{(1)}$	$\zeta_1^{(2)}$	ζ_2
1.00	0.01	100	6.532	6.532	3.764	3.764	0.74	0.74	0.74
		0.1	6.526	6.526	3.764	3.764	0.73	0.73	0.73
0.80	0.001	100	6.577	6.576	3.797	3.797	0.73	0.73	0.73
		0.1	6.576	6.575	3.797	3.797	0.73	0.73	0.73
0.80	0.005	100	6.555	6.550	3.783	3.781	0.73	0.73	0.73
		0.1	6.550	6.543	3.783	3.781	0.73	0.73	0.73
0.80	0.01	100	6.528	6.517	3.766	3.761	0.75	0.75	0.73
		0.1	6.517	6.503	3.766	3.761	0.73	0.73	0.73
0.50	0.001	100	6.578	6.574	3.797	3.796	0.73	0.73	0.73
		0.1	6.577	6.572	3.798	3.796	0.73	0.73	0.73
0.50	0.005	100	6.559	6.539	3.786	3.778	0.73	0.74	0.73
		0.1	6.553	6.527	3.786	3.778	0.73	0.73	0.73
0.50	0.01	100	6.534	6.495	3.771	3.755	0.73	0.74	0.73
		0.1	6.524	6.470	3.771	3.755	0.73	0.74	0.72
0.10	0.001	100	6.575	6.561	3.798	3.787	0.73	0.74	0.73
		10	6.575	6.539	3.798	3.787	0.73	0.74	0.73
		1	6.574	6.535	3.798	3.787	0.73	0.74	0.73
		0.1	6.574	6.534	3.798	3.787	0.73	0.74	0.73
0.10	0.005	100	6.561	6.476	3.790	3.737	0.73	0.76	0.73
		10	6.546	6.362	3.790	3.737	0.73	0.75	0.70
		1	6.542	6.338	3.790	3.737	0.73	0.75	0.70
		0.1	6.542	6.336	3.790	3.737	0.73	0.75	0.70
0.1	0.01	100	6.538	6.367	3.779	3.673	0.73	0.78	0.73
		10	6.508	6.134	3.779	3.673	0.72	0.77	0.67
		1	6.503	6.084	3.779	3.673	0.72	0.77	0.66
		0.1	6.502	6.079	3.779	3.673	0.72	0.77	0.66
0.05	0.01	100	6.536	6.312	3.780	3.564	0.73	0.83	0.77
		10	6.474	5.760	3.780	3.564	0.71	0.81	0.62
		1	6.464	5.569	3.780	3.564	0.71	0.81	0.56
		0.1	6.462	5.545	3.780	3.564	0.71	0.81	0.56
0.05	0.02	100	6.488	6.030	3.760	3.310	0.72	0.96	0.82
		10	6.364	4.799	3.760	3.310	0.69	0.92	0.45
		1	6.323	4.323	3.760	3.310	0.68	0.91	0.31
		0.1	6.318	4.261	3.760	3.310	0.68	0.91	0.29
0.01	0.001	100	6.577	6.550	3.798	3.693	0.73	0.78	0.77
		10	6.557	6.367	3.798	3.693	0.73	0.78	0.72
		1	6.533	6.145	3.798	3.693	0.72	0.77	0.66
		0.1	6.528	6.095	3.798	3.693	0.72	0.77	0.65

Figure 1-6-1. Velocity anisotropy for cracks of various aspect ratio (α) and porosity (ϕ). In the following description the cracks are assumed to be oriented with their normals vertical. V_{P1}, V_{P2}, V_{S1}, and V_{S2} are the compressional velocities parallel and perpendicular to the cracks and the horizontally polarized shear velocities parallel and perpendicular to the cracks respectively. For vertical propagation the horizontally polarized and vertically polarized shear waves have the same velocity (V_{S2}). For horizontal propagation the vertically polarized shear wave has the velocity, V_{S2}. The table has been calculated assuming $\lambda = \mu = 390$ kbar and $\rho = 2.7$ gm/cc. These values compare roughly with measured values on cored basalts (Christensen and Salisbury, 1973). For water filled cracks the fluid bulk modulus is about 25 kbar. The table is taken from Anderson et al (1974).

corresponds to one crack 0.43 units long and 0.02 units wide per unit volume.

The FAMOUS area work shows many faults and fissures in the median valley (Ballard and Van Andel, 1977). In the central volcanic province 36 fissures and 14 faults were crossed during 3.8 km of traverses; in the marginal tectonic province 71 fissures and 80 faults were crossed in 7.5 km of traverses; and in the west wall province 18 faults were crossed in 1.9 km of traverses. In the latter case some faults and fissures may have been covered with sediment. Vertical movement at the walls seemed to occur at the fissures. One fissure crossed in the marginal tectonic province was 50 cm wide and at least 50m long, giving a maximum aspect ratio of 0.01.

Based on these observations, we can construct a sample model for upper crust. Let us take one spheroidal fissure, of length 50m and aspect ratio 0.01, in every 100m cube. The resultant porosity would be 1% and the resultant velocity anisotropy (both P-wave and S-wave) should be greater than 0.2 km/sec (cf. α = 0.05, ϕ = 0.01 in Figure 1-6-1).

The model may underestimate anisotropy because fractures are not considered and the normal faulting in the mountain building process may be expected to produce more cracks. The estimate would be decreased if the fissures are filled with rubble or completely closed.

e). Anisotropy and the OSE

Shear wave anisotropy caused by preferred crack orientation is theoretically greater than compressional wave anisotropy and the OSE is ideally suited to measuring S-wave velocities (Section 1-3, point viii). The direct wave travel time curve for S-waves is approximately a straight

line for about 3 km before it is confused with refractions and reflections (Figure 2-3-6a). The compressional wave direct arrivals fall on a curve whose shape is insensitive to velocity. The direct shear wave amplitude increases with range because the P-wave to S-wave transmission coefficient increases with angle of incidence in contrast to direct compressional wave amplitude which decreases (Ergin, 1952). Unfortunately shear waves arrive later in the record and are interfered with by late compressional wave energy. However, the OSE should be able to detect seismic anisotropy in layer 2 on the order of 0.2 km/sec if it is present.

1-7. ATTENUATION

a). Outline

Attenuation is an important property in seismology because it is a measure of how well a medium satisfies the assumptions of perfect elasticity and homogeneity. After defining terms (Section 1-7b)) I will discuss the OSE and attenuation in layer 2.

b). Definitions

Attenuation is the residual loss in amplitude with distance after consideration of divergence, and transmission and reflection losses at boundaries (White, 1965). It can be subdivided into intrinsic attenuation, which is a direct measure of the anelasticity of the rock, and residual attenuation, which is what is commonly measured and includes scattering effects caused by inhomogeneities (Hamilton, 1976a). Attenuation can be expressed as

$$\alpha = kf^n$$

where α is attenuation in decibels/metre, k is a constant, f is frequency, and n is the exponent of frequency (Hamilton, 1972). Field and laboratory measurements conclude that n is not significantly different from 1 (White, 1965; O'Brien and Lucas, 1971). This result also applies to effective attenuation in thick marine sediment sections and sedimentary strata. This is surprising because one would expect scattering effects to be strongly frequency dependent (Hamilton, 1976a).

Another way of expressing attenuation is in terms of internal friction, Q^{-1}, where

$$Q^{-1} = \frac{1}{2\pi} \frac{\Delta W}{W} \quad .$$

W is the total amount of energy stored per unit cycle and ΔW is the part of W which is dissipated per cycle (Jackson and Anderson, 1970). Internal friction is frequency independent when n = 1.

c). Attenuation, Layer 2 and the OSE

The causes of intrinsic attenuation are reviewed by Jackson and Anderson (1970) and Gordon and Nelson (1966). The relation between intrinsic attenuation and dispersion poses one of the most interesting problems in seismology. Frequency independent attenuation and zero dispersion, both empirically measured in the field, are incompatible with linear theory (McDonal et al, 1958; O'Brien and Lucas, 1971). This will not be discussed further since it is unlikely that the OSE will contribute significantly to a solution. However a measure of intrinsic attenuation in oceanic crust would contribute to the sparse data available for geological conditions. An analysis of attenuation in anisotropic media has been conducted by Johnson (1974).

Residual attenuation is a worthwhile quantity in its own right in the interpretation of crustal structures using amplitude analysis. It may also give a measure of inhomogeneity in the crust. Kennett (1975b) gives a review of attenuation and synthetic seismograms for mantle studies and demonstrates the effect of attenuation in a model of the low velocity zone in the upper mantle. The importance of considering attenuation in synthetic seismogram studies is amply demonstrated.

For marine crustal work, both P-wave and S-wave attenuation in sediments have been measured (Hamilton, 1972, 1976a, 1976b). A measure of attenuation in marine basalts was reported by Neprochnov et al (1967) and Neprochnov (1971) who gave attenuation coefficients (k) from 0.02 to 0.05 (Hamilton, 1976a). The OSE is expected to supplement this measure of attenuation. As outlined in Sections 2-3d) and 1-3, point vii, the normal incidence aspect of the OSE is essential for measuring attenuation properly.

CHAPTER 2

THEORETICAL BACKGROUND

2-1. TRAVEL TIME ANALYSIS

a). Techniques

Travel time analysis of idealized models was performed initially to estimate the general appearance of an OSE record section and to determine the sensitivity of travel times to horizontal changes in structure. In the data reduction stage, travel time models are compared to the field data to determine changes in P-wave velocity horizontally from the hole (objective 1) and to obtain P- and S-wave velocities at different azimuths (objective 3).

Two Fortran IV computer programs were used to produce travel time graphs for the OSE geometry: HOLETVX and PDR2. They both use the geometrical optics approximation and they both act as if the shot were in the hole and follow ray paths until the paths hit the surface.

I wrote HOLETVX, using travel time subroutines written by D.W. Wright. This program assumes that interfaces are straight (flat or dipping), that velocity is constant in each layer and that the structure is constant in the direction perpendicular to the section. Distance travelled is evaluated trigonometrically using Snell's law and time is computed from the distances. The theory follows straight forwardly from the theory for the surface-to-surface case as reviewed by Dobrin (1976) and Grant and West (1965). HOLETVX is a faster program than PDR2. The direct arrival, and reflected and critically refracted arrivals for all interfaces below the shot are calculated. Multiples are handled by changing the input model.

PDR2, written by V. Červený and I. Pšenčik, is a ray tracing program for general two dimensional cases. It produces travel time curves for models with vertical and horizontal velocity gradients and curved interfaces. Ray paths are calculated by moving through a velocity array in fixed time steps. The program does not compute travel times for critically refracted waves. It handles multiples by means of a code.

b). Examples

Suites of travel time curves were produced to study the effect of different layer 2 structures on OSE travel times. Time-distance graphs of various models were compared with a model which represented average oceanic crust (Figure 1-1-1). Graphs were produced for a number of geophone depths including a) a position .2 km from the top of layer 2 (5.7 km), b) a position half way into layer 2 (6.4 km), c) a position .2 km from the bottom of layer 2 (7.0 km) and d) a position at the top of layer 3 (7.4 km). The scale of structures that can be considered under the geometrical optics approximation is limited by the wavelength of the signal which for marine explosive sources is about .5 km in layer 2. The study was conducted assuming that travel times could be measured to $\pm$ 0.01 sec.

Figure 2-1-1 shows a suite of travel time curves which demonstrate the effect of different layer 2 velocities for different receiver depths, assuming that the velocity is constant throughout the layer. For surface ranges up to 3 km, which correspond to ranges in layer 2 of up to 1.4 km, the shape of the direct arrival curve is insufficiently sensitive (to within the accuracy of 0.1 sec) to resolve layer 2

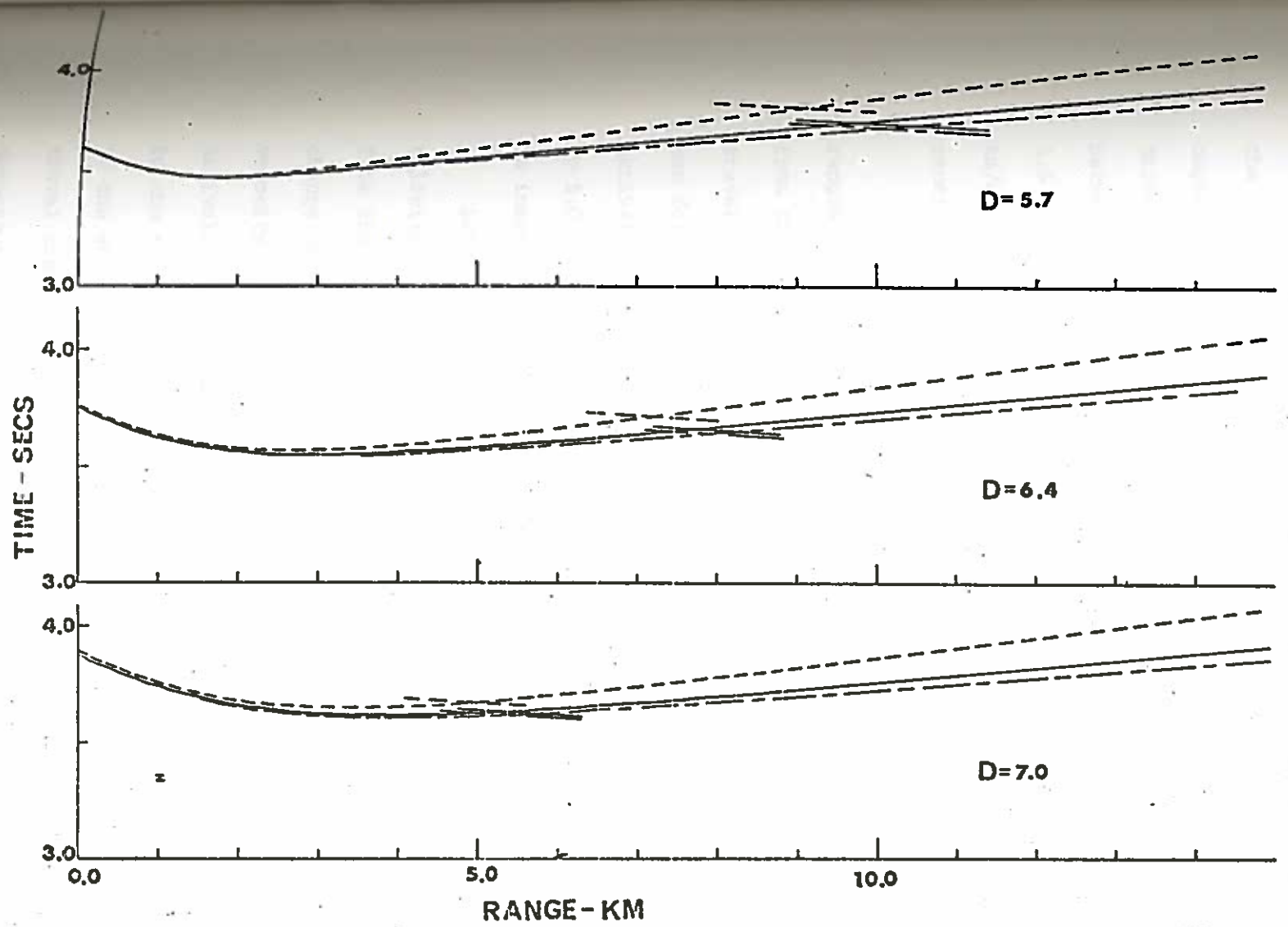

Figure 2-1-1. Travel-time curves for constant layer 2 velocity at different depths. The model for these curves is average oceanic crust (Figure 1-1-1) with layer 2 velocities of 5.0 km/sec (———), 4.7 km/sec (---) and 5.1 km/sec (—— - ——). The plots have a reduction velocity of 6 km/sec. The I symbol, in the lower left hand corner of the D = 7.0 graph, represents ± .01 km/sec which is the recommended timing accuracy. The short cross lines at middle ranges show the layer 3 critically refracted arrival times. First arrival analysis of direct waves is only valid up to these points. Deep geophone positions are essential to determine short range velocities and shallow positions are necessary to get average velocities from straight line fits. The middle geophone depth is the best compromise. D is the receiver depth below sea level in kilometres.

velocities to within 0.2 km/sec. (Table 2-1-1 gives the relationship of surface range to layer 2 range for the average crust model). The velocity of layer 2 up to 1.4 km from the hole (for a geophone depth of 6.4 km) cannot be determined from the slope or the shape of the direct arrival curve. The velocity can be obtained from the difference between travel times to shallow and deep receivers. For a receiver 1.6 km into layer 2 the vertical velocity can be resolved to $\pm$ 0.36 km/sec if the travel time in layer 2 is known to $\pm$ 0.2 secs. Shallow receivers tell one nothing about the near hole velocity.

It is evident from Figure 2-1-1 that average velocities over ranges from 3.0 to 8.0 km (1.4-6.0 km in layer 2) can be obtained from the slope of the direct arrival to within $\pm$ 0.1 km/sec if the travel time is known to $\pm$ 0.01 sec. The deep position is of little use for determining layer 2 velocity from the slope of the direct arrival curve because the direct arrival is only a first arrival up to 5.0 km. The shape of the direct arrival curve up to this point is insensitive to velocity changes of $\pm$ 0.2 km/sec.

Lateral velocity changes were studied using a model in which the velocity increased step wise in the whole of layer 2 at a fixed range from the hole. Figure 2-1-2 shows the travel time suites for a velocity change of 5.0 to 5.5 km/sec at ranges of 1.0 and 2.0 km. The average velocity at mid-ranges (4.0-8.0 km) can be obtained from the direct arrival. The velocity change near the hole causes a discontinuity in the travel time curve (the mid-range times are no longer tangential to the short range times) and an offset of the mid-range shots. The travel time differences due to the step change are largest for the deepest position.

If a block of higher velocity is considered, instead of a long

TABLE 2-1-1

LAYER 2 RANGE VS. SURFACE RANGE FOR AVERAGE OCEANIC CRUST (Figure 1-1-1)

(D is the receiver depth below sea level in kilometres.)

SURFACE RANGE (km)	LAYER 2 RANGE (km)			
	D = 5.7	D = 6.4	D = 7.0	(km)
.5	.05	.17	.23	
1.0	.12	.35	.48	
1.5	.21	.52	.74	
2.0	.40	.82	1.02	
2.5	.73	1.11	1.33	
3.0	1.19	1.47	1.67	
4.0	2.17	2.31	2.46	
5.0	3.16	3.24	3.36	
6.0	4.16	4.21	4.28	
8.0	6.16	6.18	6.22	
10.0	8.16	8.18	8.19	
12.0	10.16	10.17	10.18	

slab, the travel time curves are less diagnostic. A 1.0 km square block of material, 0.5 km from the hole, with a velocity 0.5 km/sec greater than the surrounding material, could not be detected by travel time analysis with a time uncertainty of $\pm$ 0.01 sec. The focusing effect of the block however, may be seen in the character of the arrivals.

An example of S-wave travel time curves is shown in Figure 2-1-3. At short ranges the direct S arrival will be obscured by the direct P arrival but at middle ranges the S-wave arrivals may be picked because of their larger amplitude. The slope of the asymptote to the mid-range S arrivals gives the S-wave velocity in layer 2.

The receiver at the top of layer 3 would give layer 3 velocities from direct waves in the same manner as for the layer 2 positions. These measurements may be less useful because of the effects on travel times of the layer 2 structure.

The requirement that travel time be known to $\pm$ 0.01 sec is untenable for normal explosive shooting because of the uncertainty in the flight time corrections, but may be reasonable if an air gun system is used. In either case this confidence interval must include the estimate of bathymetry and basement topography effects. An accurate knowledge of basement topography is the biggest problem in OSE interpretation. The effect of basement topography is discussed further in the data reduction section (Section 4-2c)).

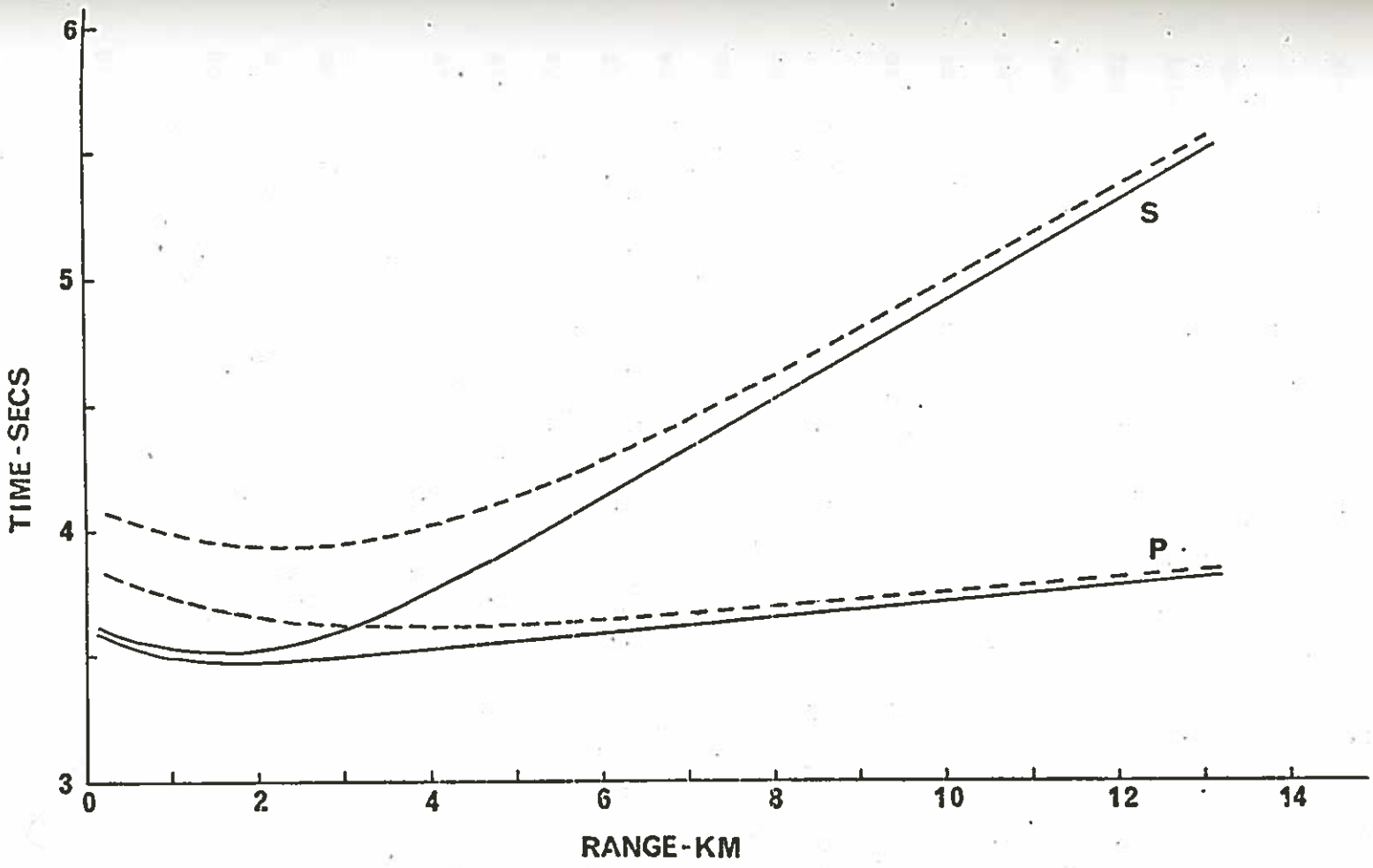

Figure 2-1-3. Typical S-wave travel-time curve. The standard model (Figure 1-1-1) was used assuming a P-S conversion at the top of layer 2. The layer 2 S-wave velocity is 2.75 km/sec and the geophone depth is 7.0 km. Direct waves (———) and layer 3 reflections (---) are shown. The plot is reduced at 6 km/sec and the P-wave arrivals are shown for comparison. Since S-wave amplitude is generally much larger than P-wave amplitude the S-wave arrival should be distinct from the P-wave arrival (approximately .3 secs long) at about 4.5 km.

2-2. SYNTHETIC SEISMOGRAMS

a). Introduction

Methods for computing synthetic seismograms for the case of the receiver within the medium were investigated as techniques for interpreting Oblique Seismic Experiment data (Stephen, 1977b). Conventional synthetic seismogram methods could be valuable tools in achieving the lateral variation and attenuation objectives. If anisotropic reflection coefficients are used, synthetic seismograms would be helpful in interpreting possible anisotropy resulting from preferred crack orientation.

Since the seismic structure of the rock immediately around the borehole can be obtained from the sonic log, it should be possible to calculate quite accurately the normal incidence waveform. The predicted waveforms should then correspond to the real data up to ranges at which the flat, homogeneous layer assumption ceases to be valid. If the synthetic seismograms can be computed by a technique that allows for attenuation, then wave form matching would provide an estimate of attenuation in the oceanic crust.

Both the ray method (Červený and Ravindra, 1971) and the reflectivity method (Fuchs, 1968b, 1970) were investigated. This discussion deals mainly with the development of the reflectivity method for the OSE case, however, an example of the ray method is given for comparison.

b). Theory for Reflectivity Method

The derivation of the horizontal and vertical displacements at the receiver for the reflectivity method with the receiver within the reflectivity zone follows the same lines as the derivation for the

surface to surface case. Consequently, following Fuchs and Müller, (1971) and using their notation, the Fourier transform of the compressional potential incident upon the reflectivity zone is:

$$\bar{\phi}_m(r, z_{m+1}^-, \omega) = \bar{F}(\omega) \int_0^\infty \frac{k}{j\nu_{\alpha 1}} J_o(kr)\, P_d(\omega, k) \exp\left[-j\left(\sum_{i=1}^{m} h_i \nu_{\alpha i}\right)\right] dk \quad (1)$$

where $\bar{F}(\omega)$ is the Fourier transform of the source function

Jo is the Bessel function of the first kind, order zero

P_d is the product of transmission coefficients in the source region for the downgoing wave,

k is the horizontal wave number in the source region

z_{m+1}^- represents the upper side of the $(m+1)^{th}$ interface,

$\nu_{\alpha i}$ is the vertical wavenumber for compressional waves, i.e.

$$\nu_{\alpha i} = \sqrt{k_{\alpha_i}^2 - k^2} \quad , \alpha_1 \geq \alpha_i$$

$$= -j\sqrt{k^2 - k_{\alpha_i}^2} \quad , \alpha_1 < \alpha_i$$

where α_i is the P-wave velocity in layer i,

and j is the square root of -1.

The geometry for the derivation is shown in Figure 2-2-1.

The solutions to the wave equations for the compressional and shear potential in the layers within the reflectivity zone have the form (Fuchs, 1971):

$$\bar{\phi}_i(r, z, \omega) = \bar{F}(\omega) \int_0^\infty \left(\bar{\Phi}_i^- + \bar{\Phi}_i^+\right) J_o(kr) \frac{k}{j\nu_{\alpha 1}} dk$$

$$\bar{\psi}_i(r, z, \omega) = \bar{F}(\omega) \int_0^\infty \left(\bar{\Psi}_i^- + \bar{\Psi}_i^+\right) J_1(kr) \frac{k}{j\nu_{\alpha 1}} dk \quad (2)$$

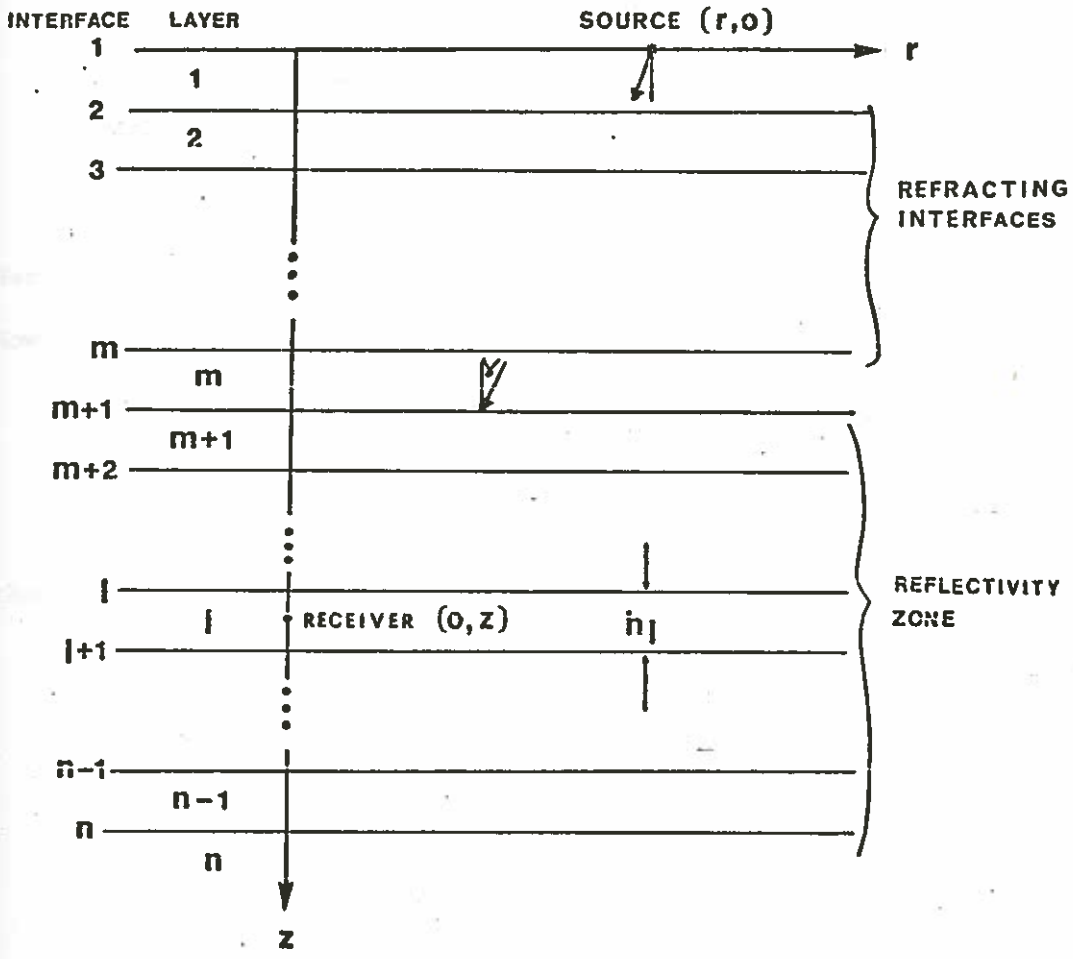

Figure 2-2-1. Geometry and nomenclature for the development of the synthetic seismogram theory.

where $\bar{\Phi}_i^-(z) = A_i \exp[j\nu_{\alpha i}(z-z_i)]$

$\bar{\Phi}_i^+(z) = B_i \exp[-j\nu_{\alpha i}(z-z_i)]$

$\bar{\Psi}_i^-(z) = C_i \exp[j\nu_{\beta i}(z-z_i)]$

$\bar{\Psi}_i^+(z) = D_i \exp[-j\nu_{\beta i}(z-z_i)]$

Here $\nu_{\beta i}$ is the vertical wavenumber for shear waves.

Now if

$$\underset{\sim}{V}_i \equiv [\bar{\Phi}_i^-(z), \bar{\Psi}_i^-(z), \bar{\Phi}_i^+(z), \bar{\Psi}_i^+(z)]^T$$

$$\equiv [\underset{\sim}{V}_i^{u\,T}(z), \underset{\sim}{V}_i^{D\,T}(z)]^T$$

then

$$\underset{\sim}{V}_m(z_{m+1}) = [\bar{\Phi}_m^-(z_{m+1}), \bar{\Psi}_m(z_{m+1}), P_d(\omega,k)\exp(j\sum_{i=1}^{m}\nu_{\alpha i}h_i), 0]^T$$

$$\underset{\sim}{V}_n(z_n) = [0, 0, \bar{\Phi}_n^+(z_n), \bar{\Psi}_n^+(z_n)]^T \qquad (3)$$

$$\underset{\sim}{V}_\ell(z_{\ell+1}) = [\bar{\Phi}_\ell^-(z_{\ell+1}), \bar{\Psi}_\ell^-(z_{\ell+1}), \bar{\Phi}_\ell^+(z_{\ell+1}), \bar{\Psi}_\ell^+(z_{\ell+1})]^T$$

$$m < \ell < n$$

These statements assume that no shear potential is incident on the reflectivity zone from above and that neither compressional nor shear potentials are incident from below.

The relations between $V_m(Z_{m+1})$, $V_n(z_n)$ and $V_\ell(Z_{\ell+1})$ are (Kennett, 1974):

$$\underset{\sim}{V}_m^u(z_{m+1}) = \underset{\sim}{R}_D \underset{\sim}{V}_m^D(z_{m+1})$$

$$\underset{\sim}{V}_n^D(z_n) = \underset{\sim}{T}_D \underset{\sim}{V}_m^D(z_{m+1}) \qquad (4)$$

$$\underset{\sim}{V}_\ell^u(z_{\ell+1}) = {}^{\ell}\underset{\sim}{R}_D^n[1 - {}^{m}\underset{\sim}{R}_u^{\ell}\,{}^{\ell}\underset{\sim}{R}_D^n]^{-1}\,{}^{m}\underset{\sim}{T}_D^{\ell}\,\underset{\sim}{V}_m^D(z_{m+1}) = \underset{\sim}{U}\,\underset{\sim}{V}_m^D(z_{m+1})$$

$$\underset{\sim}{V}_\ell^D(z_{\ell+1}) = [1 - {}^{m}\underset{\sim}{R}_u^{\ell}\,{}^{\ell}\underset{\sim}{R}_D^n]^{-1}\,{}^{m}\underset{\sim}{T}_D^{\ell}\,\underset{\sim}{V}_m^D(z_{m+1}) = \underset{\sim}{W}\,\underset{\sim}{V}_m^D(z_{m+1})$$

where $\underset{\sim}{R}$ and $\underset{\sim}{T}$ are the phase related reflection and transmission matrices for the complete reflectivity zone and ${}^{\ell}_{R}{}^{n}$, ${}^{m}_{R}{}^{\ell}$, and ${}^{m}_{T}{}^{\ell}$ are the matrices for those sections bounded by the superscripts. (The letters D and U denote incidence from above and below respectively.) Assuming that the Kennett matrices have been calculated to give the response on the upper (-) side of each interface and putting the receiver in the ℓ^{th} layer at depth Z we obtain:

$$\underset{\sim}{V}{}^{D}_{\ell}(z) = \begin{bmatrix} \exp[j\nu_{\alpha\ell}(z_{\ell+1}-z)], & 0 \\ 0, & \exp[j\nu_{\beta\ell}(z_{\ell+1}-z)] \end{bmatrix} \underset{\sim}{V}{}^{D}_{\ell}(z_{\ell+1})$$

and (5)

$$\underset{\sim}{V}{}^{u}_{\ell}(z) = \begin{bmatrix} \exp[-j\nu_{\alpha\ell}(z_{\ell+1}-z)], & 0 \\ 0, & \exp[-j\nu_{\beta\ell}(z_{\ell+1}-z)] \end{bmatrix} \underset{\sim}{V}{}^{u}_{\ell}(z_{\ell+1}) .$$

Since $v^{D}_{m}(z_{m+1})$ is known [(1) and (3)], $\underset{\sim}{V}{}^{u}_{\ell}(z)$ and $\underset{\sim}{V}{}^{D}_{\ell}(z)$ can be calculated from (4) and (5). Then the A_i, B_i, C_i, and D_i in (2) for the receiver layer can be obtained:

$$\begin{aligned} A_\ell &= \Phi^{-}_{\ell}(z_{\ell+1})\exp[-j\nu_{\alpha\ell}h_\ell] \\ B_\ell &= \Phi^{+}_{\ell}(z_{\ell+1})\exp[+j\nu_{\alpha\ell}h_\ell] \\ C_\ell &= \Psi^{-}_{\ell}(z_{\ell+1})\exp[-j\nu_{\beta\ell}h_\ell] \\ D_\ell &= \Psi^{+}_{\ell}(z_{\ell+1})\exp[+j\nu_{\beta\ell}h_\ell] . \end{aligned} \qquad (6)$$

The expressions for the potentials are:

$$\bar{\phi}_\ell(r,z,\omega) = \bar{F}(\omega)\int_0^\infty \left\{ U_{pp}\exp\left[j\nu_{\alpha\ell}(z-z_{\ell+1})\right] + W_{pp}\exp\left[-j\nu_{\alpha\ell}(z-z_{\ell+1})\right]\right\}$$
$$\times\ P_d(\omega,k)\exp\left[-j\left(\sum_{i=1}^{m} h_i\nu_{\alpha i}\right)\right] J_0(kr)\,\frac{k}{j\nu_{\alpha\ell}}\,dk$$

(7)

$$\bar{\psi}_\ell(r,z,\omega) = \bar{F}(\omega)\int_0^\infty \left\{ U_{ps}\exp\left[j\nu_{\beta\ell}(z-z_{\ell+1})\right] + W_{ps}\exp\left[-j\nu_{\beta\ell}(z-z_{\ell+1})\right]\right\}$$
$$\times\ P_d(\omega,k)\exp\left[-j\left(\sum_{i=1}^{m} h_i\nu_{\alpha i}\right)\right] J_1(kr)\,\frac{k}{\nu_{\alpha 1}}\,dk\ .$$

in terms of the matrices $\underline{U}$ and $\underline{W}$ introduced in equation (4).

Substituting these expressions into:

$$\bar{u} = \frac{\partial\bar{\phi}}{\partial r} - \frac{\partial\bar{\psi}}{\partial z} \qquad (7a)$$

$$\bar{w} = \frac{\partial\bar{\phi}}{\partial z} + \frac{\partial\bar{\psi}}{\partial r} + \frac{\bar{\psi}}{r}$$

gives the horizontal and vertical displacements:

$$\bar{u}(r,z,\omega) = \bar{F}(\omega)\int_0^\infty \left\{ -U_{pp}\exp\left[j\nu_{\alpha\ell}(z-z_{\ell+1})\right] - W_{pp}\exp\left[-j\nu_{\alpha\ell}(z-z_{\ell+1})\right]\right.$$
$$\left. + \frac{\nu_{\beta\ell}}{k}U_{ps}\exp\left[j\nu_{\beta\ell}(z-z_{\ell+1})\right] - \frac{\nu_{\beta\ell}}{k}W_{ps}\exp\left[-j\nu_{\beta\ell}(z-z_{\ell+1})\right]\right\}$$
$$\times\ P_d(\omega,k)\exp\left[-j\left(\sum_{i=1}^{m} h_i\nu_{\alpha i}\right)\right] J_1(kr)\,\frac{k^2}{j\nu_{\alpha 1}}\,dk \qquad (8)$$

$$\bar{w}(r,z,\omega) = \bar{F}(\omega)\int_0^\infty \left\{ \nu_{\alpha\ell}U_{pp}\exp\left[j\nu_{\alpha\ell}(z-z_{\ell+1})\right] - \nu_{\alpha\ell}W_{pp}\exp\left[-j\nu_{\alpha\ell}(z-z_{\ell+1})\right]\right.$$
$$\left. + kU_{ps}\exp\left[j\nu_{\beta\ell}(z-z_{\ell+1})\right] + kW_{ps}\exp\left[-j\nu_{\beta\ell}(z-z_{\ell+1})\right]\right\}$$
$$\times\ P_d(\omega,k)\exp\left[-j\left(\sum_{i=1}^{m} h_i\nu_{\alpha i}\right)\right] J_0(kr)\,\frac{k}{\nu_{\alpha 1}}\,dk\ ,$$

where $z_l \le z \le z_{l+1}$.

Following Fuchs and Müller (1971) the variable of integration can be changed to γ defined by $k = \frac{\omega}{\alpha_m} \sin\gamma = k_{\alpha m} \sin\gamma$. This gives the final form of the theoretical horizontal and vertical displacements, u and w:

$$\bar{u}(r,z,\omega) = \bar{F}(\omega)\, j k_{\alpha m}^2 \int_{\gamma_1}^{\gamma_2} \sin\gamma \cos\gamma \frac{J_1(k_{\alpha m} r \sin\gamma)}{\eta_{\alpha 1}} \rho(\omega,\gamma) P_d(\gamma) \exp\left[-j k_{\alpha m} \left(\sum_{i=1}^{m} h_i \eta_{\alpha i}\right)\right] d\gamma \qquad (9)$$

$$\bar{w}(r,z,\omega) = \bar{F}(\omega)\, k_{\alpha m}^2 \int_{\gamma_1}^{\gamma_2} \sin\gamma \cos\gamma \frac{J_0(k_{\alpha m} r \sin\gamma)}{\eta_{\alpha 1}} \sigma(\omega,\gamma) P_d(\gamma) \exp\left[-j k_{\alpha m} \left(\sum_{i=1}^{m} h_i \eta_{\alpha i}\right)\right] d\gamma$$

where
$$\rho(\omega,\gamma) = \sin\gamma \left\{ U_{pp} \exp\left[j k_{\alpha m} \eta_{\alpha l} (z - z_l)\right] + W_{pp} \exp\left[-j k_{\alpha m} \eta_{\alpha l} (z - z_l)\right] \right\}$$
$$+ \eta_{\beta l} \left\{ -U_{ps} \exp\left[j k_{\alpha m} \eta_{\beta l} (z - z_l)\right] + W_{ps} \exp\left[-j k_{\alpha m} \eta_{\beta l} (z - z_l)\right] \right\}$$

and
$$\sigma(\omega,\gamma) = \eta_{\alpha l} \left\{ U_{pp} \exp\left[j k_{\alpha m} \eta_{\alpha l} (z - z_l)\right] - W_{pp} \exp\left[-j k_{\alpha m} \eta_{\alpha l} (z - z_l)\right] \right\}$$
$$+ \sin\gamma \left\{ U_{ps} \exp\left[j k_{\alpha m} \eta_{\beta l} (z - z_l)\right] + W_{ps} \exp\left[-j k_{\alpha m} \eta_{\beta l} (z - z_l)\right] \right\} ,$$

$$P_d(\gamma) = \prod_{i=2}^{m} T_i$$

$$T_i = -2 \rho_{i-1} \eta_{\alpha, i-1} \frac{c}{D}$$

$$\eta_{\alpha i} = \sqrt{\frac{\alpha_m^2}{\alpha_i^2} - \sin^2\gamma} \quad , \quad \eta_{\beta i} = \sqrt{\frac{\alpha_m^2}{\beta_i^2} - \sin^2\gamma}$$

and C and D are defined in Fuchs and Müller (1971).

In computing the coefficients $\rho(\omega,\gamma)$ and $\sigma(\omega,\gamma)$ it is convenient to put a layer boundary at the depth of the receiver and to make the elastic parameters on either side of the boundary identical. If the boundary is put at $Z = Z_{l+1}$ then $\rho(\omega,\gamma)$ and $\sigma(\omega,\gamma)$ become:

$$\rho(\omega,\gamma) = \sin\gamma\{U_{PP} + W_{PP}\} + \eta_{\beta l}\{-U_{PS} + W_{PS}\}$$
$$\sigma(\omega,\gamma) = \eta_{\alpha l}\{U_{PP} - W_{PP}\} + \sin\gamma\{U_{PS} + W_{PS}\} \qquad (10)$$

For the exact solution to (9) $\gamma_1 = 0$ and $\gamma_2 = \pi/2 + i\infty$. The solutions in (9) are in the same form as the solutions for the surface to surface case. The integration can be performed by the stationary phase method (Fuchs, 1971) or by direct numerical integration (Fuchs, 1968b). When using direct numerical integration the length of the integration window can be reduced (Fuchs and Müller, 1971).

c). Numerical Calculations for Reflectivity Method.

A Fortran IV computer program for calculating surface to surface seismograms (Fuchs and Müller, 1971; Kennett, 1974, 1975a) was adapted to solve equation (9). The major change was to replace the subroutine for calculating reflection coefficients for reflection from the top of the reflectivity zone, with a routine for calculating the coefficients σ and ρ. Kennett's (1974) method for calculating the reflection and transmission coefficients using phase related reflection and transmission matrices was used. In the calculation of

$\underset{\sim}{m}_T^{\ell}$ the phase related coefficient method is more straight forward than the Fuchs method (Fuchs, 1968a). The expressions for reflection and transmission coefficients from the Fuchs method are:

$$R_{PP} = \frac{m\begin{vmatrix}12\\23\end{vmatrix}}{m\begin{vmatrix}12\\12\end{vmatrix}}$$

$$R_{PS} = -\frac{m\begin{vmatrix}12\\13\end{vmatrix}}{m\begin{vmatrix}12\\12\end{vmatrix}} \qquad (11)$$

$$T_{PP} = m_{31} R_{PP} + m_{32} R_{PS} + m_{33}$$

$$T_{PS} = m_{41} R_{PP} + m_{42} R_{PS} + m_{43}$$

where $m\begin{vmatrix}ij\\kl\end{vmatrix} = m_{ik}m_{jl} - m_{il}m_{jk}$ and the m_{ij} are the coefficients of matrix M defined by

$$\begin{pmatrix} 0 \\ 0 \\ T_{pp} \\ T_{ps} \end{pmatrix} = M \begin{pmatrix} R_{pp} \\ R_{ps} \\ 1 \\ 0 \end{pmatrix} \qquad (12)$$

There are numerical difficulties in calculating M directly so the determinants $m\begin{vmatrix}12\\23\end{vmatrix}$ and $m\begin{vmatrix}12\\13\end{vmatrix}$ are evaluated independently (Dunkin,1965). It is not clear how the coefficients m_{31}, m_{32}, m_{41}, m_{42} and m_{43} would be calculated to avoid the numerical difficulties. In the phase related coefficient method however the transmission coefficients are an integral part of the calculations and little additional computation is necessary to evaluate $\underset{\sim}{m}_{T_D}^{\ell}$. The numerical difficulty does not arise because the expressions for the phase related coefficients contain no terms of the form $\exp(-j\eta_{\alpha i} k_{\alpha m} z_i)$. Terms of this type become large for imaginary $\eta_{\alpha i}$ and can lead to

loss of significance in the calculations.

Originally ${}^{m}\underset{\sim}{T}_{D}^{\ell}$ was calculated from:

$$ {}^{m}\underset{\sim}{T}_{D}^{\ell} = \left({}^{\ell}\underset{\sim}{T}_{D}^{n} \right)^{-1} \underset{\sim}{T}_{D} \qquad (13) $$

because this uses a faster algorithm than calculating ${}^{m}\underset{\sim}{T}_{D}^{\ell}$ directly. The method, however, is not satisfactory because of loss of significance in the determinant. This problem is similar to numerical problems mentioned above.

From Kennett (1974) the reflection and transmission coefficients for a stack with n layers, where n is the bottom layer, are built up from

$$ \begin{aligned} {}^{i-1}\underset{\sim}{T}_{D}^{n} &= {}^{i}\underset{\sim}{T}_{D}^{n} \left[I - \underset{\sim}{r}_{u}^{i-1} \, {}^{i}\underset{\sim}{R}_{D}^{n} \right]^{-1} \underset{\sim}{t}_{D}^{i-1} \\ {}^{i-1}\underset{\sim}{R}_{D}^{n} &= \underset{\sim}{r}_{D}^{i-1} + \underset{\sim}{t}_{u}^{i-1} \, {}^{i}\underset{\sim}{R}_{D}^{n} \left[I - \underset{\sim}{r}_{u}^{i-1} \, {}^{i}\underset{\sim}{R}_{D}^{n} \right]^{-1} \underset{\sim}{t}_{D}^{i-1} \qquad (14) \\ {}^{i-1}\underset{\sim}{T}_{u}^{n} &= \underset{\sim}{t}_{u}^{i-1} \left[I - {}^{i}\underset{\sim}{R}_{D}^{n} \, \underset{\sim}{r}_{u}^{i-1} \right]^{-1} {}^{i}\underset{\sim}{T}_{u}^{n} \\ {}^{i-1}\underset{\sim}{R}_{u}^{n} &= {}^{i}\underset{\sim}{R}_{u}^{n} + {}^{i}\underset{\sim}{T}_{D}^{n} \left[I - \underset{\sim}{r}_{u}^{i-1} \, {}^{i}\underset{\sim}{R}_{D}^{n} \right]^{-1} \underset{\sim}{r}_{u}^{i-1} \, {}^{i}\underset{\sim}{T}_{u}^{n} \end{aligned} $$

Here $\underset{\sim}{r}_{D}^{i-1}$, $\underset{\sim}{r}_{u}^{i-1}$, $\underset{\sim}{t}_{D}^{i-1}$ and $\underset{\sim}{t}_{u}^{i-1}$ are phase related reflection coefficient matrices for the $(i-1)^{th}$ layer.

In the surface-to-surface case one only requires ${}^{m}\underset{\sim}{R}_{D}^{n}$. Since the evaluation of ${}^{i}\underset{\sim}{R}_{D}^{j}$ for an arbitrary interface uses only downward coefficients for the region below the interface $({}^{i}\underset{\sim}{R}_{D}^{n})$ but uses both upward and downward coefficients for the region above the interface $(\underset{\sim}{r}_{D}^{i-1}, \underset{\sim}{r}_{u}^{i-1}, \underset{\sim}{t}_{D}^{i-1}, \underset{\sim}{t}_{u}^{i-1})$ it is fastest to compute ${}^{m}\underset{\sim}{R}_{D}^{n}$ by building from the bottom of the stack. Of the four terms in (14) only ${}^{i-1}\underset{\sim}{R}_{D}^{n}$ must be computed.

In the OSE case we require ${}^{m}\underset{\sim}{R}_{D}^{n}$, ${}^{m}\underset{\sim}{T}_{D}^{n}$, ${}^{\ell}\underset{\sim}{R}_{D}^{n}$, ${}^{\ell}\underset{\sim}{R}_{u}^{m}$, ${}^{\ell}\underset{\sim}{R}_{S}^{n}$ and ${}^{\ell}\underset{\sim}{T}_{D}^{m}$. In the interest of producing a fast algorithm I originally felt that it would be worthwhile to leave out the effect of multiples in the receiver layer. In this case, only ${}^{m}\underset{\sim}{R}_{D}^{n}$, ${}^{m}\underset{\sim}{T}_{D}^{n}$, ${}^{\ell}\underset{\sim}{R}_{D}^{n}$ and ${}^{\ell}\underset{\sim}{T}_{D}^{m}$ are required. The first two are simply evaluated by using the iterations in (14) for ${}^{i-1}\underset{\sim}{R}_{D}^{n}$ and ${}^{i-1}\underset{\sim}{T}_{D}^{n}$. ${}^{\ell}\underset{\sim}{R}_{D}^{n}$ is computed in evaluating ${}^{m}\underset{\sim}{R}_{D}^{n}$ and can simply be remembered. At first glance it may seem reasonable to get ${}^{\ell}\underset{\sim}{T}_{D}^{m}$ from (13) since multiples between the upper and lower stacks are not considered. However, to evaluate (13) requires dividing by the determinant $D = {}^{\ell}t_{Dpp}^{n}\ {}^{\ell}t_{Dss}^{n} - {}^{\ell}t_{Dsp}^{n}\ {}^{\ell}t_{Dps}^{n}$, and for the simple average crust model (Figure 1-1-1) it was found that occasionally D = (0.0,0.0). This meant that the terms ${}^{\ell}t_{Dpp}^{n}\ {}^{\ell}t_{Dss}^{n}$ and ${}^{\ell}t_{Dsp}^{n}\ {}^{\ell}t_{Dps}^{n}$ were coincidentally identical up to 7 significant digits. This only occurred for imaginary $\eta_{\alpha i}$ and $\eta_{\beta i}$. Consequently ${}^{\ell}\underset{\sim}{T}_{D}^{m}$ has to be computed directly from relations (14), which means that all four terms must be calculated at each layer, leading to much longer computation times.

It is possible in the Kennett method to truncate the ray expansion for each layer to just the primary response or to the primary response plus first multiples (Kennett 1975b). This facility was maintained in the OSE version. From Kennett (1974) the overall reflection and transmission coefficients for downward propagation in terms of the coefficients at the two interfaces $Z = Z_1$ and $Z = Z_2$ are:

$$\underset{\sim}{R}_{D} = \underset{\sim}{R}_{D}^{01} + \underset{\sim}{T}_{u}^{01}\ \underset{\sim}{R}_{D}^{12}\left[I - \underset{\sim}{R}_{u}^{01}\ \underset{\sim}{R}_{D}^{12}\right]^{-1}\underset{\sim}{T}_{D}^{01}$$

$$\underset{\sim}{T}_{D} = \underset{\sim}{T}_{D}^{12}\left[I - \underset{\sim}{R}_{u}^{01}\ \underset{\sim}{R}_{D}^{12}\right]^{-1}\ \underset{\sim}{T}_{D}^{01} \qquad (15)$$

The terms on the right are Kennett coefficients: U and D represent upward and downward propagation respectively and the superscripts

denote the region for which the coefficients apply. I is the unit matrix. Expanding the inverse matrix as a truncated power series gives:

$$\underset{\sim}{R}_D = \underset{\sim}{R}_D^{01} + \underset{\sim}{T}_u^{01}\,\underset{\sim}{R}_D^{12}\left[\sum_{i=0}^{q}\left(\underset{\sim}{R}_u^{01}\,\underset{\sim}{R}_D^{12}\right)^i\right]\underset{\sim}{T}_D^{01}$$

$$\underset{\sim}{T}_D = \underset{\sim}{T}_D^{12}\left[\sum_{i=0}^{q}\left(\underset{\sim}{R}_u^{01}\,\underset{\sim}{R}_D^{12}\right)^i\right]\underset{\sim}{T}_D^{01} \qquad (16)$$

The primary response is the response due to the first term in the expansion in each equation (q = 0). For reflection it is the primary reflection from both interfaces and for transmission it is the direct wave. The second term in each case (q = 1) adds the effect of the first multiple in the layer.

For the case of the receiver within the reflectivity zone the three levels of computation can be summarized as:

1. Primary response - direct transmission through all layers above the source and primary reflections from all layers below the source (q = 1).
2. Primary response plus first multiples - as in 1. but including the first multiple reflection in each layer (q = 2)
3. Complete response - direct transmission plus all reflections and multiples. This is the response represented by equations (15).

In each case all possible P to S interconversions are included.

The program evaluates the integral by direct numerical integration using the trapezoidal rule. For computing purposes $\aleph$ is specified in degrees. Typical integration increments are $.1^{\circ}$ to $.25^{\circ}$. The integration is carried into the complex region by keeping $\aleph$ real

but greater than 90° and redefining $\sin \gamma$ appropriately. That is for $\gamma > 90^{\circ}$

$$\sin \gamma \equiv \tfrac{1}{2} \left(c + \frac{1}{c}\right)$$

$$\text{where} \quad c = \exp\left[\gamma - \pi/2\right]$$

For example $\gamma = 96.568$, $\gamma = 90 + j6.568$ and $\gamma = \pi/2 + j.115$ are equivalent in this notation. When γ is real it represents homogeneous waves incident on the reflectivity zone with angle γ. When γ is complex it represents inhomogeneous waves in the layer above the reflectivity zone.

The geometry for an OSE in average oceanic crust is shown in Figure 1-1-1. Unless otherwise stated this is the model used in all the examples. The P-wave velocity (α) is shown in Figure 1-1-1 and S-wave velocities (β) and densities (ρ) are related to it by: $\beta = \alpha/1.732$, $\rho = .252 + .3733\alpha$. In all cases for the reflectivity method the top of the reflectivity zone corresponds to the top of the sediment layer.

$0.569 + .335\alpha$ ← from Fig 176 Gabbros + Birch's Law

For all examples shown the source wavelet is defined by:

$$f(t) = \exp\left[- (2\pi\nu t)/\gamma^2\right] \cos(2\pi\nu t + \xi)$$

where $\nu = 4$ Hz, $\gamma = 4.0$ and $\xi = \pi/2$. The frequency content of the wavelet lies effectively within the window 0-13 Hz.

In a first analysis, vertical component synthetic seismograms were calculated for average oceanic crustal structure with the water replaced by a solid of equivalent P-wave velocity (Figures 2-2-2 to 2-2-4). Two factors are evident in the computation: a) For the same models the OSE requires a smaller integration increment than the surface-to-surface case. b) Integration over the complete range

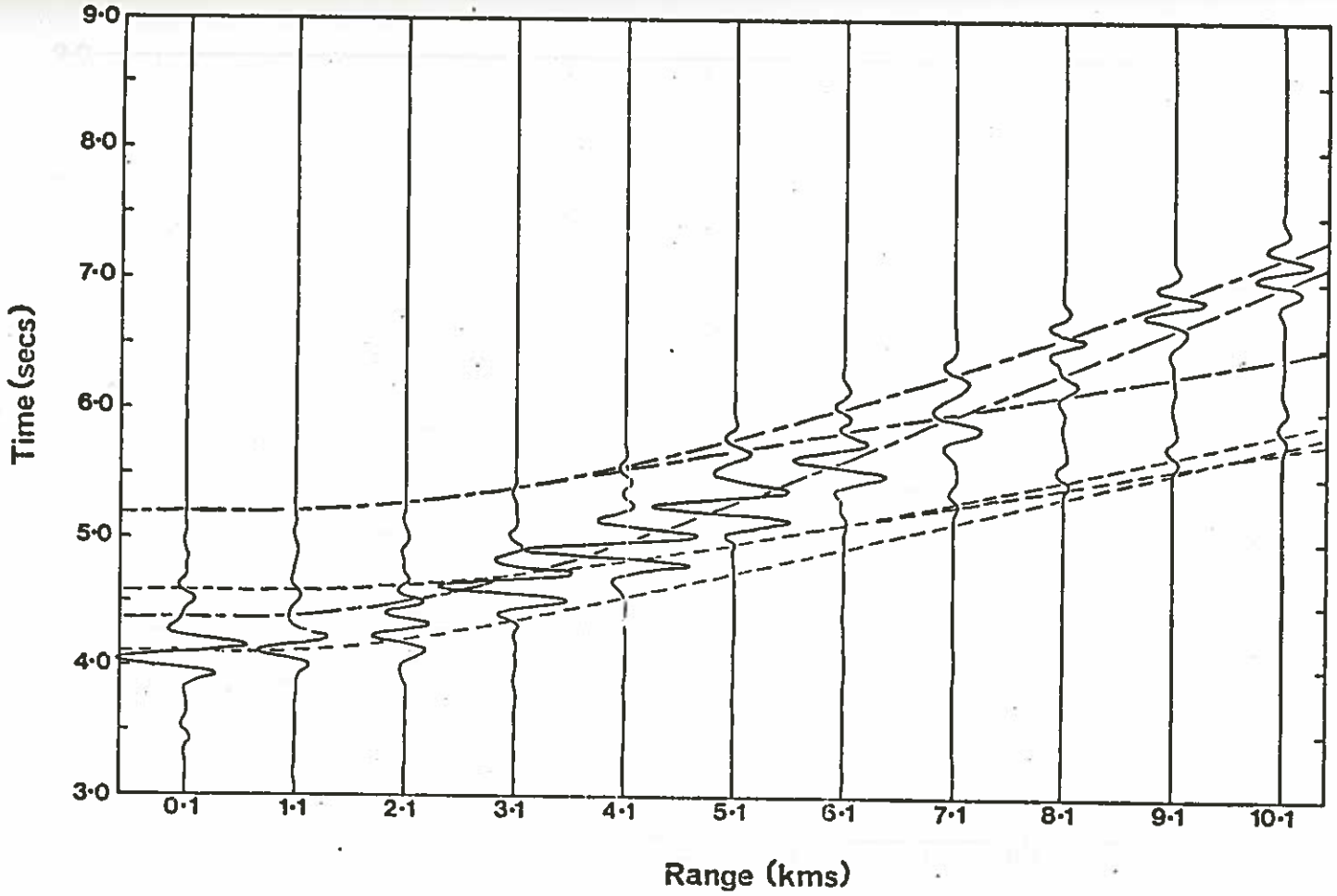

Figure 2-2-2. Reflectivity method vertical component synthetic seismograms for the model in Figure 1-1-1, primary response only. The dashed line (---) shows P-wave travel times adjusted to correspond to the centre of the source wavelet. The unevenly dashed line (—— – ——) is the same for P-S conversions at the top of the reflectivity zone (i.e. at the top of the sediment).

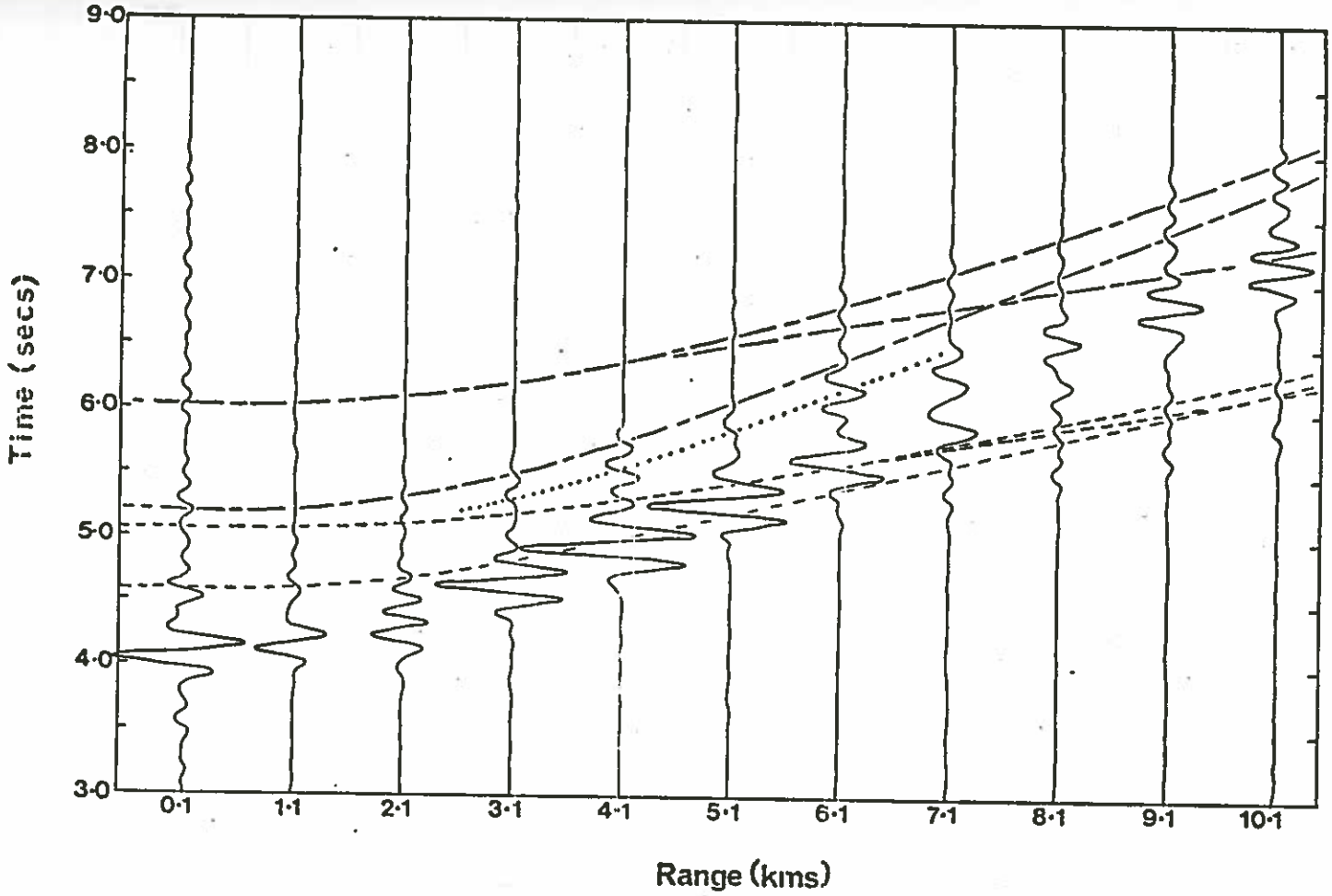

Figure 2-2-3. As Figure 2-2-2 but including first multiple response. Travel times are shown for PPP'PP (----), PSS'SS (— – —), PPP'PPP' (-·-·-), PSS'SSS' (— – —), and PPS'SS (....). The multiple notation is explained in the text.

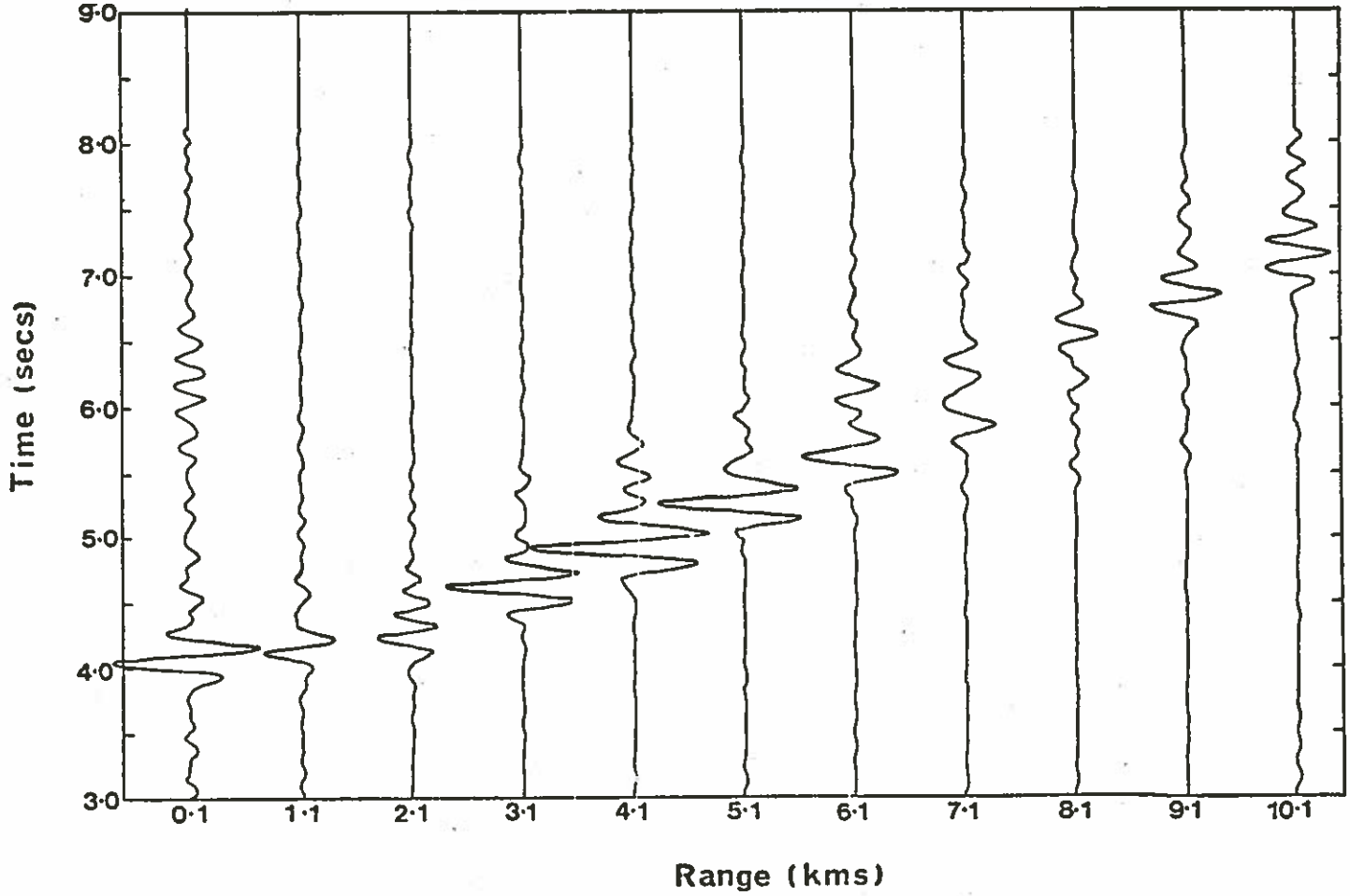

Figure 2-2-4. Reflectivity method vertical component synthetic seismograms for the model in Figure 1-1-1, complete response.

of real γ is necessary to produce a proper wavelet at short ranges and to minimize a false arrival which is generally present at short ranges.

For the seismic structure of Figure 1-1-1 the maximum integration increment for the surface-to-surface case to produce noise free structure is .25. For the OSE case this value is .15 suggesting that the integrand in (9) is varying more rapidly with respect to γ in this case.

At large ranges Fuchs and Müller (1971) suggested determining γ_1 and γ_2 from the relation

$$\gamma_{1,2} = \arcsin \frac{\alpha_m}{c_{1,2}}$$

where c_1 and c_2 are the maximum and minimum apparent velocities of the significant arrivals. From models run on both the surface-to-surface case and the OSE case this rule of thumb seems to be adequate for γ_1 at all ranges but for γ_2 the relation is satisfactory only at large ranges. Figure 2-2-5 shows the effect of different γ_2 on the seismograms. With increasing γ_2 the direct wave form at short ranges looks more like the source wave form and the false arrival diminishes. Note that carrying the integration a short distance into the complex γ region has little effect on the magnitude of the false arrival.

Distortion of the direct arrival and the presence of false arrivals appear to be related effects and both phenomena can be explained by the integration in (9) not being carried out to a high enough γ.

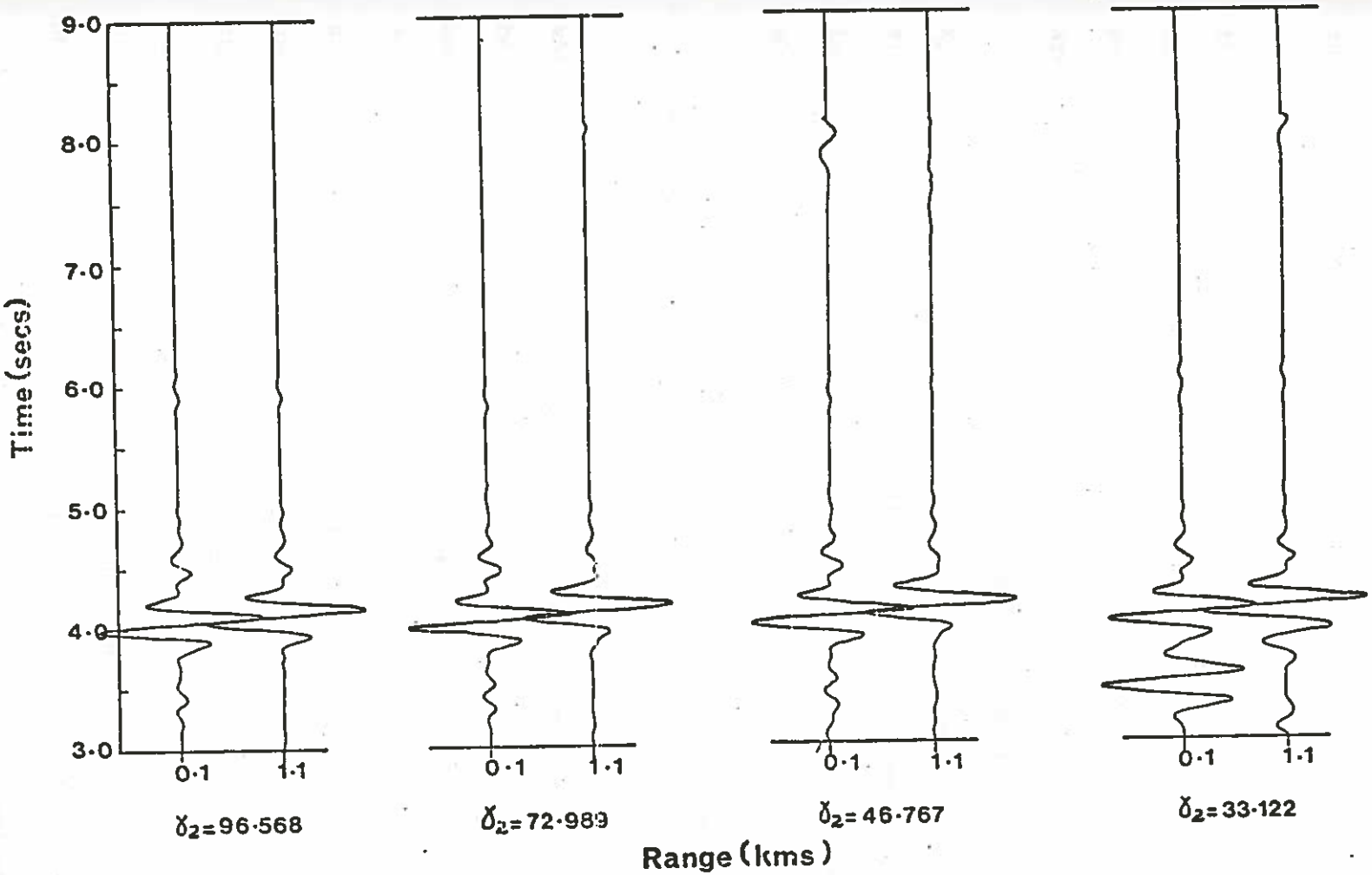

Figure 2-2-5. The effect on the false arrival with varying γ_2.

The γ integration in (9) is a Hankel transform and at large ranges the integral approaches a Fourier transform. If the Fourier transform interpretation is applied to short ranges the ommission of energy in the transform results in aliasing (Kanasewich, 1973). Not only is the energy less for proper arrivals in the time domain, but this lost energy reappears folded back into the time period producing a false arrival.

'Large ranges' in this discussion means ranges large enough that $k_{\alpha_m} r \sin\gamma$, the argument of the Bessel function, is greater than fifteen for those values of ω and γ which contribute most to the integral. If this is the case then the Bessel function can be approximated by

$$J_o(x) = \frac{-j}{\sqrt{2\pi x}} \left\{ \exp\left[j\left(x - \frac{\pi}{4}\right)\right] - \exp\left[-j\left(x - \frac{\pi}{4}\right)\right] \right\}$$

which is an oscillating function and the stationary phase method could be used to evaluate the integral in (9) (Fuchs, 1971). This method assumes that the bulk of the contribution to the integral comes from a region immediately about the γ's corresponding to the stationary phases. At small ranges the Bessel function becomes less oscillatory until at $r = 0$, $J_o(k\alpha_o r \sin\gamma) = 1$, for all γ. The stationary phase technique cannot be applied and significant contributions to the integral are made by γ's over a large window. Since the $\frac{1}{\sqrt{x}}$ term is no longer present higher values of γ are more heavily weighted than for the long range case.

Note that for the pseudo-oceanic model a false arrival still exists for $r = .1$ when the integration is performed over all real γ.

This implies that a certain amount of energy in the integrand comes from complex γ. The assumption that it is sufficient to consider only real angles of incidence into the reflectivity zone appears to break down in the OSE case. Since the receiver is in the reflectivity zone it is very possible that complex γ may make large contributions to the response. At large ranges these complex γ represent evanescent waves and Stoneley waves which cling to boundaries. The effect of these waves becomes more important as the receiver gets closer to an interface.

The extent to which inhomogeneous waves at the receiver are considered however is limited by the restriction to real angles of incidence and the velocity of the incident layer α_m. Since the angles of incidence in the layer are restricted to $[0, \pi/2)$ the contributing angles in the receiver layer are limited to $\left[0, \sin^{-1}(\alpha_\ell/\alpha_m)\right)$ which may not be adequate. Indeed, if $\alpha_m = 2.8$, a γ_2 of $90^\circ + j66^\circ$ is necessary to get the same contribution in the receiver layer as a γ_2 of 90° at $\alpha_m = 2.1$. Thus some models, those where the receiver is close to a boundary, where α_m is large, or where there is extensive channeling of evanescent waves, may require the integration of (9) to be carried a long way into the complex γ region.

Since the integration increment cannot be made larger than .15, the extension of the limits of integration in (9) to complex values of γ can increase the computing time prohibitively.

In spite of the computational problems the seismograms are interesting. Figure 2-2-2 shows the vertical component seismogram for average pseudo-oceanic crust for the case of primary response only. Travel time curves are included for direct P- and PS-waves and reflected P- and PS-waves from the top of layer 3. The conversion for the PS-wave is at the top of the reflectivity zone. Note the change

at 2.1 - 3.1 km from dominantly P-wave arrivals to dominantly S-wave arrivals.

Figure 2-2-3 shows the same case as Figure 2-2-2 but includes first multiples. Travel time curves are shown for PPP'PP, PSS'SS, PPP'PPP', PSS'SSS' and PPS'SS. (In this notation each letter represents one way travel in a layer. The first ray path starts at the source and the last ray path ends at the receiver. Compressional and shear waves are represented by P and S respectively. Unprimed quantities represent downward propagation and primed quantities represent upward propagation.) At short ranges the direct P-wave which has bounced once in the sediment can be detected. At larger ranges the combined effect of the direct and reflected P-waves is noticeable. Also at large ranges the P-S conversion at the sea bed lengthens the S-wave arrivals. At intermediate ranges the PPS'SS arrival can be seen. This seismogram shows the effect of waves reflected off the top of the reflectivity zone.

The full response is shown in Figure 2-2-4. The arrivals are a little more broad but there is no major change. The rippling on the .1 km trace has little significance and may be the result of bias in the Fourier transform.

d). Ray Method

There are two approaches to ray theory synthetic seismograms: asymptotic ray theory (Červený and Ravindra, 1971) and exact ray theory (Helmberger, 1968; Müller, 1968). In asymptotic ray theory the solution to the equation of motion,

$$\rho \frac{\partial^2 \vec{w}}{\partial t^2} = (\lambda+\mu)\nabla\cdot(\nabla\cdot\vec{w}) + \mu\nabla^2\vec{w} + \nabla\lambda(\nabla\cdot\vec{w}) + \nabla\mu\times(\nabla\times\vec{w}) + 2(\nabla\mu\cdot\nabla)\vec{w} \qquad (17)$$

is expressed as a series

$$\vec{w} = \exp[i\omega(t-\tau)]\sum_{k=0}^{\infty}(i\omega)^{-k}\vec{W}_k \qquad (18)$$

where $\vec{w}$ - particle displacement vector

ρ - density

λ, μ - Lamé's constants

ω - frequency

t - time

τ - phase function

$\vec{W}_k$ - amplitude coefficients } independent of ω and t

Where the first term, $\vec{W}_o$, dominates the solution (as for reflected and refracted rays) only it is considered. For head waves it is necessary to consider the first two terms of the series to obtain a good approximation. Equation (18) is not a valid solution to (17) near caustics or in critical regions and this is a limiting factor of the method. Other techniques must be used to determine accurate amplitudes in these regions (e.g. wave theory). The size of the region of inapplicability is inversely proportional to frequency and therefore asymptotic ray theory is better at higher frequencies.

In exact ray theory the solutions to (17) are expressed in terms of compressional, ϕ, and shear, ψ, potentials, related to displacements as in equations (7a). The source potential is converted by the Sommerfeld integral to an integration over wave number to yield an equation similar to (1). The exponential term and transmission coefficient term ($P_{\bar{d}}$) must be adjusted to allow for all reflections, transmission and interconversions of interest. Discussions of ways

of evaluating the integral analytically to obtain solutions for reflected waves, head waves, Stoneley waves, Rayleigh waves, etc. are liberally dispersed throughout the literature (ref. Helmberger, 1968; Müller, 1968).

The common feature of both ray methods is that they require a specification of the particular rays to be considered. Kennett (1974) cites attempts made to determine the errors introduced by considering a limited number of rays (Müller, 1970; Kanasewich et al , 1973; Chapman, 1974; Hron et al , 1974) but in general the reflectivity method must be used if the total response is to be guaranteed.

The calculation of synthetic seismograms by the ray method for the OSE was based on asymptotic ray theory because a copy of Červený's program (SEIS4) was available at the department. A new version of this program has been written by V. Červený and I. Pšenčik to include P to S conversions for laterally varying media with arbitrary receiver and source depths (Červený, pers. comm). In my study, however, no conversions to S-waves were included and P-wave multiple reflections in each flat, laterally homogeneous layer could be specified to a certain extent. I modified SEIS4 to accept a receiver at depth.

As in the reflectivity method the receiver was considered to be at the interface between two layers of identical properties. Layers above the receiver would have a path corresponding to transmission and layers below the receiver would contain the conventional reflection paths. Codes were generated in the form K, J(N), N = 1,K (Hron, 1972) where K is the number of layers and J(I) is the number of multiples to be considered in the I^{th} layer. There is a restriction at the receiver interface because of the identical layers on either side. If

L is the receiver interface then J(L-1) = J(L), J(L) + 1. The first case represents waves incident from above and the second case waves incident from below. Figure 2-2-6 shows some examples.

The vertical component synthetic seismogram computed by the ray method for average oceanic crust with the water replaced by a solid of equivalent P-wave velocity is shown in Figure 2-2-7. The source wavelet is the same as for the reflectivity seismograms however, the wavelets have been moved ahead 0.45 secs so that the proper arrival time corresponds to the middle cross over point. First multiples are included.

The direct arrival and reflection from the top of layer 3 can be seen at short ranges, however, the amplitude of the reflection is smaller than in the reflectivity case. With increasing range the direct P-wave amplitude dies away rapidly until only the reflected-refracted arrival from the top of layer 3 is detectable. No later arrivals are evident. This behaviour contrasts sharply with the strong direct wave arrivals seen throughout the section in the reflectivity case. The decrease of P-wave amplitude with distance is reasonable since at large ranges the direct wave approaches the receiver at large angles and P-wave motion is horizontal. Also at large ranges the S-wave arrival is significant and P- to S-wave conversions become important. Thus, to model the response for the receiver within the medium would require a consideration of S-waves for which this program was not designed.

e). Conclusions

The reflectivity method applied to the OSE case is certainly capable of producing accurate seismograms at large ranges. At small

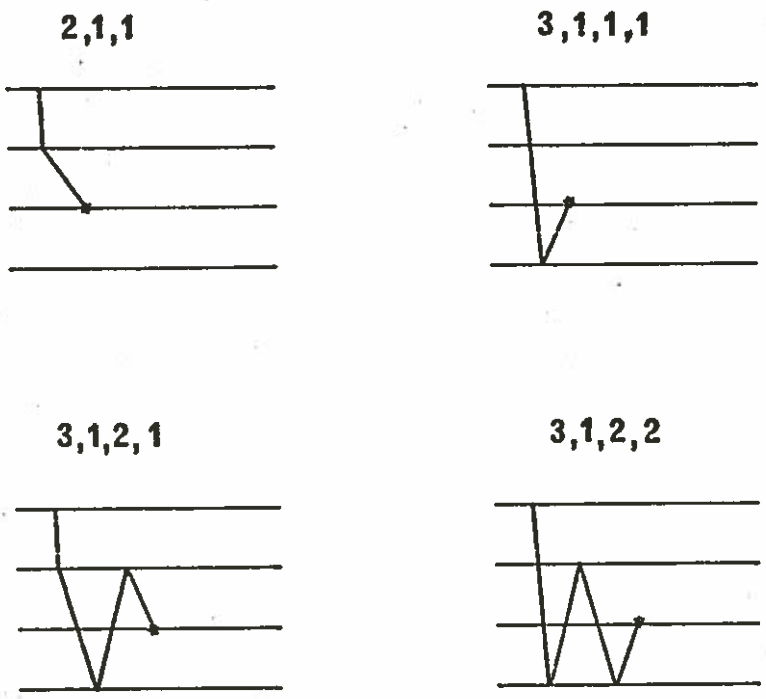

Figure 2-2-6. Examples of the coding system, K,J(I), I = 1,K, for the OSE case.

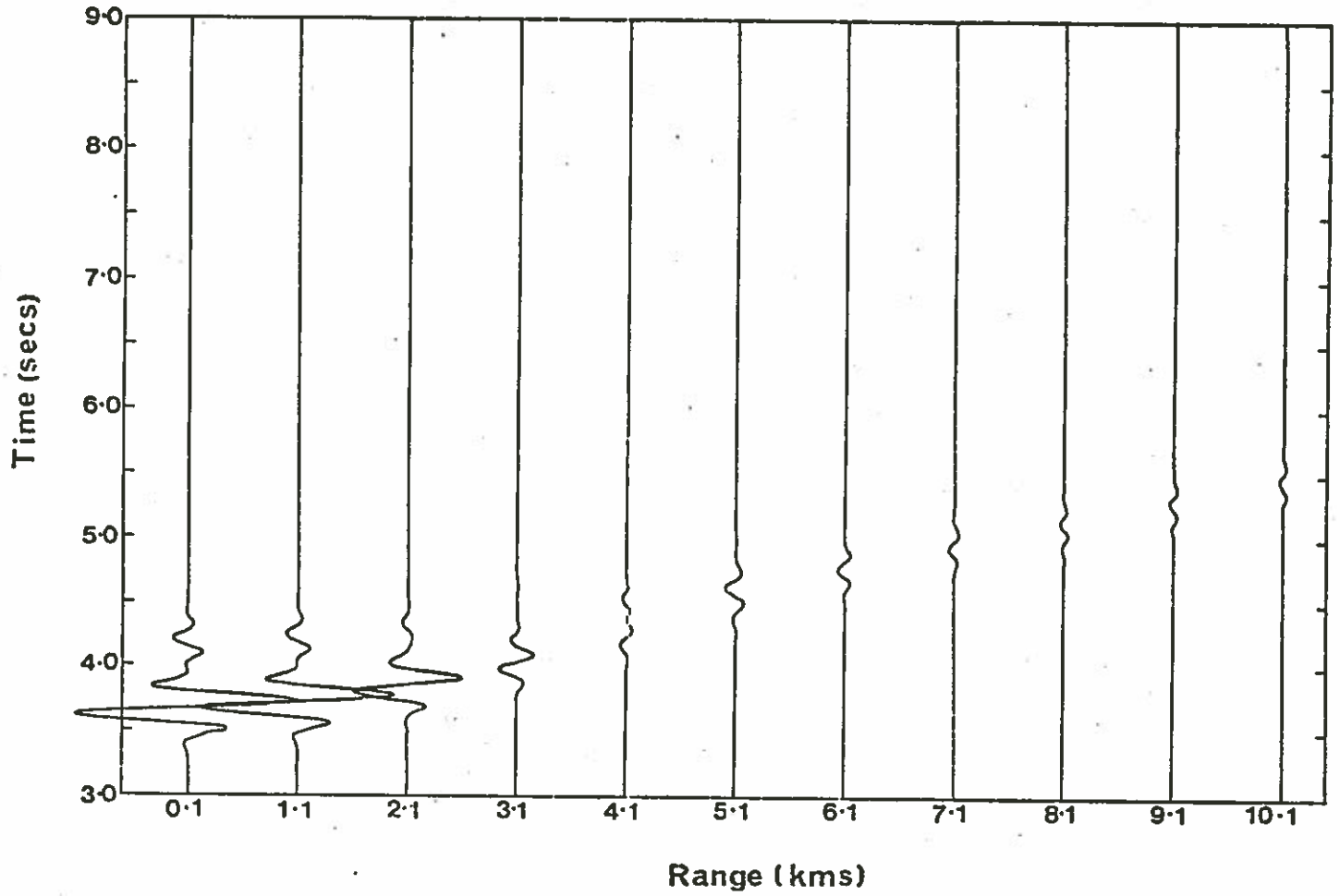

Figure 2-2-7. Ray method synthetic seismogram for primary waves and first and second multiples. The model is the same as for the previous examples (Figure 1-1-1) and only the vertical component is shown.

ranges, however, where the synthetic seismograms are likely to be of most help, the quality of the seismograms will be a function of the model. As with surface-to-surface reflectivity programs the OSE program is expensive in terms of computing time. The program , however, is considered to be a valuable tool for interpreting OSE data.

Synthetic seismograms based on ray theory which include only P-wave multiples are generally inadequate for the OSE case. The more complicated problem of including all significant S-wave and P- to S-wave interconversions, (Hron, 1972) must be considered.

2-3. IDEAL DESIGN OF THE OSE

a). Travel Time Work

The information obtained from the travel time study (Section 2-1) can be summarized as follows:

i. The direct arrival from ranges greater than 3 km gives velocity information for rays travelling at large angles in layer 2. This follows immediately from consideration of the velocity contrast at the sediment/basement interface.

ii. The maximum range required to obtain all the direct arrivals for the geophone at a position half-way in layer 2 (6.4 km) is 11 km. This corresponds to an extreme layer 2 velocity of 6.0 km/sec.

iii. To detect changes in layer 2 velocity of 0.1 km/sec from wide angle shots the travel times must be known to $\pm$ 0.01 sec.

iv. If travel times are known to $\pm$ 0.01 sec the vertical velocity can only be obtained to $\pm$ 0.36 km/sec.

v. The confidence limits on travel times include the effect of bathymetry and layer 2 topography so that bathymetry and layer 2

topography must be known accurately. The OSE should be run in an area which is as flat as possible.

vi. The locations of the shots and receivers must be known to $\pm$ 0.01 km.

Based on travel time studies, the ideal Oblique Seismic Experiment in a hole 2 km deep in average oceanic crust, would have four geophone positions: at the top, bottom and middle of layer 2 and at the top of layer 3. The first two positions would be necessary to obtain a measure of vertical velocity and the middle position would be the best position for measuring horizontal velocity. The layer 3 position would give layer 3 velocities over short ranges.

The models described in the previous section almost certainly do not apply to real oceanic crust. Inhomogeneities are probably present both vertically and horizontally on a scale of 0.5 km or less. In this environment it may be worthwhile to correlate phases vertically in the seismic section which would require much closer geophone spacing: half a wavelength or 0.2 km. Only near vertical incidence shots would be fired at these positions.

In order to guarantee that all possible direct waves are received at the middle layer 2 geophone, shots should be fired up to 12 km. The shot interval should be as short as possible.

In trying to determine the lateral extent of the structure intersected by the borehole (Section 1-4) it would be worthwhile to run lines in a number of directions. This could be combined with a programme to look for anisotropy in layer 2 caused by preferred crack orientation (Section 1-6). In a first analysis it is recommended that two lines be run both parallel and perpendicular to the spreading axis at the time of formation of the crust (four directions

from the hole as in Figure 2-3-1). Although only two azimuths are insufficient to prove anisotropy (Section 1-6c) ; Backus, 1965) they would certainly indicate whether it is worthwhile to look more closely for anisotropy. Some continuity between azimuths could be obtained by shooting charges on 12 km arcs while steaming from one line to another (Section 1-6c); Raitt et al, 1969). This pattern should be fired for all geophone positions.

b). Synthetic Seismogram Examples

Synthetic seismograms can be computed for the four geophone depths which were recommended on the basis of travel time analysis. Also it is interesting to show, for comparison, conventional seismic refraction seismograms. Figure 2-3-2 shows synthetic seismograms for conventional refraction work using surface receivers and sea bottom receivers. Figure 2-3-3 shows synthetic seismograms for the OSE case with receivers in layer 2 at 5.7, 6.4 and 7.0 km. Figure 2-3-4 shows an OSE synthetic seismogram with the receiver at the top of layer 3.

The model (Figure 1-1-1) for these calculations is the same as was used for the examples in the discussion of synthetic seismograms (Section 2-2c)). Since all of the models shown here assume that the water has been replaced with a solid of equivalent P-wave velocity one should look at the effect of this approximation. Figure 2-3-5 compares the land case to a marine case for OSE geometry with the receiver at 6.0 km depth. Compressional wave amplitudes are unaffected but shear wave amplitudes are slightly less between 2.0 and 6.0 km for the land case.The general appearance of the seismograms remains

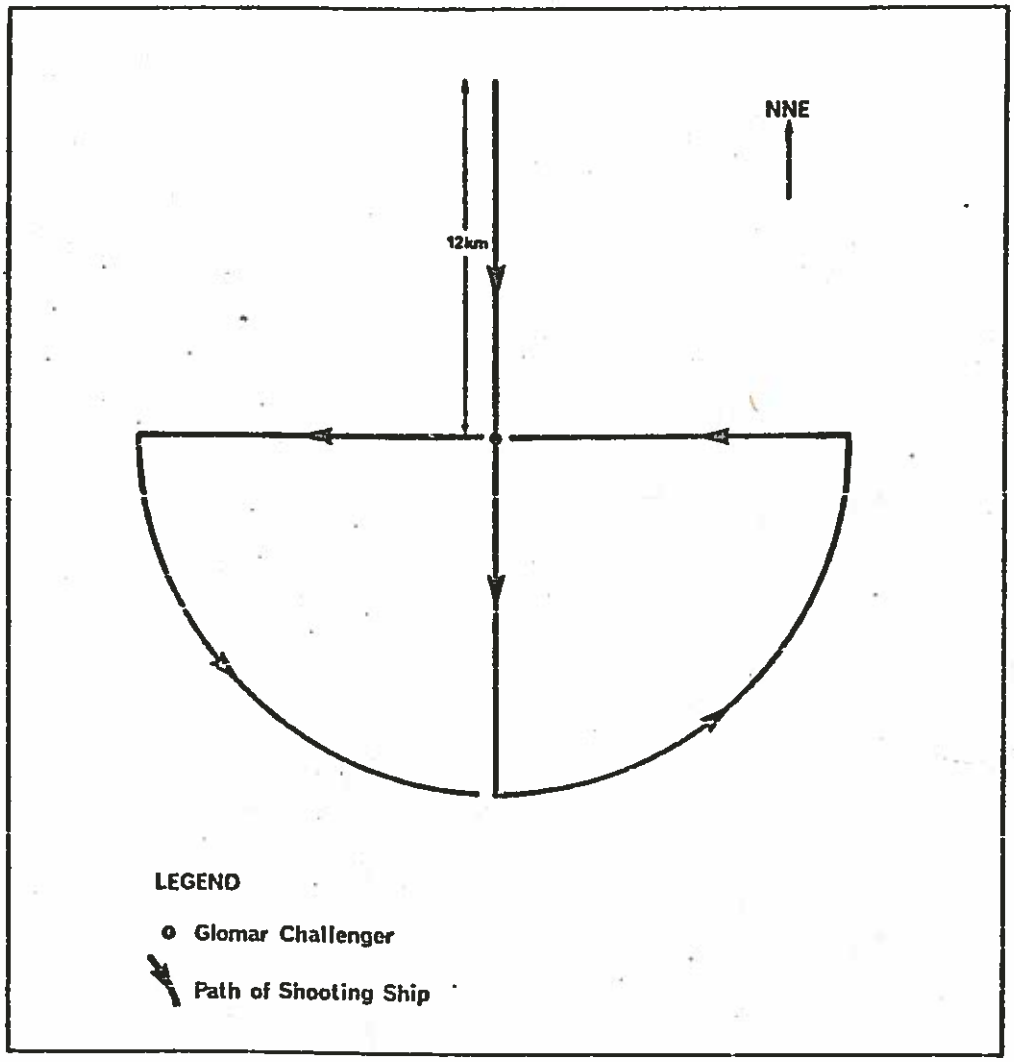

Figure 2-3-1. Plan view of recommended shooting programme. In this case, NNE is the direction parallel to the magnetic lineations. Shots should be fired as close as possible on the straight lines and as close as reasonable on the arcs. The straight line shots represent a minimum program to consider anisotropy and the arcs (ideally a full circle) provide continuity.

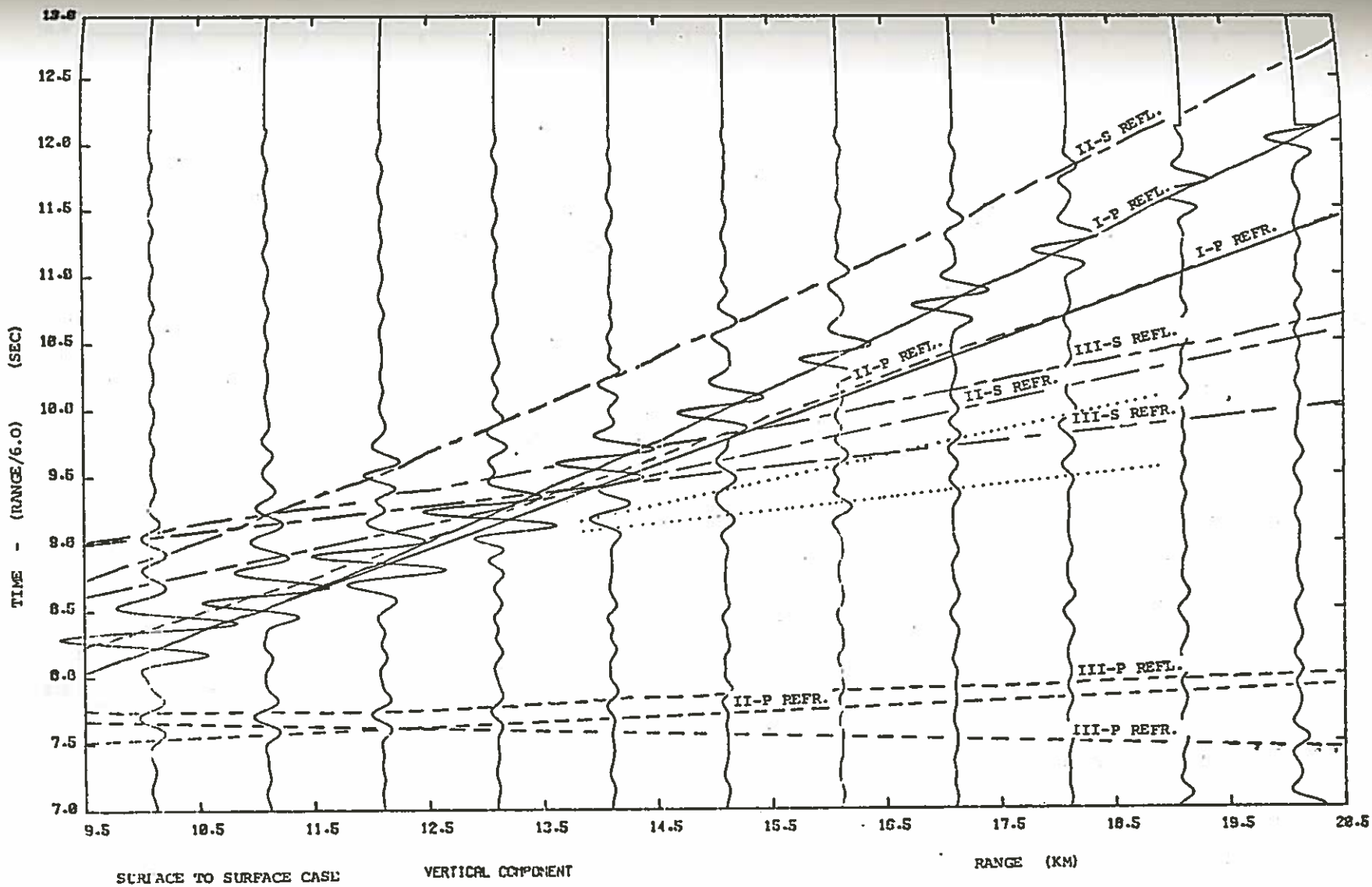

.gure 2-3-2a&b. Synthetic seismograms for conventional refraction experiments using surface receivers (Figure a) and ocean ɔttom receivers (Figure b). The model is the average crust model of Figure 1-1-1 and Section 2-2c). Travel time curves correspond ɔ the central cross-over point of an anti-symmetrical wavelet. The curves are labelled according to the following code: I - ɛdiment, II - layer 2, III - layer 3, P-compressional waves (—— and – – –), S-shear waves (—— –), REFL - reflected arrivals ɔd REFR - refracted arrivals. The layer 2 and 3, S-wave refractions with conversion at the top of layer 2 are shown (.....). The ɛrge arrivals between 7.0 and 8.0 secs at ranges of 19.1 and 20.1 km are unreal and are caused by "folding" in the Fourier ɛansform (Fowler, 1976). The curves have been reduced at 6.0 km/sec. No amplitude weighting with range has been applied.

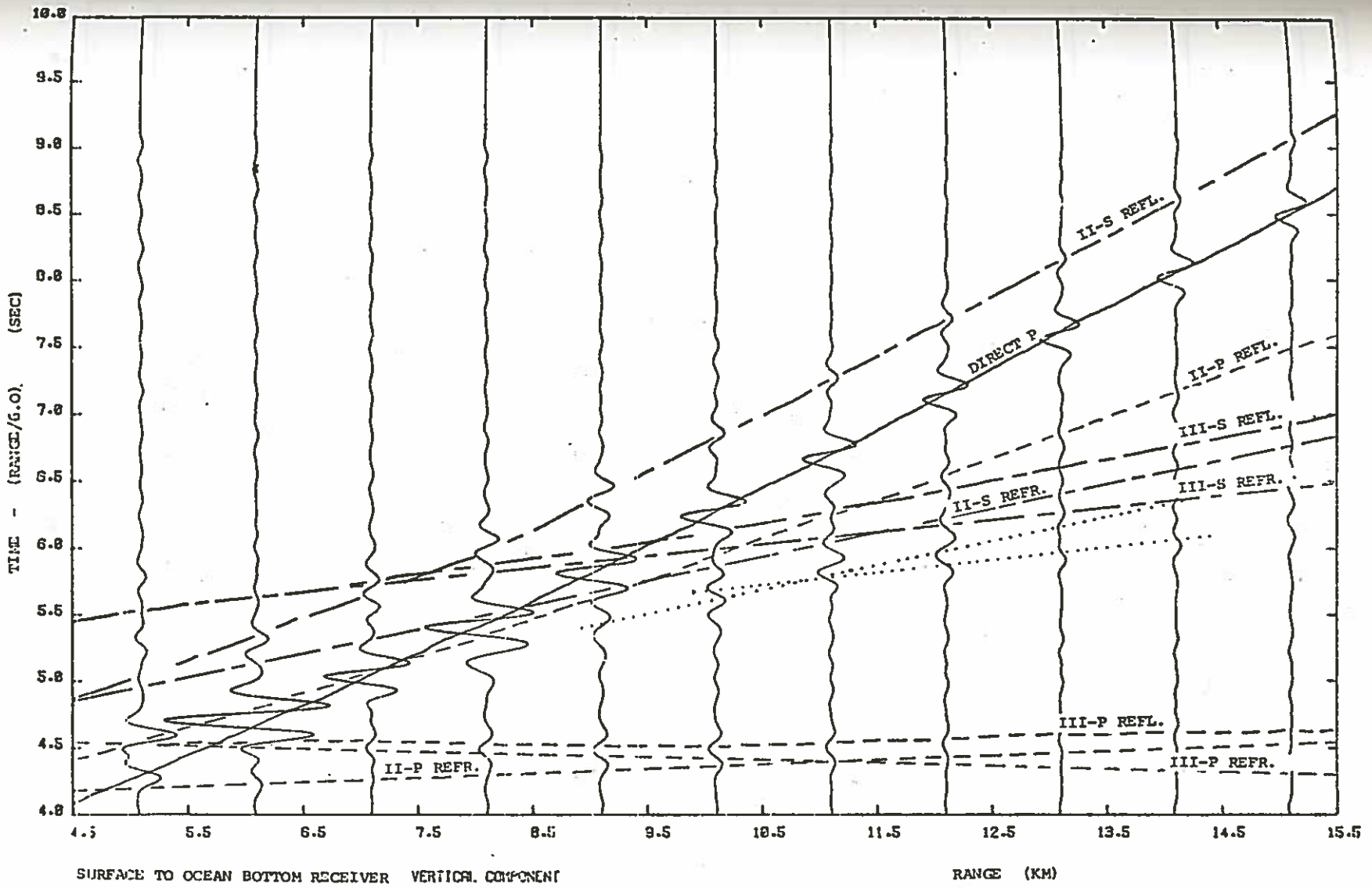
10.0
9.5
9.0
8.5
8.0
7.5
7.0
6.5
6.0
5.5
5.0
4.5
4.0
TIME - (RANGE/6.0) (SEC)
II-S REFL.
DIRECT P
II-P REFL.
III-S REFL.
III-S REFR.
II-S REFR.
III-P REFL.
III-P REFR.
II-P REFR.
4.5
5.5
6.5
7.5
8.5
9.5
10.5
11.5
12.5
13.5
14.5
15.5
SURFACE TO OCEAN BOTTOM RECEIVER VERTICAL COMPONENT
RANGE (KM)

Figure 2-3-2b

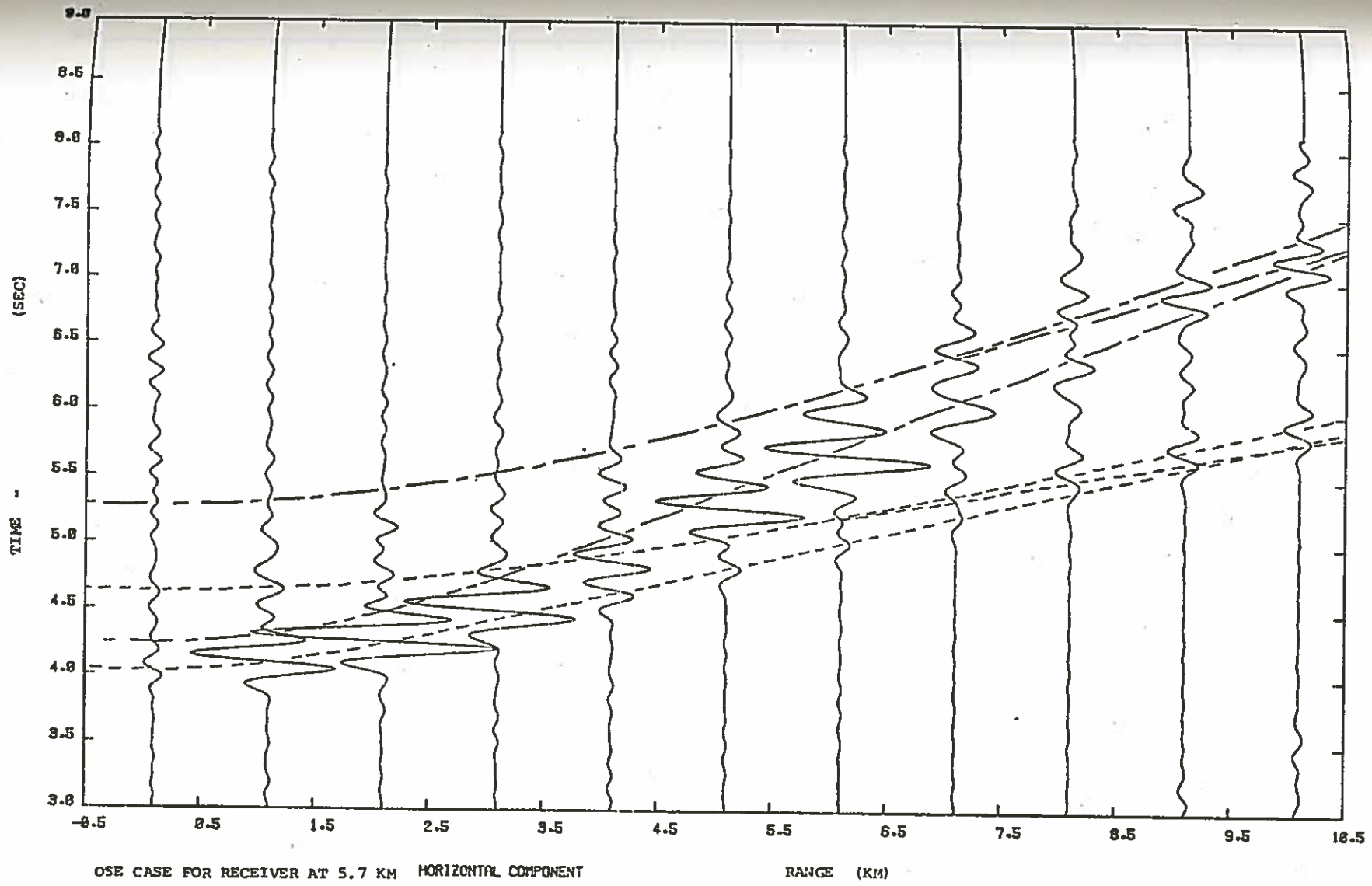

Figure 2-3-3a,b&c. Synthetic seismograms for an oblique seismic experiment with the receiver in layer 2 at depths of 5.7 km (Figure a), 6.4 km (Figure b) and 7.0 km (Figure c). The model is the average crust model of Figure 1-1-1 and Section 2-2c. The travel time curves correspond to the central cross-over point of an anti-symmetrical wavelet. Curves are shown for compressional (– – –) and shear (——– –) arrivals. In each case the earlier curve is the direct arrival and the later curves represent reflections and refractions from layer 3. The curves have not been reduced. No amplitude weighting with range has been applied.

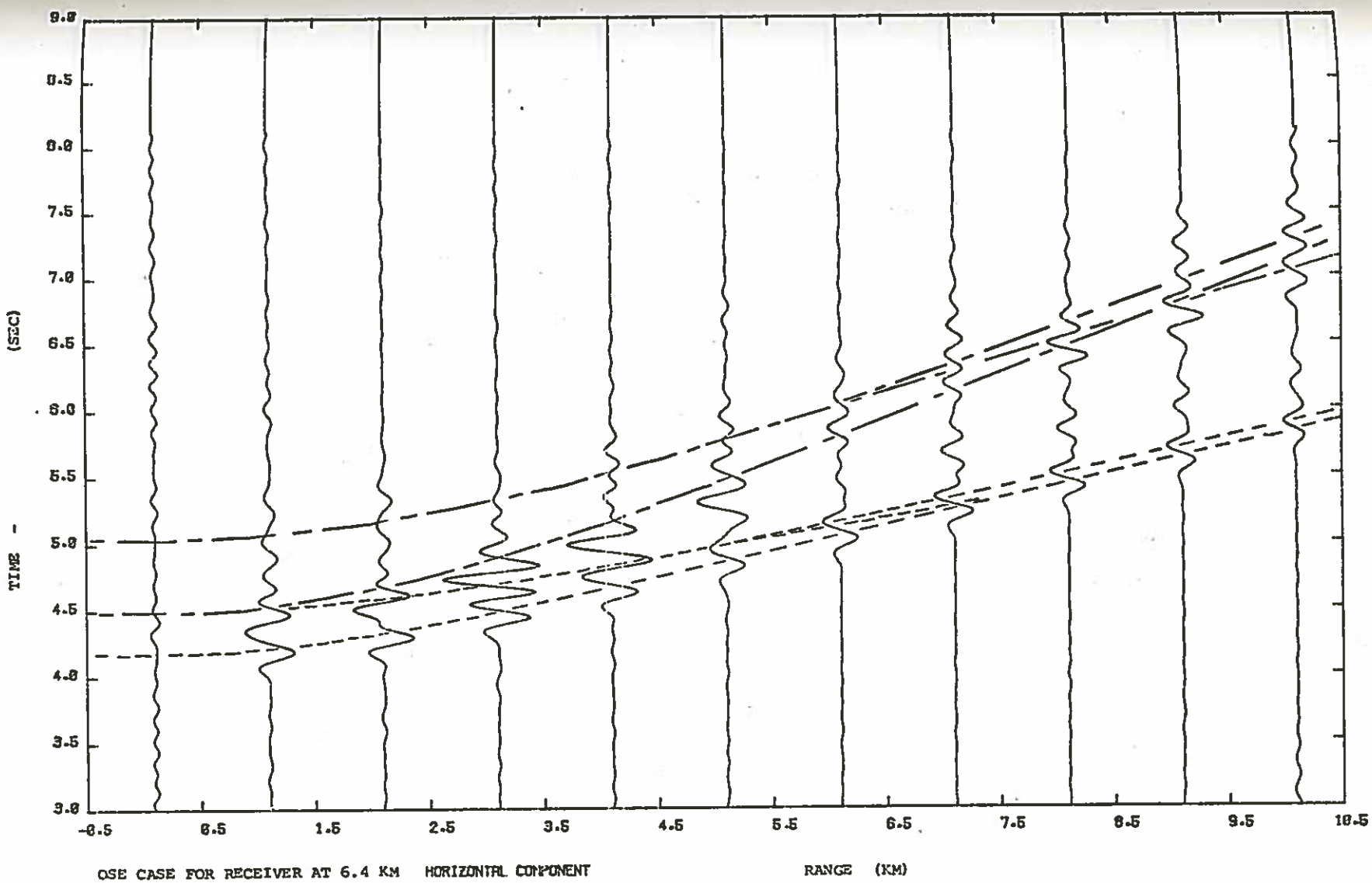
9.0
8.5
8.0
7.5
7.0
6.5
6.0
5.5
5.0
4.5
4.0
3.5
3.0
TIME - (SEC)
-0.5
0.5
1.5
2.5
3.5
4.5
5.5
6.5
7.5
8.5
9.5
10.5
RANGE (KM)
OSE CASE FOR RECEIVER AT 6.4 KM HORIZONTAL COMPONENT

Figure 2-3-3b

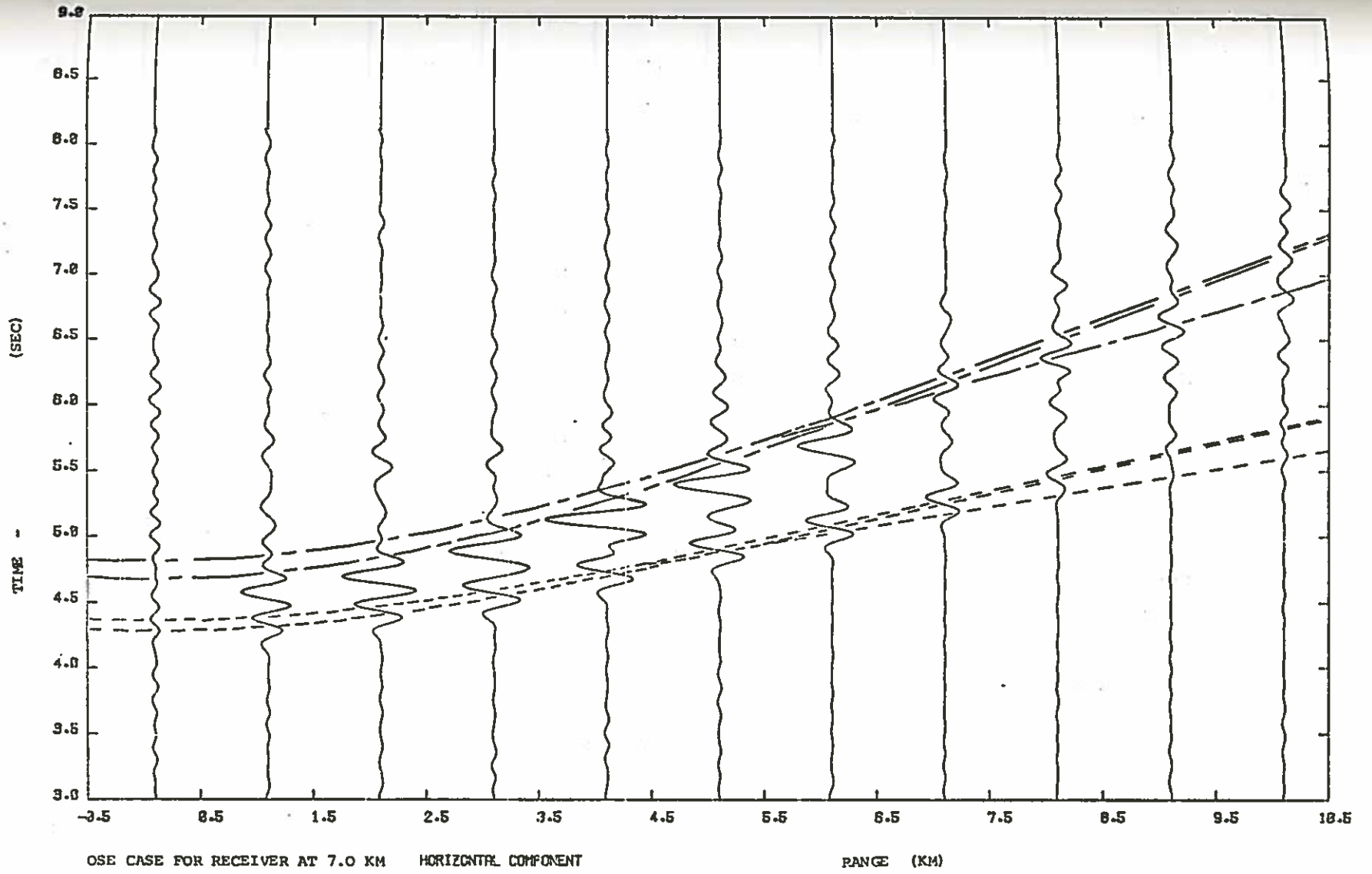
9.0
8.5
8.0
7.5
7.0
6.5
6.0
5.5
5.0
4.5
4.0
3.5
3.0
TIME - (SEC)
-3.5
0.5
1.5
2.5
3.5
4.5
5.5
6.5
7.5
8.5
9.5
10.5
OSE CASE FOR RECEIVER AT 7.0 KM HORIZONTAL COMPONENT
RANGE (KM)

Figure 2-3-3c

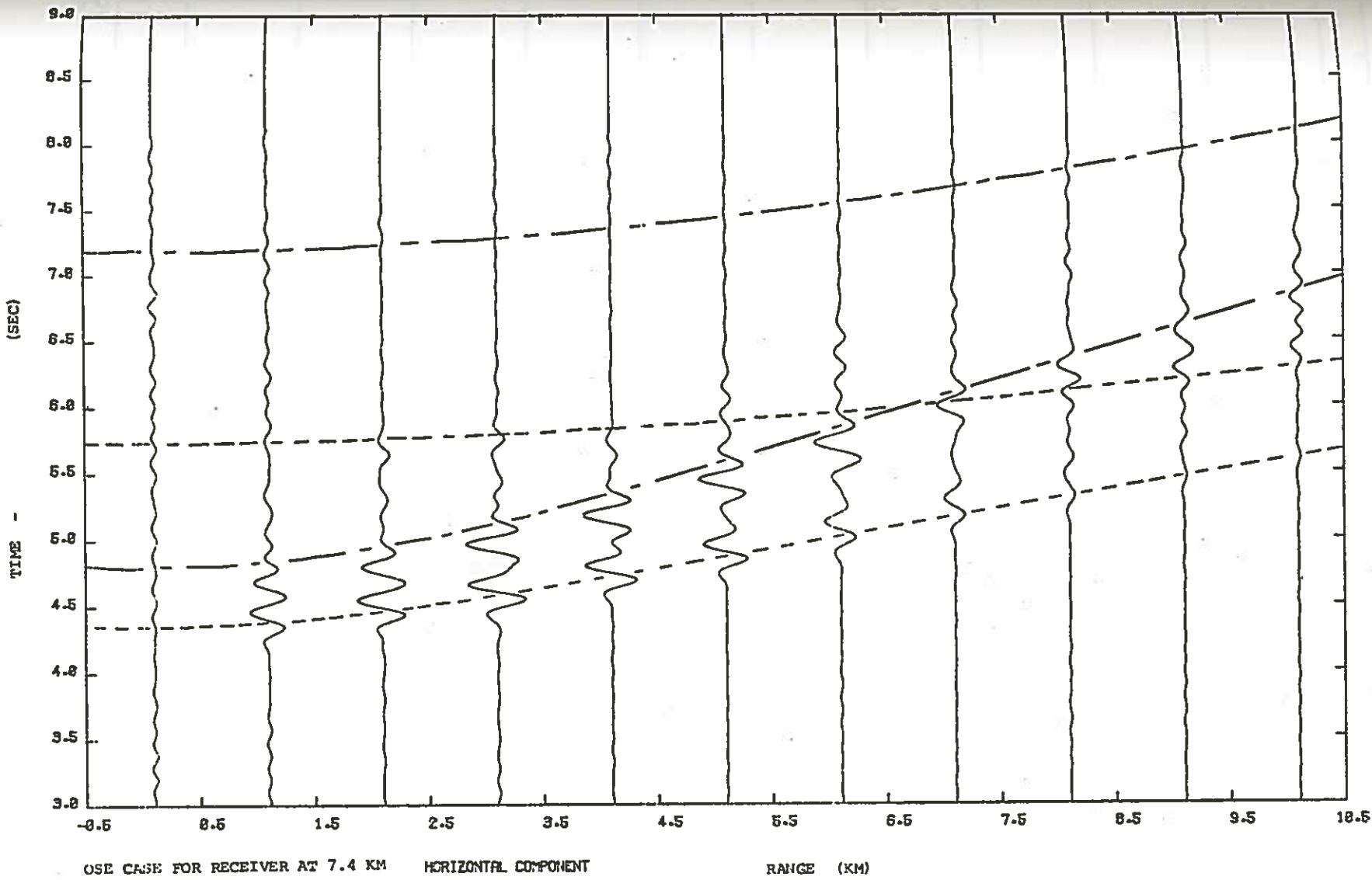

Figure 2-3-4. Synthetic seismogram for an oblique seismic experiment with the receiver at the top of layer 3 (at a depth of 7.4 km). The model is the average crust model of Figure 1-1-1 and Section 2-2c). The travel time curves correspond to the central cross-over point of an anti-symmetrical wavelet. Curves are shown for compressional (– – –) and shear (——– –) arrivals. In each case the earlier curve is the direct arrival and the later curve is the MOHO reflection. The curves have not been reduced. No amplitude weighting with range has been applied.

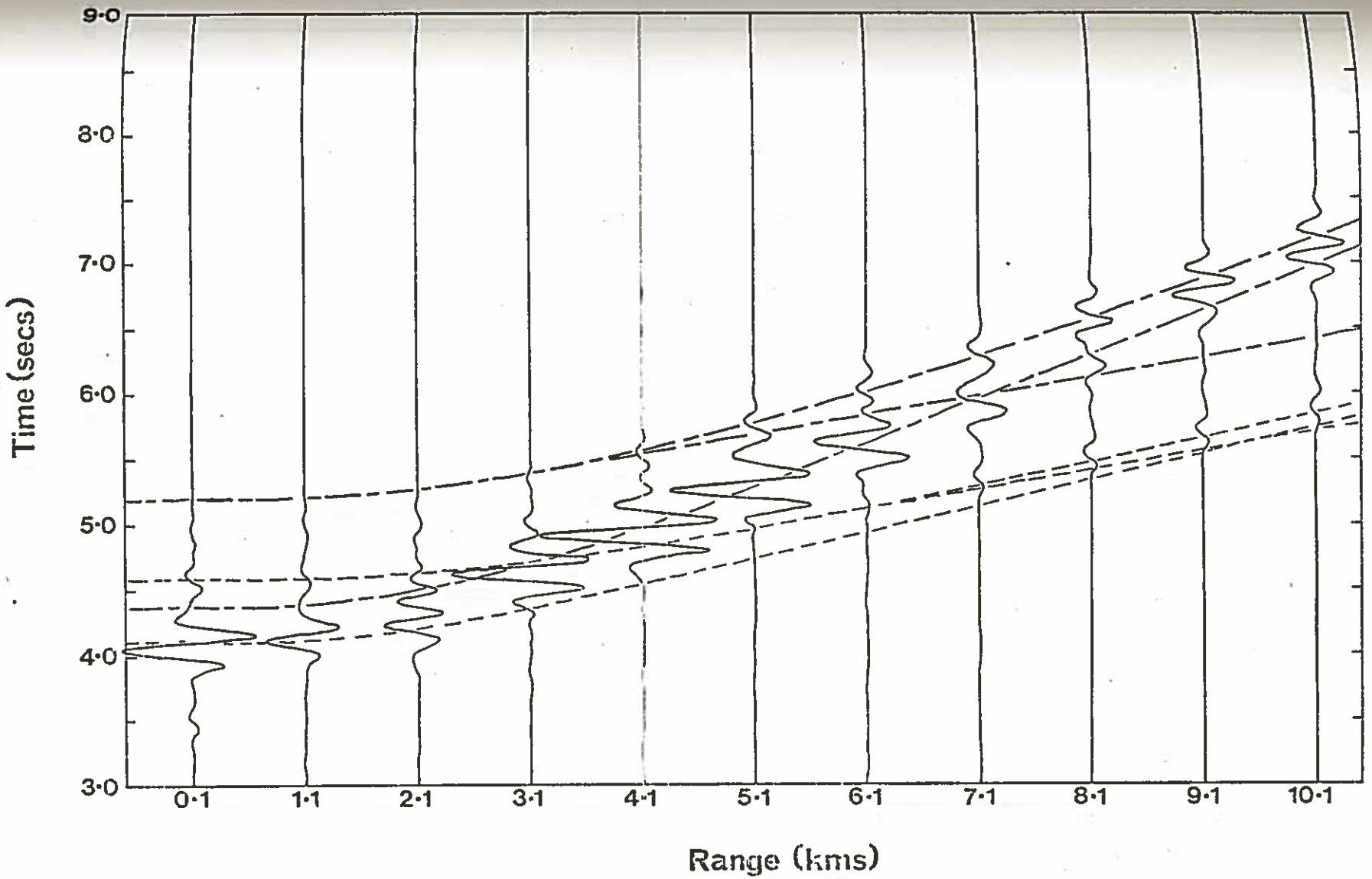

Figure 2-3-5a&b. Comparison between OSE synthetic seismograms for the land case (Figure 1-1-1 and Section 2-2c)) (Figure a) and the marine case (Figure b). The marine case allows for water in the top layer (ie. the ocean). The receiver in this example is at 6.0 km depth. Compressional and shear wave travel time curves are shown as in Figure 2-3-3. Amplitudes corresponding to shear waves below the ocean are slightly larger in the marine case but the general appearance remains the same.

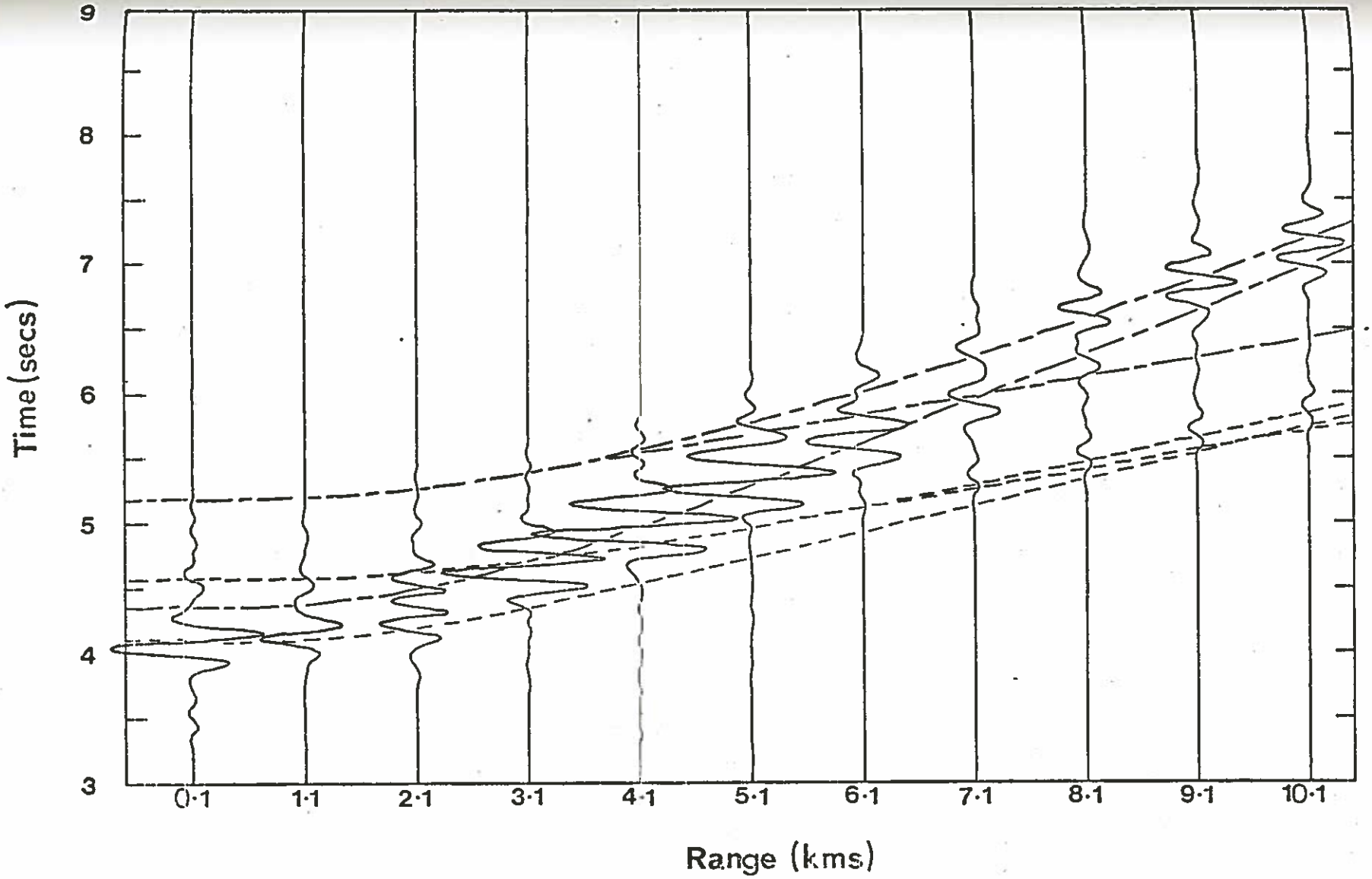

Figure 2-3-5b

unchanged and unless very detailed amplitudes are required it is acceptable to consider land seismograms.

For the two seismograms calculated for conventional refraction geometries (Figure 2-3-2) the strongest arrivals occur for the reflected wave from the sediment (surface receivers) or for the direct water wave (sea bottom receivers). These waves cannot be used to study layer 2. The next strongest arrivals are S-wave refractions from layers 2 and 3 with the P-wave to S-wave conversion occuring at the top of layer 2. These are seldom used in practice because they are difficult to see above the P-wave energy (R.S. White, pers. comm.). The layer 2 and layer 3 P-wave refractions which form the basis of the refraction method have generally low amplitudes compared to the overall section. Layer 3 arrivals are large near the critical region.

In contrast, the largest arrivals for a receiver within layer 2 (Figure2-3-3) correspond to direct P-waves and S-waves which give layer 2 velocities (Section 2-1). (Horizontal components only have been considered here but a discussion of vertical versus horizontal components is given in Section 2-3c)). The synthetic seismograms confirm that direct wave arrivals of significant amplitude can be picked on the sections as was assumed in the travel time analysis (Section 2-1). The shallow position (Figure 2-3-3a) has direct first arrivals over the longest range. Compressional to shear wave conversion at the top of layer 2 is significant. This can be seen by the high energy arriving just before the plotted S-wave arrival curves on all the OSE sections. (The plotted S-wave curves correspond to P-wave to S-wave conversion at the top of the sediment.)

The synthetic seismogram for a receiver at the top of layer 3 (receiver depth of 7.4 km) has been shown for completeness (Figure

2-3-4). The direct P-wave occurs as a strong arrival. Again there is evidence for strong P-wave to S-wave conversion at the top of layer 2.

The synthetic seismograms show the general appearance of an Oblique Seismic Experiment section. The synthetic seismogram analysis confirms that the arrivals on which the travel time study was based are relatively strong and can be detected.

c). Vertical Versus Horizontal Components

Figure 2-3-6 compares a vertical component and a horizontal component seismogram for a receiver at 6.0 km depth in average oceanic crust. The obvious feature is that compressional wave energy is strongest on the horizontal component. In fact, it is essential to have a horizontal component to detect the direct P arrival. This behaviour would be expected for rays travelling horizontally. Because of the high velocity contrast at the top of layer 2 (2.1 to 5.0 km/sec) the compressional wave from middle to large ranges ($>$ 4 km) does indeed arrive at the geophone at near horizontal incidence (Figure 1-3-1).

The layer 2 compressional wave velocity can be determined from the slope of the straight line of the first arrivals on the horizontal component between 3.0 and 9.0 km. The shear wave velocity can be determined from the S-wave arrivals on the vertical component between 5.0 and 7.0 km.

Figure 2-3-6 demonstrates that a three component geophone is necessary to successfully run an Oblique Seismic Experiment in oceanic crust.

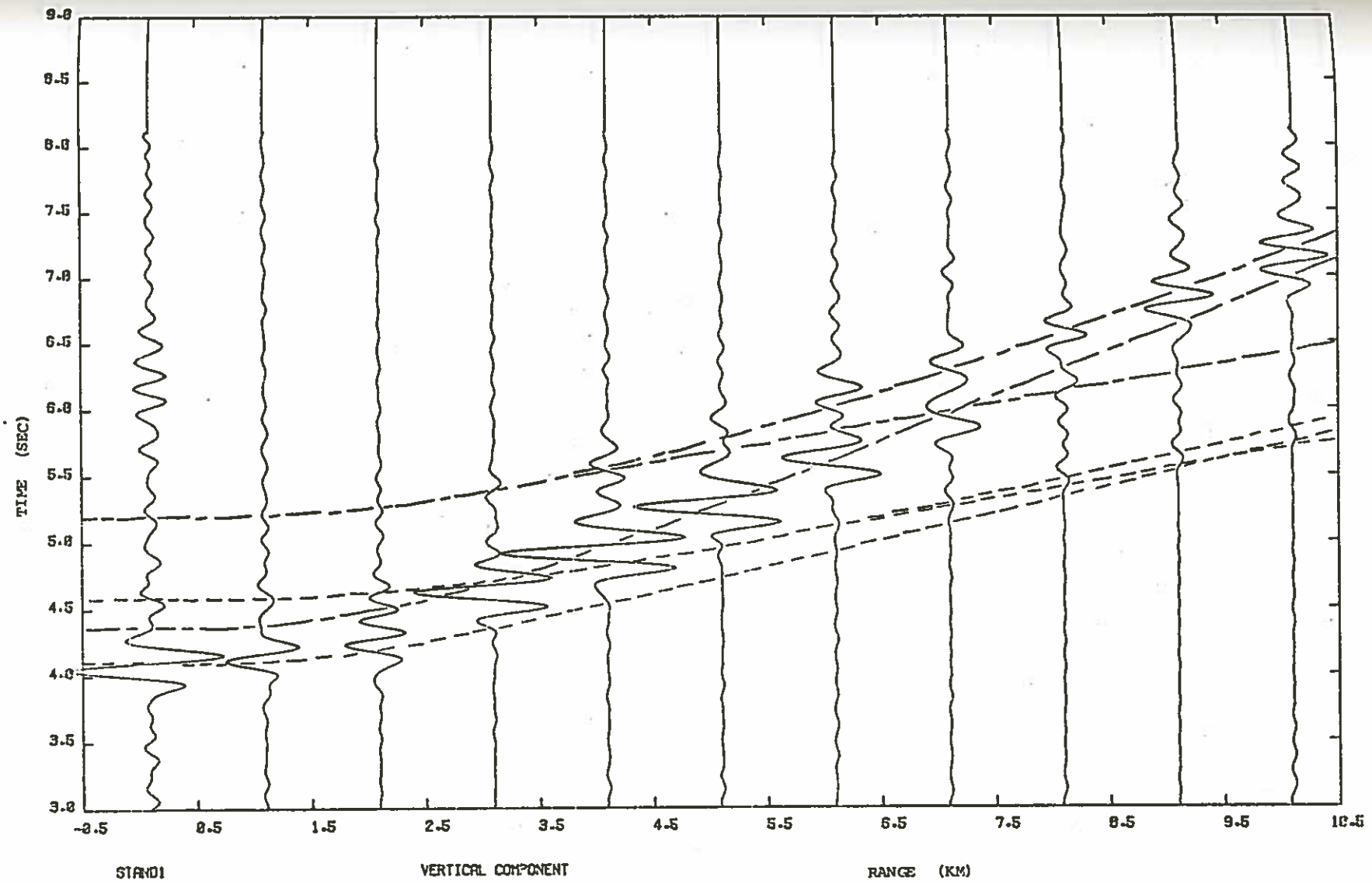

Figure 2-3-6a&b. Comparison between vertical (Figure a) and horizontal (Figure b) synthetic seismograms for the OSE case. The model and curves are the same as in Figure 2-3-5. The geophone is at 6.0 km depth. The direct P-wave arrival is strongest on the horizontal component and the direct S-wave arrival is strongest on the vertical component for ranges greater than 2.0 km.

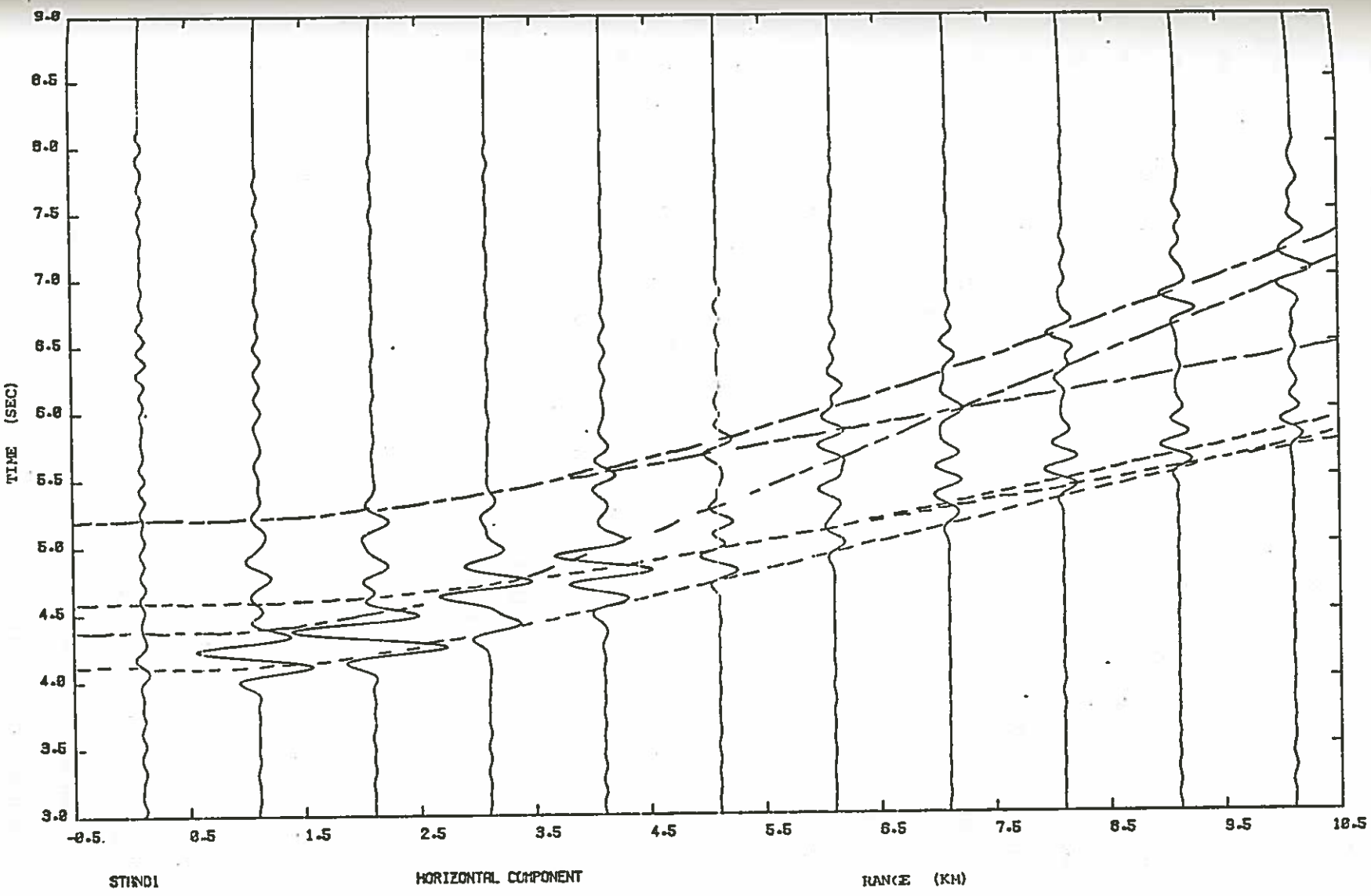
9.0
8.5
8.0
7.5
7.0
6.5
6.0
5.5
5.0
4.5
4.0
3.5
3.0
TIME (SEC)
-0.5
0.5
1.5
2.5
3.5
4.5
5.5
6.5
7.5
8.5
9.5
10.5
STIND1
HORIZONTAL COMPONENT
RANGE (KM)

Figure 2-3-6b

d). Attenuation

In addition to determining the general appearance of an OSE record section (Figures 2-3-3 to 2-3-6) synthetic seismogram studies were performed to look at the effect of attenuation on amplitudes as a function of depth and range. Field measurements of attenuation at seismic frequencies are not common. White (1965) gives a review. McDonal et al (1958) and O'Brien and Lucas (1971) demonstrate two classic approaches. Neprochnov (1967, 1971) obtained attenuation values from a less well documented method based on reflection wave amplitudes (Hamilton, 1976a).

McDonal et al (1958) was the first serious attempt to measure attenuation. To minimize the effects of reflection and transmission on amplitude, the study was carried out in Pierre shale, an exceptionally uniform structure, 1.3 km thick in Eastern Colorado. They recorded signals from explosive sources at ranges from 0.033 to 0.166 km. Both shots and receivers were in boreholes. Since the structure was uniform, only corrections for spherical divergence were necessary and the signals could be Fourier transformed with confidence that all energy in the wavelet followed the same path from the source. Attenuation was obtained from the slopes of corrected amplitude-distance curves at frequencies from 60 Hz to 500 Hz. In view of the OSE it is worthwhile to note their requirements for an accurate study of attenuation:

1. A thick, uniform section of rock is necessary.
2. Only amplitudes from the same shot should be correlated.
3. At least two detectors should be in line with the shot.
4. The detectors should be well coupled to the rock for the frequencies of interest. They suggest that the resonance of a clamping mechanism be checked in situ. Hydrophones

should definitely not be used,

5. A wide band recording system with known response is needed.

In the initial, low cost approach to the OSE in oceanic crust the first three requirements are out of the question. The fourth point is taken, but tests of the coupling in situ were not made because this would increase the complexity of the downhole circuitry and increase the chances of a failure in the clamping mechanism. As will be shown in the next chapter the clamping circuitry is independent of the pre-amplifiers. Reliability of the clamp is essential to ensure retrieval of the tool. A driving geophone as used by McDonal et al would require switches in the clamp leads.

The method of O'Brien and Lucas (1971) is less accurate but more feasible. Shots were received from surface sources, primarily explosives, at a clamped geophone in the hole. Maximum shot-receiver distances in different holes varied from 1.2 km to 3.3 km and the geophone spacing was typically 0.33 km. Measured amplitudes of the first two peaks of an arrival were corrected for charge weight, spherical divergence, reflection and transmission losses (based on structure from a sonic log) and angle of incidence of the ray path. Again, the slope of the amplitude-distance plot gives attenuation although in this case the measure is only for the dominant frequency of the signal. Except for varying charge weight, the corrections can be made by computing a synthetic seismogram using a straight forward, normal incidence technique (O'Brien and Lucas, 1971; Smith, S.G. 1976). Depending on the velocity profile, however, it may be necessary to consider intrabed multiples (O'Brien and Lucas, 1971; O'Doherty and Anstey, 1971; Schoenberger and Levin, 1974). The reflectivity synthetic seismogram technique, discussed in this chapter, is not suitable for determining

near normal incidence amplitudes because of the numerical difficulties encountered at short ranges.

To measure vertical attenuation on the OSE the O'Brien and Lucas technique is preferred. In general it requires a hole at least 0.6 km deep with amplitude measurements at three depths. A velocity log of the hole is essential. Interpretation would be based on residuals from synthetic seismogram amplitudes computed using a normal incidence technique.

Attenuation measurements from the wide angle shots can be made if the lateral variation in structure is not significant. Synthetic seismograms for the flat, homogeneous model can be computed using the modified Fuchs-Müller method. A plot of the amplitude differences between real and synthetic seismograms would give the attenuation. Alternatively, the synthetics can be computed with attenuation included and direct comparisons made. Figure 2-3-7 shows amplitude-distance curves for three depths in the same model with $Q = \infty$ and $Q = 50$. The effects of attenuation can be seen earlier if the geophone is deeper but at long ranges, depth is not significant.

e). Velocity Gradients

To what extent does the difference between a constant velocity layer 2 and a layer 2 with continuously increasing velocity affect the amplitudes of the first P arrival? Figure 2-3-8 shows the log of the vertical component amplitude plotted against range for the two cases, at a depth half-way in layer 2 (6.4km). The amplitudes for the case of a velocity gradient are slightly higher because of the higher transmission coefficient. The geometrical effect, in which rays

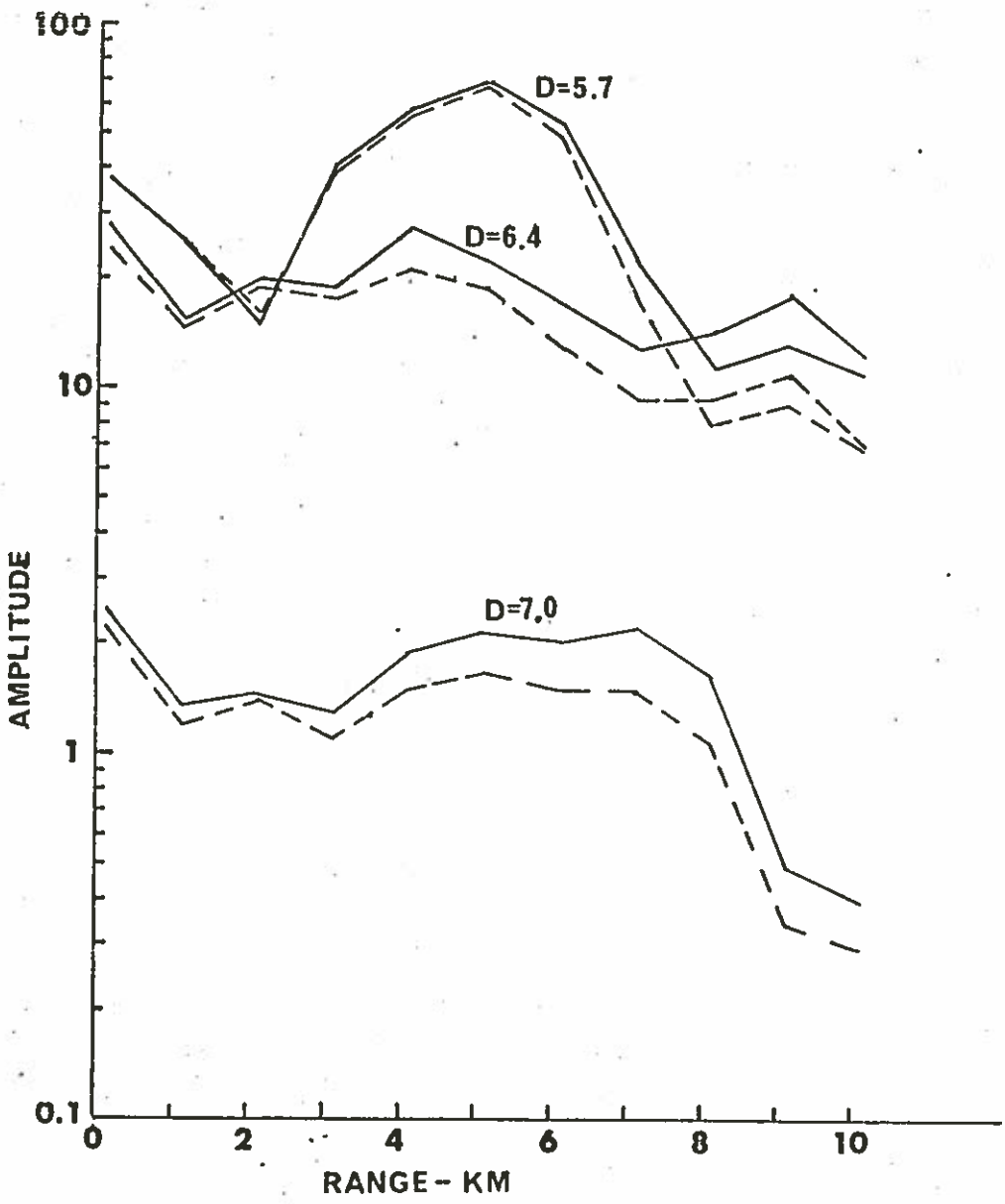

Figure 2-3-7. Amplitude vs range plots for different depths in average oceanic crust (Figure 1-1-1). The peak-to-peak amplitudes of the first arrival on the vertical component are shown for Q = ∞ (———) and Q = 50 (- - -). The modelling parameters are the same as for the discussion in Section 2-2c). For the D = 7.0 curve, the amplitudes have been divided by 10 for clarity. The amplitude character changes considerably at different depths due to different interference effects. The deep geophone is the best for looking at vertical attenuation. Horizontal attenuation has roughly the same effect at all depths. (D is the receiver depth below sea level in kilometres.)

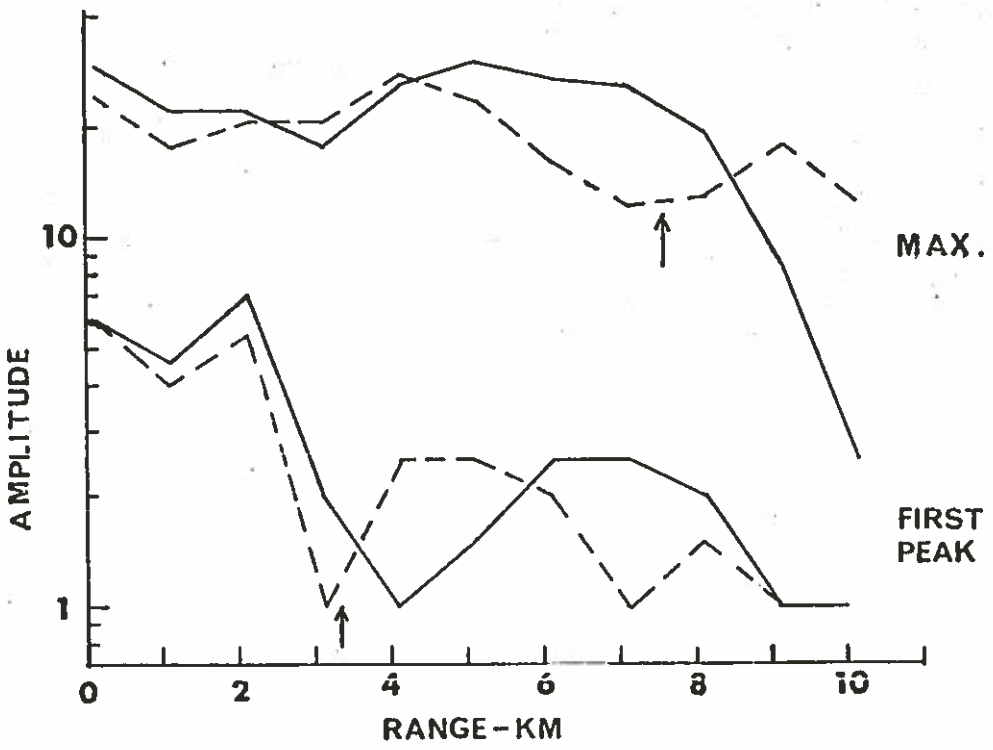

Figure 2-3-8. Effect of a gradient in layer 2 on amplitudes. Vertical component amplitude curves are shown for the constant layer 2 velocity (5 km/sec) case (---) and for the case of a gradient (———) with 4.2 km/sec at the top increasing by 1 km/sec/km. The receiver is at a depth of 6.4 km. The top curve represents maximum peak to peak amplitude on a trace, which for ranges greater than 3.0 km is predominantly S. The bottom curve represents first peak amplitude and hence P energy. In the constant velocity case one would expect the amplitudes to decrease continuously with range due to the geometrical effect of the rays arriving at the geophone at larger angles. In a gradient the amplitudes should decrease to zero at a range corresponding to horizontal incidence and then increase again 180° out of phase. The arrows mark the points at which pure direct waves cease. Gradient amplitudes are generally higher for the direct waves, because of a higher transmission coefficient at the top of layer 2, and reach their minima at larger ranges. The expected gradient effect is not observed.

of near horizontal incidence have a shorter range in the case of a gradient, is not significant.

The curves in Figure 2-3-8 do not decrease smoothly because of interference with the S-wave arrival. At deeper positions, direct P- and S-wave arrivals are more distinct and their amplitudes can be measured independently to shorter ranges. Also, the effect of interference due to reflections at short ranges is reduced if continuous rather than step-wise changes in velocity are present.

Gradients in layers below the receiver will have the same effects on seismograms as gradients in conventional refraction studies (Helmberger, 1968, 1977; Helmberger and Morris, 1969, 1970; Braille and Smith, 1975; Orcutt et al, 1975, 1976; Whitmarsh, 1978). Positive gradients decrease the amplitudes of sub-critical reflections and increase the amplitudes of the super-critical reflections and refractions.

The OSE has an advantage over conventional refraction in looking at lower layers because it is generally better coupled to the rock and reliable S-wave arrivals as well as P-wave arrivals are recorded. For this reason it would be interesting to shoot long (70 km) refraction lines into a clamped borehole geophone.

As will be seen in the data reduction stage (Chapter 4) general qualitative analysis of both P- and S-wave amplitudes can help to distinguish between models which satisfy the same travel time criteria.

CHAPTER 3

EQUIPMENT DEVELOPMENT AND DATA ACQUISITION

3-1. EQUIPMENT

a). General Description

The basic objective of the Oblique Seismic Experiment is to obtain seismic recordings from shots at various ranges from the borehole. This can be accomplished by recording the shot instant, the direct arrival of sound at the drilling ship, the sound in the borehole and a reference clock.

Stephen (1976 and 1977a) gives a detailed review of the equipment used on the experiment. Figures 3-1-1 and 3-1-2 are block diagrams of the equipment on the drilling and shooting vessels.

The borehole geophone is a Geo Space Wall-Lock Seismometer (Figure 3-1-3) (Geo Space Corp. 1972). It has an electrically driven arm, which can be extended from the tool when it is in the open hole, to clamp the unit in place. (A spring maintains pressure on the arm when the motor is switched off). This reduces the effect of pressure waves in the well (McDonal et al , 1958; White, 1965; O'Brien and Lucas, 1971; Gal'perin, 1974) and isolates the tool from the ship's motion.

The Geo Space unit was purchased as a vertical component seismometer. The geophone package at the bottom of the tool contained six vertical component geophones. The unit also had a preamplifier which amplified the signals by 25.6 times (48db).The OSE however requires a three component system because the first P-wave arrival from large ranges has a horizontal motion. In addition, the background acoustic noise on Glomar Challenger is so high that the fixed gain preamplifier is overloaded and testing is difficult. Consequently I adapted the Geo Space seismometer to a

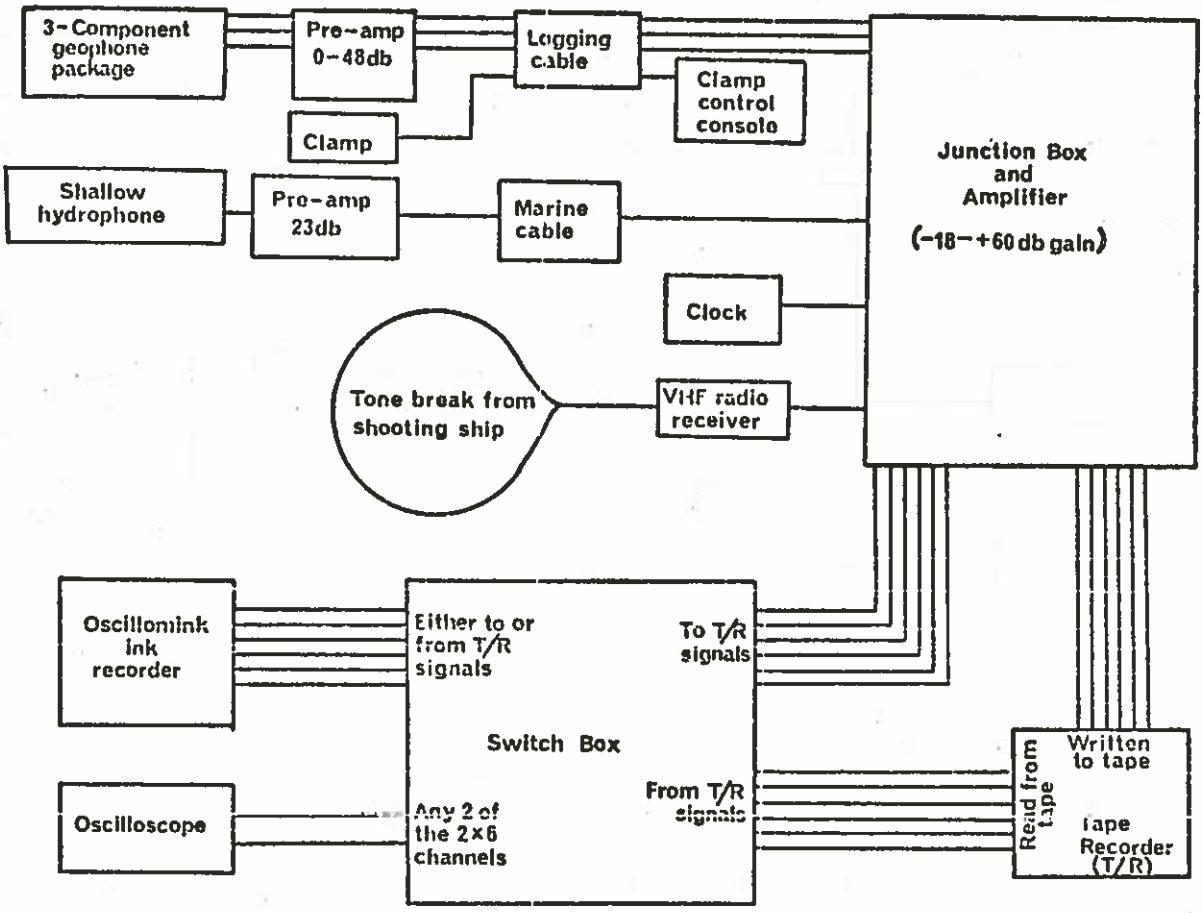

O.S.E. Equipment for Drilling Vessel

Figure 3-1-1. Block diagram of the drilling vessel equipment. Inputs are 3 geophone signals, hydrophone signal, clock, and tone break. In the junction box the 4 seismic signals can be attenuated or amplified. Records are made on paper and tape and any 2 channels can be displayed on the oscilloscope. The tape recorder has a read head so that the signals on the tape can be monitored in real time.

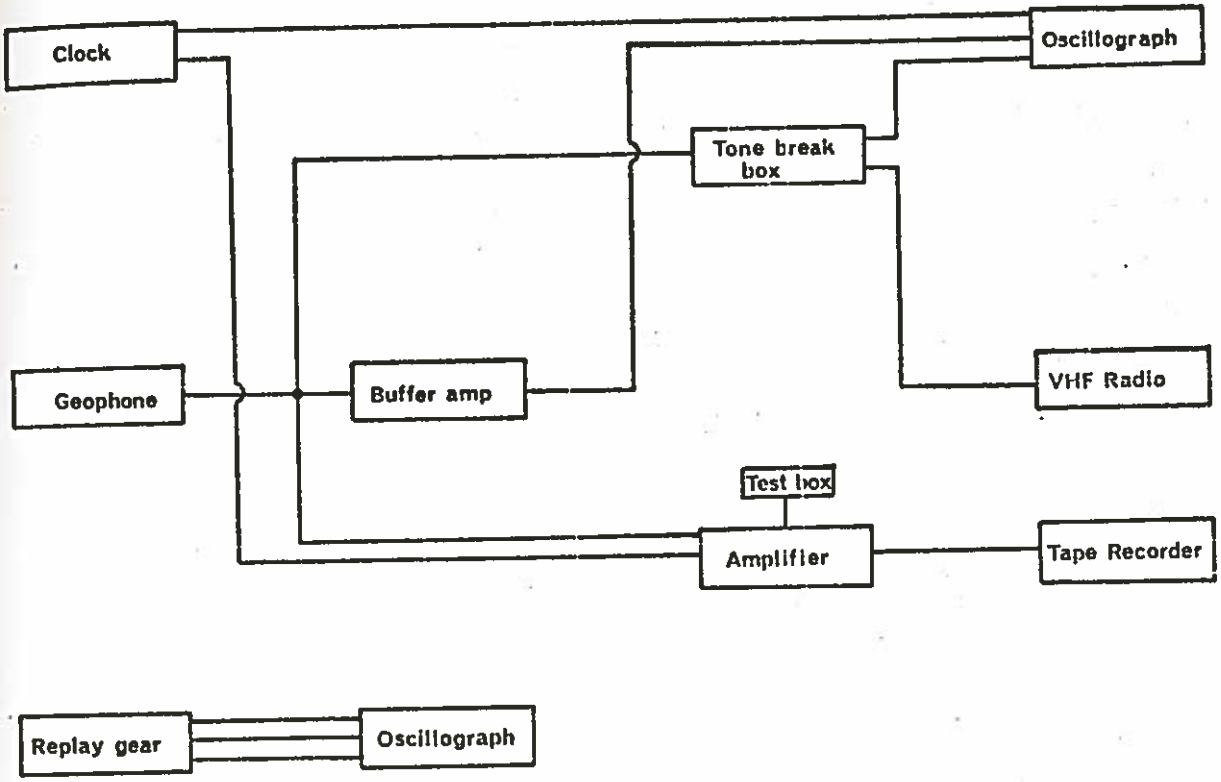

O.S.E. Equipment for Shooting Ship

Figure 3-1-2. Block diagram of the shooting ship equipment. The purpose of this gear is to record and transmit the shot instant which is detected by a hull geophone. The signal is converted to a tone break for transmission to the shooting ship. If this system fails the shot instant can be recorded on board (both paper and tape records) in which case the clocks on the two ships must be synchronized.

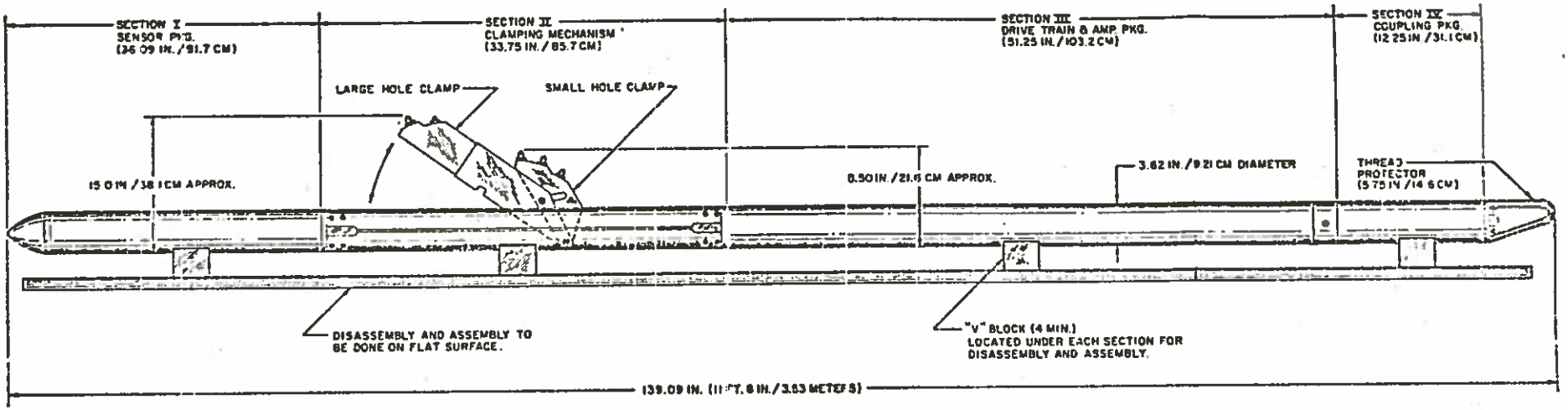

SPECIFICATIONS

GENERAL

LENGTH	11 FT. 6 IN./3.53 METERS
DIAMETER	3.62 IN./9.21 CM
WEIGHT	220 LBS/99.8 KILOS
TEMPERATURE LIMITS	150° C
PRESSURE LIMITS	12,000 PSI MAX.
LOCK-IN HOLE SIZE	4 TO 15 IN./10.2 TO 38.1 CM
HOLE CONDITION	CASED OR UNCASED

SENSORS

TYPE	HS-1 GEOPHONES 4.5 Hz 215 Ω
FREQ RESPONSE	WITHIN 3db 8 TO 300 Hz
QUANITY	6 VERT. IN SERIES PARALLEL

AMPLIFIER

POWER	± 12 VDC BATT. FROM CONTROL UNIT
GAIN	48 db FIXED
FREQ RESPONSE	3 db FROM 5 TO 200 Hz
INPUT NOISE	MAX. EQUIV. LESS THAN 1 MICROVOLT RMS

CONTROL UNIT

POWER REQUIREMENTS	115 VAC 60 Hz 100 W
OUTPUT	115 VDC TO LOCK-IN MECHANISM

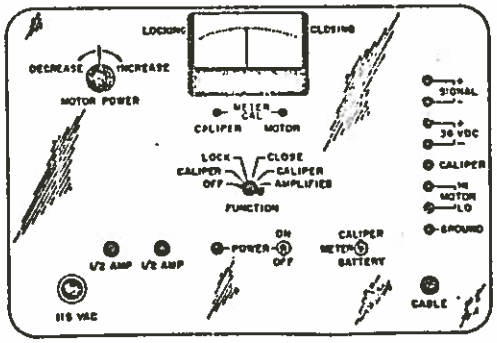

CONTROL UNIT FRONT PANEL

Figure 3-1-3. The Geo Space Wall-Lock Well Geophone. The Wall-Lock Geophone described here was modified at Cambridge to a three component system with discrete variable gain preamplifiers. The clamping system was unmodified. (Geo Space Corporation, 1972).

three component unit with variable gain preamplifiers. Mr. A. Claydon designed and built a jig to hold two vertical and four horizontal (two each in the x and y directions) geophones which was a direct substitute for the six vertical geophones. Geo Space, Houston had modified the Wall Lock Seismometer to bring four leads up from the geophone package. I designed and built the Cambridge Three Component Borehole Preamplifier which is discussed in the next section. It can be interchanged with the original preamplifier and it was not necessary to alter the pressure case.

The geophone has an outside diameter of 3⅛ inches and is too big to pass through a normal bit (2.44 inches ID). The tool can be used with a special logging bit which has an inside diameter of 4 inches.

A seven-conductor Schlumberger Logging cable conducts the seismic signals to the surface. Appendix A lists the specifications of the cable.

The shot instant is picked up on a hull geophone on the shooting ship. This signal triggers a tone break (Mason, 1975a) which is transmitted via VHF radio to the drilling ship.

A hydrophone (Smith, S.G. 1976) slung over the side of the drilling vessel to a depth of 0.330 km, receives the direct sea wave arrival for the calculation of ranges. It consists of a piezoceramic element entirely potted in araldite and a preamplifier with fourteen times (23 db) amplification. The hydrophone cable is suspended by a series of floats to decouple the sensor from wave motion.

A digital clock (Mason, 1975b) outputs a coded series of voltage pulses as a time reference.

The six signals are fed into an OSE amplifier box in the drilling

vessel laboratory. The box modifies the tone break and clock signals for recording and the geophone and hydrophone signals can be either amplified or attenuated to satisfy the 1.0V peak-to-peak input requirement of the tape recorder. The signals then go to an OSE switching/terminal box which directs them to a Thermionic's T8000 tape recorder, an oscillomink paper recorder and an oscilloscope.

The frequency response of the system is flat between 5 Hz and 100 Hz. The amplitude response for the geophones (Appendix B), preamplifier (refer to next section), cable and laboratory amplifiers (measured on board ship) and tape recorder (Racal Thermionic Ltd, 1970) is well within 3 db over the frequency range of interest. The total phase response of the electronics is less than 1.5 msec but the phase response of the geophone output relative to case displacement varies from 0° to 90° between 4.5 and 100 Hz (Appendix B). This phase response is inherent in spring mounted systems and causes significant delays (12 msec for 10 Hz signals). This should be considered when interpreting the data.

A certain amount of redundancy was built into the system in case of minor failures. Mr. R. Theobold, Mr. A. Claydon, and I built the Cambridge High Pressure Hydrophone as a back-up unit for the well geophone. The piezo-electric crystal was immersed in oil contained in a rubber tube, and a preamplifier to provide a gain of 23 db (14x) was put in a high pressure case. The unit has been tested up to 10,000 psi. It does not have a clamp but it is only 2.25 inches in diameter and can pass easily through the normal drilling bit.

The tone break and a separate digital clock are recorded on both tape and paper on the shooting vessel. If the VHF radio link fails it is only necessary to calibrate the clocks occasionally during the experiment by recording the same event (eg a tone break) on both systems.

b). The Cambridge Three-Component Borehole Preamplifier

The Cambridge three-component borehole preamplifier consists of three preamplifier units controlled by a logic circuit which makes it possible to adjust the gain by factors of four from unity to 256 times (0-48 db). Figure 3-1-4 displays the amplifier circuit. The gain is selected by changing the negative feedback resistance across the first operational amplifier. The positive feedback loop is adjusted to eliminate DC shift in the system. (This feature was adopted from the LISPB (Lithospheric Seismic Profile of Britain) amplifiers and after the experiment, it was discovered that the performance of this loop is sensitive to the specifications of the operational amplifier (Smith, W.A.,1977). Although it did not jeopardize the experiment, the feedback loop shouldbe redesigned). The zener diodes at the output clip the signal at about $\pm$ 6.0V so that it will not overload the analog gates in the logic circuit.

Figure 3-1-5 shows the control circuit. There are six logic states: 1) DC level, which is proportional to the logic supply voltage, 2) unamplified seismic signal direct from geophones, 3) signal amplified four times (12 db) 4) signal amplified sixteen times (24 db) 5) signal amplified 64 times (36 db) and 6) signal amplified 256 times (48 db). The states are switched through in sequence by applying a step voltage between 3.5 and 10 V to the first relay. In states 1) and 2)the power to the amplifier circuits is off and very little power is consumed

The three signals are brought to the preamplifier about a common line. Each signal is generated by two Geo Space HS-1 geophones (with a natural frequency of 4.5 Hz and a coil resistance of 215Ω) in series. The geophones are damped to 50% critical damping by shunt resistances

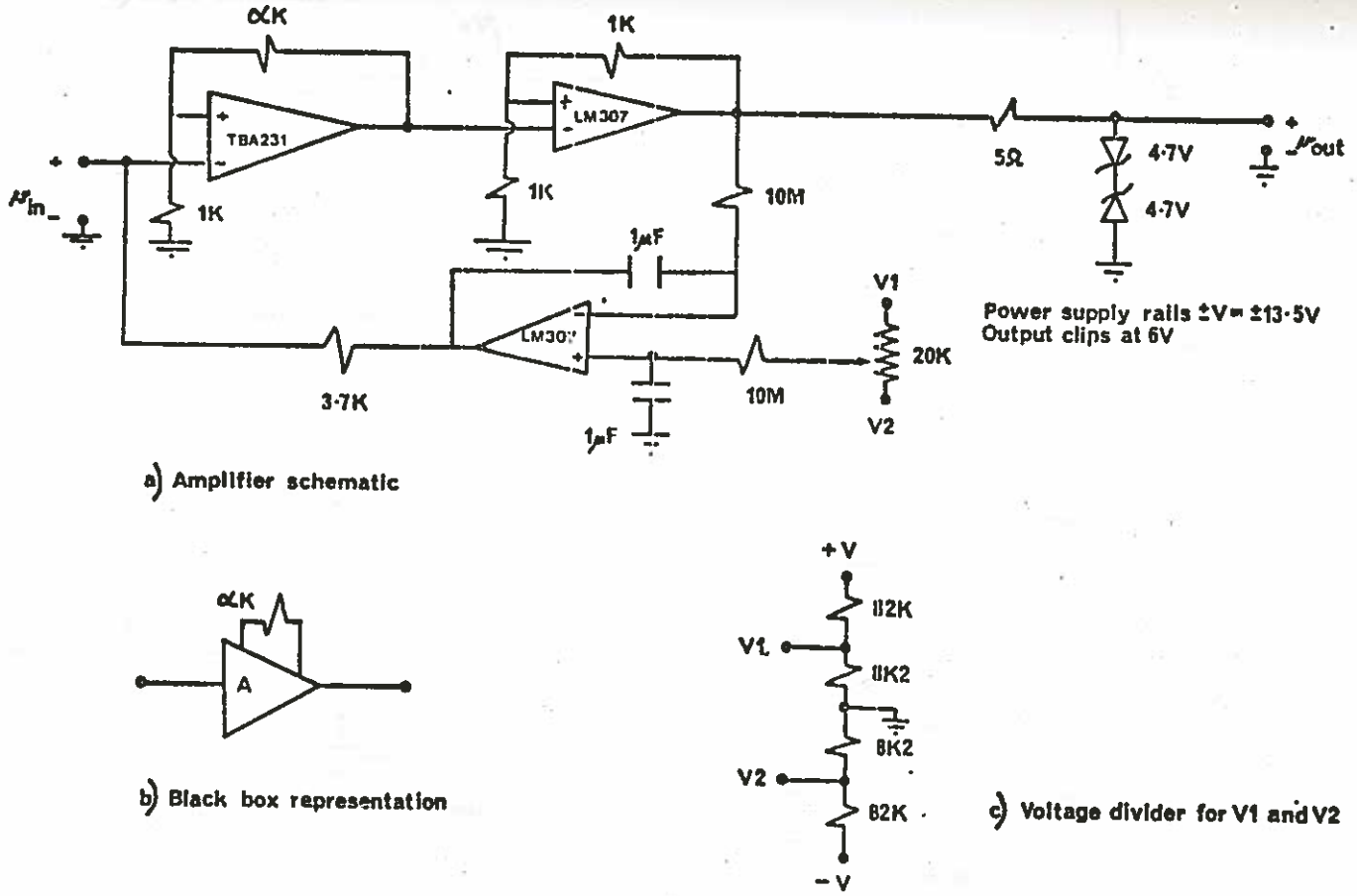

Amplifier Circuits

Figure 3-1-4. Amplifier circuits for the Cambridge Borehole Preamplifier. Diagram a) shows the basic amplifier design and diagram b) is its black box representation. Three of these units were installed and controlled by the logic circuitry (Figure 3-1-5). Diagram c) is the voltage divider for power to the feedback loop. The amplifier circuits run from ± 13.5V power rails.

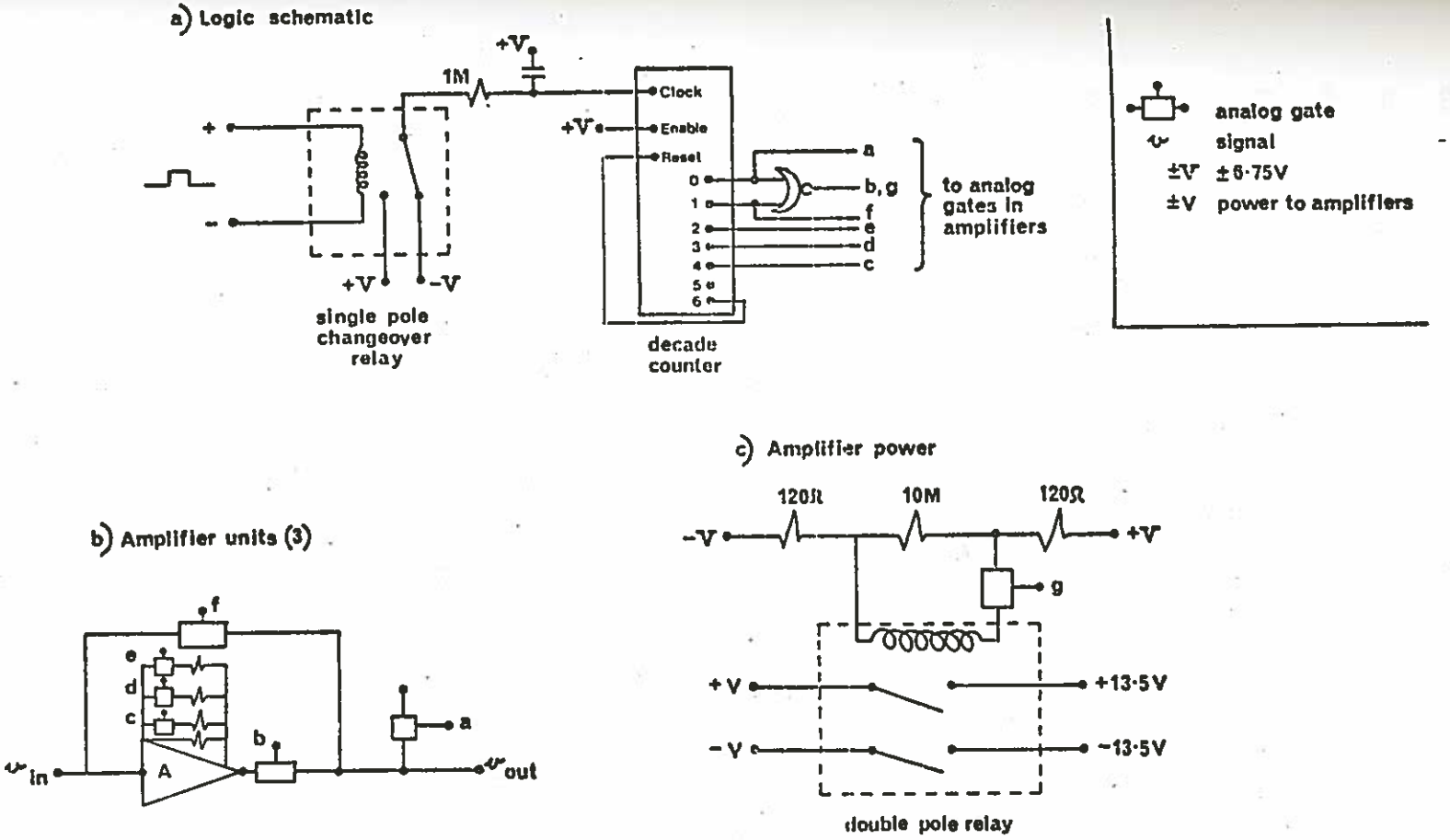

Logic Circuits

Figure 3-1-5. Logic circuits for the Cambridge Borehole Preamplifier. Diagram a) shows the circuitry which allows pulses on the line to alter the state of the amplifier. The 3 analog amplifiers are controlled by gates a through f (diagram b)). Gate g controls power to the amplifier (diagram c)). The logic circuits are supplied by ± 6.75V.

of 825Ω (Appendix B). The output impedance of the source is 350Ω and the input impedance to the preamplifier is greater than 10 KΩ for all states at frequencies up to 100 Hz. The frequency response of the preamplifier is unity to within 1 db up to 100 Hz with a phase shift of less than 0.5 msecs. Crosstalk is less than 1% up to 100 Hz.

The preamplifier was designed to drive into 24,000 feet of Schlumberger logging cable which has a resistance of 10 Ω/1000 ft and a capacitance of 0.065 μF/1000 ft, (Appendix A). Tests on a mock cable in the laboratory showed that the analog gate, in this configuration, can drive a ± 6V signal into the cable without distortion.

Of the seven conductors in the cable, two are used to supply power to the motor and four are used to bring the three seismic signals up. The seventh conductor has two functions: a) the resistance between the seventh conductor and the negative motor power lead is a measure of arm extension and b) pulses between the signal earth and seventh conductor trigger the logic in the preamplifier.

Because of the shortage of leads to the surface the preamplifier is powered by mercury batteries in the tool. There are two sets of power rails: the logic runs from ± 6.75V and the preamplifiers from ± 13.5V. The logic components are low power CMOS chips and will run for years on the batteries supplied. The amplifier circuits take a maximum of 40mA and can operate at least 25 hours before the batteries must be replaced.

It was anticipated that most of the electrical noise would be due to pick up on the cable and ship. Therefore the signals out of the preamplifier should be large. Peak-to-peak output signal of ± 6V was chosen because this was roughly the maximum signal which could be passed

through an analog gate using ± 6.75V power rails (which is the voltage specification of the mercury batteries which conveniently fit in the tool). It was necessary to power the amplifier circuits from ± 13.5V so that they could produce and drive the ± 6V signal without distortion. The maximum operating temperature of the present unit is limited to 70°C by the batteries. If high temperature batteries (maximum temperature 130°C) are used the operating temperature is limited to 105°C by the relays. In any case, the maximum reliable temperature for any instrument using integrated circuits is limited to 125°C (the temperature specification for military quality chips).

Taking reasonable estimates of heat flow over oceanic crust and conductivity of oceanic rocks of 1.5×10^{-6} cal $cm^{-2} s^{-1}$ and 5×10^{-3} cal $C^{-1} cm^{-1} s^{-1}$ (Sclater and Francheteau, 1970) gives a thermal gradient of 30°C/km, assuming no hydrothermal circulation. This represents a maximum average gradient since hydrothermal circulation does occur. Thus the tool should be capable of operation to at least two kilometres depth in oceanic crust provided that the hole is not near a recent intrusion (Hyndman, pers. comm.).

The preamplifier and four batteries were made to fit into a space 7½ inches long and 2⅛ inches in diameter, which was left after the original Geo Space amplifier and transformers were removed. Six more batteries were fastened around the electric motor (Figures 3-1-6).

3-2. CRUISES

a). Glomar Challenger Leg 46

The first attempt at the OSE was made on Glomar Challenger Leg 46 in March 1976. Leg 46 was the second of two legs scheduled to obtain deep penetration into oceanic crust. The experiment was to be

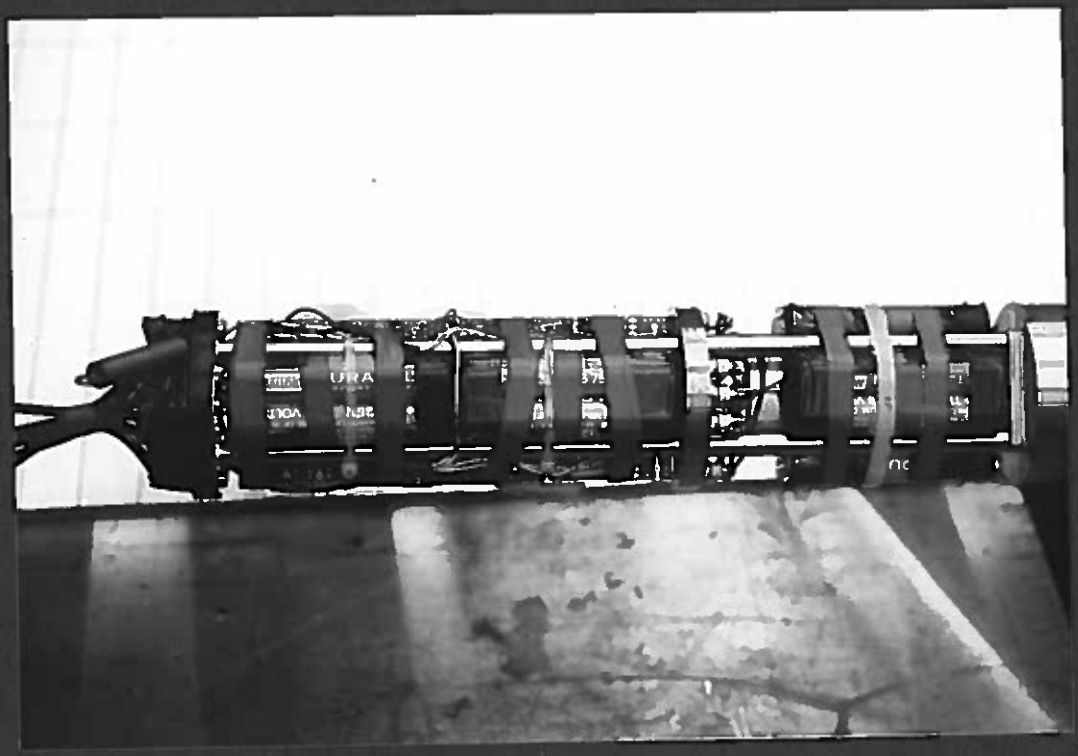

Figure 3-1-6. The Cambridge Borehole Preamplifier. The upper photo shows the preamplifier board installed in the tool before the batteries have been attached. Below is the preamplifier with ten 6.75V batteries in place, ready for the pressure case to be fitted.

carried out at Site 396, 100 miles west of the Mid-Atlantic Ridge at 20°N. Dr. D.H. Matthews was on board Glomar Challenger and I was on board the shooting ship, R/V Knorr. Chief Scientist on the Knorr was Dr. G.M. Purdy from the Woods Hole Oceanographic Institution. Unfortunately the derrick broke on the Glomar Challenger only six days before the experiment was scheduled and the Glomar Challenger sailed immediately for Las Palmas.

We learned a number of things from the cruise (Matthews, 1976). The borehole geophone (vertical component unit) had been tested in the pipe and the background noise overloaded the preamplifier. This suggested that a variable gain preamplifier would be valuable. It also led us to suspect that the noise in the hole may be high.

The Cambridge High Pressure Hydrophone was tested by lowering it into the open hole and firing a 40 cubic inch air gun at the surface. Irregularly spaced bursts of noise were recorded, which may have corresponded to the drill pipe clanging in the hole or to jerks on the cable, but no arrivals from the air gun could be detected.

After Leg 46 it was evident that the 1/16 inch clearance around the geophone (3⅛ inch outside diameter) as it passed through the modified drill bit (3 3/4 inch inside diameter) was inadequate. Subsequently DSDP redesigned the special logging bit to have a 4 inch internal diameter.

The Leg 46 trials also gave us experience in operating the geophone clamping mechanism and indicated some bugs in the recording system.

b). Glomar Challenger Leg 52

The Oblique Seismic Experiment was successfully completed on Leg 52 of the Deep Sea Drilling Project. I was in charge of the experiment and ran the operations on the drilling vessel, Glomar Challenger. Dr. K.E. Louden was chief scientist on the shooting ship. The Glomar Challenger sailed from San Juan, Puerto Rico, on January 20th, 1977 and put in to San Juan on March 9th, 1977.

The experiment was run in hole 417D, at 25°06'N and 68°02'W, just north of the Vema Gap (Figure 3-2-1). The hole was started on Leg 51 and logging was performed on that leg. Leg 52 continued drilling at 417D until the pipe broke in the hole on February 3rd. We made a number of attempts to fish the pipe out but had re-entry difficulties, and on February 9th we left Site 417 to drill at Site 418 which was roughly 3 miles south. At this stage statistics for Site 417D were as follows (all depths are below rig floor):

Water depth 5489 m

Casing shoe 5515 m

Basement depth 5832 m

Max. Leg 51 penetration 6021 m

Max. Leg 52 penetration 6197 m

Depth to top of broken pipe 6092 m

Sonic log run from 5626 m - 5928 m

A test of the OSE gear was run on February 22nd while pulling in the pipe for a bit change at Hole 418. The geophone was lowered to 3 km inside the drill pipe and clamped. The shallow hydrophone was put over the fantail to a depth of 330 m and we fired the 120 cubic inch air gun. There were 3400 m of pipe and 220 m of bottom hole assembly out at the time. The VHF radio was tested by communicating with the bridge. All the equipment worked well except the amplifier unit in the geophone. Even without amplification the background noise on the geophone was large and no arrivals corresponding to

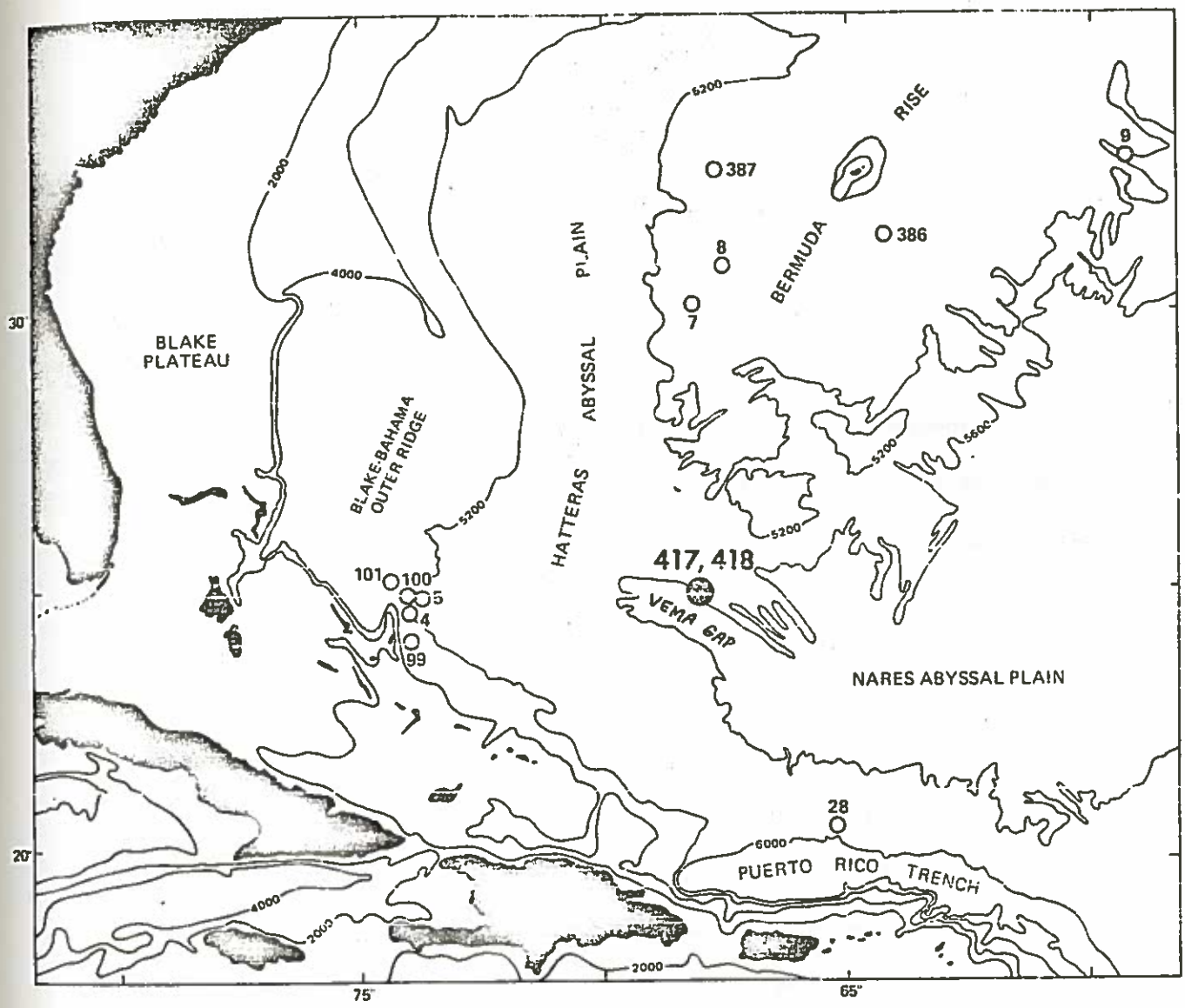

Figure 3-2-1. Location of DSDP Sites 417 and 418. (Courtesy of Deep Sea Drilling Project.)

the air gun could be detected. Total time for the test, including running the tool in and pulling out, was 5 hours. The test was valuable because it familiarized people with the operation.

With the tool back on board it was discovered that the amplifier failure was due to a broken ceramic soldering pin which had shorted the minus power supply rail. This was repaired and all bare joints were then well insulated with tape.

We returned to Site 417 at about noon on March 2nd. The Virginia Key, the shooting vessel from the National Oceanographic and Atmospheric Administration labs in Miami, joined us as we came on site. It had left Miami at 0400 on February 27th. Dr. K. Louden ran the laboratory on the Virginia Key and Mr. A. Claydon was shot firer.

We had difficulty re-entering with the special logging bit and at 2200 on March 3rd we decided to try re-entry with an ordinary bit which we could drop in the hole. Successful re-entry was made at 0730 on March 5th. The hole was cleared to 6078m, the bit was dropped, the hole filled with mud, and then the drill string pulled to 5825m, just above the basement/sediment interface. Shortly after 2000 on March 5th we started running the tool in. An amplifier and head phones had been wired up to the geophone channels so that I could listen to the tool as it descended. While running in, the shallow hydrophone was put over the side. A bad cut was discovered in the cable and this was repaired. At 2330 the tool was at 6060m and I extended the clamp. The caliper mechanism which tells how far the arm has extended, was not working properly, but the tool was clamping and unclamping satisfactorily.

At 2400 the geophone channels were plugged into the recording gear which was located in the palaeo-laboratory. The same signals were

appearing on all channels at all borehole amplifier gains and at first this was interpreted as failure of the amplifiers. There was also about 200mV DC shift on all channels which was unexplained and could not be eliminated using the feed-back loops in the amplifier box. At 0100 on March 6 Virginia Key fired some test shots with the geophone in the no gain condition and no arrivals were seen on the geophone or hydrophone. The geophone was unclamped and pulled up and down in the hole to check the individual channels. I concluded that the geophone was operating properly and that the seismic noise in the hole was too low to be detected at a gain of x256 (48 db) on an oscilloscope at the 100 mV/cm scale. The noise originally observed must have been electrical pick-up in the cable because it was independent of the pre-amplifier gain. The hydrophone cable was repaired a second time and more test shots were fired. By 0630 the system was working well except for the 200 mV DC shift which was acceptable.

The Virginia Key took up position at 12 km NNE of the Glomar Challenger and we started firing the pattern shown in Figure 2-3-1 at 0700. All charges were 20 lbs of Tovex Extra. Fuses were cut to burn for 60 secs which gave a shot depth of about 50 m. Virginia Key was steaming at 5 knots. Charges were fired every 3 minutes on the orthogonal lines and every 10 minutes on the arcs. The gain of the geophone preamplifier was constant at 48 db. Attenuations of ½, ¼, and ⅛ (-6,-12 and -18 db) were applied to the signals in the laboratory to ensure that the signals going to the tape recorder were less than 1 V peak-to-peak. The weather was clear and calm. The pattern was completed at 1600.

Since the hole was only open 230 m into the basalt it was decided that only one full pattern should be run with the geophone at that depth. The geophone was then pulled to 5840 m (just below the

basalt/sediment contact) and a single line was shot from 12 km SSW of Glomar Challenger to 12 km NNE. Shooting terminated at 1900 hours with 165 shots. Altogether we fired 3600 lbs of Tovex Extra. The Virginia Key came alongside Glomar Challenger to refuel before heading back to Miami (it reached Miami by 0800 March 10).

The tool was back on deck shortly after 2000 on March 6th. The arm was seen to be extended about 2 inches. (Total time for the OSE was 24 hours).

Tests on deck, with the tool attached to the cable showed that the whole system was working well. The electrical noise and DC shift were associated with the cable when it was strung out. The DC shift may have affected the caliper circuit so that it gave false readings.

The signal-to-noise ratio of the records is generally good. The electrical noise, which is the same on all channels, is erratic. Occasionally it coincides with an arrival. Signals were recorded on both tape and paper. Examples of raw records made during the shooting are shown in Figures 3-2-2 and 3-2-3. These figures show that for long range shots the maximum signal is on one horizontal component and that the geophone appears to be oriented to the shooting pattern.

A more detailed account of the Leg 52 operation is given by Stephen et al (1977).

Figure 3-2-4 shows the Glomar Challenger laboratory set-up and Figure 3-2-5 shows the geophone on board Glomar Challenger. Photographs of the D/V Glomar Challenger and the Virginia Key are shown in the Frontispiece and Figure 3-2-6 respectively.

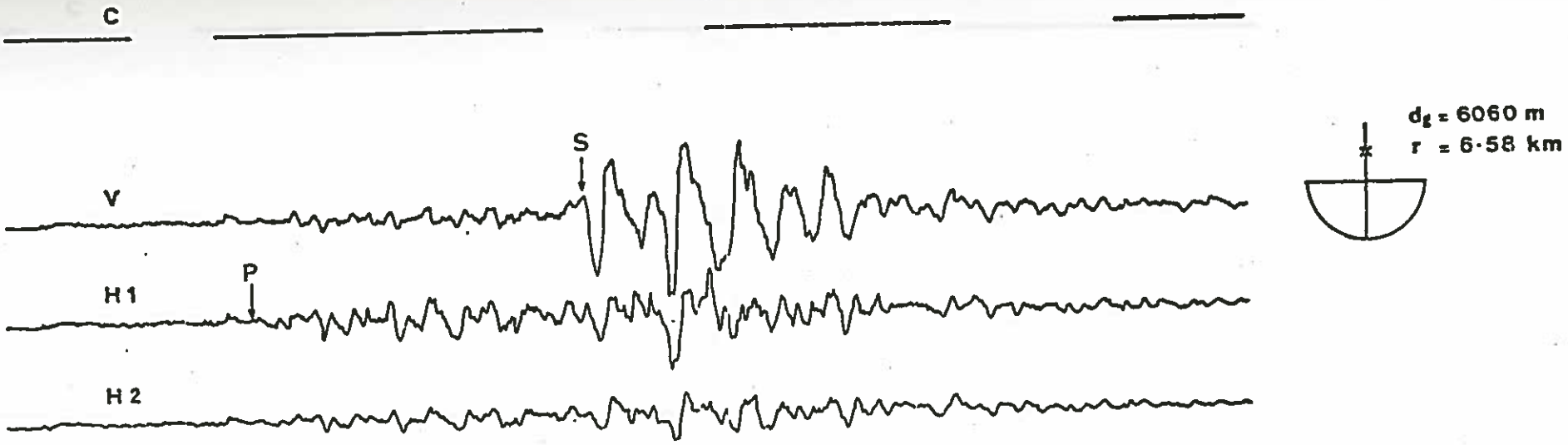

Figure 3-2-2. Typical record for north-south line. Clock channel (c), vertical component signal (V) and the two horizontal component signals (H1 and H2) are shown as they were recorded on board Glomar Challenger. The distance between right hand ends of lines on the clock channel is 1 second. The strongest P-wave signal is arriving on the H1 component which implies that the axis of this geophone is aligned approximately N-S. The angle of incidence of the arrivals is large, confirming that at long ranges the direct arrivals are travelling almost horizontally.

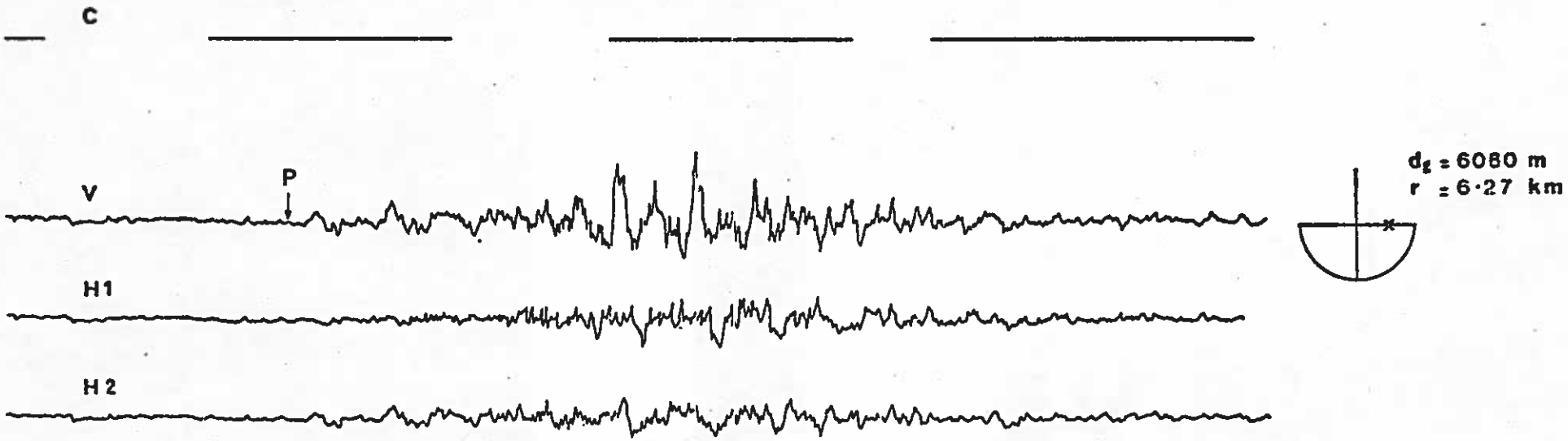

Figure 3-2-3. As Figure 3-2-2 but for a shot on the E-W line. The strongest horizontal signal is H2, confirming that the tool is almost oriented with the shooting pattern.

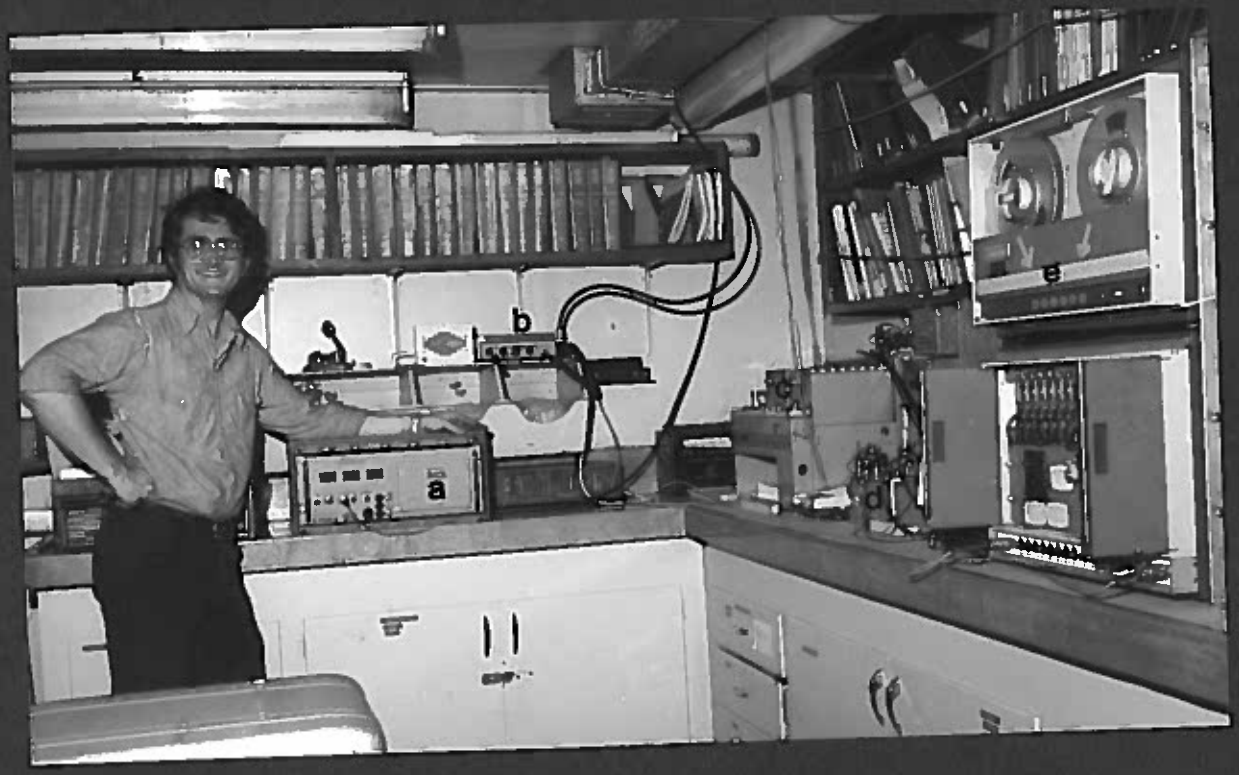

Figure 3-2-4. OSE laboratory on Glomar Challenger. The OSE laboratory equipment is set up in the palaeontology lab of the Glomar Challenger: a) digital clock, b) VHF radio receiver and transmitter, c) Oscillomink paper recorder, d) amplifier and switch boxes and e) seven channel tape recorder. The oscilloscope is behind the tape recorder.

Figure 3-2-5. The Cambridge Borehole Geophone in the hold of Glomar Challenger with arm extended.

Figure 3-2-6. The Virginia Key at Site 417.

CHAPTER 4

DATA ANALYSIS

4-1. DATA REDUCTION

a). Digitization

The data of the March, 1977 Oblique Seismic Experiment were digitized to facilitate plotting and to manipulate amplitudes for the improvement of the signal-to-noise ratio, which, for the first P-wave arrival at long ranges, is about two or less.

The majority of the noise was caused by electrical switching on the ship and is the same on all three downhole channels (Figure 4-1-1). Since the P-wave is stronger on some channels than others, the signal-to-noise ratio can be improved by subtracting channels to eliminate the coherent noise. This procedure is very straightforward with digital data.

True amplitude record sections are conveniently produced from digitized data. Once digitized the data can be amplitude weighted, filtered with zero phase shift filters and plotted on the computer at any convenient scale. For large quantities of data the savings in time can be considerable.

There were six channels of data: clock, hydrophone, 3 geophone channels and the tone break. The 500 Hz tone was rectified and all channels were low pass filtered at 100 Hz to prevent aliasing before digitizing at a sample interval of 3.91 msec (256 samples per second).

The datawere then edited using a program sequence written by A.W. Bunch and W.A. Smith (Bunch, 1977). The digital clock signal was 'read' automatically allowing one to select just the time interval corresponding to the data of interest at each shot. The tone break was

picked from the original paper records to within $\pm$ 0.002 secs. A second program i) despiked the records (spikes were produced randomly by the digitizer), ii) corrected records for drop-out (caused by overloading), iii) corrected records for fluctuations in sampling rate, iv) corrected records for amplitude changes made during recording, v) applied flight time corrections, vi) filtered records and vii) plotted the data as reduced, weighted amplitude record sections (Appendix C).

Figure 4-1-1 demonstrates the effect on the signal-to-noise ratio of subtracting a channel with little signal from a channel with a large signal for a long range shot. The difference seismograms for the deep geophone position, are useful for picking first arrival times because the first P-wave energy is generally small on one horizontal component (Figure 4-1-2).

b). Flight Time Corrections

The greatest limitation in reducing explosive shot data is the flight time correction. The flight time enters into the calculation of ranges, travel times, and shot depths. The tone break occurs when the sound of the charge reaches the hull geophone but the shot time is obviously some time before this.

There are two methods of computing the flight time correction. The first method (Method A) assumes that the sound travels from the shot to the stern of the ship at the velocity of sound in water and then travels along the hull of the ship to the hull geophone (Section 3-1a)) at the velocity of sound in steel. An alternate method (Method B) assumes that sound travels directly to the hull geophone position through the water. The method which should be used is the one which gives the shortest time between the shot and the hull geophone. In this experiment

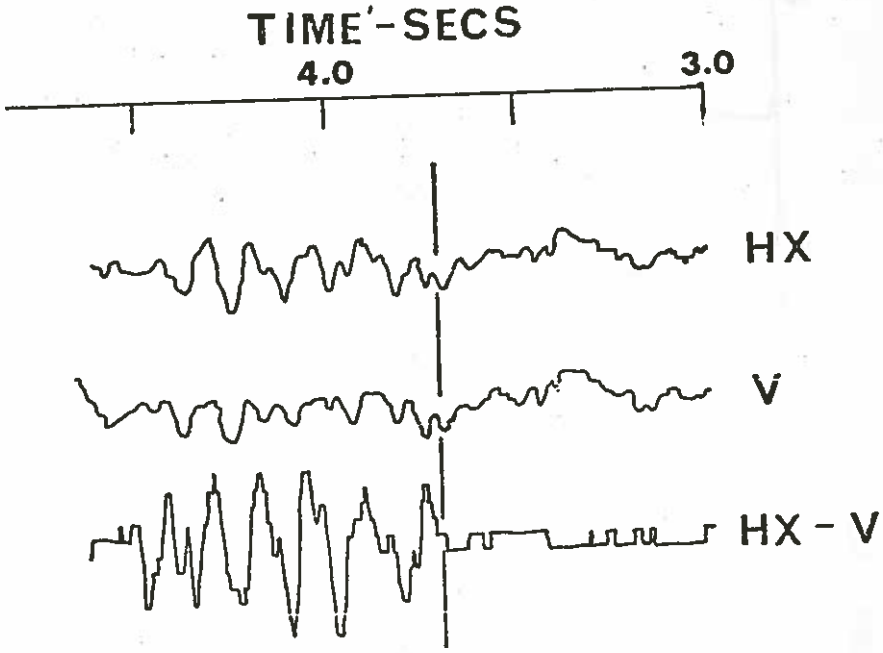

Figure 4-1-1. Elimination of noise on downhole channels. Most of the noise on the geophone records is pick-up from motors on the Glomar Challenger and is the same on all channels. In this case HX has stronger signal than V and the difference, HX-V, is almost pure signal. The steps to the right of the vertical time marker on the difference channel are the height of a single discrete amplitude step. The HX and V channels are shown at a different amplification than the HX-V channel.

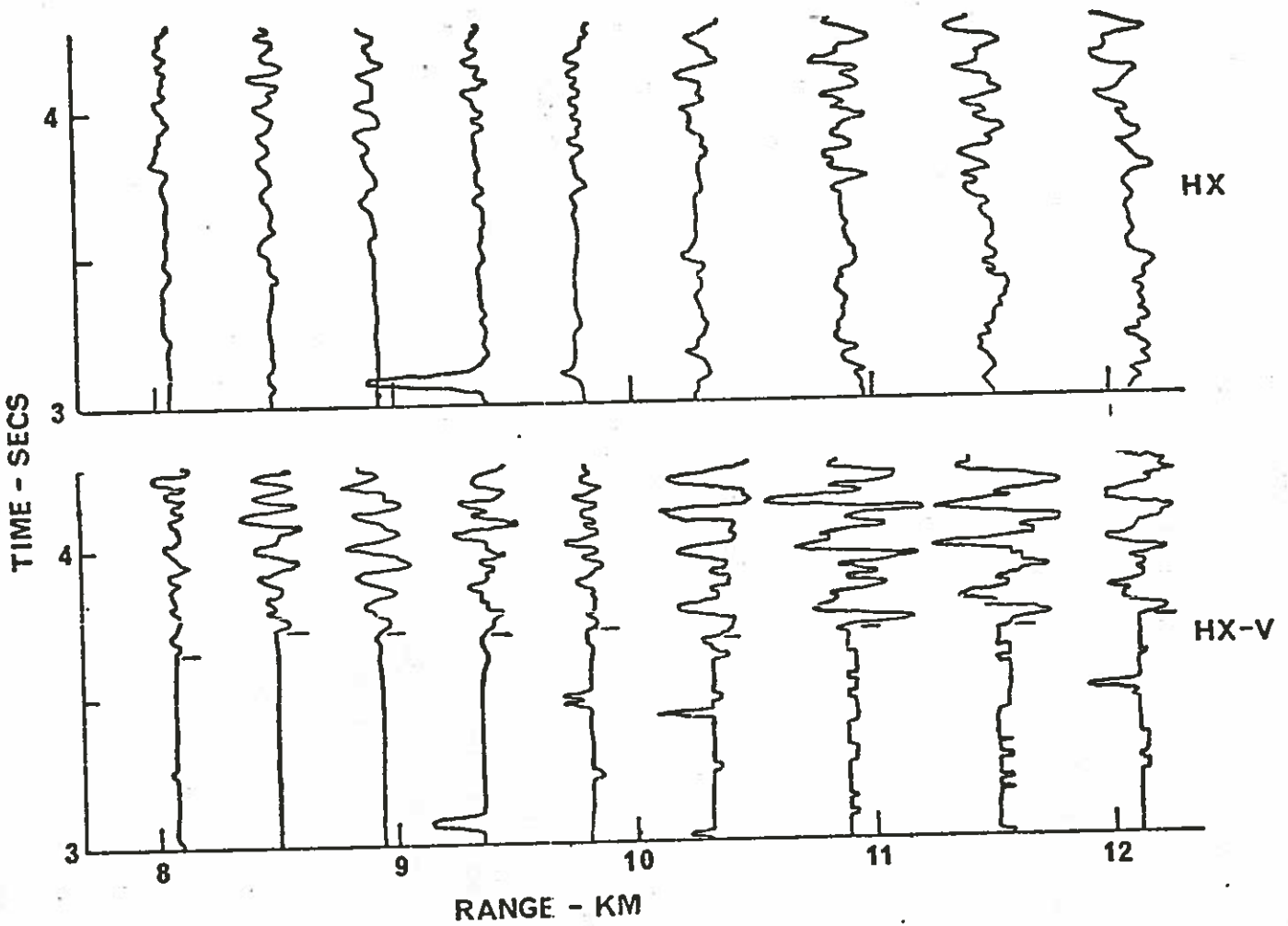

Figure 4-1-2: Difference seismogram at long ranges (HX-V) compared to unmodified seismogram (HX) for the north line and deep geophone position. It is generally easier to pick first P arrival times on the difference seismogram although amplitudes will be distorted. The HX section is weighted by $(\text{Range}/7.0)^{2.9}$ but the amplitudes on the HX-V section are not significant.

the minimum horizontal distance between the shot and the Virginia Key was 131 m and the maximum depth was 61 m. (These values were calculated from data which will be discussed below.) The hull geophone was about 15 m from the deployment point of the charge on the Virginia Key. For this geometry, which represents the worst case, the travel time for Method A is more than 6 msec less than the travel time for Method B. For the other possible combinations of depth and horizontal distance the difference in times between the two cases would be greater. Certainly in this experiment Method A is more correct than Method B.

The flight time correction (Δt_f) is:

$$\Delta t_f = \frac{t_f}{V_w}\left(\nu_c^2 + \nu_s^2\right)^{1/2} + \frac{\ell}{V_{st}}$$

where V_w is the velocity of sound in water, V_{st} is the velocity of sound in steel, ν_c is the sink rate of the charge, ν_s is the shooting ship's speed, t_f is the flight time and ℓ is the distance on the ship between the hull geophone and where the charge is thrown over the side. In the following paragraphs each of these factors will be discussed and an estimate made of the error in the flight time correction. All error estimates are considered reasonable maximum errors.

The average velocity of water in the top 50 m of the ocean for the location of Site 417 in the months February, March and April is 1534 m/sec (Marine Information and Advisory Service, 1977). All of the recorded readings for the 6 published stations fall within $\pm$2 m/sec of this value.

The sink rate of the explosive charge (20 lbs of Tovex) is 0.79 $\pm$ 0.15 m/sec (Stetson & Koelsch, 1974).

Since the Virginia Key did not have a velocity log, the ship's speed relative to the Glomar Challenger (fixed relative to the sea bed)

has been obtained from the time and range (uncorrected for flight time) between near and far shots on the same line. (There is no reason to suspect that the velocities of different lines should be the same since the Virginia Key changed speed for manoeuvring.) The velocity required for the correction however is the velocity of the Virginia Key in the water and is different from the calculated value by the velocity of the current around the ship (Whitmarsh, pers. comm.). Unfortunately no measure of the current during the experiment was made. Site 417D is east of the Gulf Stream and currents in the area are not strong in one particular direction. Indeed the strength and direction of the current did change significantly within a few hours (Captain Clarke, pers. comm.). The magnitude of the prevailing current in the region of Site 417 is less than 0.1 m/sec and the preferred direction is towards the northwest (Figure 158 in Defant,1961).

A feel for the effect of current during the experiment can be obtained by looking at the velocity of the Virginia Key relative to the Glomar Challenger between successive shots. If we assume that the Glomar Challenger was fixed relative to the sea bed and that the Virginia Key was making a constant speed through the water for each line (both wind and swell were calm during the experiment) then fluctuations in their relative velocity would be caused by fluctuations in the current. The ranges for this study have been computed as described in Section 4-1d) with flight time corrections made from the "line" velocity discussed in the previous paragraph. The means and standard deviations of the velocities between successive shots for the six lines (north, south, east and west for the deep geophone position and north and south for the shallow geophone position) are 2.49 $\pm$ 0.07 m/sec, 2.46 $\pm$ 0.12 m/sec, 2.89 $\pm$ 0.10 m/sec, 2.71 $\pm$ 0.10 m/sec,

2.73 ± 0.06 m/sec and 2.71 ± 0.06 m/sec. The effect of currents which change within a few minutes or a few hundred metres is likely to be on the order of the standard deviations (i.e. about 0.12 m/sec). It would seem reasonable that the speed of the Virginia Key through the water was within 0.22 m/sec (0.12 m/sec plus 0.10 m/sec for the contribution of a possible large scale steady current) of the velocity relative to the Glomar Challenger. The 0.12 m/sec estimate may be low because it is a standard deviation of measurements but the additional 0.10 m/sec estimate is likely to be high since only the component of this current along a line should be considered.

The Virginia Key slowed down for manoeuvring around the Glomar Challenger and flight time corrections for very near (< 0.75 km) shots are uncertain. The Virginia Key's speed on the arcs has been taken as the average speed of the two adjacent lines and is unreliable.

The flight time was measured on a stop watch by the laboratory scientist. The time when the charge was to go over the side was indicated by an audio tone which could be heard by both the shot firer and the laboratory scientist. The time when the shot went off was of course heard by the laboratory scientist. An error of ± 1.0 sec has been chosen to allow for fluctuations in the response of both the shot firer and the laboratory scientist. The travel time of the sound between the shot and the ship is on the order of 0.1 sec and is insignificant. Typical values of the flight time are around 60 secs.

The longitudinal distance between the hull geophone and the deployment point of the charge should be included in the flight time correction (Whitmarsh, pers. comm.). In the Leg 52 OSE experiment this distance is 15 ± 2 m since the explosives were dropped over the stern of the ship and the geophone was clamped near the bow to reduce

interference from engine noise. It is not unreasonable that when the sound hits the stern of the ship it continues along the hull at the speed of sound in steel (5917 ± 43 m/sec, Kaye & Laby, 1975). The term ℓ/V_{st} has a typical magnitude of 2.54 msec.

A typical flight time correction based on the values mentioned above is 0.111 ± 0.012 sec.

c). Depth of Shot

The mean shot depth has been obtained by taking the mean sink rate of the explosive (Stetson and Koelsch, 1974) and multiplying by the mean flight time. A typical value for the shot depth is 47.4 ± 9.9 m. The minimum and maximum values for the shot depth corresponding to extreme flight time values are 35.8 m and 60.6 m respectively.

d). Ranges

A range vs shot-to-hydrophone - travel-time plot was computed by the ray tracing technique for an oceanic velocity gradient typical of the area and the time of year (Marine Information and Advisory Service, 1977). Shot ranges were picked from this using the flight time corrected travel times. The hydrophone depth was 0.302 km and it was assumed that the shots went off at 46.0 m depth. Radar ranges were logged during the experiment but were not as consistent as ranges from travel times.

The error introduced by assuming that the shot depth was constant was less than ± 5 m for a shot at 750 m range and was less than ± 2 m for a shot at 2 km range. This error decreases with increasing range. The error in ranges, caused by the flight time correction (± 0.012 sec), picking error of the hydrophone arrivals (± 0.002 sec), and picking error

of the tone break (± 0.002 sec), is ± 24 m.

Figure 4-1-3 shows the positions of the shots relative to the Glomar Challenger. Azimuths were recorded during the experiment.

e). Hydrophone Location

During the experiment the hydrophone was suspended from a crane off the port side of the Glomar Challenger just forward of the derrick. Because of the calm seas, its position relative to the Glomar Challenger did not vary by more than ± 2m during the experiment. The necessary correction for hydrophone offset is +16m for the north line, -16m for the south line and no corrections for the east and west lines. Since the range corrections are small and constant for each line they have not been applied.

Although the drift of the Glomar Challenger relative to the beacon was monitored during the experiment no correction has been made for this either. Readings were taken every five minutes but did not change smoothly. There may have been a problem with the positioning computer.

f). Record Sections

A complete set of record sections from the OSE is given in Appendix C. All the records, including the synthetic seismograms used for interpretation, have the same amplitude weighting. That is, up to 7.0 km no weighting has been performed and over 7.0 km the amplitudes have been multiplied by $(R/7.0)^{2.9}$. (This relationship was determined empirically to produce record sections of satisfactory appearance.) Direct comparison of amplitudes can be made between sections. Traces on the hydrophone records are normalized individually. (The maximum

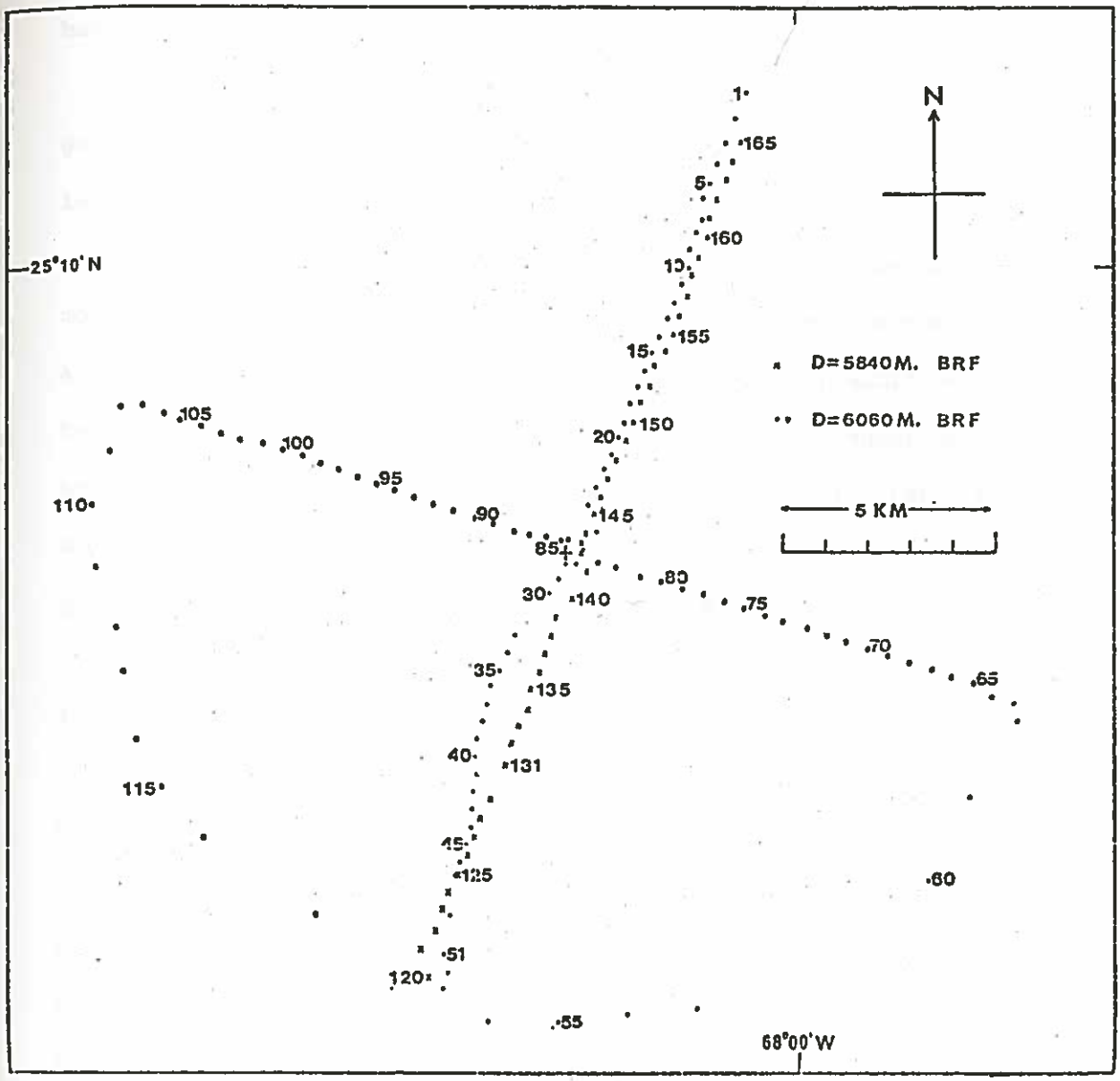

Figure 4-1-3. Shot locations relative to the Glomar Challenger (+). Ranges were computed from the direct water wave travel time and bearings were monitored from the Glomar Challenger during the experiment. The lines referred to in the text and in Appendix C are defined as follows:

North (6060m)	shots 1-24
South (6060m)	shots 29-53
East (6060m)	shots 64-84
West (6060m)	shots 87-108
North (5840m)	shots 144-165
South (5840m)	shots 120-141
South-East azimuths	shots 53-63
South-West azimuths	shots 108-119

amplitudes of the traces are the same height.) No terrain corrections have been made on the sections.

The signal-to-noise ratio of the geophone records is generally good up to 10.0 km. At ranges greater than 10.0 km the first arrival is sometimes obscured by noise.

The long range P-wave arrivals are stronger on the horizontal components than on the vertical component as would be expected for a compressional wave at large angles of incidence. In addition, the two horizontal components were almost aligned with the shooting pattern and the strongest P-wave arrivals occur on horizontal X for the north and south lines and on horizontal Y for the east and west lines These components have been used for the travel time study.

g). Bathymetry and Basement Topography

As will be shown in Section 4-2c) and Figure 4-2-4 basement topography can effect travel times considerably. Because of the high contrast between sediment and basement velocities (approximately 1.6 km/sec compared to 5.0 km/sec) basement topography effects travel time more than sea-bottom topography (bathymetry). A typical value for the effect of basement topography on P-wave arrival times is about 0.085 secs for a change in topography of 200 m (Figure 4-2-4) compared with a value of 0.02 secs for the corresponding bathymetric correction. For S-wave arrival times the effect is less, typically 0.055 secs for a 200 m change in basement topography.

In this study I differentiate between regional topography and small scale topography. Regional topography is an estimate of the basement depth from reflection profiling records (Figures 4-1-5a to 4-1-5c). However as discussed in Section 4-2c) there are small scale

topographic features which effect the travel times but cannot be resolved on the profiling records. The remainder of this section is a discussion of the regional topography.

Regrettably the Virginia Key did not have operating bathymetry or seismic profiling gear so that bathymetry and basement topography underneath the lines could not be obtained. In addition, the hydrophone records from the Glomar Challenger are not suitable for determining basement arrivals. The hydrophone depth (302 m) is about the same as the sediment thickness (330 m) and the sea surface reflection of the sea bed arrival coincides with the first basement arrival. The interference makes picking accurate travel times impossible. Thus basement topography was not determined during the experiment.

Seismic profiling had been performed in the area earlier by the Glomar Challenger and the USNS Lynch (The Lynch data was courtesy of H. Hoskins and R.C. Groman). These lines were used for the bathymetry and basement topography corrections. Figure 4-1-4 shows their positions relative to the OSE lines and Figures 4-1-5a to 4-1-5c show the actual profiling records with the estimated basement surface indicated. For the purpose of the terrain correction, the sea bottom and basement surfaces were approximated by straight line segments and the layer 3 surface was assumed to be a constant vertical distance from the basement surface (Figure 4-1-6a).

The terrain correction for the layer 3 refractor was calculated as follows. The velocities for water, sediment, layer 2 and layer 3 were assumed to be 1.5 km/sec, 1.8 km/sec, 5.0 km/sec and 6.8 km/sec respectively. For each line the effect of the deviation from flat, level surfaces was calculated for the water-sediment, sediment-layer 2

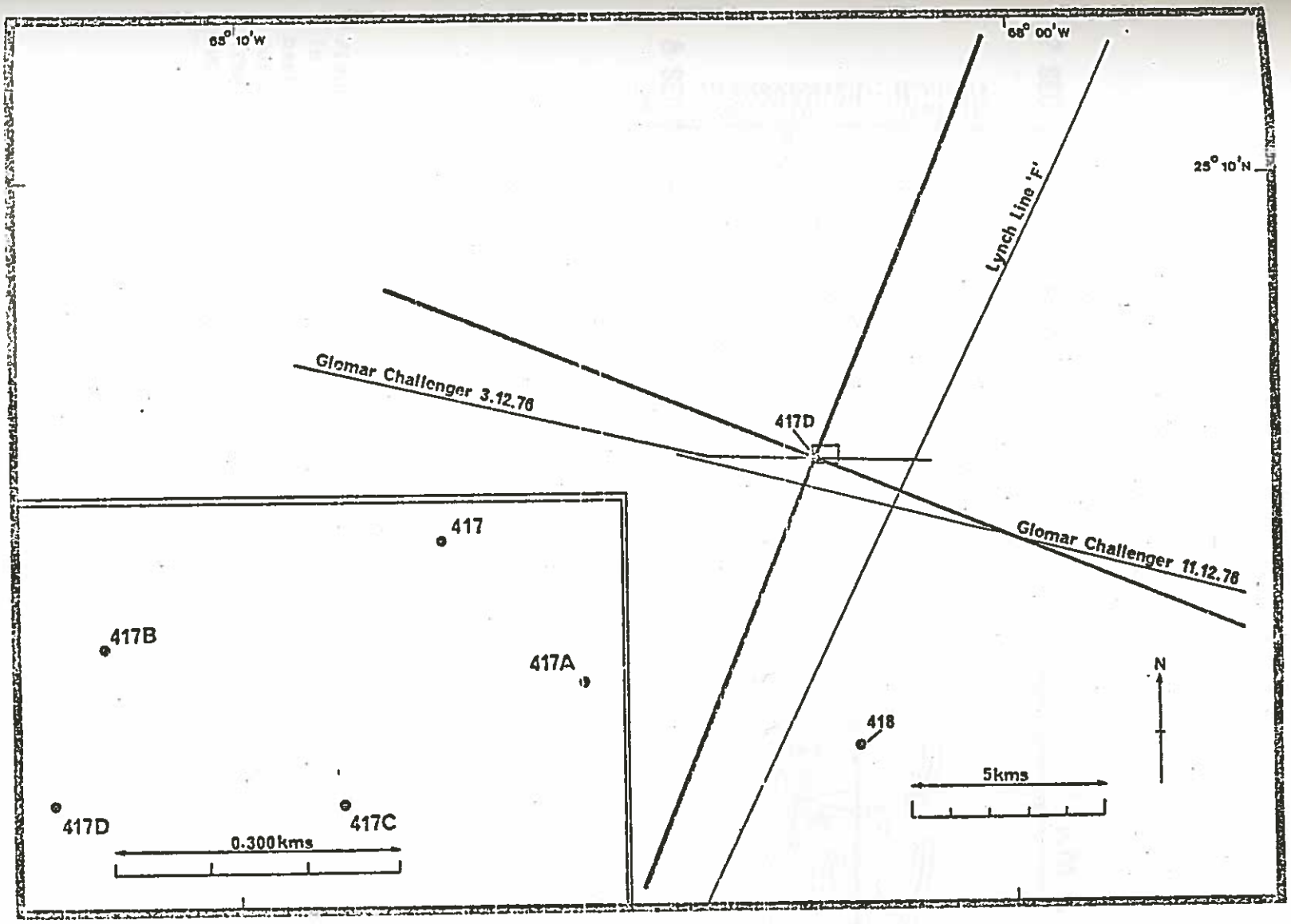

Figure 4-1-4: The locations of the Lynch and Glomar Challenger profiles relative to the OSE lines. The inset shows the locations of the holes drilled at Site 417. Hole 417A reached basement at 5689m BRF compared to 5832m BRF for hole 417D.

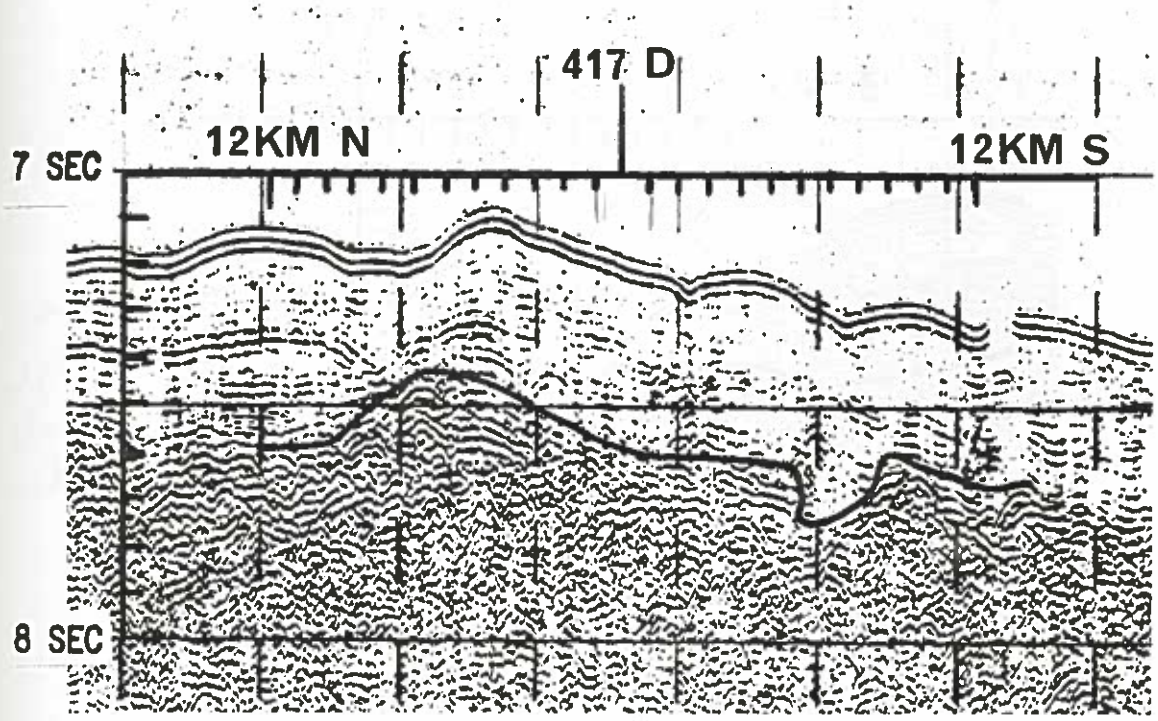

Figure 4-1-5a

Figure 4-1-5a-c. Sections of the Lynch and Glomar Challenger profiles used in the interpretation of the OSE data. The estimated location of the basement topography is shown by the thick black line. The strong mid-sediment reflector is evident about half way between basement and the sea bed. (The Lynch profile (Figure 4-1-5a), courtesy of H. Hoskins and R.C. Groman, WHOI).

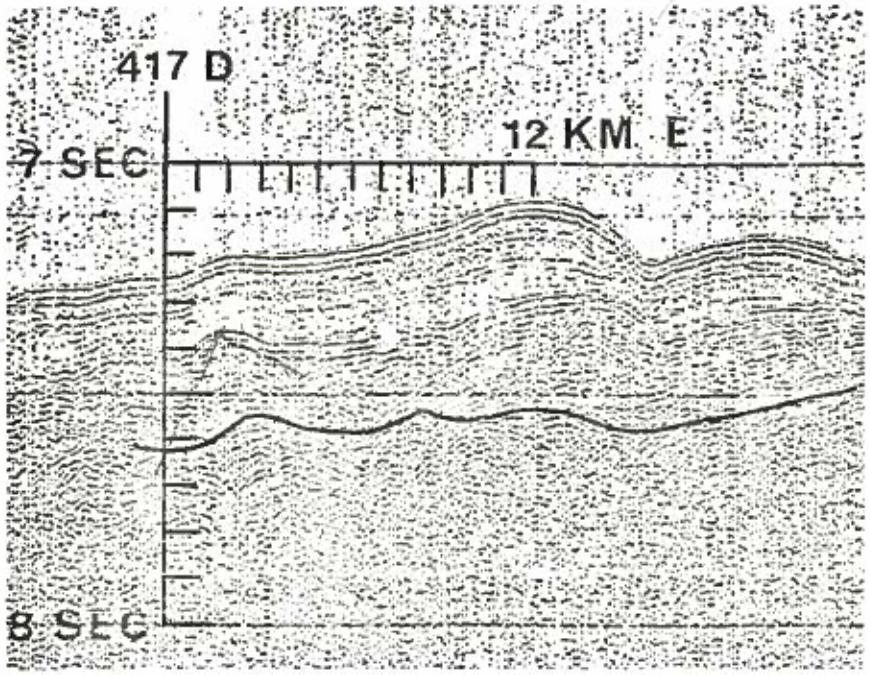

basement high drilled at 417-D

Figure 4-1-5b

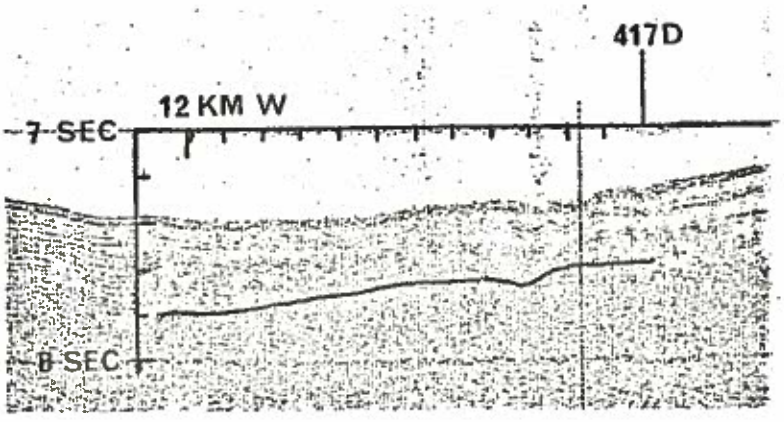

Figure 4-1-5c

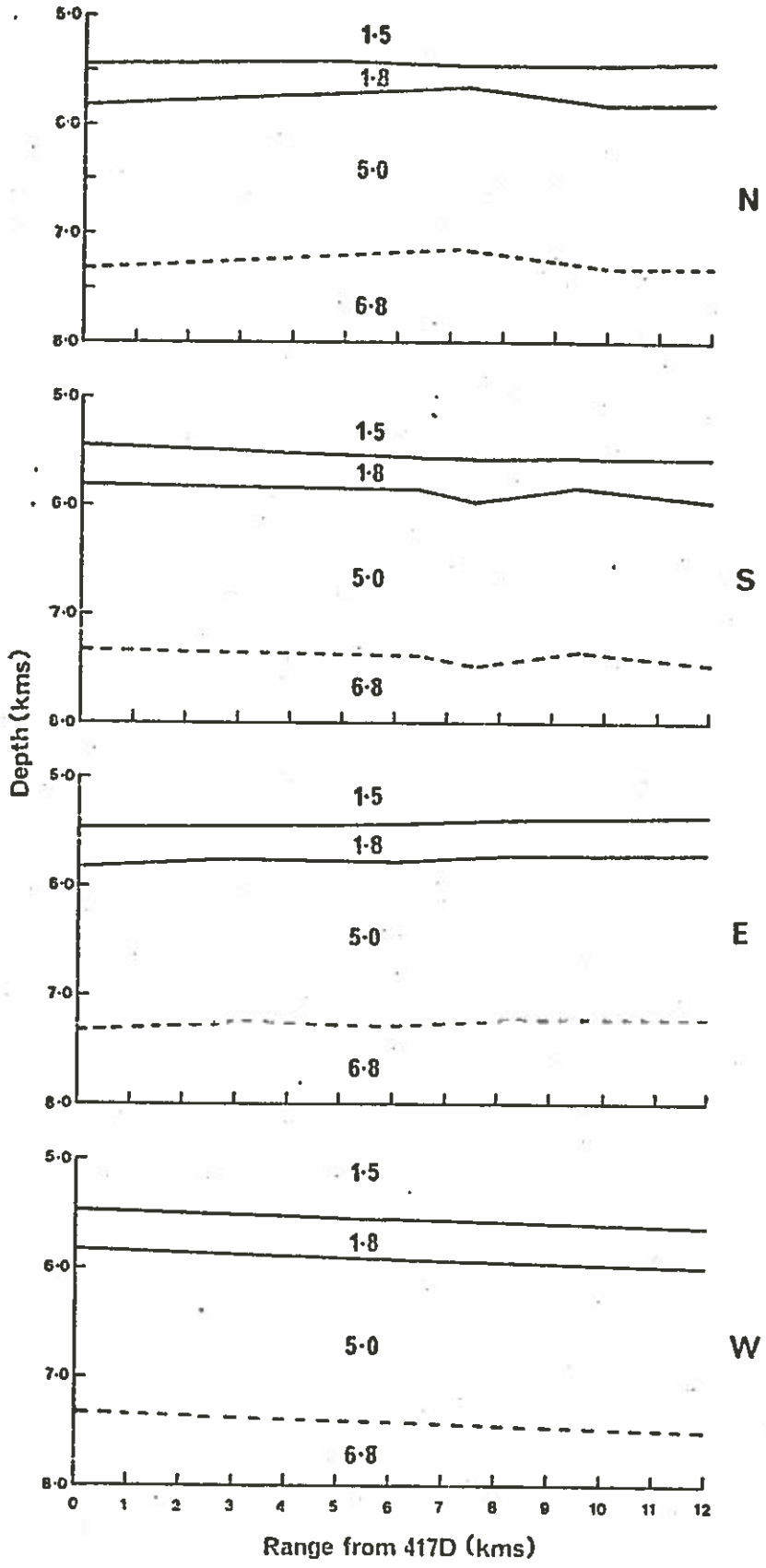

Figure 4-1-6a

Figure 4-1-6a&b. Terrain correction summary. Figure a) shows the straight line approximations made to the bathymetry and basement topography in Figure 4-1-5. The inferred velocities in (km/sec) and the inferred layer 2 - layer 3 boundary are included. Figure b) summarizes the terrain correction. The deviation from flat topography in the sections has been calculated for each interface: water-sediment (—— – ——), sediment-layer 2 (----) and layer 2-layer 3 (——·——) in the inferred models. The curves are then shifted sideways to allow for horizontal offset for a layer 3 refraction and summed

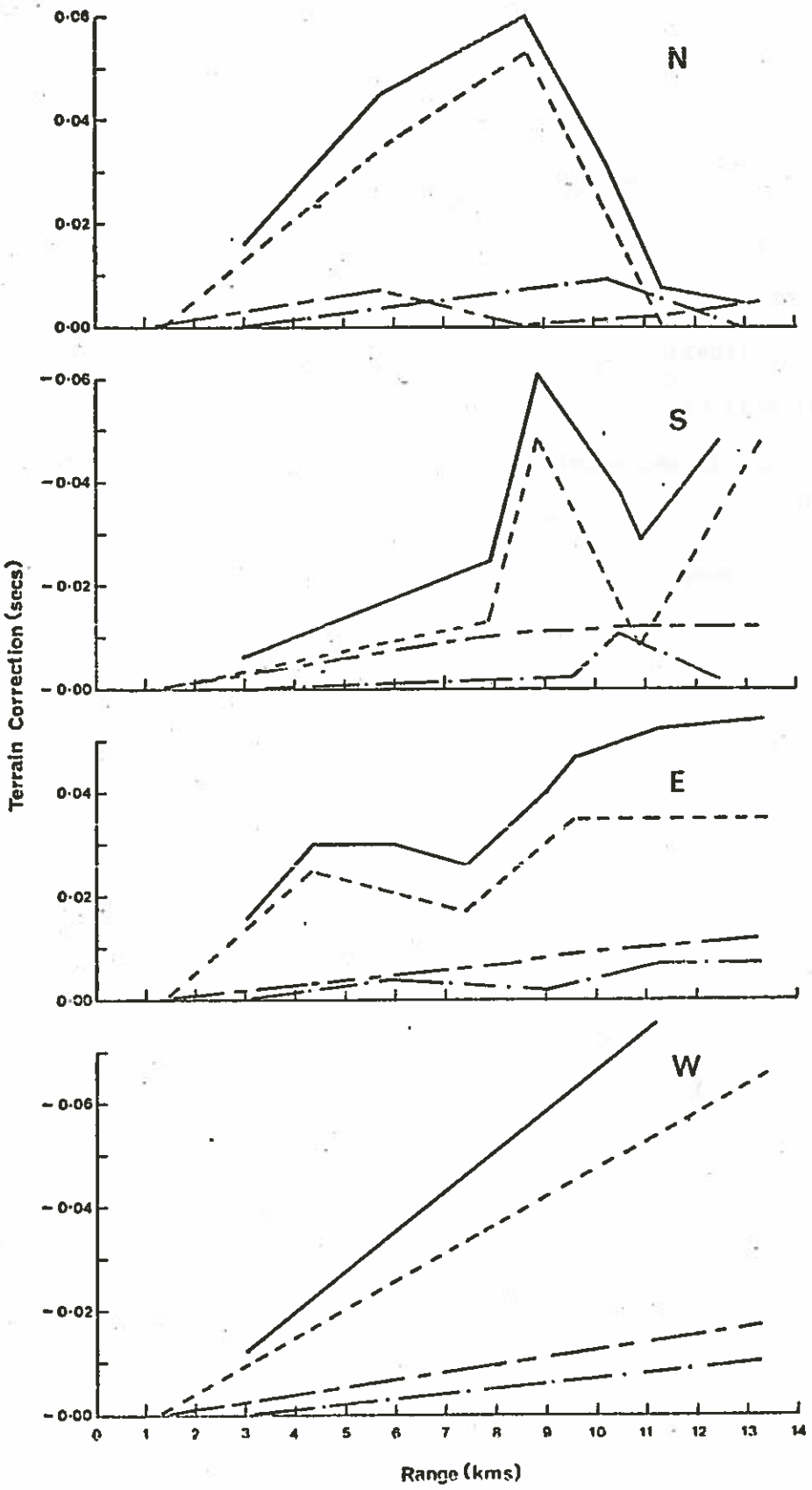
N
S
E
W
0·06
0·04
0·02
0·00
-0·06
-0·04
-0·02
-0·00
Terrain Correction (secs)
0 1 2 3 4 5 6 7 8 9 10 11 12 13 14
Range (kms)

Figure 4-1-6b

and layer 2-layer 3 interfaces (Figure 4-1-6b). Angles in each layer corresponded to the critical angle for a refraction along a level layer 3. The curves which give the effect on travel times were then shifted in range to allow for the fact that rays were not at normal incidence. For example, the ray which leaves the surface at a range of 8.0 km reaches the sea bed at a range of 6.8 km and it is the depth of the sea bed at 6.8 km which should be used in the correction. The effects of the three interfaces are then summed (the solid line in Figure 4-1-6b). This method is equivalent to simple ray tracing. The correction for shear waves was made in the same manner.

The terrain correction for the direct P-wave and S-wave arrivals was made directly in the computation of travel times using the program of Červený & Pšenčik (PDR2, Section 2-1a)). The terrain models of Figure 4-1-6a were used and velocities were chosen as necessary to fit the models.

h). Borehole Structure

Direct measurement of the sediment and layer 2 velocities by laboratory studies of cores and sonic logging provides a basis for seismic modelling techniques. Table 4-1-1 outlines the significant depths in hole 417D. Leg 51 drilled through 343 m of sediment and 188 m of basalt. Leg 52 extended the basement penetration to 355 m. Cores were taken continuously for the bottom 150 m of sediment and for all of the basalt. The sonic log was run from 137 to 439 m sub-bottom.

Estimates of sediment velocity range from 1.57 km/sec from the sonic log to 1.61 km/sec from a study of reflected wave travel times. Core velocities between 200 and 280 metres sub-bottom are from 1.60-1.73 km/sec (DSDP Leg 51 Shipboard Party, pers. comm.). Because only 343m

	Depth from Rig floor (m)	Depth from Mudline (m)	Depth into Basement (m)
Sea Level	10		
Mud Line	5489		
Casing Shoe	5515	26	
Sonic Log-Top	5626	137	
Basement	5832	343	
Geophone Position 2	5840	351	8
Sonic Log-Bottom	5928	439	96
Leg 51 Penetration	6021	532	188
Geophone Position 1	6060	571	228
Depth to top of pipe	6092	603	260
Leg 52 Penetration	6197	708	355

TABLE 4-1-1

SIGNIFICANT DEPTHS IN HOLE 417D

of sediment are present, the sediment velocity does not significantly affect relative travel times. A mean velocity of 1.60 km/sec is considered representative.

The strong mid-sediment reflection (Figure 4-1-5a to 4-1-5c) is associated with a thin (16m thick) clay layer at 156m sub-bottom (DSDP Leg 51 Shipboard Party, pers. comm.) and log velocities at this point jump from 1.56 km/sec to a maximum of 1.90 km/sec. Twenty metres of high velocity (1.67 km/sec) chalk is present ten metres above basement.

The mean laboratory velocity of basalt cores is 5.47 $\pm$ 0.02 km/sec, (a twenty metre thick high velocity (5.75 km/sec) sill is present 72m into basement), the average density of the cores is 2.80 $\pm$ 0.05 gm/cc and the mean sonic log velocity is 4.83 km/sec (Salisbury and Hamano, pers. comm.).

i). Error Estimates

Travel time errors can be classified as random errors or systematic errors. Random errors change unpredictably from shot to shot. Systematic errors are constant for each shot and cancel when travel time differences between shots are required. Examples of random errors are timing and range errors due to uncertainty in flight time correction and charge sink rate, and errors in picking arrival times. Examples of systematic errors are phase shifts in the geophones and recording equipment, and uncertainties in geophone and hydrophone depths and the velocity-depth profile of the ocean and sediments.

The tone break can be picked to within $\pm$ 0.002 secs, the geophone arrivals to within $\pm$ 0.004 secs and the flight time correction is good to within $\pm$ 0.012 secs. The error in flight time caused by the uncertainty in shot depth (47.4 $\pm$ 9.9. m) is $\pm$ 0.007 secs. The total

estimated maximum random error is ± 0.025 secs. Absolute travel times which are affected by systematic errors as well as random errors are not used.

Arrivals have been picked by locating the first cross-over (with constant polarity) and assuming that the arrival time was one-half of the predominant period before this. For the very sharp close range arrivals this proved to be justified and picking errors for these arrivals are very small compared to the estimated maximum error. For the long range (> 6km) compressional wave arrivals and the shear wave arrivals, the error in picking these cross-overs may be on the order of half a period because of the poorer signal to noise ratio. For these arrivals an additional error of ± 0.05 secs (for a dominant frequency of 10 Hz) should be included.

Errors in travel times caused by unknown detailed basement topography of ± 200 m are ± 0.085 secs for P-waves and ± 0.055 secs for S-waves (Sections 4-1g) and 4-2c)).

The maximum random error for ranges is ± 29 m for ranges between 0.75 km and 1.00 km. This decreases with incresing range to an error of ± 24 m for ranges greater than 5 km (Section 4-1d)). North and south ranges are too short and too long respectively by 16 m (Section 4-1e)).

4-2. DATA INTERPRETATION - TRAVEL TIMES

a). Initial Travel Time Analysis

The first approach to the travel time study was to model the times of the significant arrivals by trial and error. This was carried out in order to obtain a feel for the travel times and the type of model which could explain them. The procedure was simply to generate models and compare the resulting travel time curves with the observed

sections. It was assumed that the same model should at least approximately fit all four lines.

For direct and reflected arrivals the travel time curves were computed by ray tracing through a model which included regional topography (Sections 2-1a) and 4-1g)). The terrain corrections were only applied explicitly to correct the critically refracted arrivals.

Figure 4-2-1 shows an example of the results of this analysis. This figure is for the horizontal component of the north line but an analysis of all the lines was carried out. Arrivals were determined from vertical component and difference seismograms (e.g. Figure 4-1-2) as well. The model of Figure 4-2-1 was considered satisfactory to explain the significant arrivals on all of the seismograms (Figure 4-2-3).

A few words concerning the features of this model are in order. The gradient at the top of layer 2 was introduced to explain the direct wave amplitude. The amplitudes die away much more quickly than one would expect from the theoretical analysis (e.g. Figure 2-3-4). This could be caused by interference with the layer 3 refracted arrival, by local topographic effects or by a gradient. The subsequent analysis of the effects of gradients on direct wave amplitudes (Section 2-3e) and Figure 4-3-11) indicated that gradients had a negligible effect on these amplitudes. The gradient is not necessary but its effect on travel times is not significant.

The compressional wave velocity for the bulk of layer 2 is the poorest determined parameter in the analysis. A study of the direct wave can only give the velocity of the section of layer 2 above the receiver. Figure 4-2-2 shows theoretical travel time curves superimposed on the direct arrival data for the north line. (The north line was selected since it had the cleanest waveforms and arrival times could be picked with confidence. The direct wave amplitudes can be compared on the

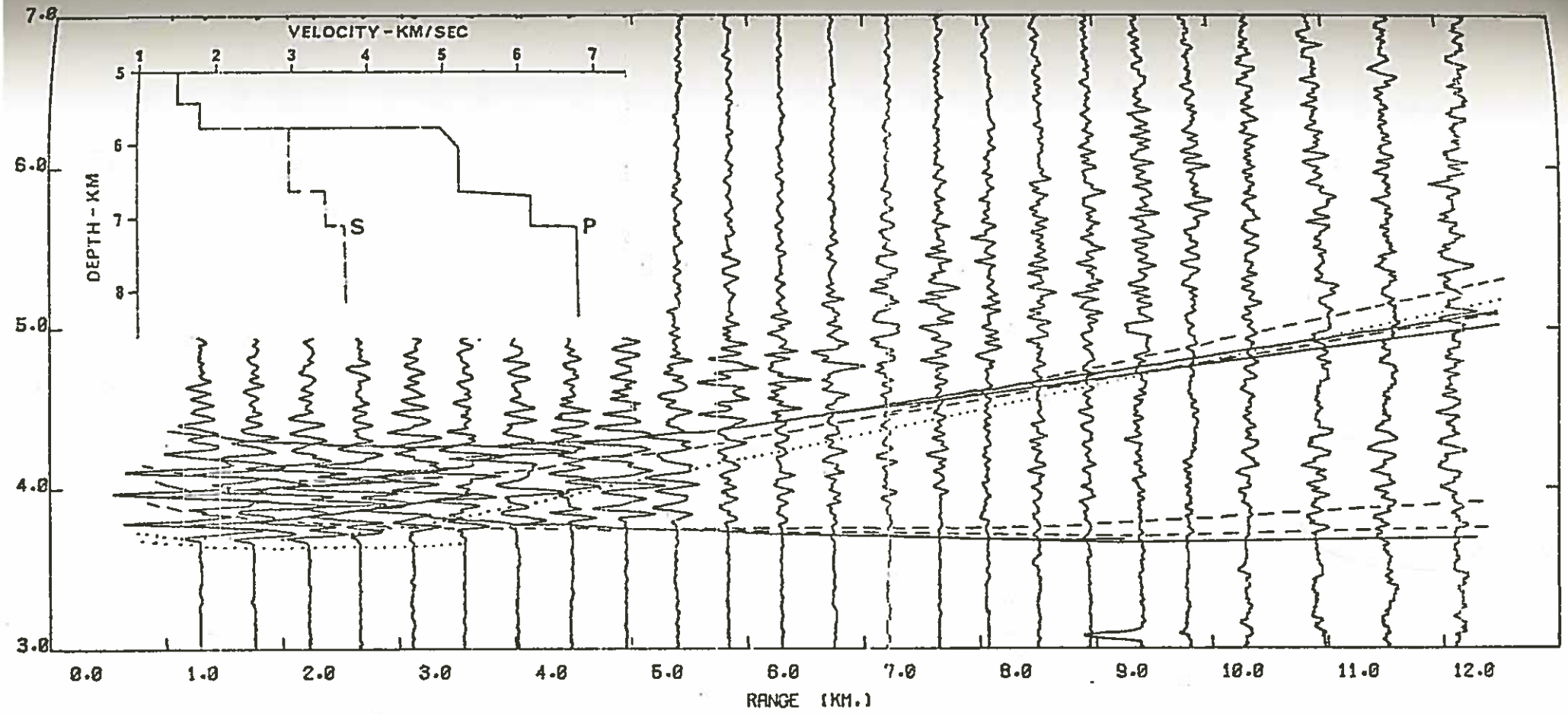

NORTH LINE - HORIZONTAL X COMPONENT - D = 6060 M. BRF

LOW PASS FILTERED AT 30.00 HZ - REDUCTION VELOCITY OF 6.00 KM/SEC
AMPLITUDES WEIGHTED BY (R/7.0)**2.8 FOR R>7.0 KM.

Figure 4-2-1: Record section for north line and deep geophone position with the initial travel time interpretation. Direct arrivals (....), reflections and refractions from the 6.2 km/sec layer (---) and reflections and refractions from the 6.8 km/sec layer (———) are shown for both P and S waves. The direct P-arrival stops abruptly at 3.6 km because of the gradient. Travel times for arrivals between 7 and 12 km were picked from the difference seismogram (Figure 4-1-2). The reflection curves from the 6.2 and 6.8 km/sec layers were calculated using the ray tracing technique of Červený and Pšenčik (Section 2-1) with terrain included. The refracted arrivals are kinked corresponding to the terrain corrections (Figure 4-1-6). The S-wave arrivals are clearer on the vertical component (Appendix C).

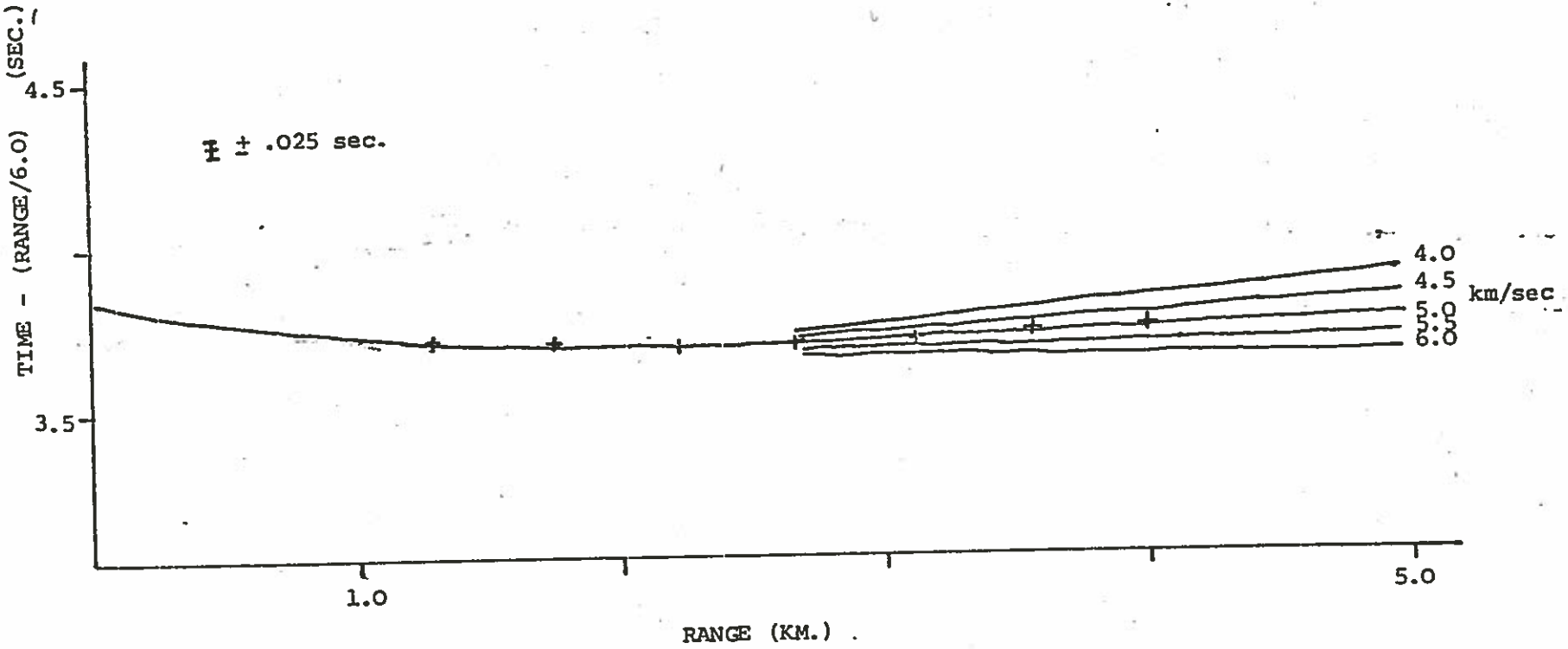

Figure 4-2-2. Original method for determining upper layer 2 travel times. The model curves corresponding to layer 2 velocities of 4.0, 4.5, 5.0, 5.5 and 6.0 km/sec are superimposed on the travel times for the north line (+). The travel times have been shifted in time to agree with the model curve at short ranges. The model curve at short ranges is insensitive to layer 2 velocity. The error bars of ± 0.025 sec correspond to timing errors in the experiment. The effect of detailed basement topography on these arrivals is discussed in Section 4-2c).

sections in Appendix C.) Since travel times for the short range direct arrivals varied by as much as 0.15 sec between lines, only the shape and slope of the travel-time curve was considered. (The discrepancy in short range arrival times is discussed further in Section 4-2c).) Based on these travel times the upper layer 2 velocity is 5.0 $\pm$ .25 km/sec and no distinction can be made between a sharp discontinuity (straight to 5.0 km/sec) or a gradient (5.0 to 5.25 km/sec over 0.25 km). Since it was impossible to place the geophone lower in layer 2 and since no conventional refraction was run in the area a velocity for the bulk of layer 2 could not be measured. (The hydrophone records were not of sufficiently good quality to measure layer 2 refraction arrivals.) However the velocity of 5.0 $\pm$ 0.25 km/sec falls within the range of layer 2B velocities given by Houtz and Ewing (1976). For crust in the Atlantic Ocean at about 100 My age (the crust at Site 417 was 110 My) they give layer 2B velocities of 5.18$\pm$ .27 km/sec. It certainly appears that layer 2A does not exist near Site 417 to within the resolution of seismic waves ($\sim$ 200m). Thus based on their general results a gradient from 5.0 to 5.25 km/sec in the first 0.25 km and then a constant velocity for the remainder of layer 2 of 5.25 km/sec is not unreasonable. It must be emphasized however that the velocity for the bulk of layer 2 cannot be determined from this experiment because the hole was not deep enough.

The 6.8 km/sec velocity typical of layer 3 was obtained from the first arrivals between 5.0 and 9.0 km on the north and south lines and between 5.0 and 7.0 km on the east and west lines (see Figure 4-3-2). These arrivals are generally clear and the signal-to-noise ratio is good. Some of these arrivals however are very weak (e.g. on the north line between 7.0 and 8.0 km in Figure 4-3-2).

A common feature of all the seismograms for the deep geophone position is that at large ranges (10.0 to 12.0 km for the north and south lines and 8.0 to 12.0 km for the east and west lines) no arrivals correspond to the layer 3 refraction line which is based on the good arrivals at mid-ranges (5.0 to 9.0 km on the north and south lines and 5.0 to 7.0 km on the east and west lines). Instead, the first arrivals appear consistently later. This can be easily seen on the plot of first arrival times shown in Figure 4-2-3a. The 6.2 km/sec layer above the 6.8 km/sec layer was introduced to explain this behaviour. The relatively large first arrivals at large ranges were attributed to refractions from the 6.2 km/sec layer. The velocity and depth of this layer were chosen by trial and error to produce an acceptable time difference between the 6.2 km/sec refraction line and the extrapolated 6.8 km/sec refraction line as shown in Figure 4-2-3a.

The thickness of basement down to layer 3 is 1.34 km. This is just within one standard deviation from the mean for crust of this age (1.74 ± 0.41 km , Houtz and Ewing, 1976).

The S-wave velocities in layer 2 were chosen to give the 3.75 km/sec refraction from layer 3 an acceptable intercept. Depths for the S-wave case were taken from the P-wave model. Shear waves can be detected better on vertical component seismograms than on horizontal component seismograms because the waves which are detected by the geophone within the basement travel almost horizontally (Section 2-3c)).

The most significant general point that can be made about this travel time analysis (Figure 4-2-1) is the importance of interference phases. Some interference between the direct and critically refracted layer 3 arrivals occurs between 3.5 and 5.0 km. In fact, the direct wave arrival seems to disappear in this region and picking of travel

times for this arrival within these ranges is difficult. The curious behaviour of the layer 3 refraction arrivals may also be caused by interference effects. The amplitudes of this arrival come and go with range (see Figure 4-3-2b for an example). The large arrivals between 10.0 and 12.0 km which are attributed to the 6.2 km/sec layer may contain some contribution from the layer 3 refraction. The arrival times for the S-wave energy are also so close together that constructive and destructive interference between phases of different origin must occur. The problem in identifying pure phases makes the travel time analysis of the seismograms difficult. The importance of destructive and constructive interference is discussed further in the amplitude analysis (Section 4-3).

How well does the model of Figure 4-2-1 fit the data? Figure 4-2-3 shows the picked P-wave and S-wave travel times for the significant arrivals of the six lines. Superimposed on these points are the travel time curves for the model of Figure 4-2-1. Error bars are shown corresponding to error in determining times, error in picking arrivals and error caused by unknown basement topography. All the points agree with the travel time model to within the total error.

The modelled lines (Figure 4-2-1) do not represent least squares fits of the data points. Since many of the arrivals represent interference effects it is questionable whether a least square fit analysis of all the points would be justified. (An analysis of the single phase arrivals is given in Section 4-2b).) This is particularly evident in the plot for P-wave arrivals at the deep geophone position. Strong, well-defined arrivals between 5.0 and 9.0 km for the north and south lines give definite evidence for a 6.8 km/sec refractor. However the amplitudes die away with range from the critical region and strong arrivals gradually appear arriving somewhat later than would be expected for a 6.8 km/sec refractor. The slope of these points between 10.0 and 12.0 km (for the

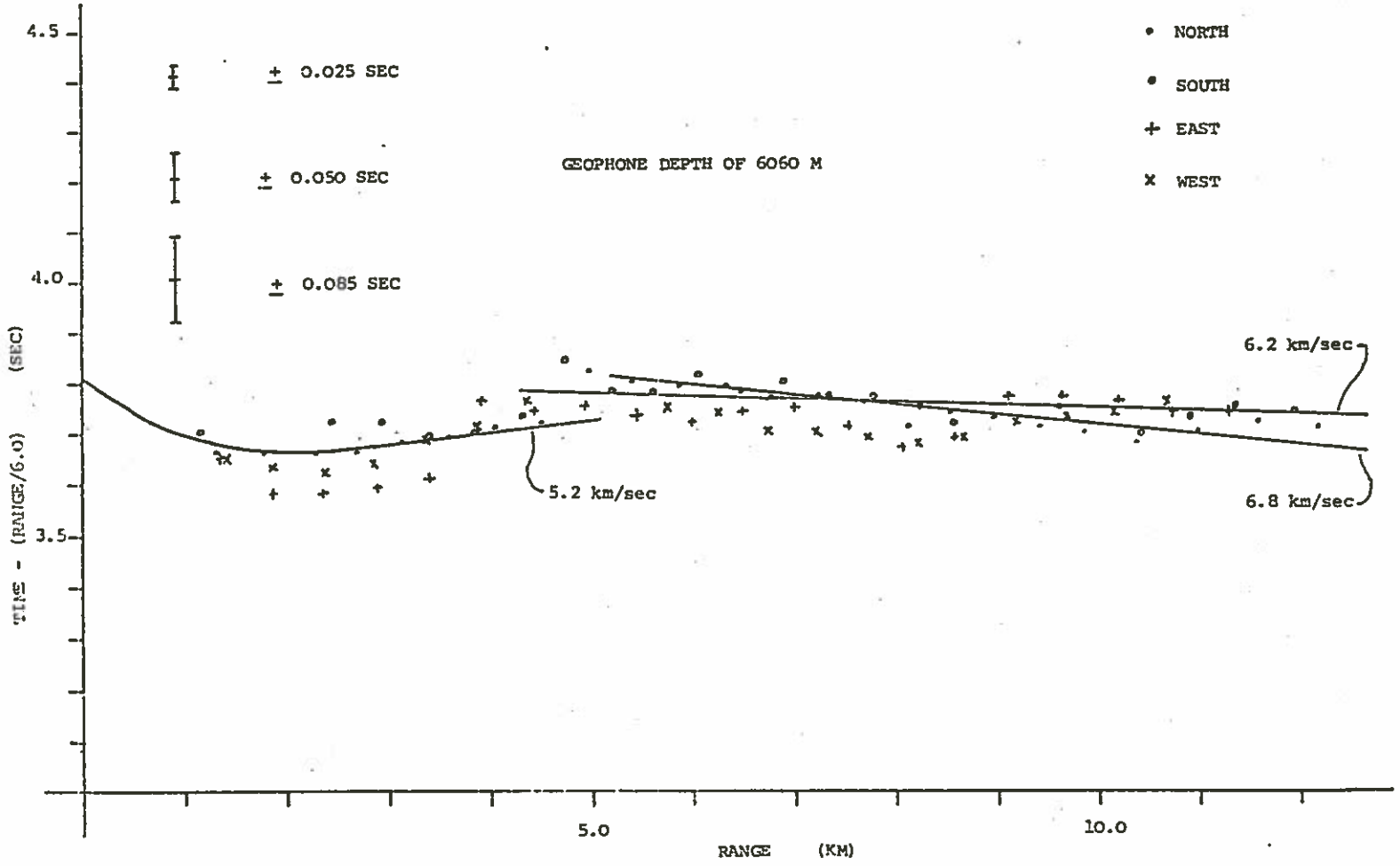

Figure 4-2-3a,b,c&d. Picked arrival times and modelled travel times for the model of Figure 4-2-1. Figures a) and c) are P-wave travel times for deep and shallow geophone positions respectively. Figures b) and d) are the corresponding S-wave travel times. The error bars correspond to errors in timing (± 0.025 sec), phase errors when picking arrivals out of noise (± 0.050 sec) and the error caused by unknown topography (± 0.085 sec for P and ± 0.055 for S). The model is acceptable within the total error.

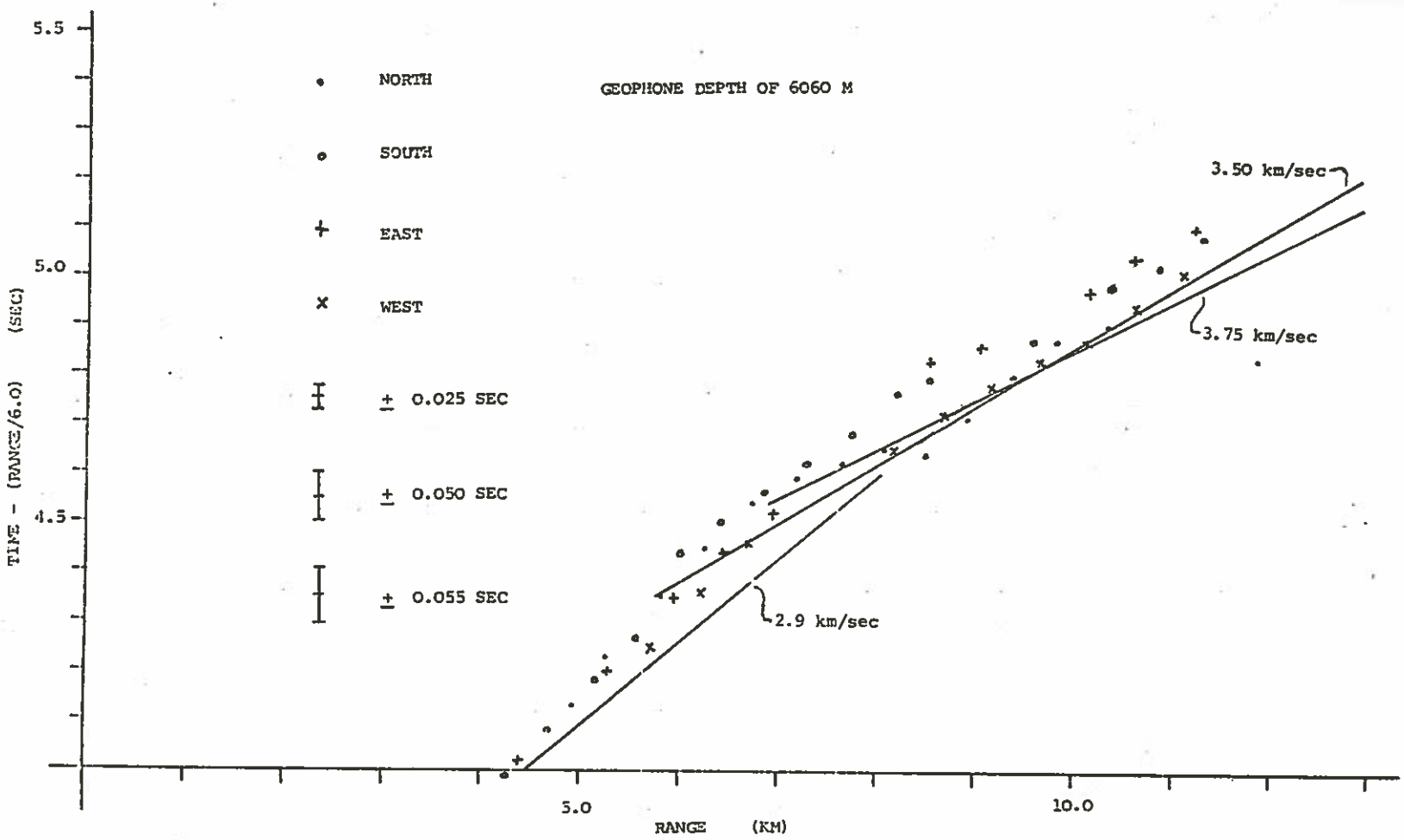
GEOPHONE DEPTH OF 6060 M
NORTH
SOUTH
EAST
WEST
± 0.025 SEC
± 0.050 SEC
± 0.055 SEC
3.50 km/sec
3.75 km/sec
2.9 km/sec
TIME - (RANGE/6.0) (SEC)
5.5
5.0
4.5
5.0
10.0
RANGE (KM)

Figure 4-2-3b

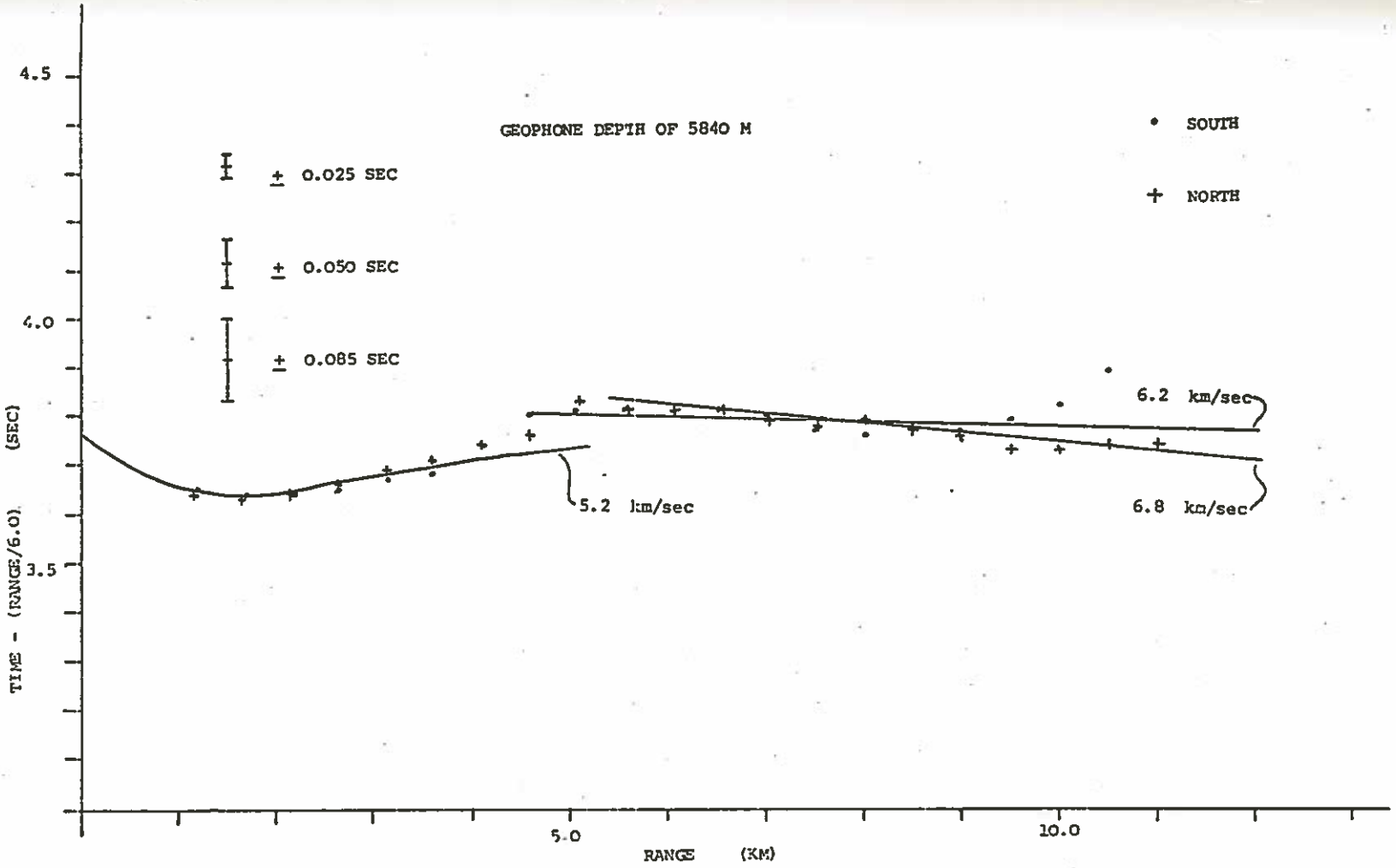
GEOPHONE DEPTH OF 5840 M
SOUTH
NORTH
± 0.025 SEC
± 0.050 SEC
± 0.085 SEC
6.2 km/sec
5.2 km/sec
6.8 km/sec
4.5
4.0
3.5
TIME - (RANGE/6.0) (SEC)
5.0
10.0
RANGE (KM)

Figure 4-2-3c

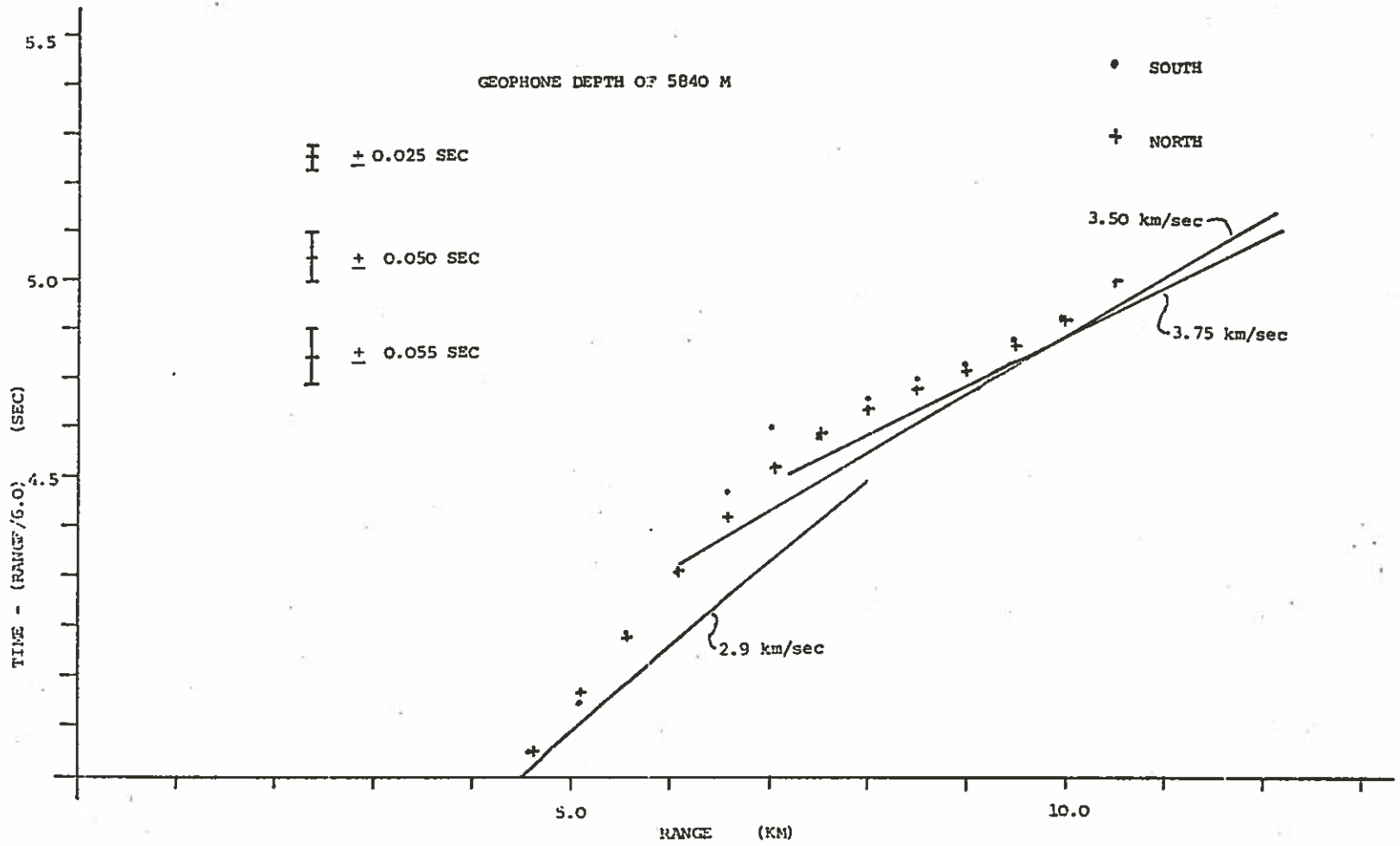
GEOPHONE DEPTH OF 5840 M
SOUTH
NORTH
± 0.025 SEC
± 0.050 SEC
± 0.055 SEC
3.50 km/sec
3.75 km/sec
2.9 km/sec
5.5
5.0
4.5
TIME - (RANGE/6.0) (SEC)
5.0
10.0
RANGE (KM)

Figure 4-2-3d

north and south lines where this effect is dominant) which is fairly well defined does not correspond to a realistic travel time curve. These arrivals must correspond to interference between the two refracted phases from the 6.2 km/sec and 6.8 km/sec layers. (The same effect appears to occur on the east and west lines between 8.0 and 12.0 km.) It would be wrong to do a least squares fit of all of the first arrivals at ranges greater than 5.0 km even for individual lines. It must be considered whether the arrivals correspond to pure phases or are the result of interference between phases.

b). Least Squares Fit Analysis

In order to obtain more accurate velocities to look for azimuthal effects, linear regression by the method of least squares was performed on the mid-range P refractions, the S refraction curve and the direct S-wave arrivals. The results of this study are summarized in Table 4-2-1. There is no significant evidence for azimuthally dependent velocity in either P-waves or S-waves for layer 3 or in S-waves for layer 2. The best estimate for layer 3 compressional and shear wave velocities is highest in the north, lowest in the west and about the same in the east and south.

The layer 3 P-wave and S-wave refractions give velocities which agree well with the initial model (6.67 ± 0.34 and 3.71 ± 0.10 km/sec compared with 6.8 and 3.75 km/sec). The direct S-wave velocity is lower (2.60 ± 0.06 km/sec compared with 3.0 km/sec) but this may be a consequence of an S-wave gradient in layer 2. The 2.60 km/sec value was determined from rays which only travelled in upper layer 2 (the top

LINE	Layer 3. P Velocity (Refracted) (km/sec)	Layer 3 S Velocity (Refracted) (km/sec)	Layer 2 S Velocity (Direct) (km/sec)
North - D = 6060m	6.97 ± .44 (6)	3.75 ± .12 (11)	2.49 ± .02 (5)
North - D = 5840m	6.66 ± .20 (7)	3.88 ± .02 (6)	2.48 ± .04 (6)
South - D = 6060m	6.70 ± .30 (11)	3.63 ± .08 (8)	2.61 ± .05 (4)
South - D = 5840m	6.50 ± .27 (7)	3.81 ± .19 (5)	2.67 ± .04 (3)
East - D = 6060m	6.75 ± .44 (8)	3.68 ± .11 (6)	2.72 ± .21 (4)
West - D = 6060m	6.46 ± .37 (8)	3.51 ± .06 (7)	2.60 ± .01 (4)
MEANS	6.67 ± .34	3.71 ± .10	2.60 ± .06

6.71 3.77 2.56

6.61 3.60 2.66

TABLE 4-2-1

LINEAR REGRESSION SUMMARY FOR THE SIX LINES.

The number in brackets is the number of points used in the velocity determination

$\sin\theta_1 = \frac{v_1}{v_2}$

$\theta_1 = 42.77°$ - N-S.

$\theta_2 = 47.64°$ - E-W

300 m) but the 3.0 km/sec value represents a mean velocity for the top 0.875 km. The latter velocity was chosen to obtain a reasonable intercept for the layer 3 refraction.

c). Study of Direct Wave Arrivals and Small Scale Topography

In constructing the model of Figure 4-2-1 the upper layer 2 velocity was determined by fitting model curves to the direct arrivals on the north line. That study considered the regional topography discussed in Section 4-1g). Arrivals for the north line were used because they were clearest and most well defined out to ranges of 5.0 km. It was evident however that the discrepancy between direct arrival times for different lines was greater than the effect of regional topography ($<$ 0.03 sec) and the estimated error in travel times ($\pm$ 0.025 sec). A detailed look at these travel times indicated that small scale topography on the order of 200 m high exists.

Travel time residuals between the observed data and the data for a standard model with regional topography (Figures 4-1-5 and 4-1-6a) are plotted in Figure 4-2-4. This model is the same as the one in Figure 4-2-1 except that no gradient exists at the top of the basement and the velocity for the basement layer is 4.8 km/sec rather than 5.25 km/sec. The upper layer 2 velocity in this model (4.8 km/sec) was selected because it gave the smallest time discrepancies between deep and shallow positions for the north and south lines.

The residuals can be attributed solely to the effect of small scale basement topography. The east line shows the hill into which hole 417A was drilled (DSDP Leg 51 shipboard party, pers. comm.). An almost equally high hill appears to the west but it is less steep. In contrast the north and south lines are flat, that is, the regional trend is valid.

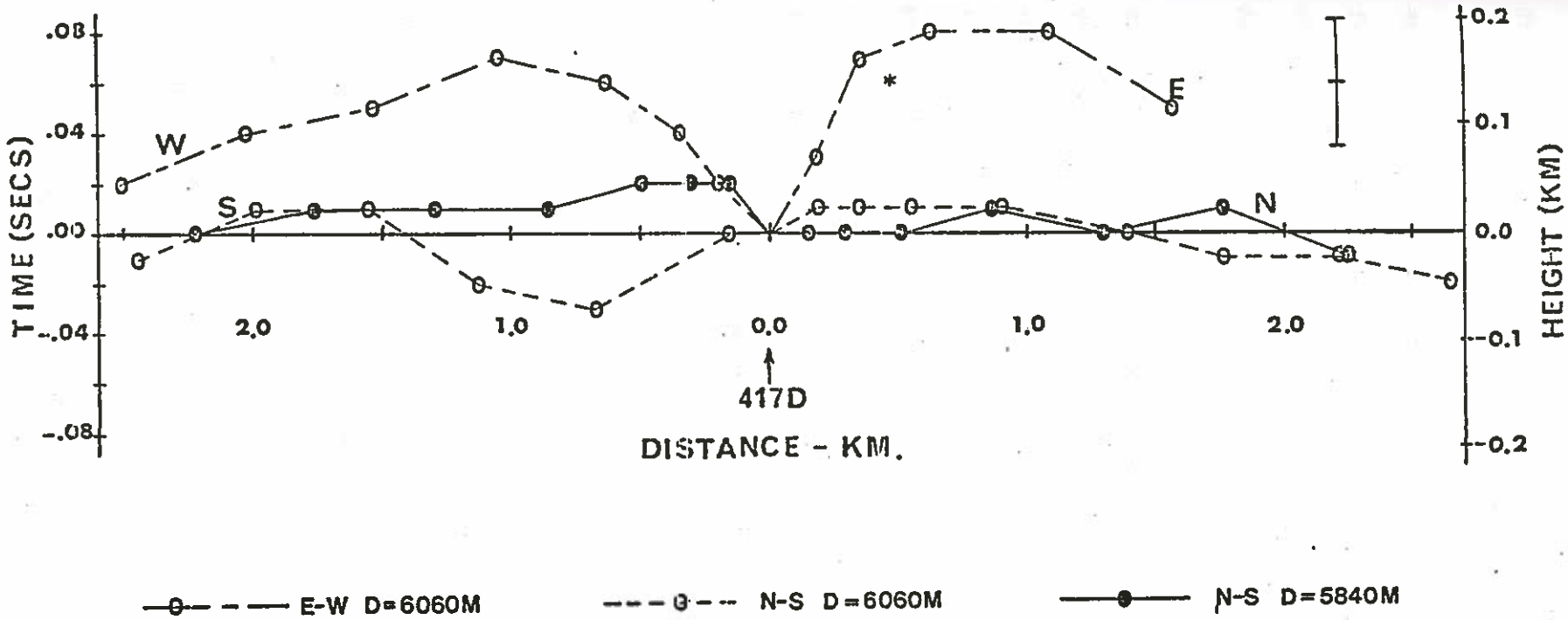

Figure 4-2-4. Travel time residuals between observed travel times and times calculated assuming a layer 2 velocity of 4.8 km/sec and regional topography (Figure 4-1-6). These residuals can be explained by small scale basement topography not seen on the profiling records. (Figures 4-1-5a-c). Basement terrain is much rougher perpendicular to the spreading axis (E-W) than parallel to it (N-S). The error bars in the upper right hand corner represent $\pm$ 0.025 sec which is the estimated timing error in travel times. The smoothness of the curves indicates that the actual error may be somewhat less than this. The star (*) shows the depth of basement at hole 417A. The deviation in the south lines up to 1.5 km may be the result of navigational error (Figure 4-1-4). All lines pass through the origin by definition.

The south lines have significantly different residuals between 0.6 and 1.2 km. This may occur because the two lines are about a kilometre apart in plan view (Figure 4-1-3). Some evidence for these small scale features appears on the reflection profiles (Figure 4-1-5). Bumps in the mid-sediment reflector correspond roughly to the basement highs. Allowance should be made for navigational irregularities.

From the profiles and OSE data it appears that hole 417D was drilled into a trough between two steep (at least 10^{o} and 26^{o}) hills. The topography is much less rugged parallel to the magnetic lineations than perpendicular to them, reminiscent of mid-Atlantic ridge topography (Ballard et al , 1975; Ballard and van Andel, 1977; Macdonald and Luyendyk, 1977). The hills are about 180m high.

There is no point in studying lateral velocity effects from direct arrivals unless the small scale topography is known accurately from detailed profiling. Since sharp features on the sea bed are masked by diffractions (Laughton et al, 1960; Laughton, 1963; Spiess and Mudie, 1970) conventional reflection profiling may not be adequate in the deep ocean.

4-3. DATA INTERPRETATION - AMPLITUDES AND SYNTHETIC SEISMOGRAMS

a). Source Wavelets

Comparison between the observed signals on the geophone channels at short ranges and a theoretical explosive source function (Fowler, 1976) shows that the theoretical source is much shorter than the apparent direct arrival (Figure 4-3-1). An even more disturbing phenomenon in the observed data is that the amplitude of the first bubble pulse wavelet is greater than the initial wavelet. If this were inherent in the source function it would violate the principle of

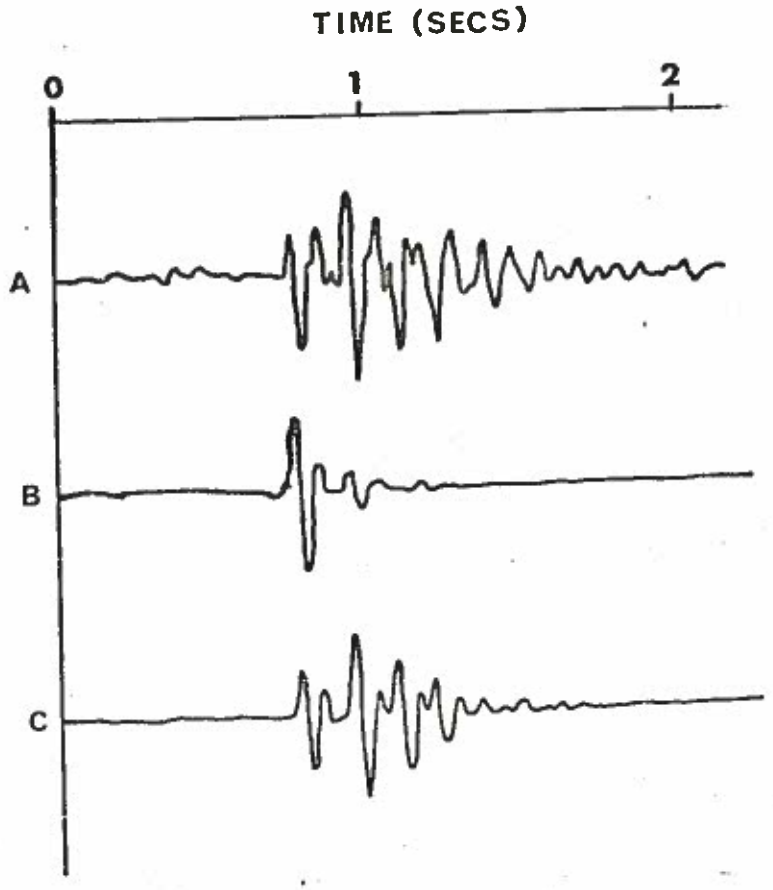

Figure 4-3-1. Comparison of source wavelets for synthetics. Wavelet A is a typical seismogram for a near normal incidence arrival. Wavelet B is the theoretical explosion wavelet and wavelet C is the empirically selected source wavelet.

conservation of energy. Both observations can be attributed to reverberations in the sediment. The time interval between the first two pulses is 0.19 secs. An intra-sediment multiple would have this period if it occurred between horizons 0.17 km apart. Such a multiple could be generated between basement and the strong mid-sediment reflector on the reflection profiles (Figure 4-1-5). Unfortunately attempts to model this effect, using the methods described in Section 2-2, failed because of numerical difficulties. Evidently the integrand in the integration varies so quickly that numerical evaluation of the integral is impossible using reasonable increments.

It is unreasonable to expect that the extended waveform at short ranges could be caused by reflecting horizons below the receiver. Such horizons would necessarily be sharp to cause large reflections at short ranges and no evidence for sharp interfaces has previously been reported. Also the nature of the waveform does not vary significantly at large ranges. Consequently it is assumed that the waveform incident on the basement has the form of a short range arrival. Figure 4-3-1 compares the empirical waveform, the theoretical waveform, and a sample observed waveform.

b). Discussion of Synthetic Seismograms

Synthetic seismogram analysis is particularly helpful in studying seismograms which contain a large amount of interference information as in this experiment (Section 4-2a)). Rather than trying to match the amplitudes of an isolated pure phase, it is necessary to consider regions on the seismic section which seem to display characteristic behaviour.

In the following discussion I will compare the horizontal component

seismograms for the deep geophone position (6060 m BRF, below rig floor) with seven models. With this work as a background I will then compare the vertical component data and the data for the shallow geophone position (5840 m BRF) to three of these models to demonstrate the extent to which the additional data effect the original discussion.

Figure 4-3-2 shows horizontal component seismograms for the four lines shot with the geophone at 6060 m BRF. Five regions have been circled on the seismograms which exhibit characteristic behaviour when comparisons are made with synthetic seismograms. Region A is the critical region for P-wave arrivals from layer 3. Amplitudes in this region are large on the north, south and east lines when compared to the amplitudes on each section in general. The applicable ranges for the west line are missing. Region B is the critical region for S-wave arrivals from layer 3. Amplitudes here are large on the south and east lines and about normal on the north and west lines. Region C is an area of destructive interference in the S-wave energy. All four sections show relatively low amplitudes in the early part of Region C. Region D is an area of interference effects for the P-wave energy. In general it is an area of low amplitudes. Region E includes the long range layer 3 refraction arrivals and is also an area of low amplitudes. This is most evident on the north and south lines. (Amplitudes on the east and west lines are low in general for long range P-wave energy.) Since these record sections have not been corrected for regional topography there appears to be some energy in the circled areas. When the arrival times of this energy are plotted on travel-time curves, however, the arrivals fall later than the extrapolated layer 3 refraction curve (Figure 4-2-3a).

Figure 4-3-3 shows the synthetic seismogram corresponding to the model in Figure 4-2-1. The P-wave and S-wave amplitudes in the critical

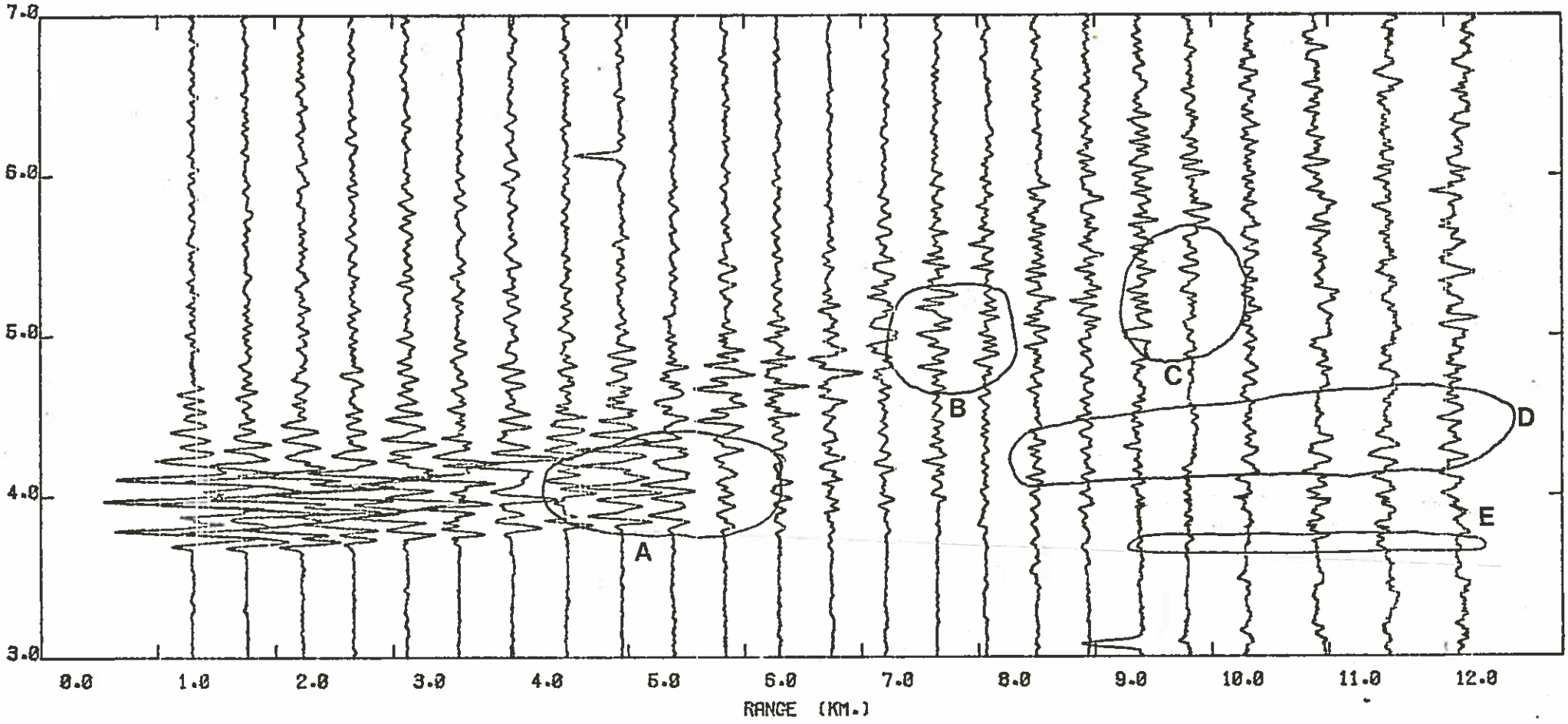

NORTH LINE - HORIZONTAL X COMPONENT - D = 6060 M. BRF

LOW PASS FILTERED AT 30.00 HZ - REDUCTION VELOCITY OF 6.00 KM/SEC
AMPLITUDES WEIGHTED BY (R/7.0)**2.9 FOR R>7.0 KM.

Figure 4-3-2a,b,c&d. Horizontal component seismograms for the receiver at 6060 m BRF (below rig floor). All the seismograms shown in this chapter (including the synthetics) are displayed with a reduction velocity of 6.0 km/sec and an amplitude weighting of (range/7.0)**2.9 for ranges greater than 7.0 km. The areas marked are discussed in the text.

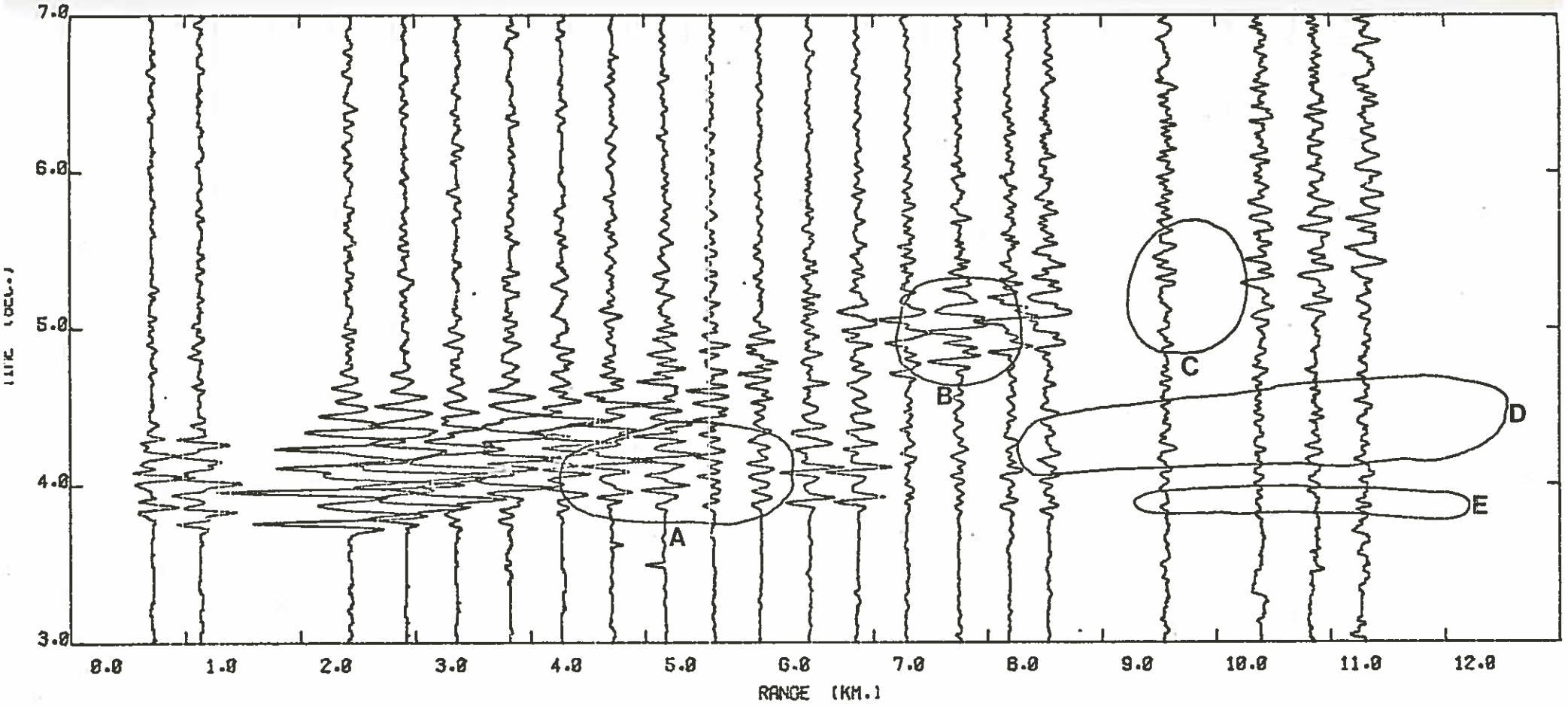

SOUTH LINE - HORIZONTAL X COMPONENT - D = 6060 M. BRF

LOW PASS FILTERED AT 30.00 HZ - REDUCTION VELOCITY OF 6.00 KM/SEC
AMPLITUDES WEIGHTED BY (R/7.0)**2.9 FOR R>7.0 KM.

Figure 4-3-2b

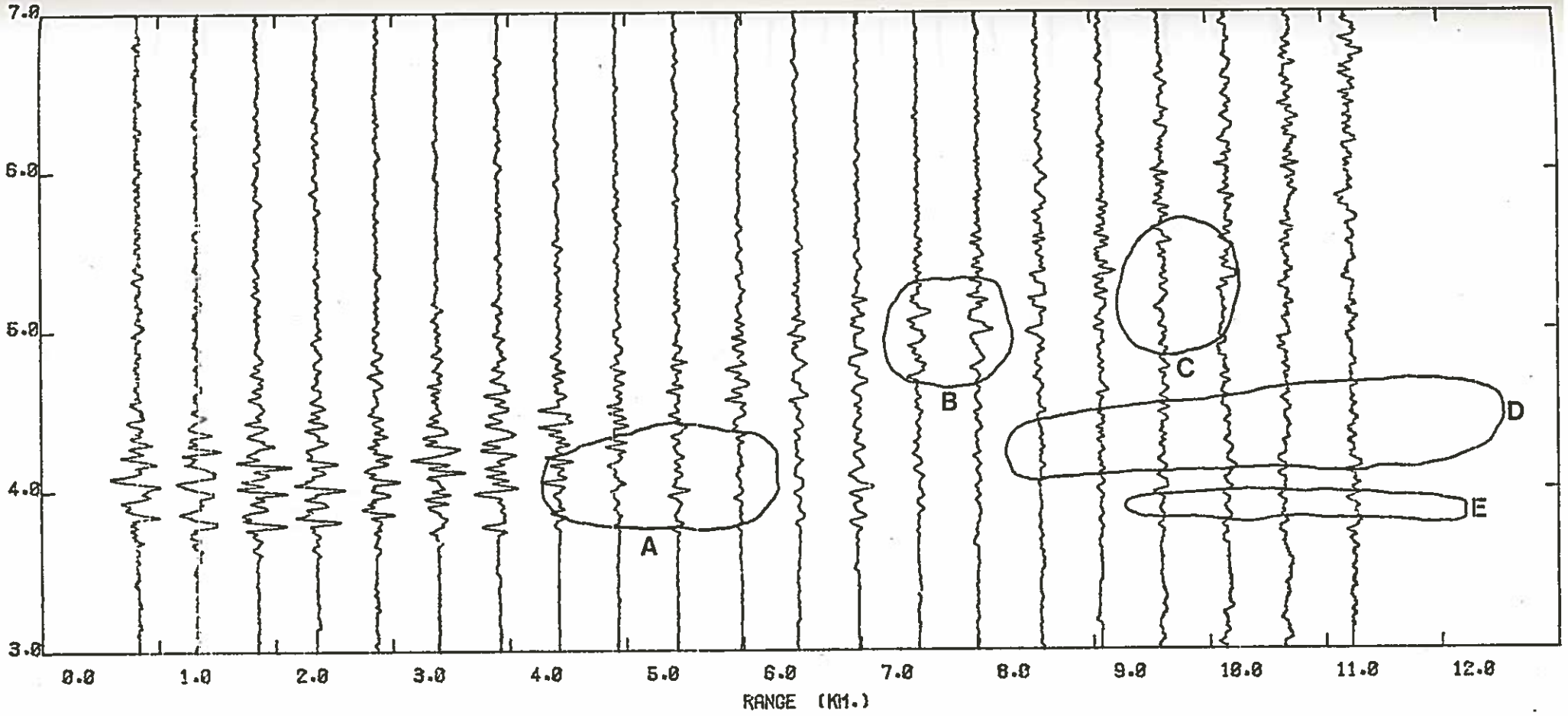

EAST LINE - HORIZONTAL Y COMPONENT - D = 6060 M. BRF

LOW PASS FILTERED AT 30.00 HZ - REDUCTION VELOCITY OF 6.00 KM/SEC
AMPLITUDES WEIGHTED BY (R/7.0)**2.9 FOR R>7.0 KM.

Figure 4-3-2:

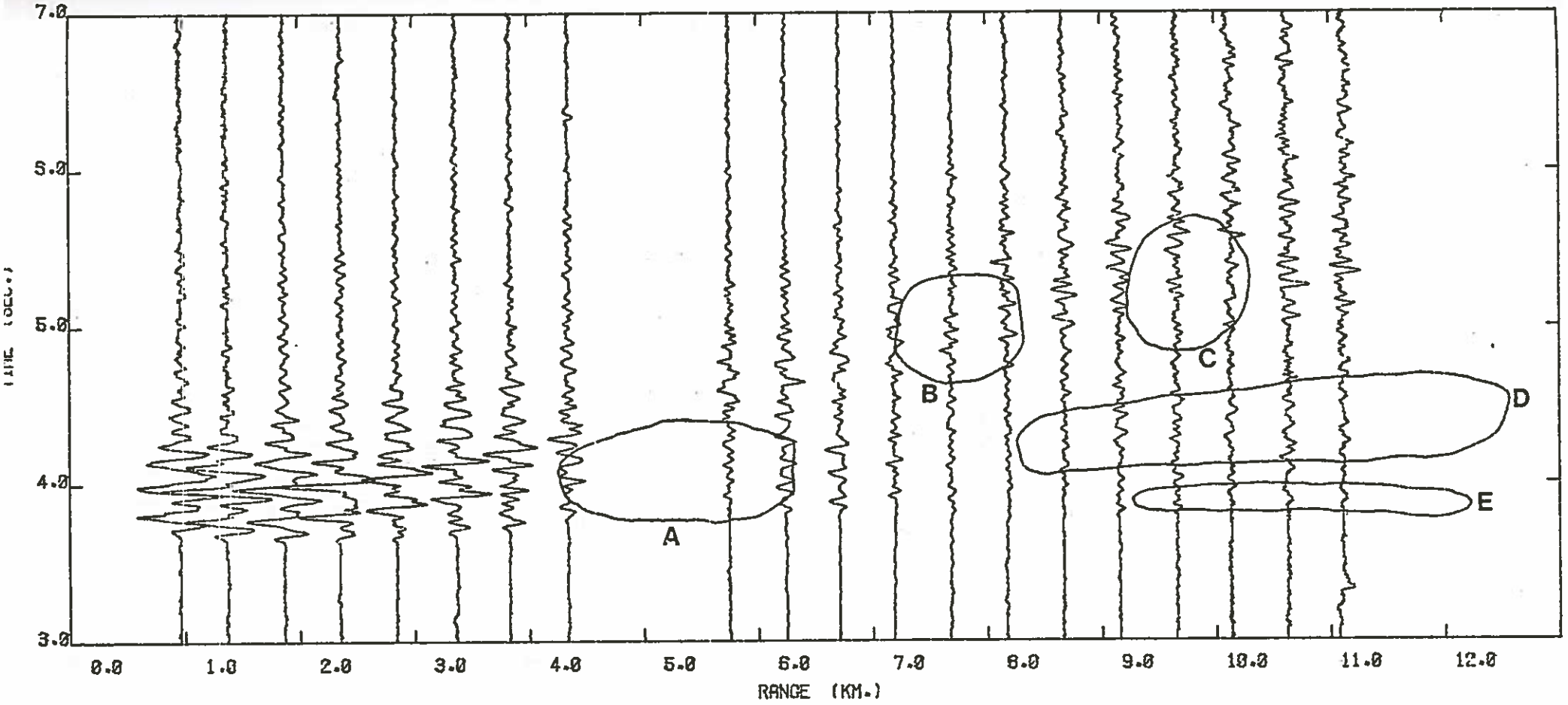

WEST LINE - HORIZONTAL Y COMPONENT - D = 6060 M. BRF

LOW PASS FILTERED AT 30.00 HZ - REDUCTION VELOCITY OF 6.00 KM/SEC
AMPLITUDES WEIGHTED BY (R/7.0)**2.9 FOR R>7.0 KM.

Figure 4-3-2d

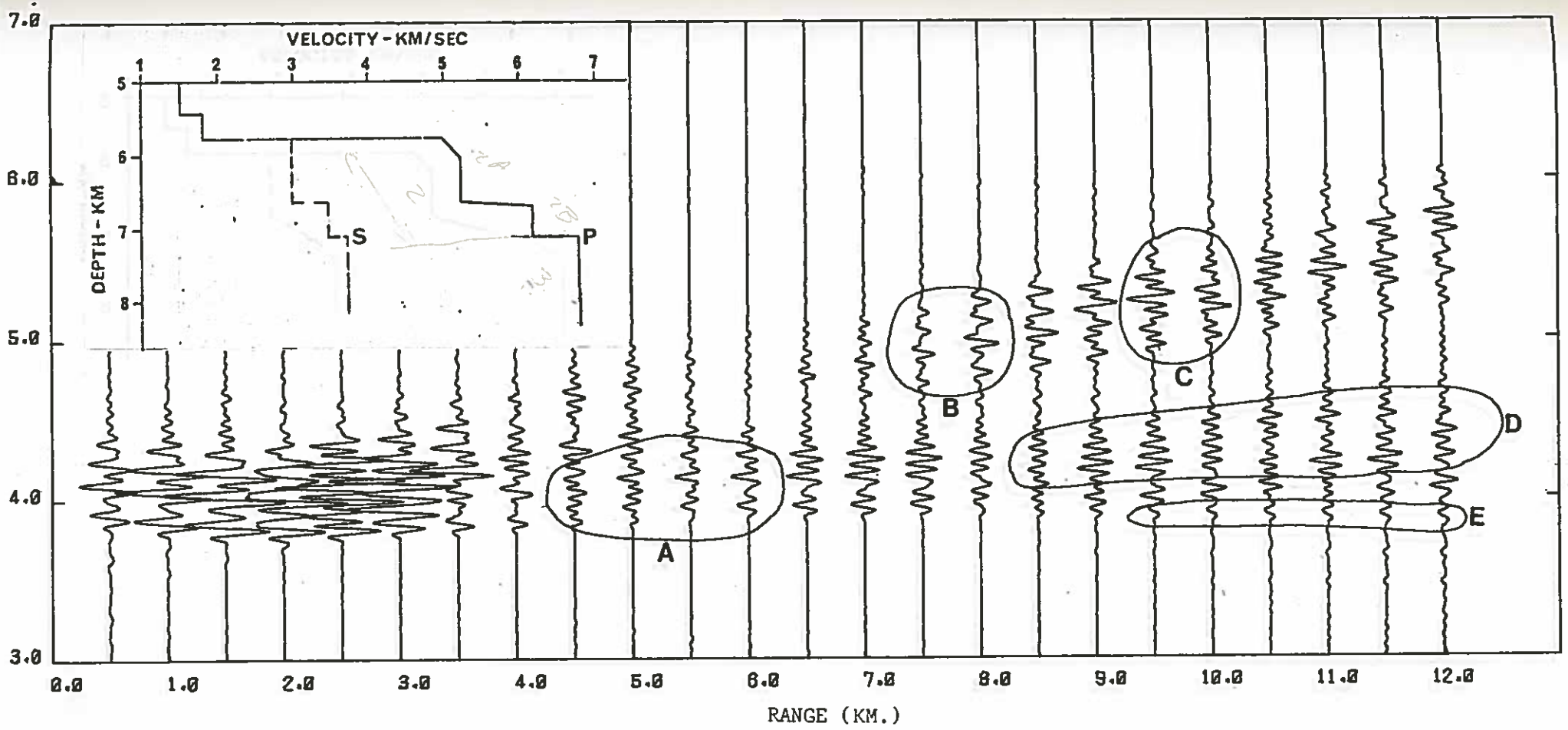

Figure 4-3-3. Horizontal component synthetic seismograms for the receiver at 6060 m BRF. The model is the step model (defined in the travel time analysis (Figure 4-2-1)).

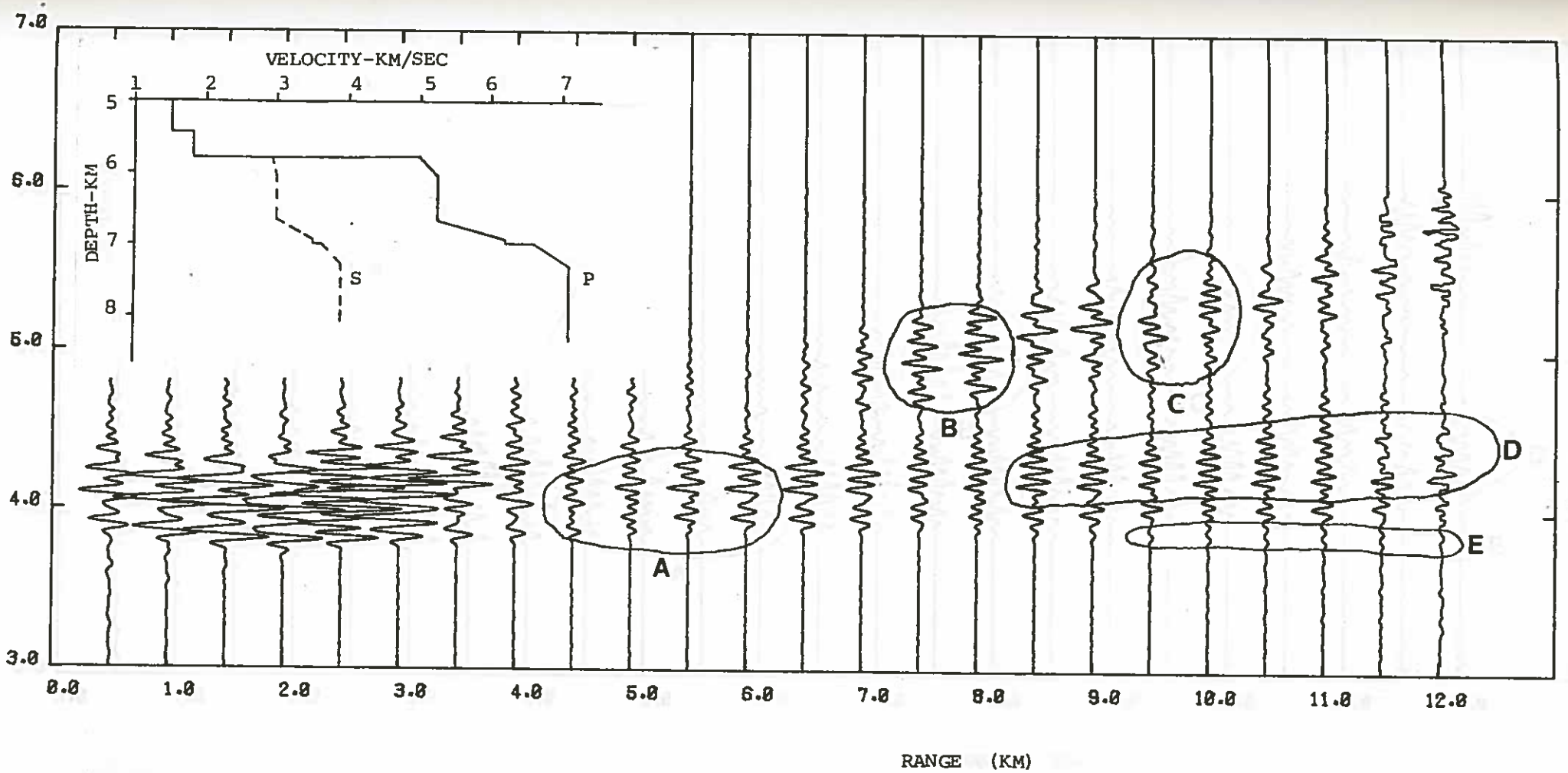

Figure 4-3-4a-f. Horizontal component synthetic seismograms for the receiver at 6060 m BRF. The models are discussed in the text.

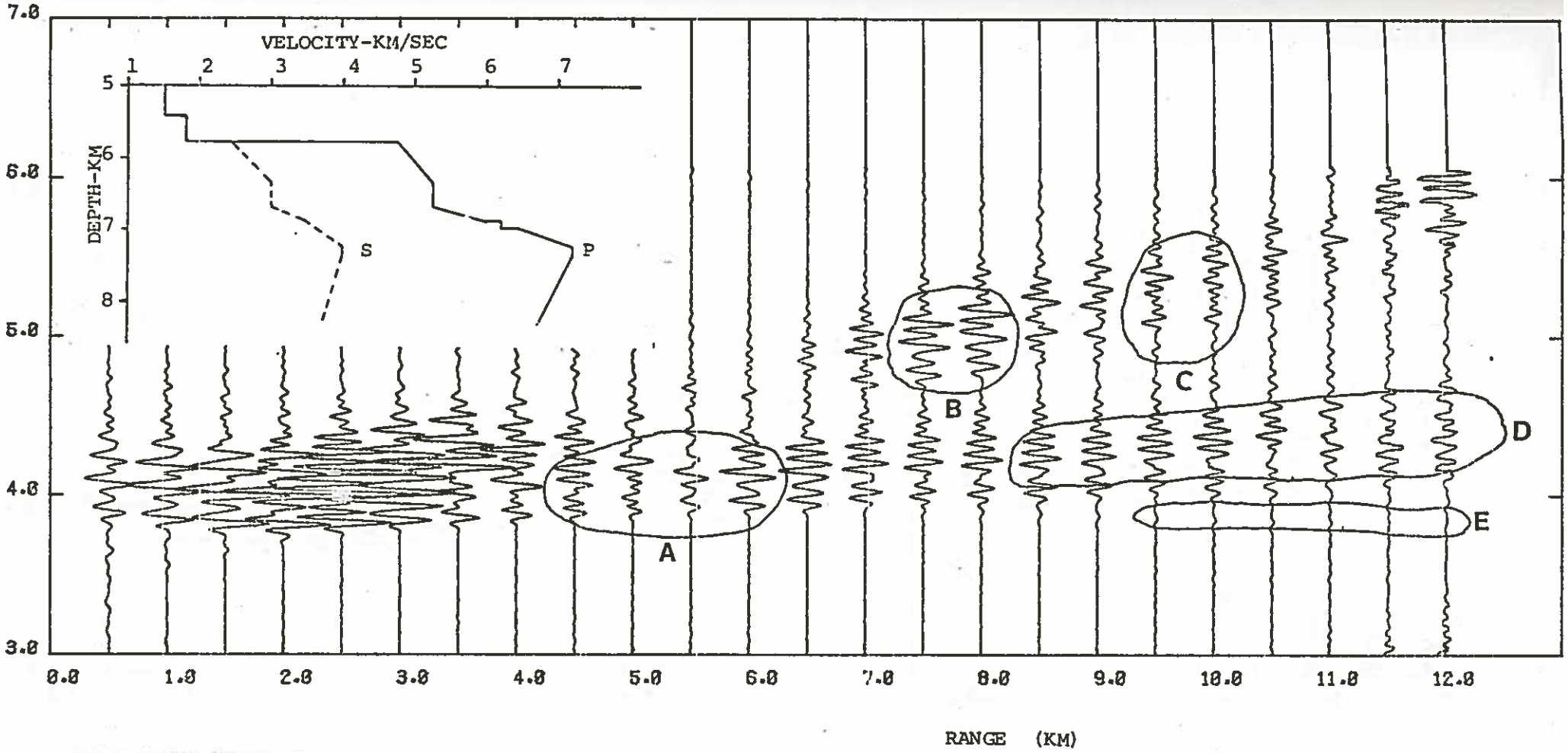
VELOCITY-KM/SEC
1
2
3
4
5
6
7
DEPTH-KM
5
6
7
8
S
P
A
B
C
D
E
7.0
6.0
5.0
4.0
3.0
0.0
1.0
2.0
3.0
4.0
5.0
6.0
7.0
8.0
9.0
10.0
11.0
12.0
RANGE (KM)

Figure 4-3-4b

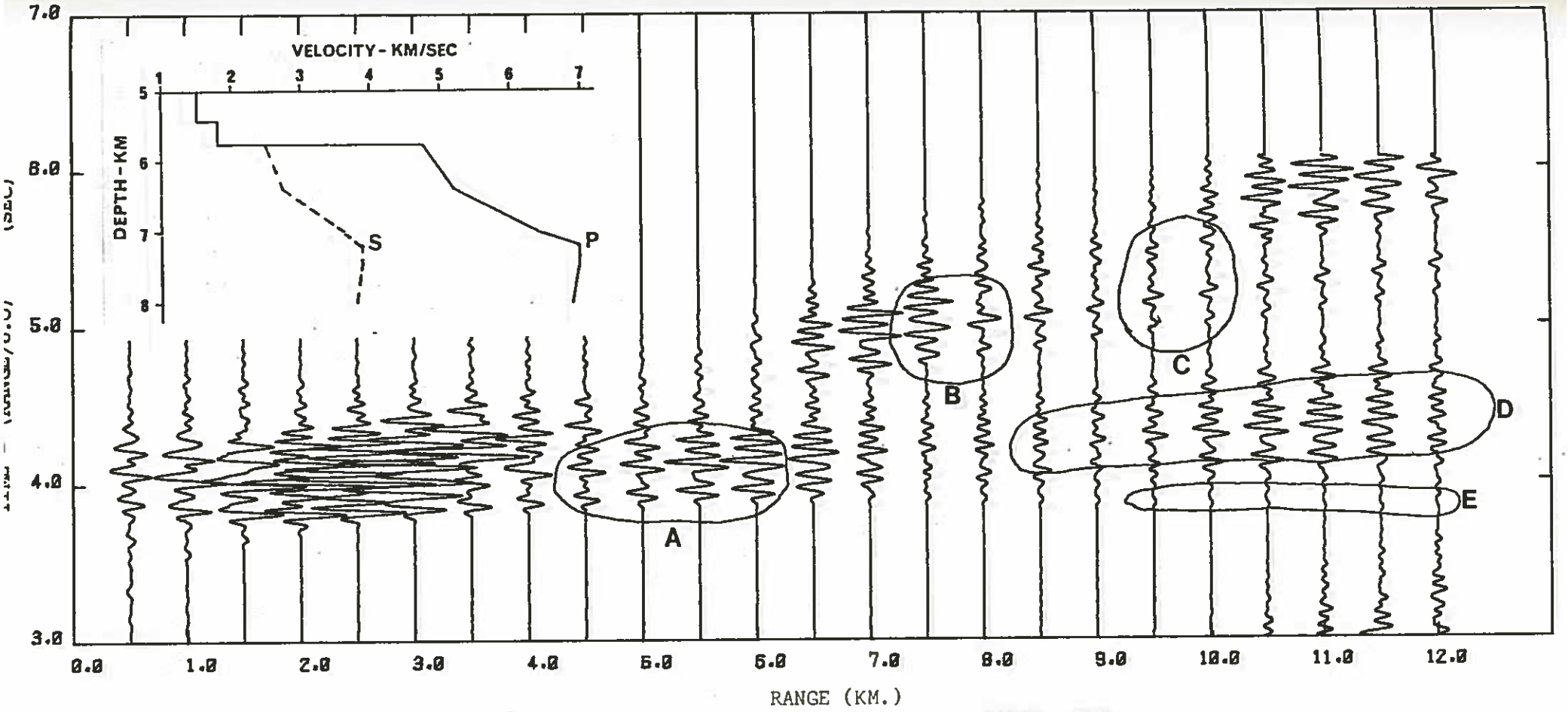
VELOCITY - KM/SEC
1
2
3
4
5
6
7
DEPTH - KM
5
6
7
8
S
P
A
B
C
D
E
7.0
6.0
5.0
4.0
3.0
0.0
1.0
2.0
3.0
4.0
5.0
6.0
7.0
8.0
9.0
10.0
11.0
12.0
RANGE (KM.)

Figure 4-3-4c

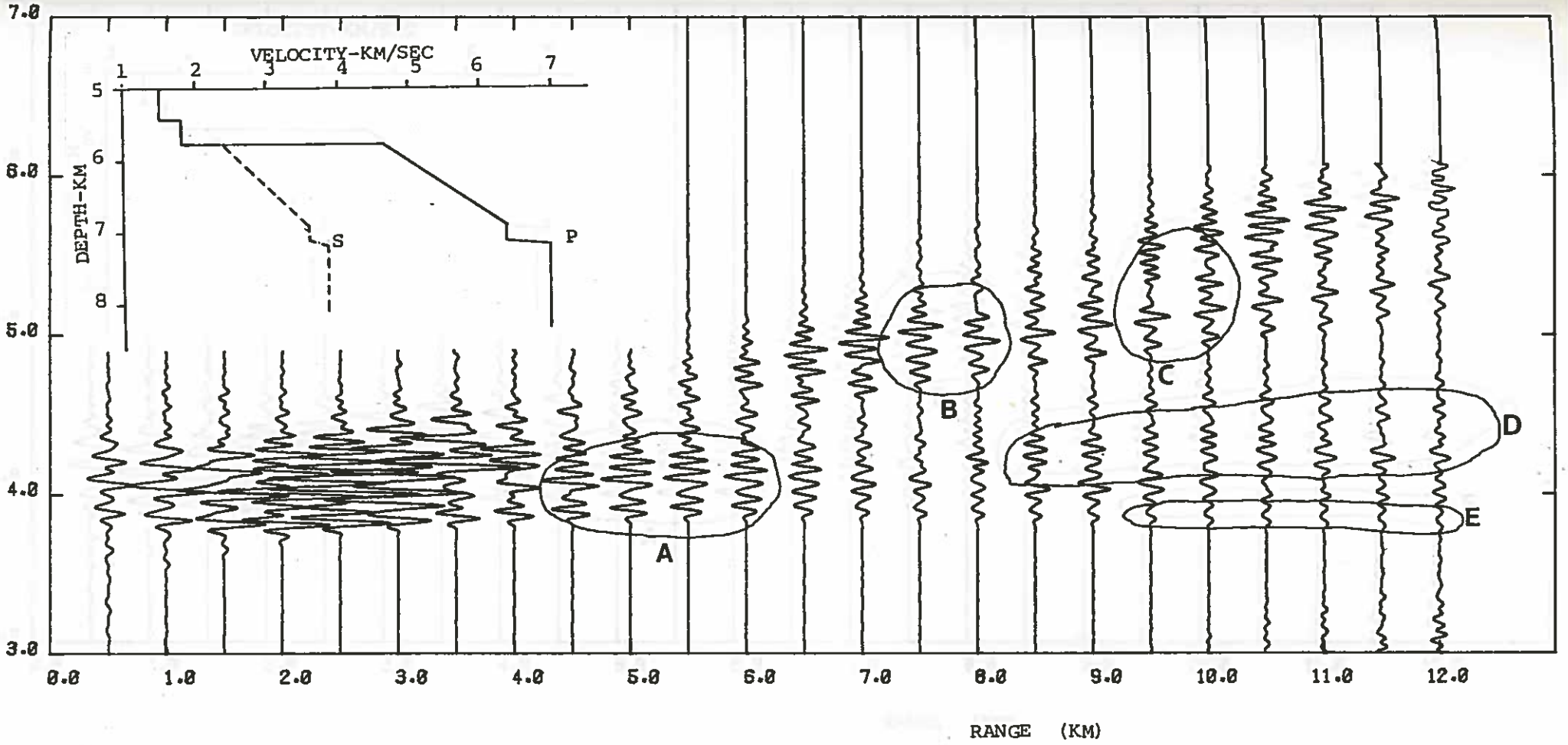
VELOCITY-KM/SEC
1
2
3
4
5
6
7
DEPTH-KM
5
6
7
8
S
P
A
B
C
D
E
7.0
6.0
5.0
4.0
3.0
0.0
1.0
2.0
3.0
4.0
5.0
6.0
7.0
8.0
9.0
10.0
11.0
12.0
RANGE (KM)

Figure 4-3-4d

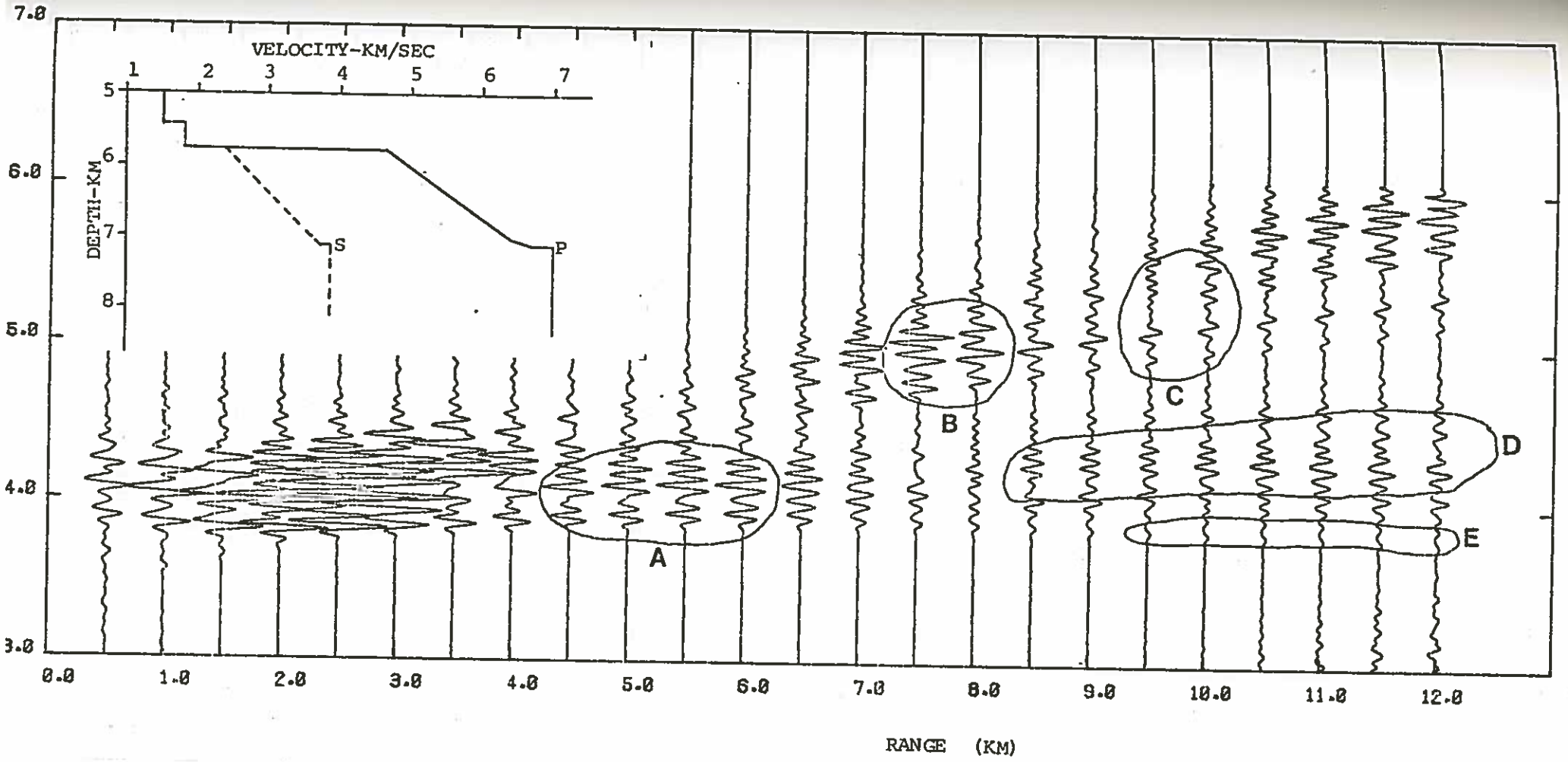
VELOCITY-KM/SEC
1
2
3
4
5
6
7
DEPTH-KM
5
6
7
8
S
P
A
B
C
D
E
7.0
6.0
5.0
4.0
3.0
0.0
1.0
2.0
3.0
4.0
5.0
6.0
7.0
8.0
9.0
10.0
11.0
12.0
RANGE (KM)

Figure 4-3-4e

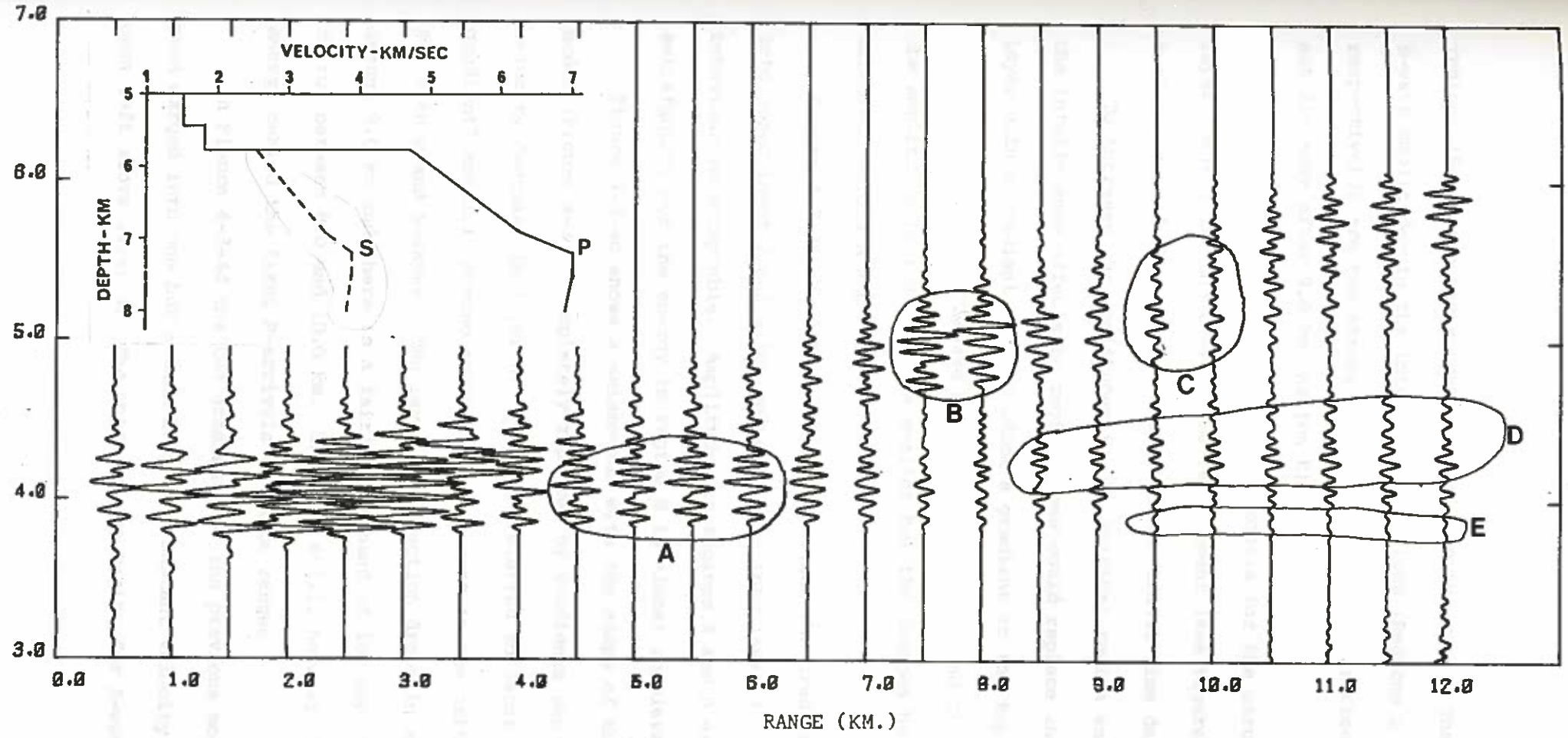

Figure 4-3-4f

NEWS

regions (Regions A and B respectively) are too weak. The P-wave and S-wave amplitudes in the interference regions (Regions D and C respectively) are too strong and the critically refracted P-wave does not die away after 9.0 km (Region E).

Figure 4-3-4 shows six different models for the structure of layer 2 which fit the travel time requirement (see Figure 4-3-12 for a comparison of three of the models to the travel time data).

To increase the amplitudes in the critical region and to change the interference effects in region D one could replace the 6.2 km/sec layer with a gradient and introduce a gradient to the top of layer 3 (Figure 4-3-4a). The S-wave behaviour (regions B and C) improves and the amplitudes in region E are smaller but the changes have not affected regions A and D.

Figure 4-3-4b shows the effect of putting the gradient deeper into upper layer 2 and a low velocity zone into layer 3. Again S-wave behaviour is acceptable. Amplitudes in regions A and D are not satisfactory but the energy in region E is almost completely eliminated.

Figure 4-3-4c shows a seismogram with the steps of the initial model (Figure 4-3-3) completely replaced by gradients and with a slight velocity decrease in layer 3. (This is referred to later as the "double gradient" model.) Strong arrivals are present in the critical regions for both P-and S-waves. The layer 3 refraction drops in amplitude around 9.0 km and there is a fairly wide band of low amplitude shear energy between 8.0 and 10.0 km. There is still, however, too much energy behind the first P-arrivals at large ranges.

In Figure 4-3-4d the two gradients of the previous model have been merged into one but a thin layer of constant velocity material has been left above layer 3. The interference region for S-waves (C) is

not satisfactory and there is still too much energy in region D.

The next figure (Figure 4-3-4e) has the constant velocity layer removed and the amplitudes in region C are much better. In fact this model is acceptable except for the amplitudes in region D. Even the behaviour in region E is satisfactory. This is significant since it implies that a low velocity zone is not required in layer 3.

By decreasing the gradient slightly at the top of layer 3 and introducing a small velocity inversion an acceptable seismogram is produced (Figure 4-3-4f). (This is referred to later as the "single gradient" model.) In view of Figure 4-3-4e it is questionable whether the velocity inversion in layer 3 is necessary.

Having discussed a number of models for the horizontal component at the deep geophone position I will now show data for the vertical component and shallow positions which will confirm in general the above analysis. The following discussion only considers the step model (Figure 4-2-1), the double gradient model (Figure 4-3-4c) and the single gradient model (Figure 4-3-4f).

Figure 4-3-5 shows the observed vertical component seismograms with the geophone at 6060 m BRF. The same regions as outlined in Figure 4-3-2 are shown. Figure 4-3-6a shows the synthetic seismogram for the initial step model of Figure 4-2-1. The amplitudes of the synthetic agree fairly well with the observed data for all the lines in regions A, B, and D. In region E some energy appears on the east line but if travel times are picked from this and terrain corrections applied the arrivals fall later than the extrapolated line from the mid-range (5.0-8.0 km) arrivals (Figure 4-2-3a). The greatest shortcoming of the initial model for the vertical component is in region C where strong amplitudes appear. The observed data in region C show very low

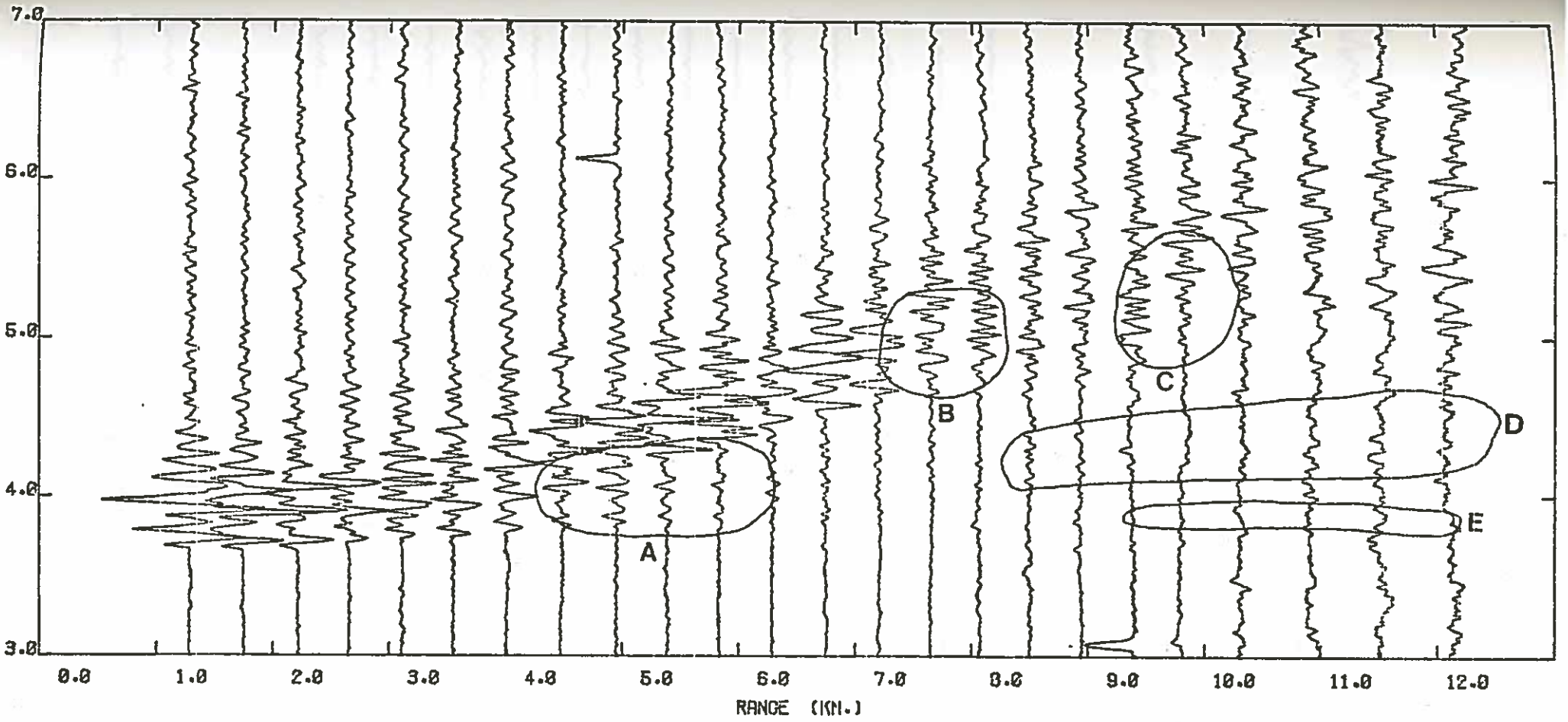

NORTH LINE - VERTICAL COMPONENT - D = 6060 M. BRF

LOW PASS FILTERED AT 30.00 HZ - REDUCTION VELOCITY OF 6.00 KM/SEC
AMPLITUDES WEIGHTED BY (R/7.0)**2.0 FOR R>7.0 KM.

.Figure 4-3-5a-d. Vertical component seismograms for the receiver at 6060 m BRF. The areas marked are discussed in the text.

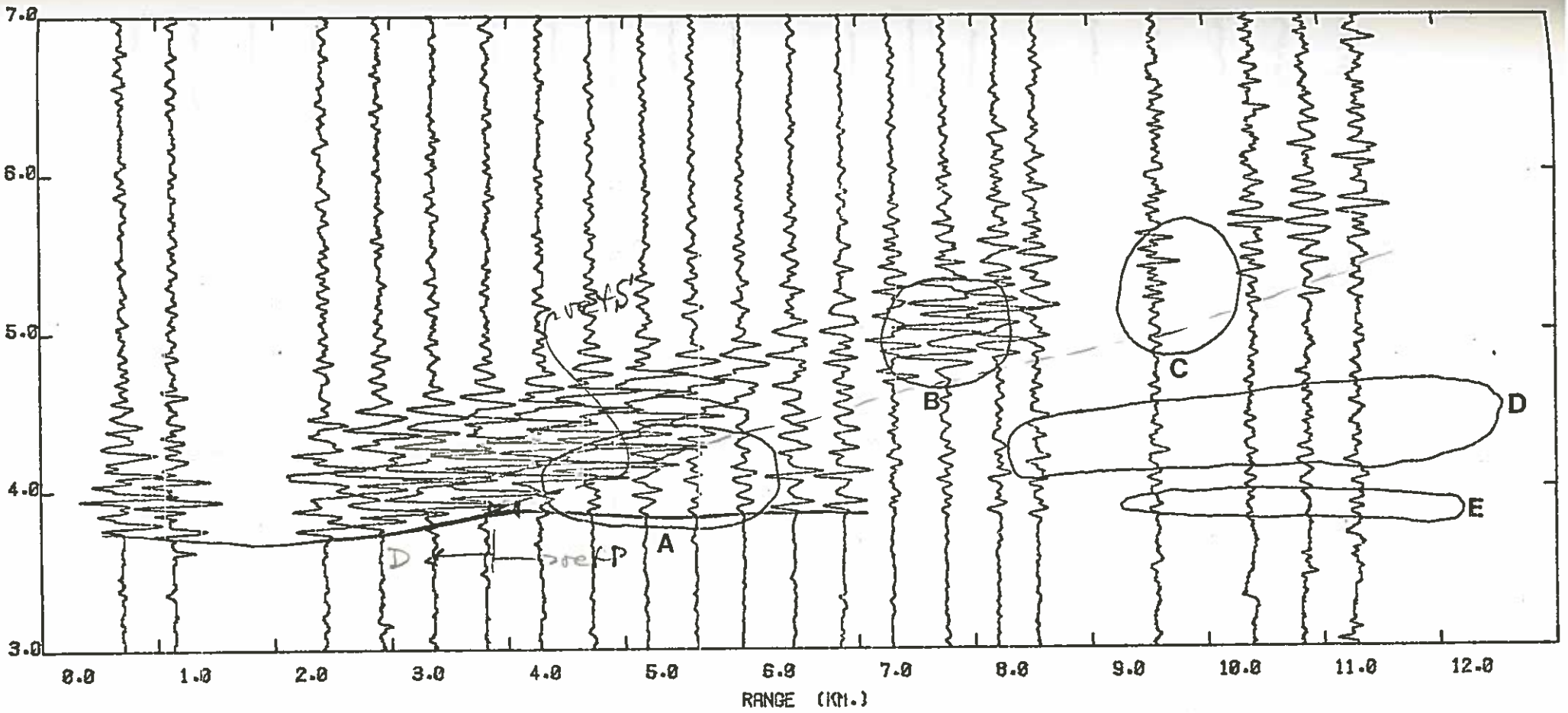

SOUTH LINE - VERTICAL COMPONENT - D = 6060 M. BRF

LOW PASS FILTERED AT 30.00 HZ - REDUCTION VELOCITY OF 6.00 KM/SEC
AMPLITUDES WEIGHTED BY (R/7.0)**2.9 FOR R>7.0 KM.

Figure 4-3-5b

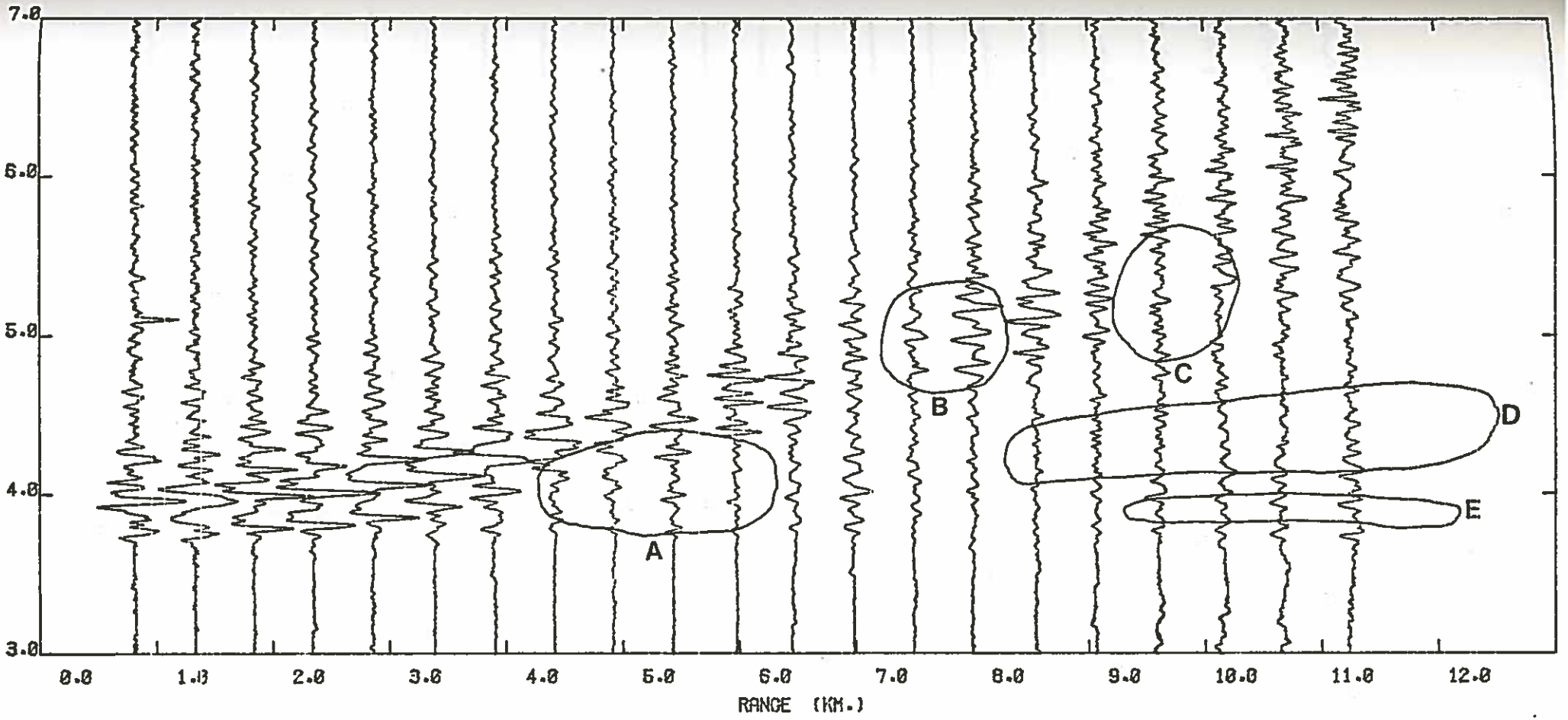

EAST LINE - VERTICAL COMPONENT - D = 6060 M. BRF

LOW PASS FILTERED AT 30.00 HZ - REDUCTION VELOCITY OF 6.00 KM/SEC
AMPLITUDES WEIGHTED BY (R/7.0)**2.9 FOR R>7.0 KM.

Figure 4-3-5c

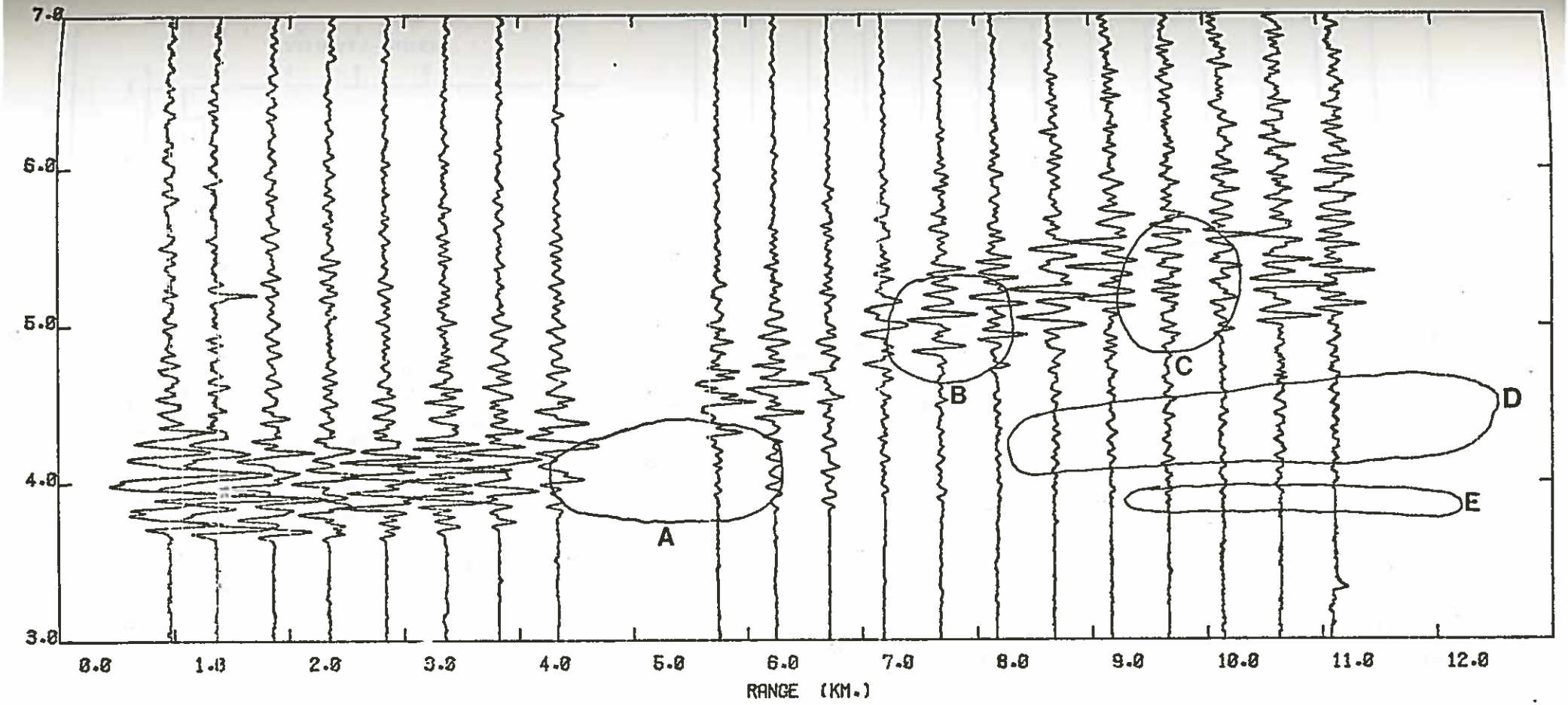

WEST LINE - VERTICAL COMPONENT - D = 6050 M. BRF

LOW PASS FILTERED AT 30.00 HZ - REDUCTION VELOCITY OF 6.00 KM/SEC
AMPLITUDES WEIGHTED BY (R/7.0)**2.9 FOR R>7.0 KM.

Figure 4-3-5d

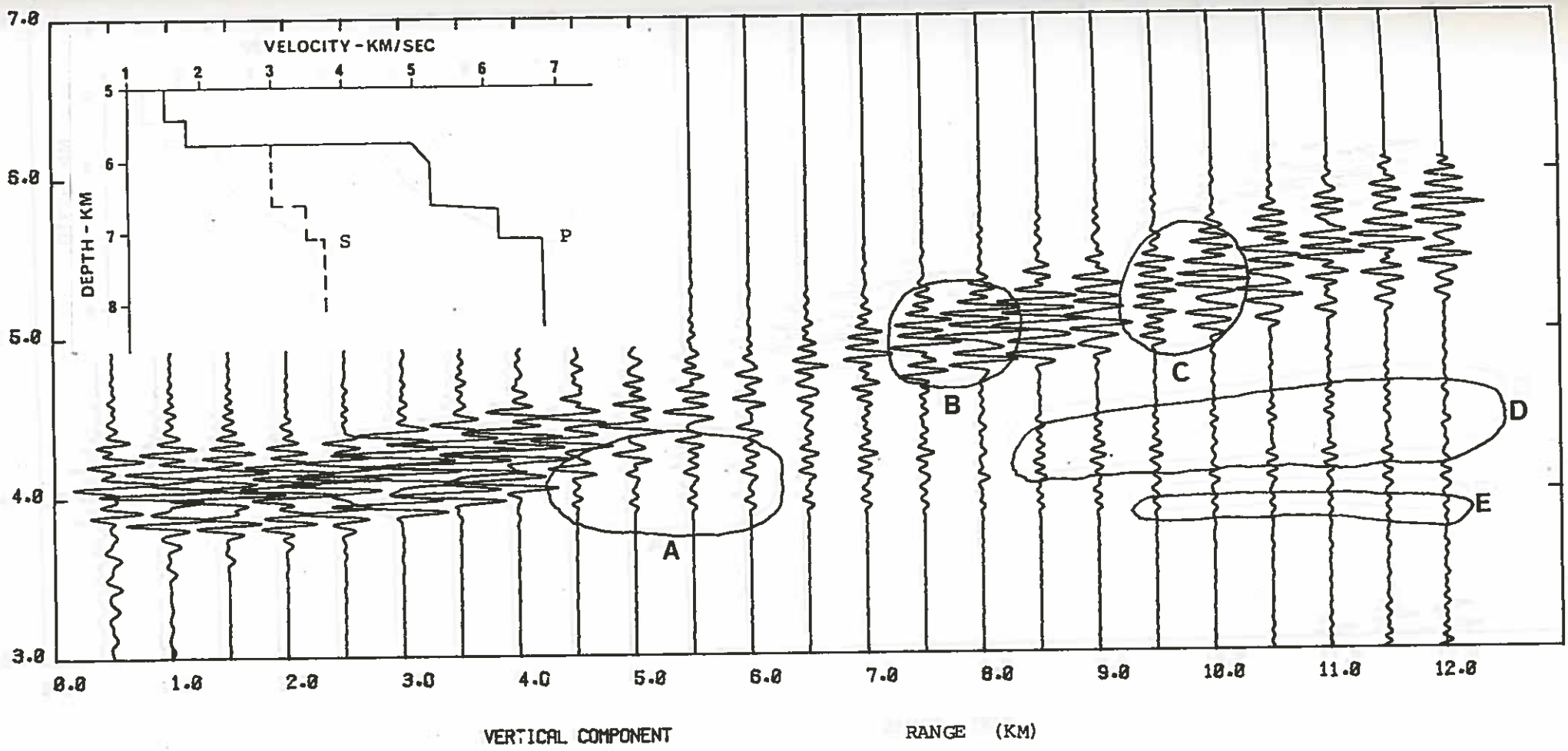

Figure 4-3-6a-c. Vertical component synthetic seismograms for the receiver at 6060 m BRF. The models are discussed in the text.

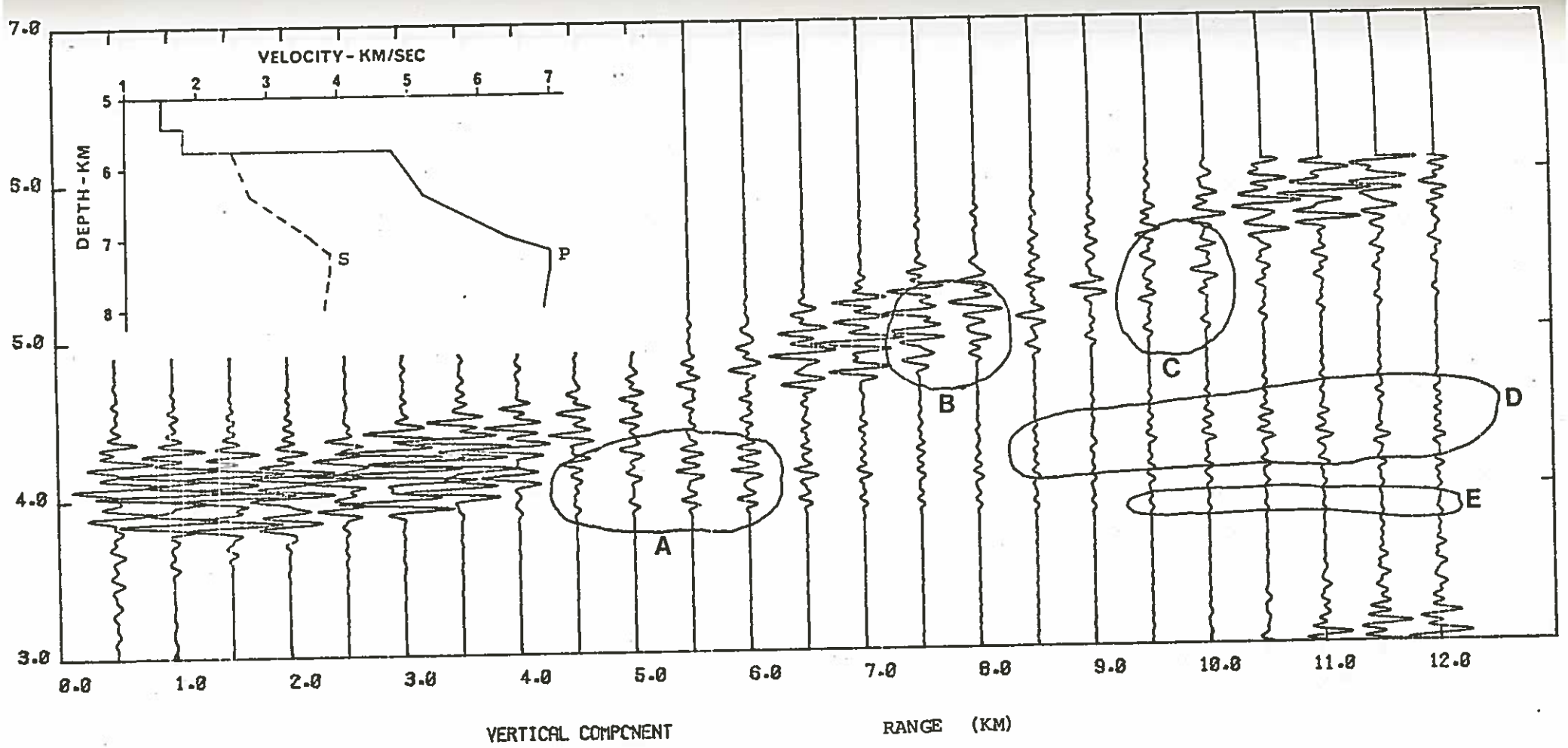
VELOCITY - KM/SEC
1
2
3
4
5
6
7
DEPTH - KM
5
6
7
8
S
P
7.0
6.0
5.0
4.0
3.0
A
B
C
D
E
0.0
1.0
2.0
3.0
4.0
5.0
6.0
7.0
8.0
9.0
10.0
11.0
12.0
VERTICAL COMPONENT
RANGE (KM)

Figure 4-3-6b

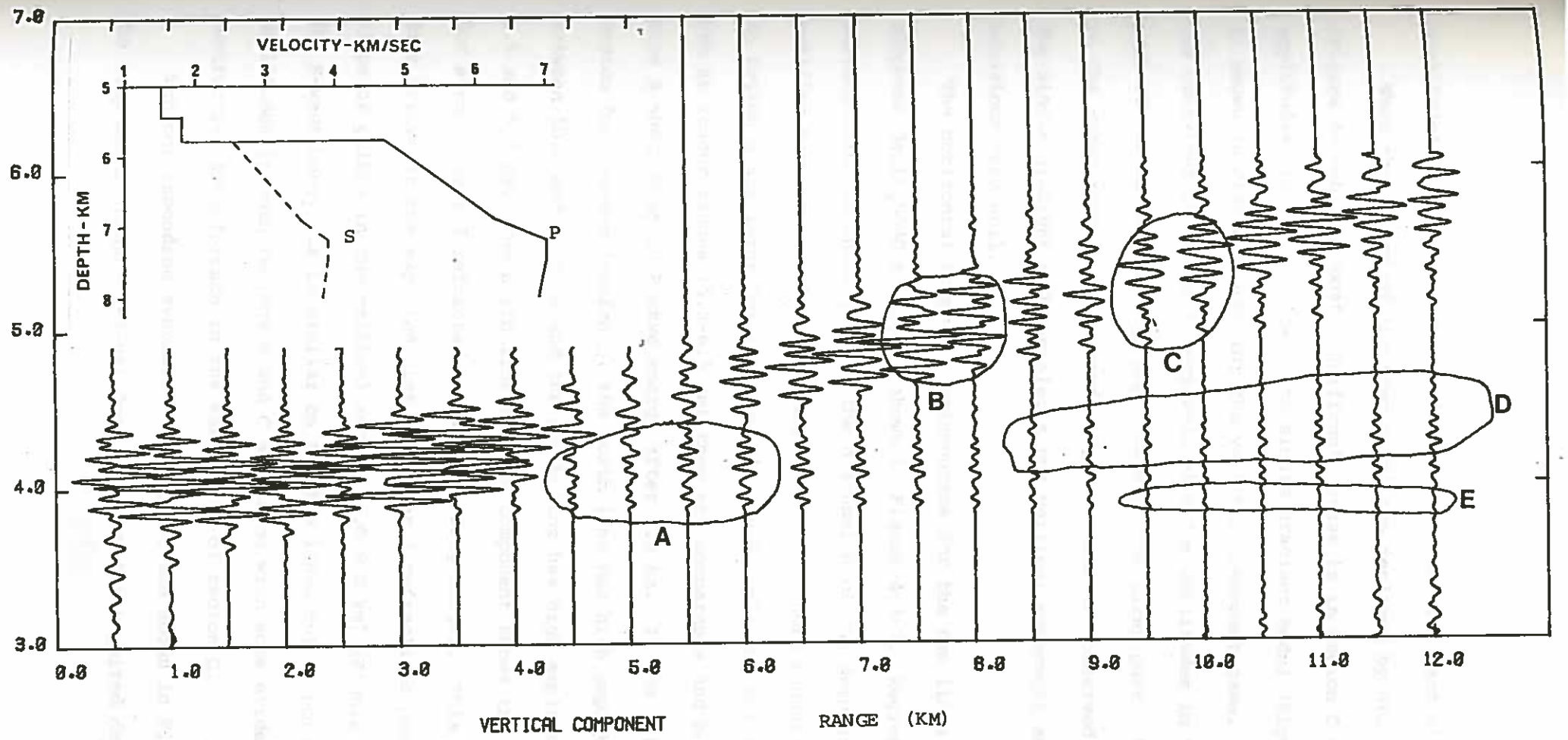
VELOCITY-KM/SEC
1
2
3
4
5
6
7
DEPTH-KM
5
6
7
8
S
P
7.0
6.0
5.0
4.0
3.0
A
B
C
D
E
0.0
1.0
2.0
3.0
4.0
5.0
6.0
7.0
8.0
9.0
10.0
11.0
12.0
VERTICAL COMPONENT
RANGE (KM)

Figure 4-3-6c

amplitudes on all lines particularly in the earlier part of the region.

When the layers of the step model are replaced by gradients (Figure 4-3-6b) the most significant change is in region C where the amplitudes are now too low. The single gradient model (Figure 4-3-4f) is shown in Figure 4-3-6c for the vertical component case. It models the behaviour in region C very well with low amplitudes in the earlier part of the region and high amplitudes in the later part. The amplitudes in the other regions agree perfectly well with the observed data. The single gradient model explains the vertical component amplitude behaviour very well.

The horizontal component seismograms for the two lines at the geophone depth, 5840 m BRF, are shown in Figure 4-3-7. Regions corresponding to those used in the discussion of the deep geophone position have been marked. The amplitudes for short ranges (4.0-5.5 km) in region A are large for the north line and small for the south line but at longer ranges (5.5-6.5 km) they are comparable and both lines show a sharp drop in P-wave energy after 6.5 km. In the interference region for P-waves (region D) the north line has high amplitudes between 10.0 and 11.0 km and the south line has high amplitudes between 8.5 and 9.5 km. The north line shallow component shows the best case for strong layer 3 refracted arrivals at long ranges. This energy does arrive at the expected time for layer 3 refractions based on the slope of points in the critical region (5.0-8.0 km) (Figure 4-2-3c). The S-wave behaviour is similar on the two lines but is not dramatic. Amplitudes in both regions B and C are large with some evidence for destructive interference in the early part of region C.

The corresponding synthetic seismograms are shown in Figure 4-3-8. The step model (Figure 4-3-8a) does not show the required drop in P-wave

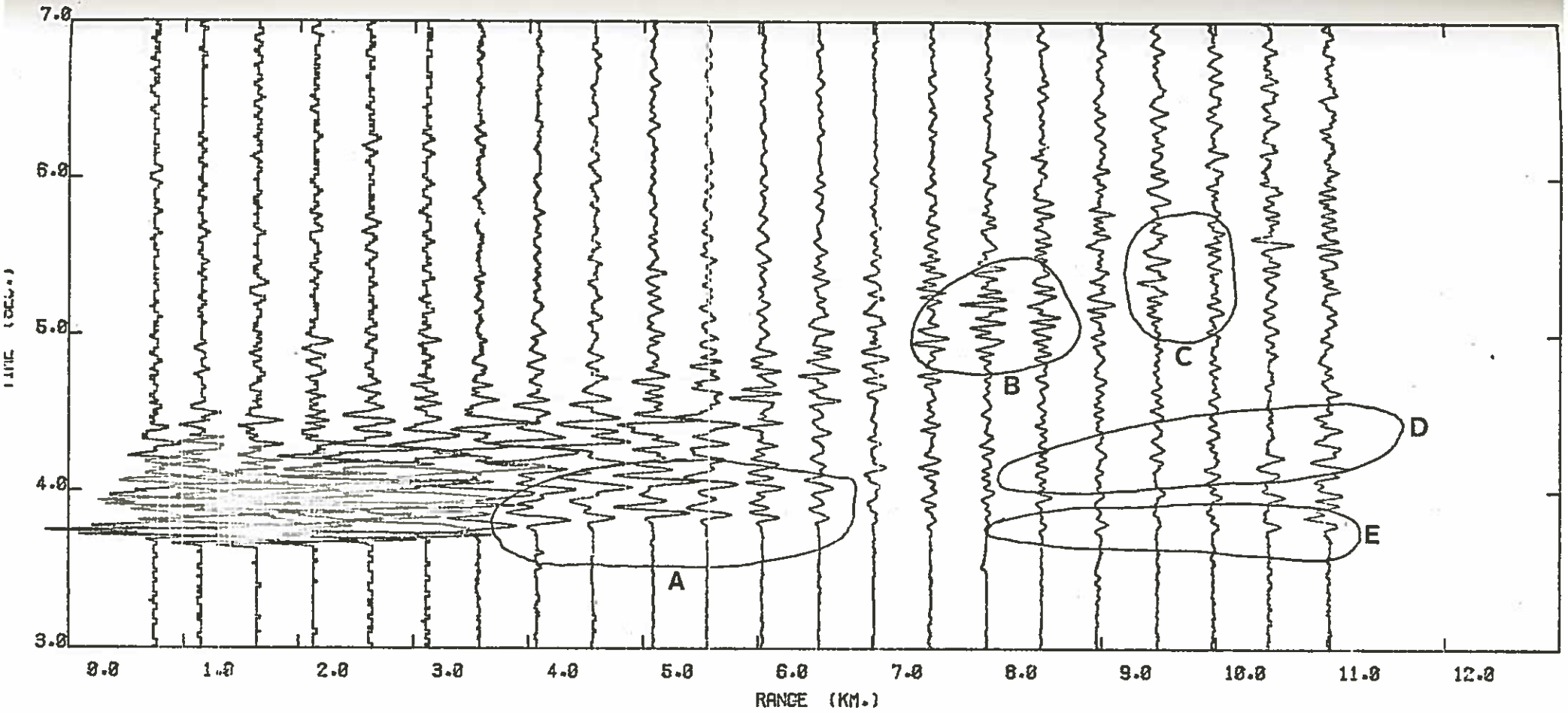

NORTH LINE - HORIZONTAL X COMPONENT - D = 5840 M. BRF

LOW PASS FILTERED AT 30.00 HZ - REDUCTION VELOCITY OF 6.00 KM/SEC
AMPLITUDES WEIGHTED BY (R/7.0)**2.9 FOR R>7.0 KM.

Figure 4-3-7a&b.Horizontal component seismograms for the receiver at 5840 m BRF. The areas marked are discussed in the text.

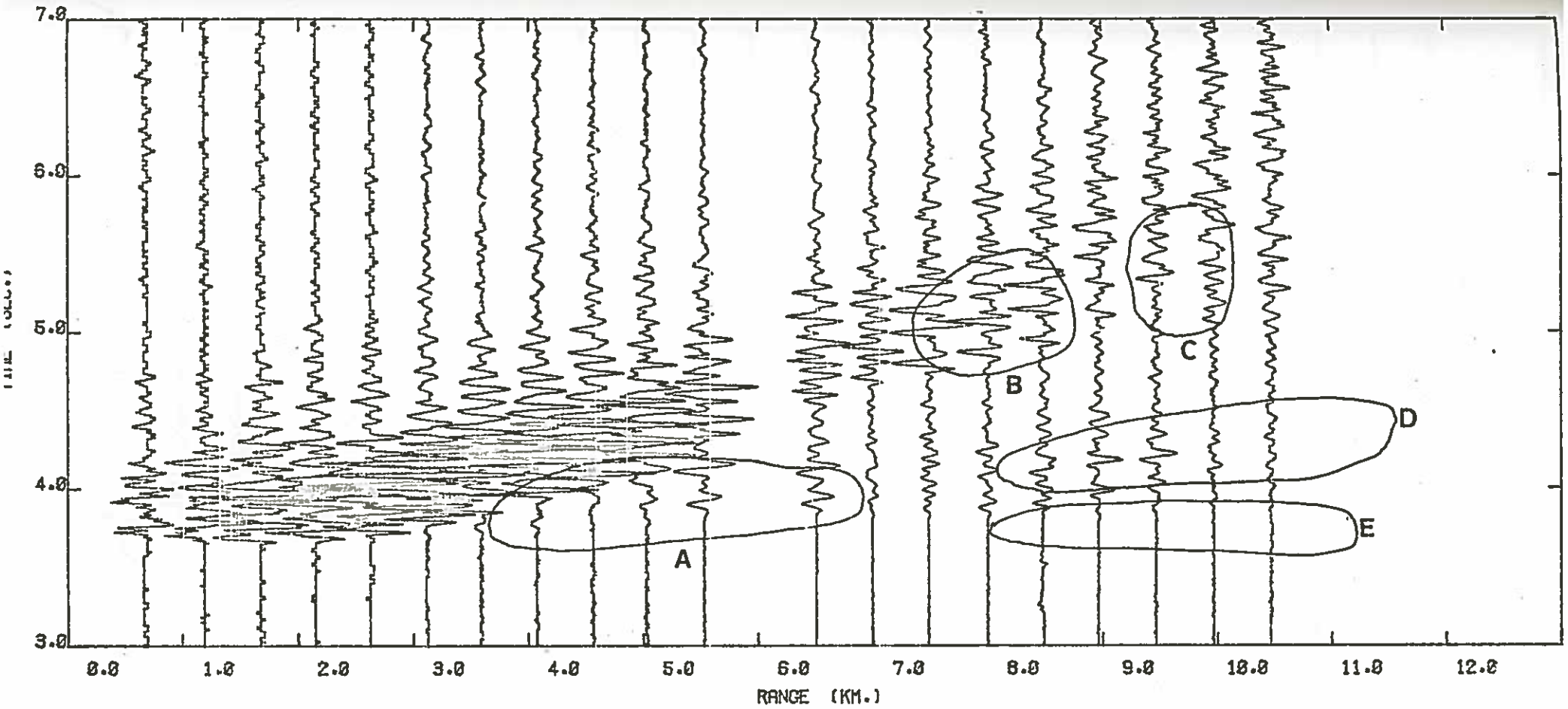

SOUTH LINE - HORIZONTAL X COMPONENT - D = 5840 M. BRF

LOW PASS FILTERED AT 30.00 HZ - REDUCTION VELOCITY OF 6.00 KM/SEC
AMPLITUDES WEIGHTED BY (R/7.0)**2.9 FOR R>7.0 KM.

Figure 4-3-7b

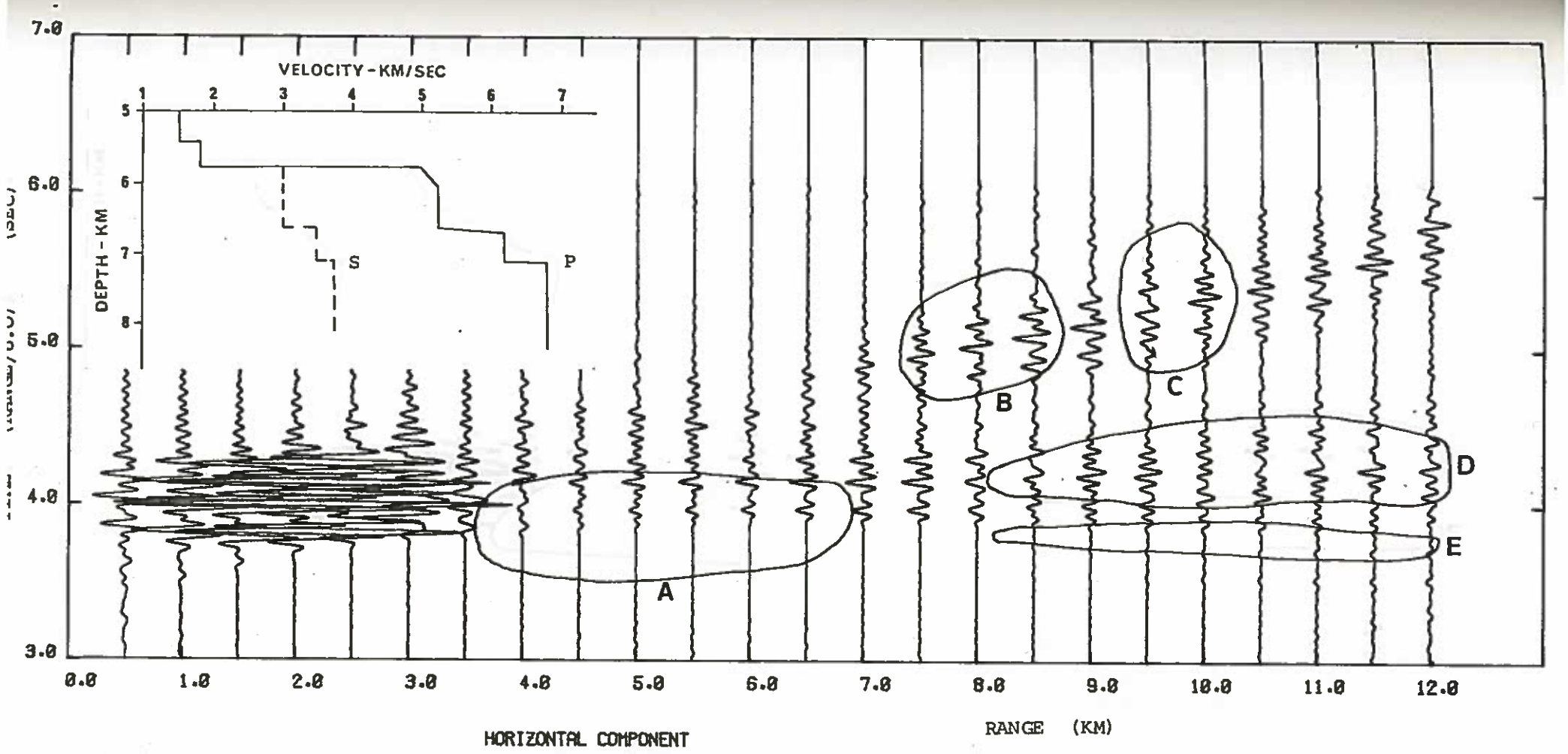

Figure 4-3-8a,b&c. Horizontal component synthetic seismograms for the receiver at 5840 m BRF. The models are discussed in the text.

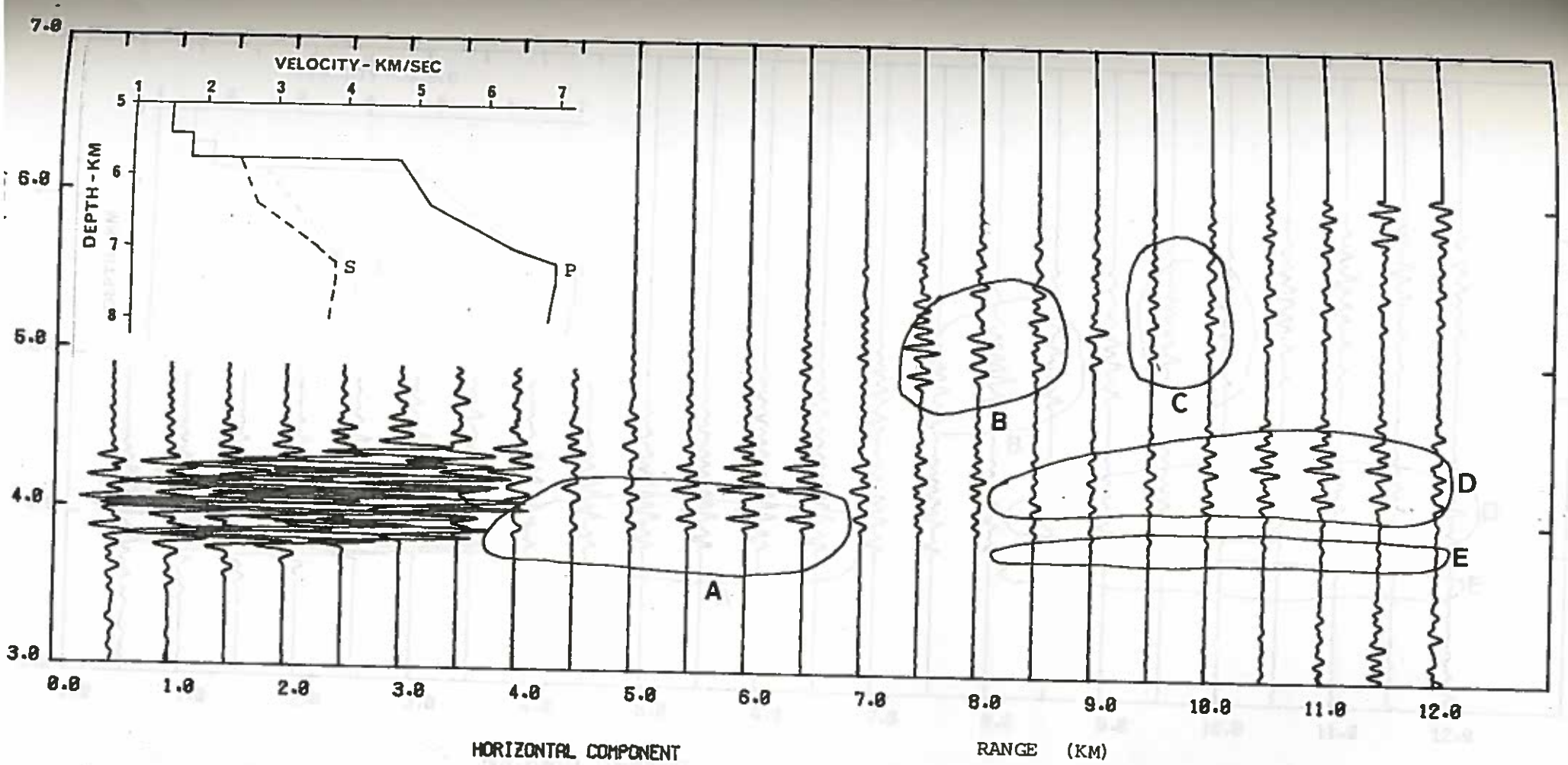
VELOCITY - KM/SEC
1
2
3
4
5
6
7
DEPTH - KM
5
6
7
8
S
P
7.0
6.0
5.0
4.0
3.0
A
B
C
D
E
0.0
1.0
2.0
3.0
4.0
5.0
6.0
7.0
8.0
9.0
10.0
11.0
12.0
HORIZONTAL COMPONENT
RANGE (KM)

Figure 4-3-8b

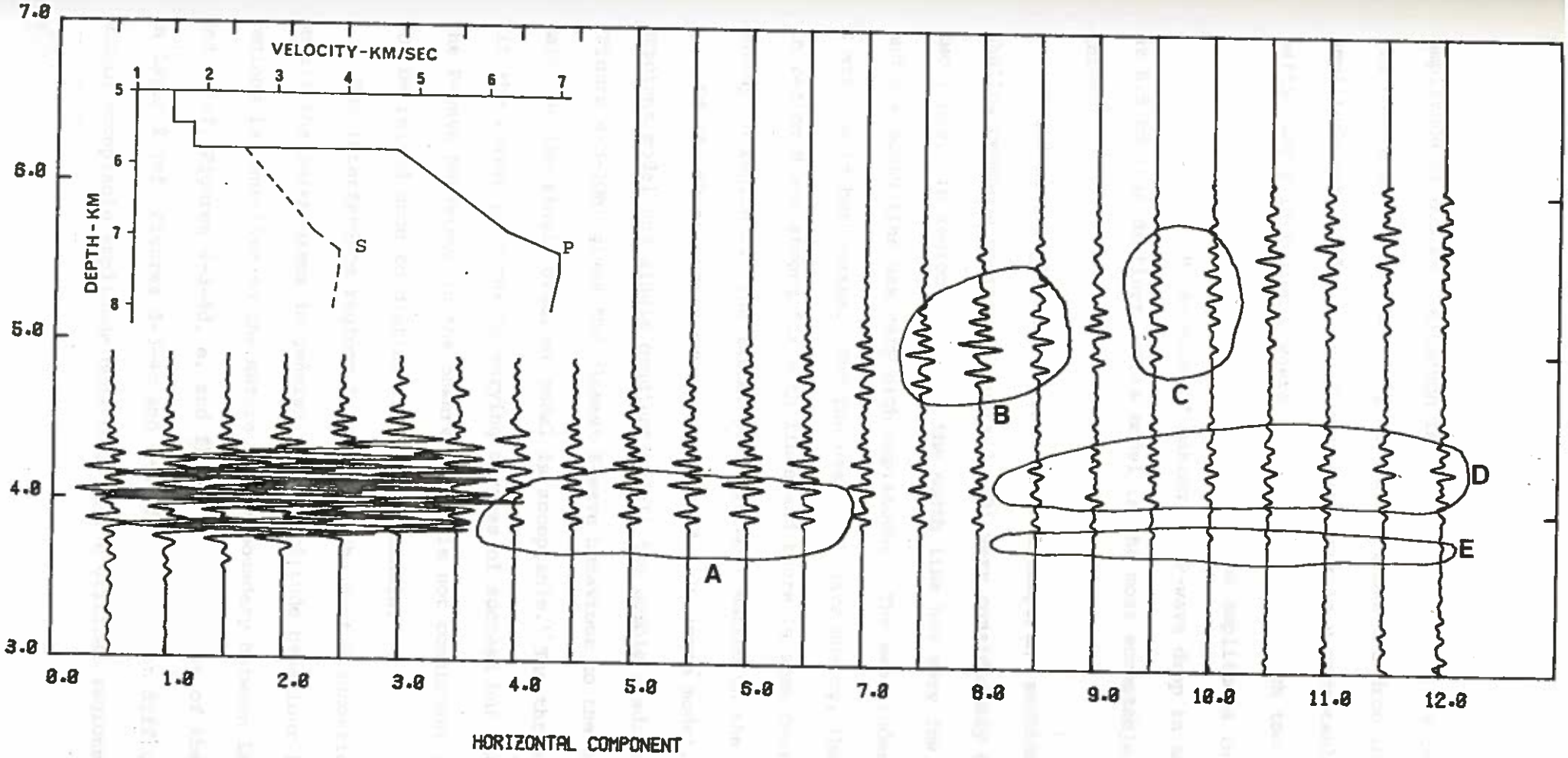
VELOCITY-KM/SEC
1
2
3
4
5
6
7
DEPTH-KM
5
6
7
8
S
P
7.0
6.0
5.0
4.0
3.0
A
B
C
D
E
0.0
1.0
2.0
3.0
4.0
5.0
6.0
7.0
8.0
9.0
10.0
11.0
12.0
HORIZONTAL COMPONENT
RANGE (KM)

Figure 4-3-8c

amplitude at 6.5 km., although in other respects it is acceptable. The double gradient model (Figure 4-3-8b) shows the drop in P-wave amplitude very well but the S-wave behaviour is unacceptable particularly in region C where the amplitudes are much too low. In the single gradient model (Figure 4-3-8c) the amplitudes in region C are increased at the expense of making the P-wave drop in amplitude at 6.5 km less distinct. This model is the most acceptable of the three.

The P-wave amplitudes on the vertical component sections for the shallow geophone position (Figure 4-3-9) vary considerably between the two lines. In regions A and D, the north line has very low amplitudes and the south line has very high amplitudes. The amplitudes in region E are low in both cases. For the case of S-wave energy, the amplitudes in region B are strong for both lines and there is some decrease in energy in region C. The latter point is most marked on the south line.

Of the three models shown in Figure 4-3-10 (step model, double gradient model and single gradient model) the double gradient model (Figure 4-3-10b) gives the closest S-wave behaviour to the observed data but the single gradient model is acceptable. The three models fit the P-wave patterns to varying degrees of success but because the P-wave behaviour in the observed data is not consistent it can not be relied upon to distinguish between models.

The interference regions D and C are the most diagnostic regions on all the seismograms in general. The amplitude behaviour in these regions is sensitive to the nature of the boundary between layers 2 and 3 (cf. Figures 4-3-4d, e, and f) and to the nature of the gradients in layer 2 (cf. Figures 4-3-4c and 4-3-4f). It is not difficult to obtain acceptable amplitude behaviour in the critical regions A and B.

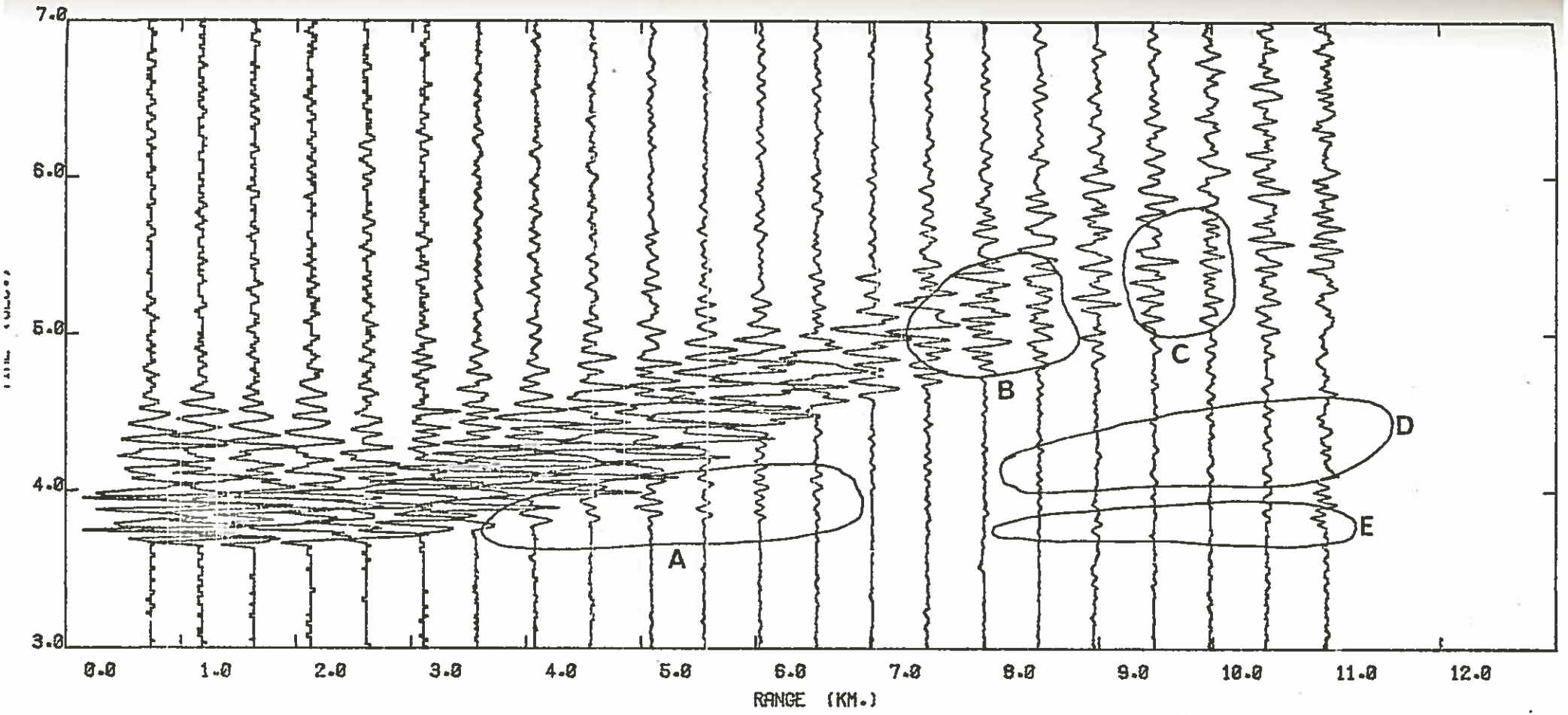

NORTH LINE - VERTICAL COMPONENT - D = 5840 M. BRF

LOW PASS FILTERED AT 30.00 HZ - REDUCTION VELOCITY OF 6.00 KM/SEC
AMPLITUDES WEIGHTED BY (R/7.0)**2.9 FOR R>7.0 KM.

Figure 4-3-9a&b. Vertical component seismograms for the receiver at 5840 BRF. The areas marked are discussed in the text.

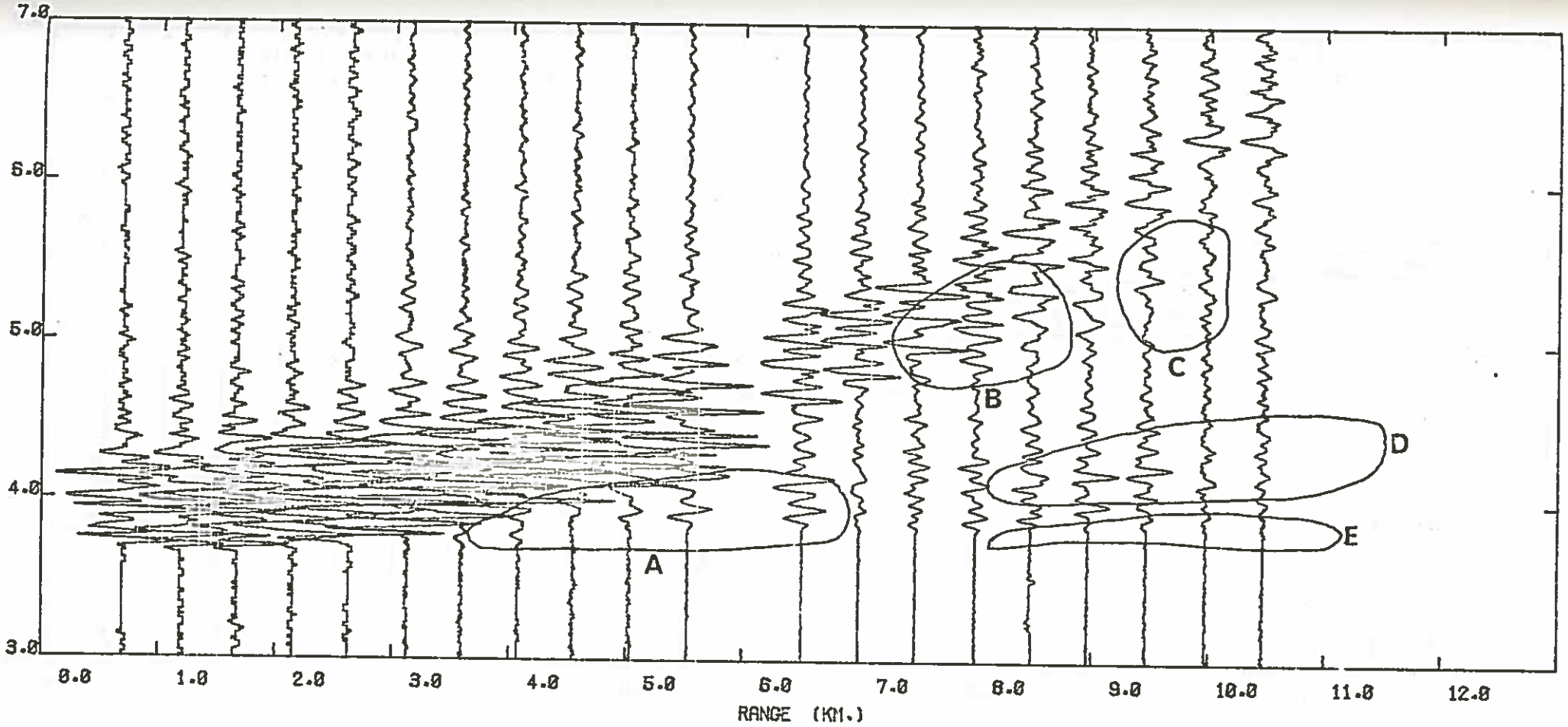

SOUTH LINE - VERTICAL COMPONENT - D = 5840 M. BRF

LOW PASS FILTERED AT 30.00 HZ - REDUCTION VELOCITY OF 6.00 KM/SEC
AMPLITUDES WEIGHTED BY (R/7.0)**2.9 FOR R>7.0 KM.

Figure 4-3-9b

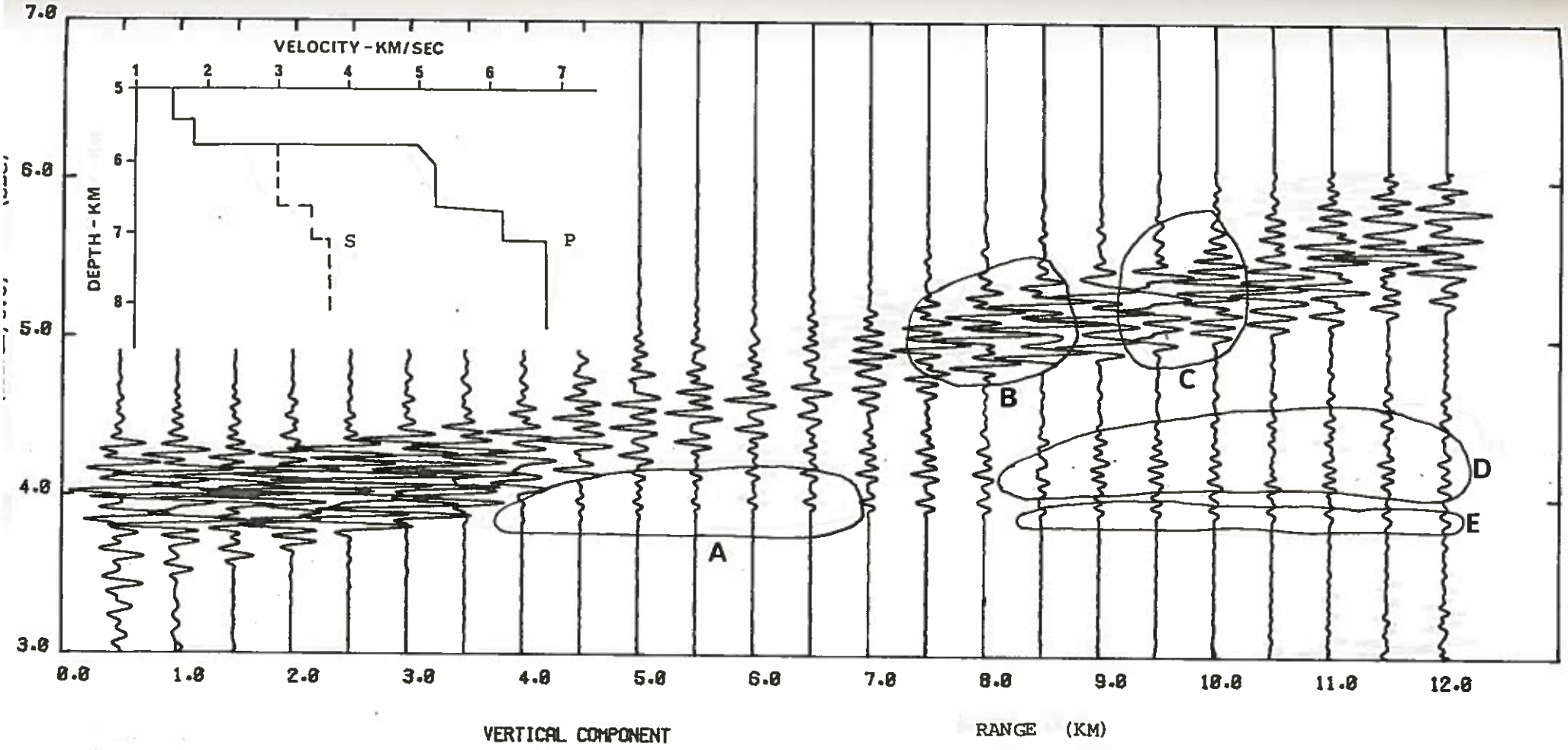

Figure 4-3-10a,b&c. Vertical component synthetic seismograms for the receiver at 5840 m BRF. The models are discussed in the text.

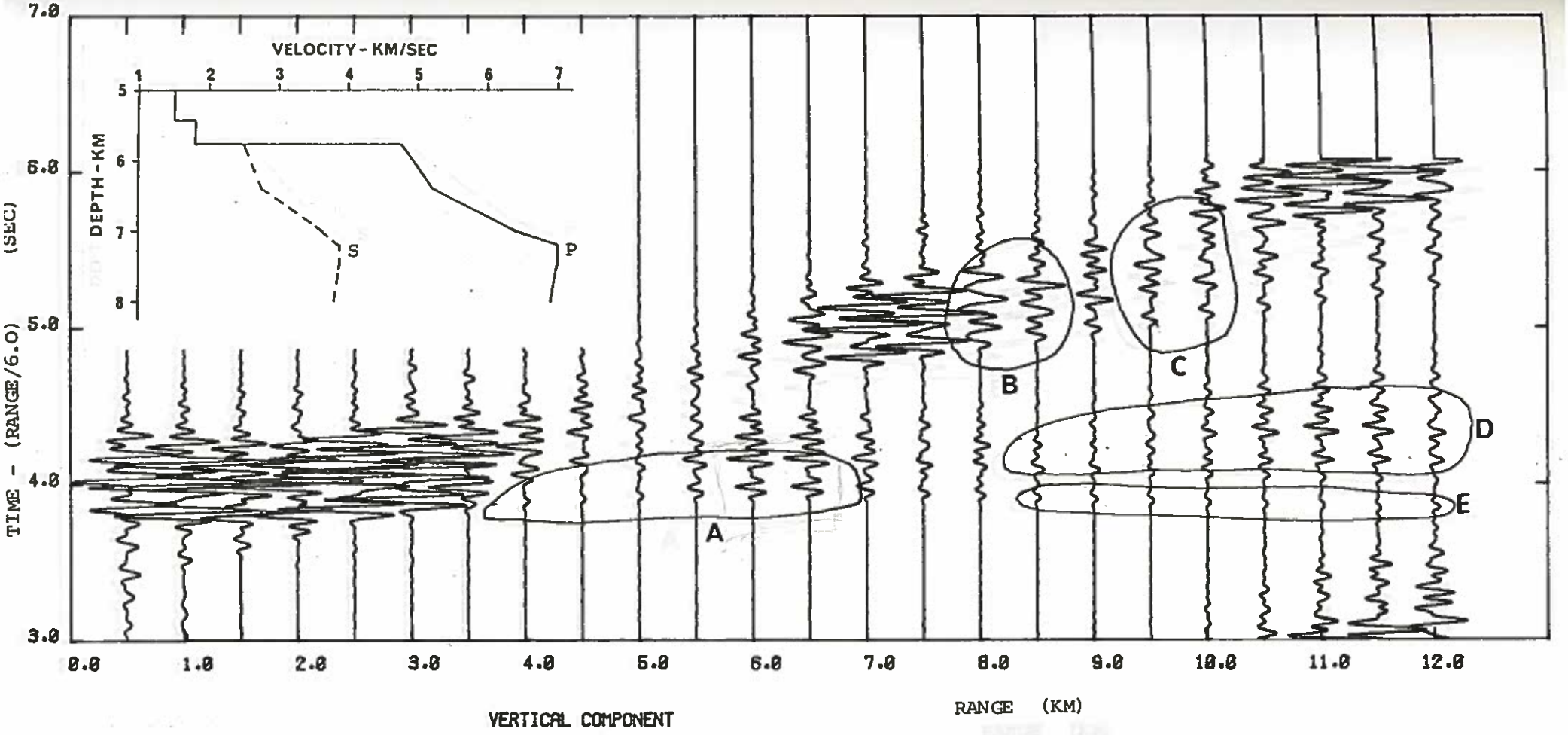

Figure 4-3-10b

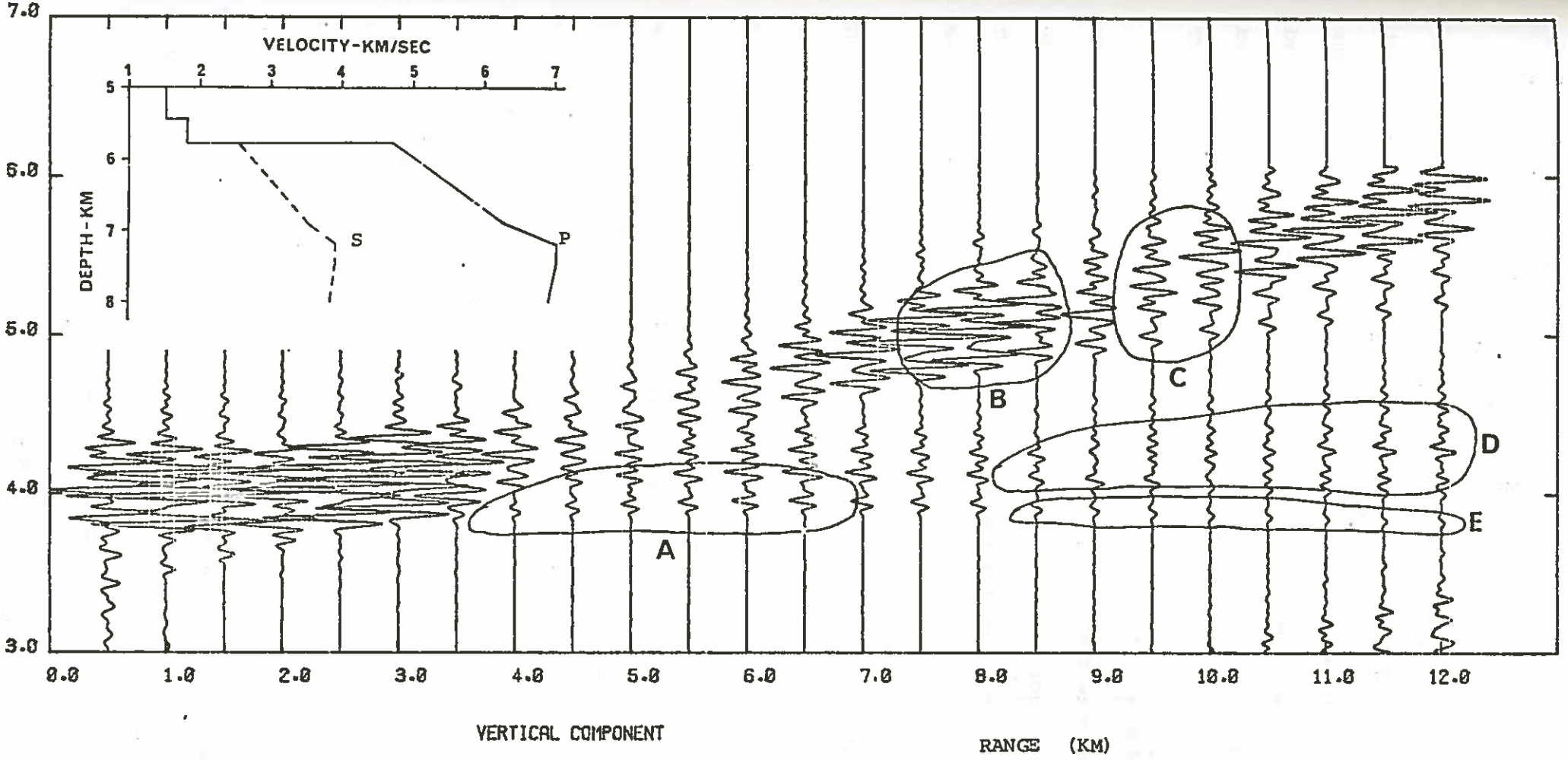

Figure 4-3-10c

It is only necessary to eliminate constant velocity sections in upper layer 2 (e.g. Figure 4-3-4a and 4-3-4b). Low layer 3 refraction amplitudes at large ranges (region E) can be most easily modelled by putting a low velocity zone in layer 3, but the effect could also be accomplished by altering the gradients in layer 2 (e.g. Figure 4-3-4e). The latter case is the most geologically acceptable.*

What has the introduction of a gradient done to the direct wave arrivals? Figure 4-3-11 demonstrates that the direct wave arrivals are unaffected in character by changing gradients at the top of layer 2. This figure confirms the conclusions of Section 2-3e) by showing actual seismograms with realistic wavelets.

The travel time curves corresponding to the step model, double gradient model and single gradient model are shown in Figure 4-3-12 with the picked arrival times of Figure 4-2-3. All three curves are acceptable within the overall error of the points.

In view of all the data and models shown the single gradient model is preferred because it fits most of the data. The step model is definitely not acceptable. The preference for gradients rather than steps concurs with work of Whitmarsh (1978) and Kennett and Orcutt (1976). The higher velocities at the bottom of layer 2 are consistent with Houtz and Ewing's (1976) results.

An attempt to make any more than a general analysis of the seismograms would be unwise. Comparison of seismograms for all the lines (Appendix C) shows significant variation in amplitude patterns within ranges of a kilometre or so, even for lines in the same direction. This behaviour may be simply a result of inadequate coupling between the geophone and the rock. Alternatively the effects of varying shot signal, unknown basement topography, lateral variations (possibly in the

---

* Since this account was written a velocity inversion in layer 3 has been reported by Salisbury and Christensen (1978).

It is only necessary to eliminate constant velocity sections in upper layer 2 (e.g. Figure 4-3-4a and 4-3-4b). Low layer 3 refraction amplitudes at large ranges (region E) can be most easily modelled by putting a low velocity zone in layer 3, but the effect could also be accomplished by altering the gradients in layer 2 (e.g. Figure 4-3-4e). The latter case is the most geologically acceptable.*

What has the introduction of a gradient done to the direct wave arrivals? Figure 4-3-11 demonstrates that the direct wave arrivals are unaffected in character by changing gradients at the top of layer 2. This figure confirms the conclusions of Section 2-3e) by showing actual seismograms with realistic wavelets.

The travel time curves corresponding to the step model, double gradient model and single gradient model are shown in Figure 4-3-12 with the picked arrival times of Figure 4-2-3. All three curves are acceptable within the overall error of the points.

In view of all the data and models shown the single gradient model is preferred because it fits most of the data. The step model is definitely not acceptable. The preference for gradients rather than steps concurs with work of Whitmarsh (1978) and Kennett and Orcutt (1976). The higher velocities at the bottom of layer 2 are consistent with Houtz and Ewing's (1976) results.

An attempt to make any more than a general analysis of the seismograms would be unwise. Comparison of seismograms for all the lines (Appendix C) shows significant variation in amplitude patterns within ranges of a kilometre or so, even for lines in the same direction. This behaviour may be simply a result of inadequate coupling between the geophone and the rock. Alternatively the effects of varying shot signal, unknown basement topography, lateral variations (possibly in the

---

* Since this account was written a velocity inversion in layer 3 has been reported by Salisbury and Christensen (1978).

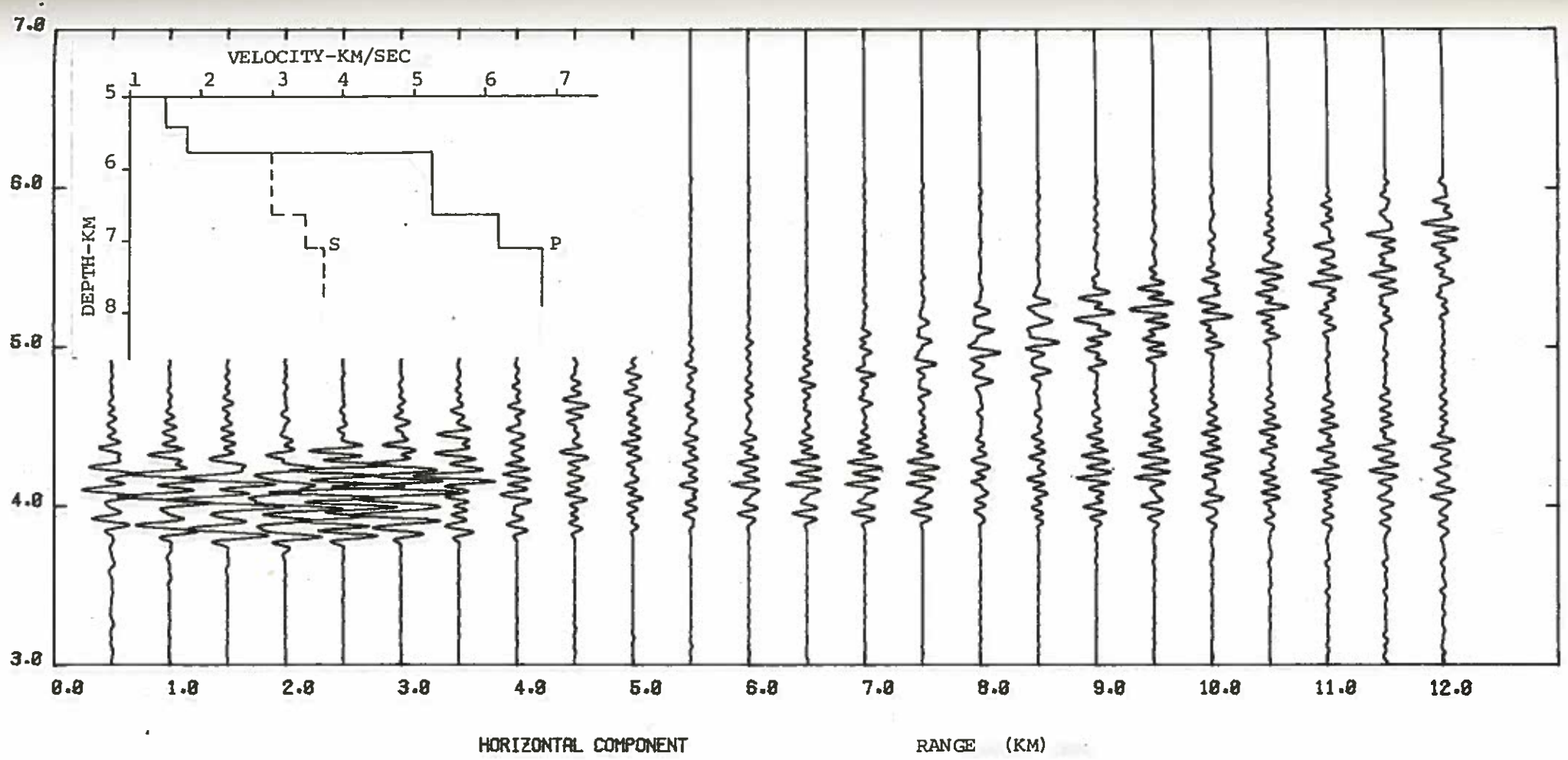

Figure 4-3-11a,b&c. Synthetic seismograms to demonstrate that the character of the direct wave arrival (the first arrival up to 5.0 km) is insensitive to gradients at the top of layer 2. The receiver is at 6060 m BRF.

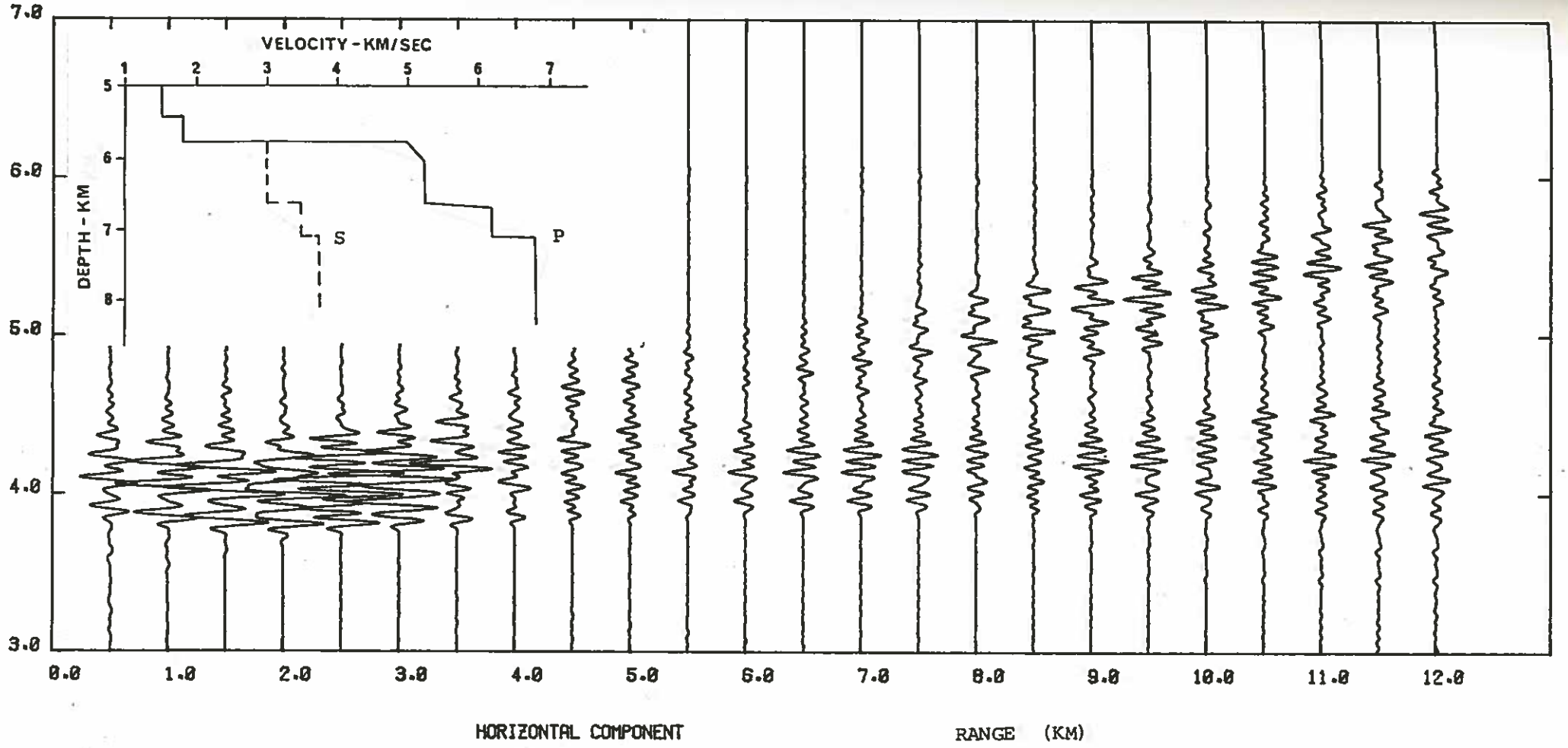

Figure 4-3-11b

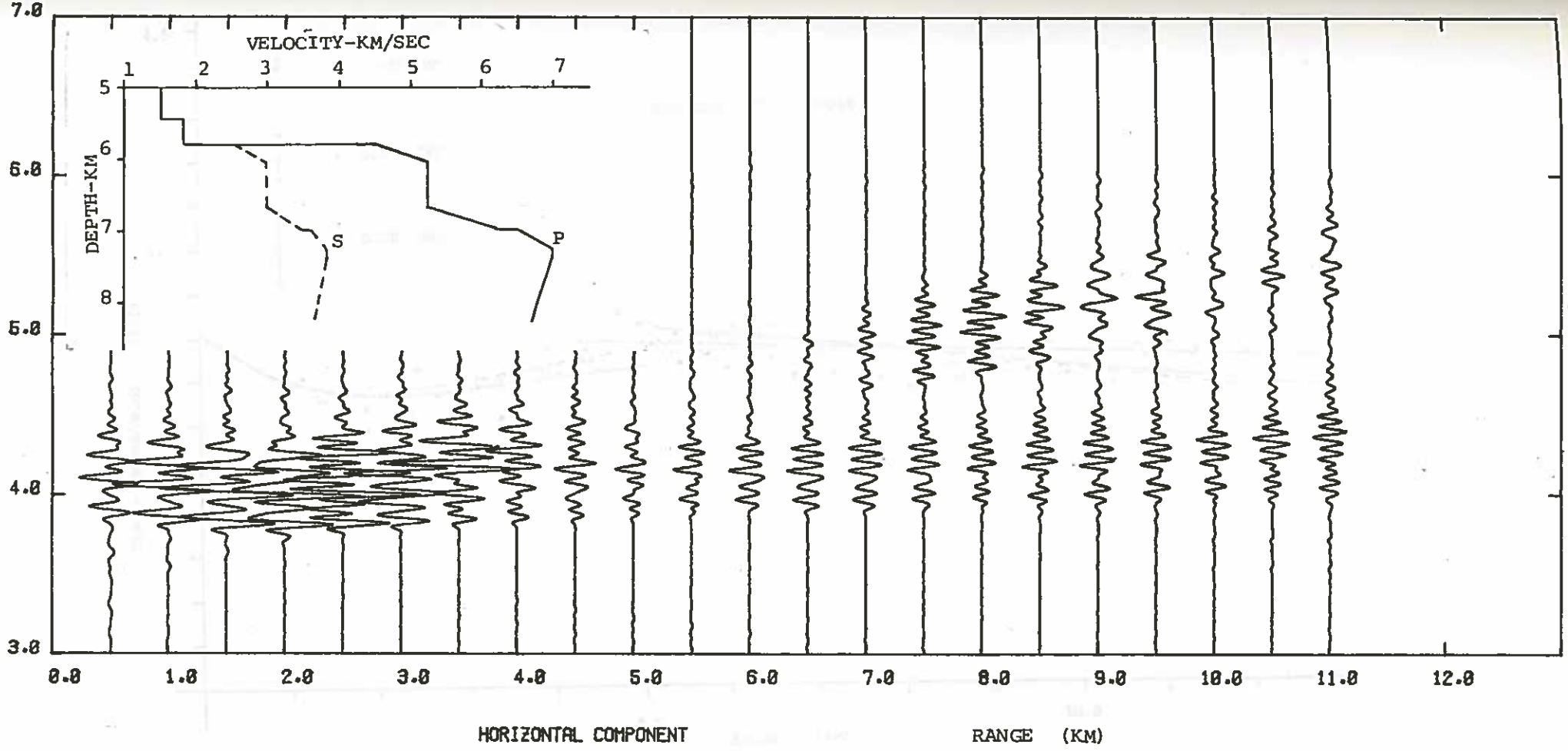

Figure 4-3-11c

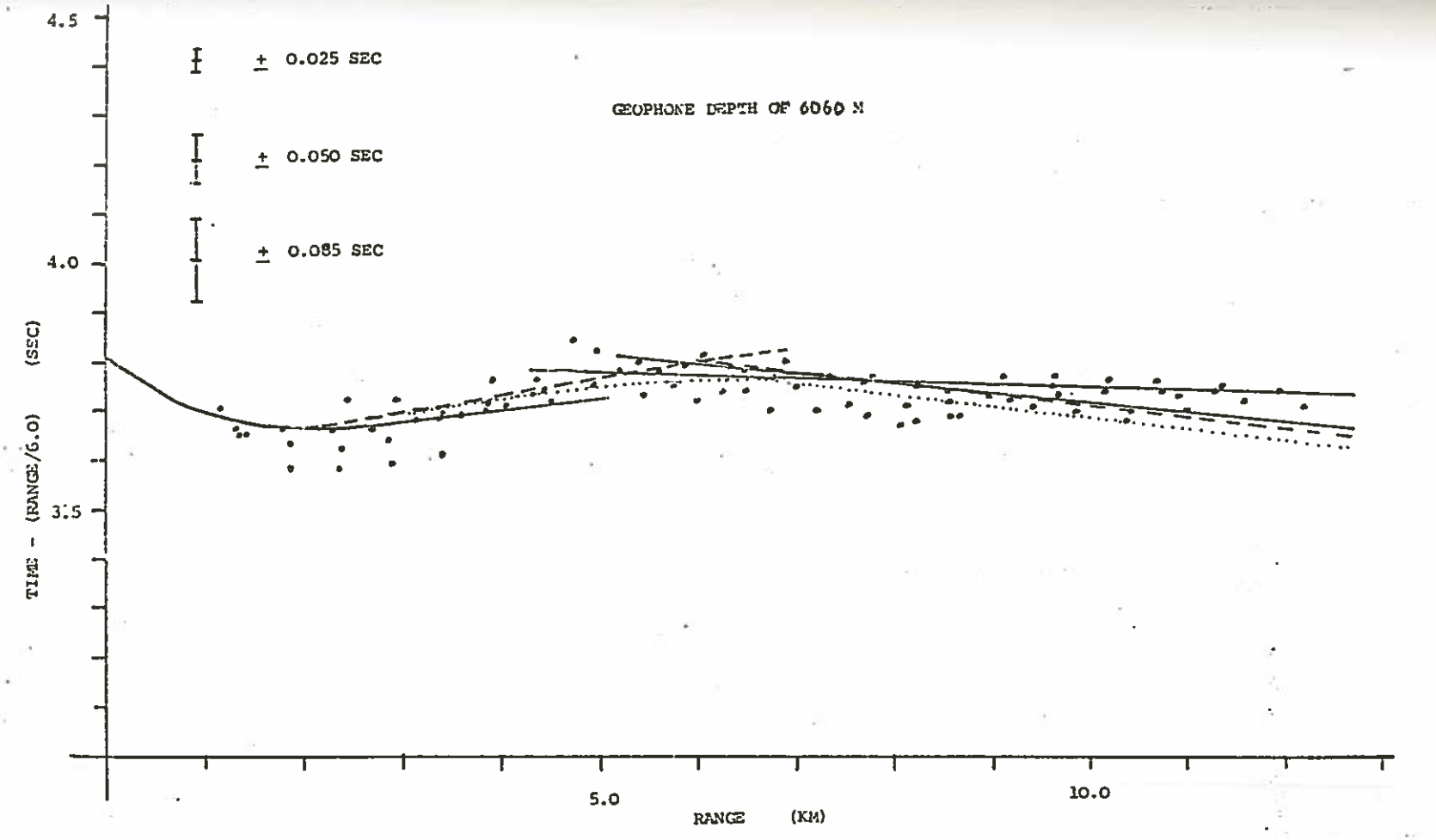

Figure 4-3-12a-d. Travel time curves for the step model (———), double gradient model (- - -) and single gradient model (.....). The error bars are given as in Figure 4-2-3. Figures a) and c) are for P-wave arrivals and Figures b) and d) are for S-wave arrivals. For the gradient models the curves represent first arrival times. Hence these curves are not within the error bars for some arrivals at large ranges (>10.0 km) which are interference arrivals (see the text).

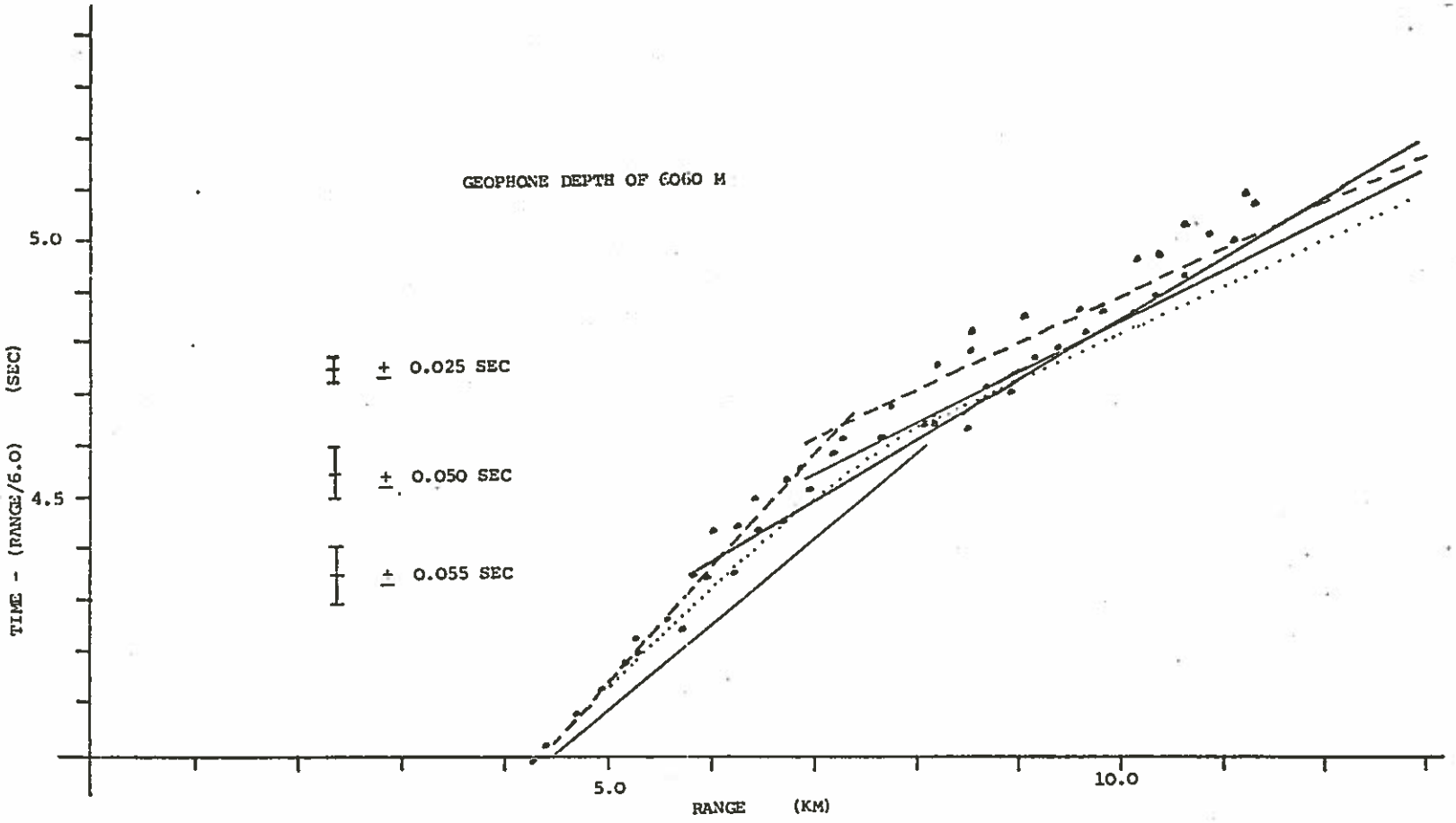

Figure 4-3-12b

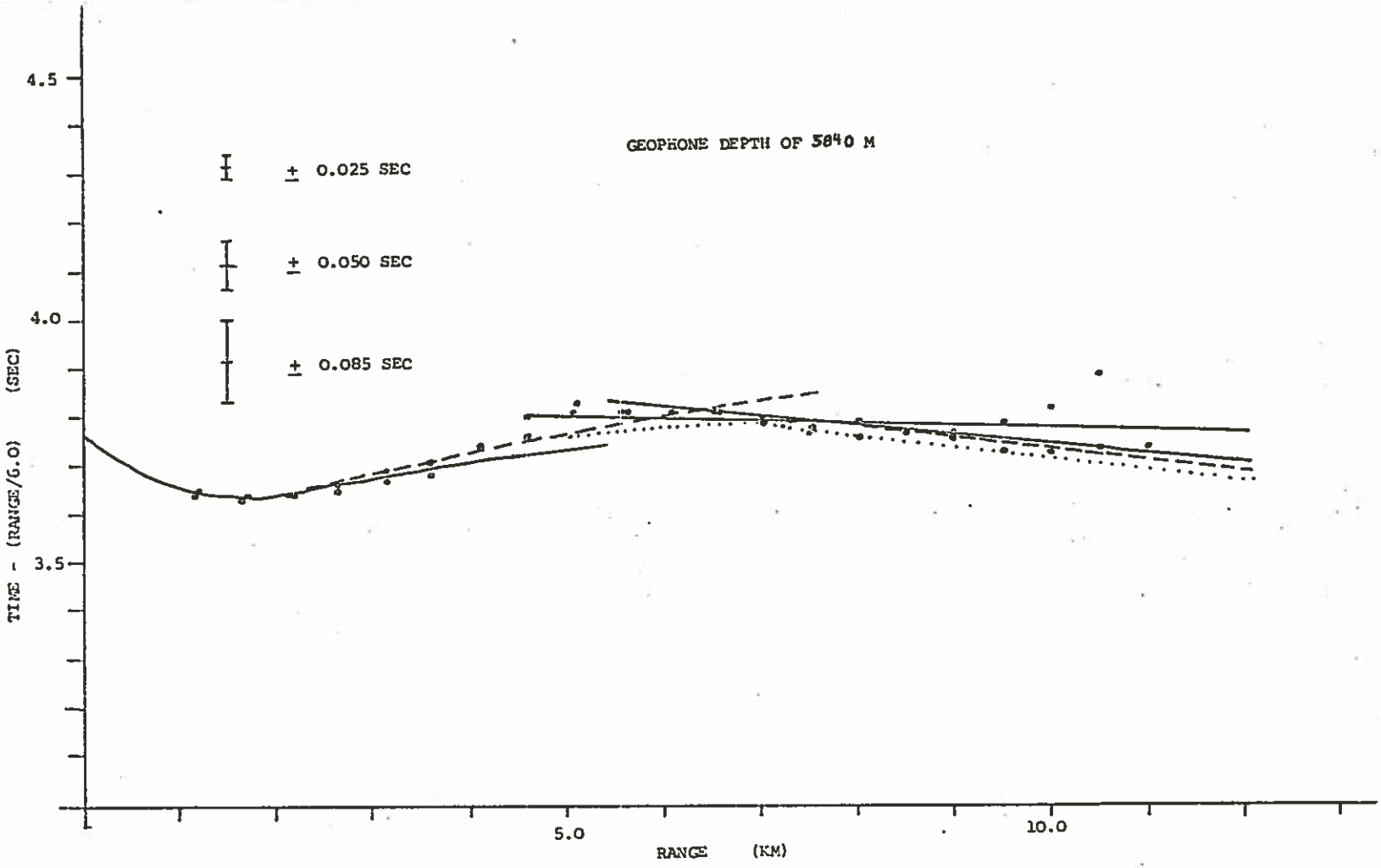

Figure 4-3-12c

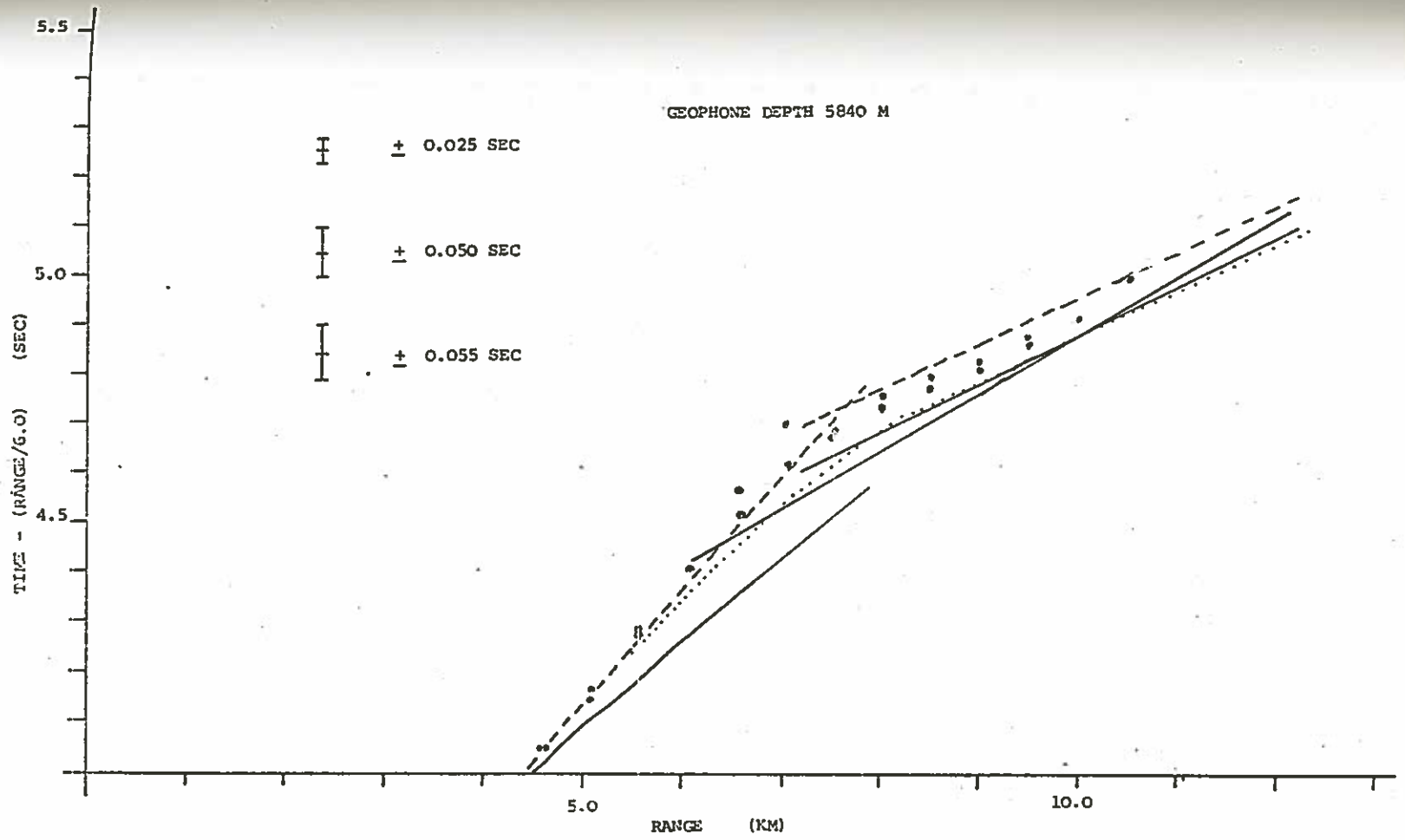

Figure 4-3-12d

mid-sediment reflector) and inhomogeneities may be too complex to model adequately by conventional means. Interference effects at ranges where more than one ray path arrive at the same time (e.g. regions C and D) have particularly sensitive amplitudes. The use of synthetic seismograms is essential to study these regions.

c). Attenuation

The effect of varying the attenuation factor, Q, on the seismograms can be seen in Figure 4-3-13 where horizontal component synthetic seismograms for the single gradient model are shown for Q= ∞ , 200 and 50. The same Q was used for both P-waves and S-waves. The difference between a Q of ∞ and a Q of 200 is noticeable but is much smaller than the variation in amplitude between lines. The same features of constructive and destructive interference as mentioned above can be observed equally well on both sections. A Q of 50 changes the appearance of the seismogram considerably. A Q of 50 obviously is unreasonable for S-waves but it is tempting to consider it for P-wave energy on the east and west lines (cf. Figure 4-3-13c with Figures 4-3-2c and d). However, as will be discussed in the next paragraph and shown in Figure 4-3-14 the total energy for arrivals from all three components does not indicate a significantly lower Q for different azimuths. The apparent low energy for the horizontal examples of east and west lines just indicates that for these lines, the vertical component and the other horizontal component have a greater share of the energy. This behaviour suggests that a polarization analysis of this data may be worthwhile.

Figure 4-3-14 shows amplitude distance plots of the first P-wave and S-wave arrivals for the four lines shot with the geophone at 6060 m BRF.

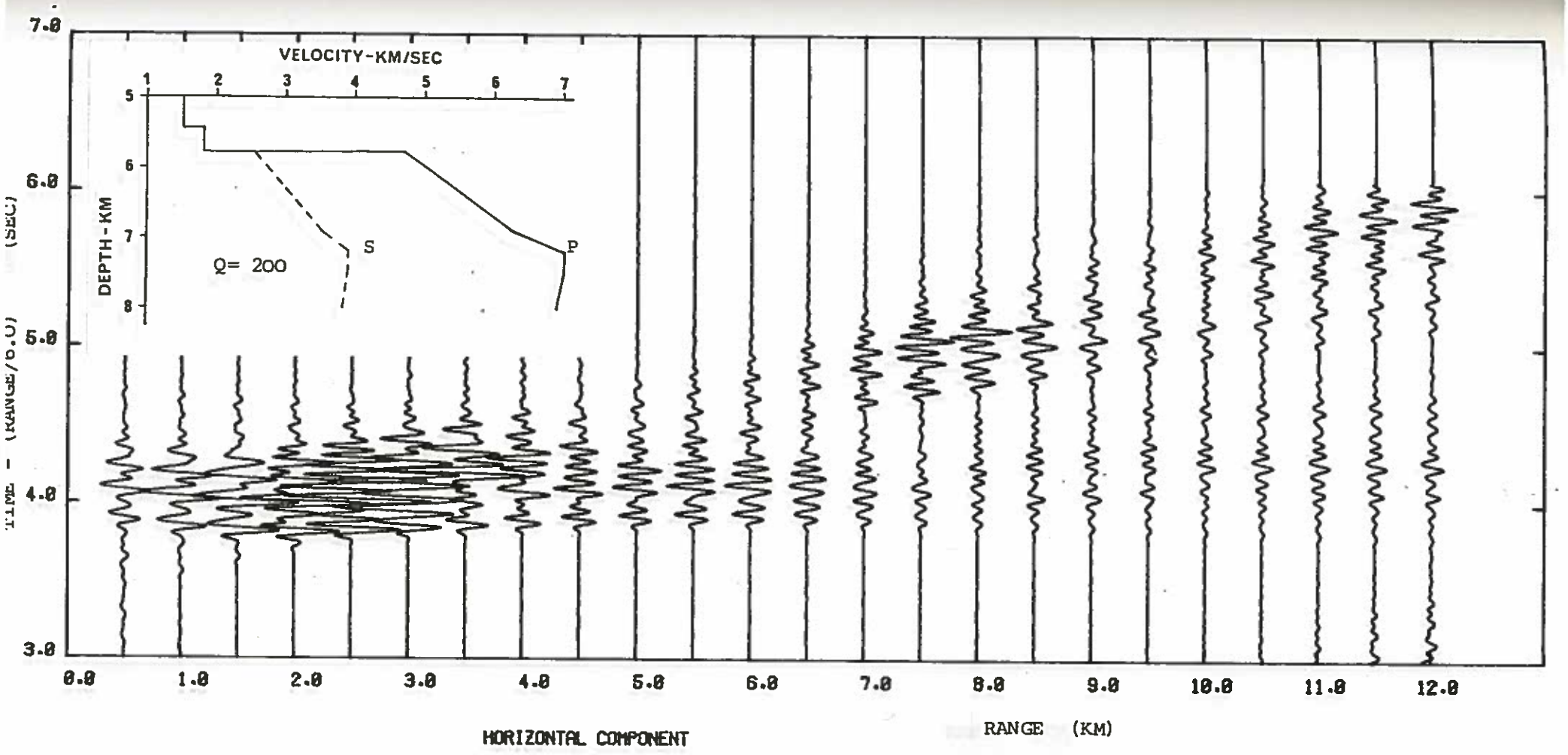

Figure 4-3-13a,b&c. Synthetic seismograms for the single gradient model to show the effect of attenuation (Q =∞, 200, 50). The figures are discussed in the text.

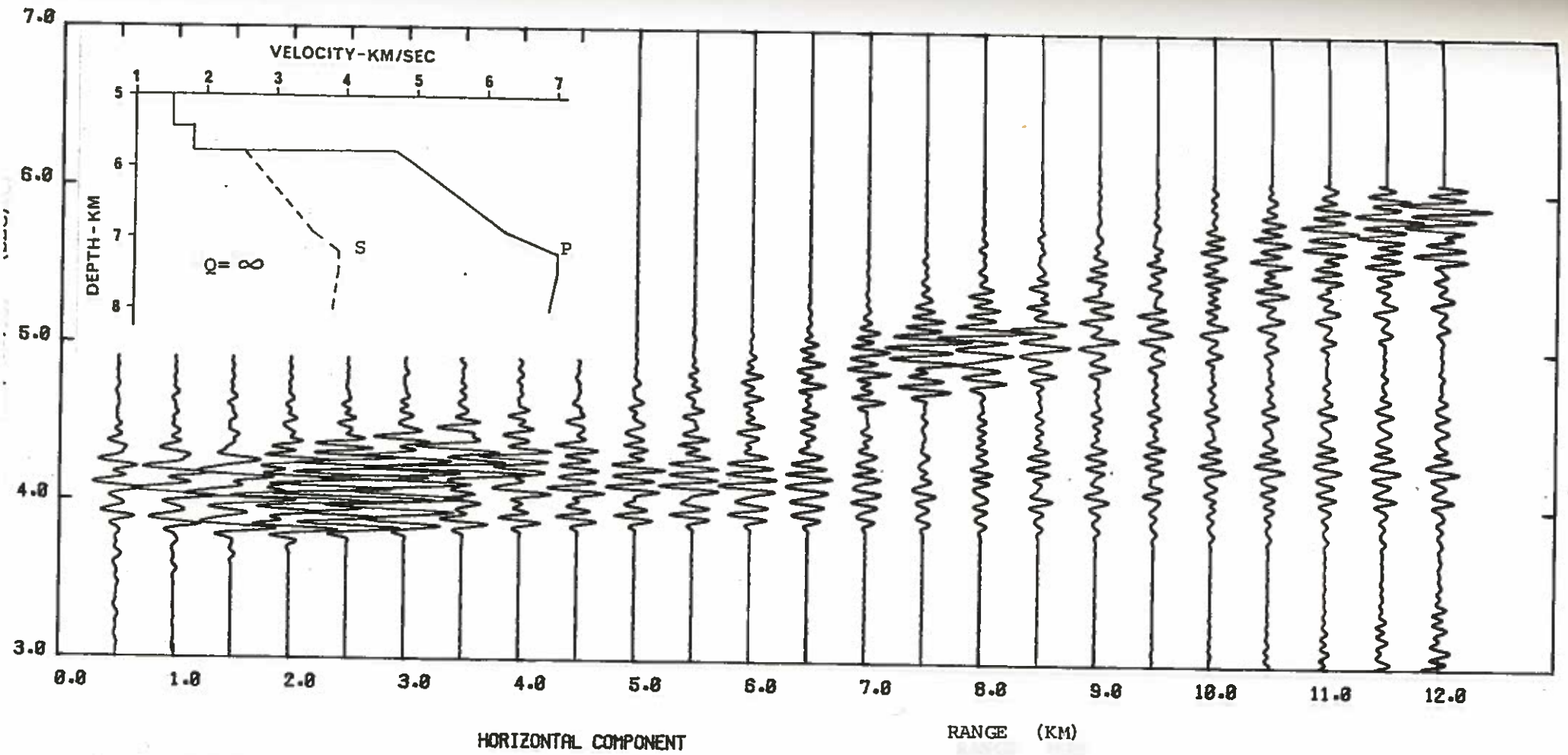

Figure 4-3-13b

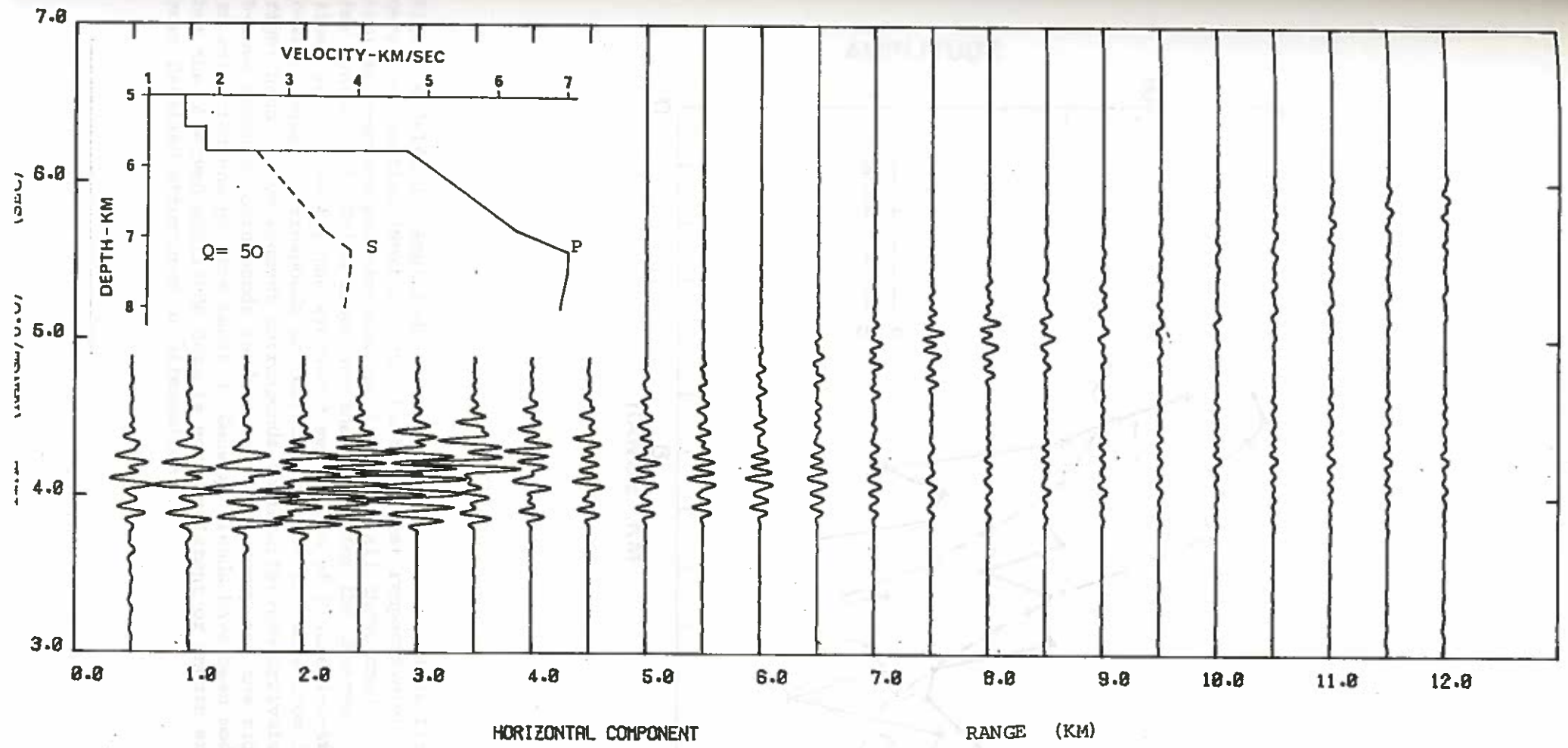

Figure 4-3-13c

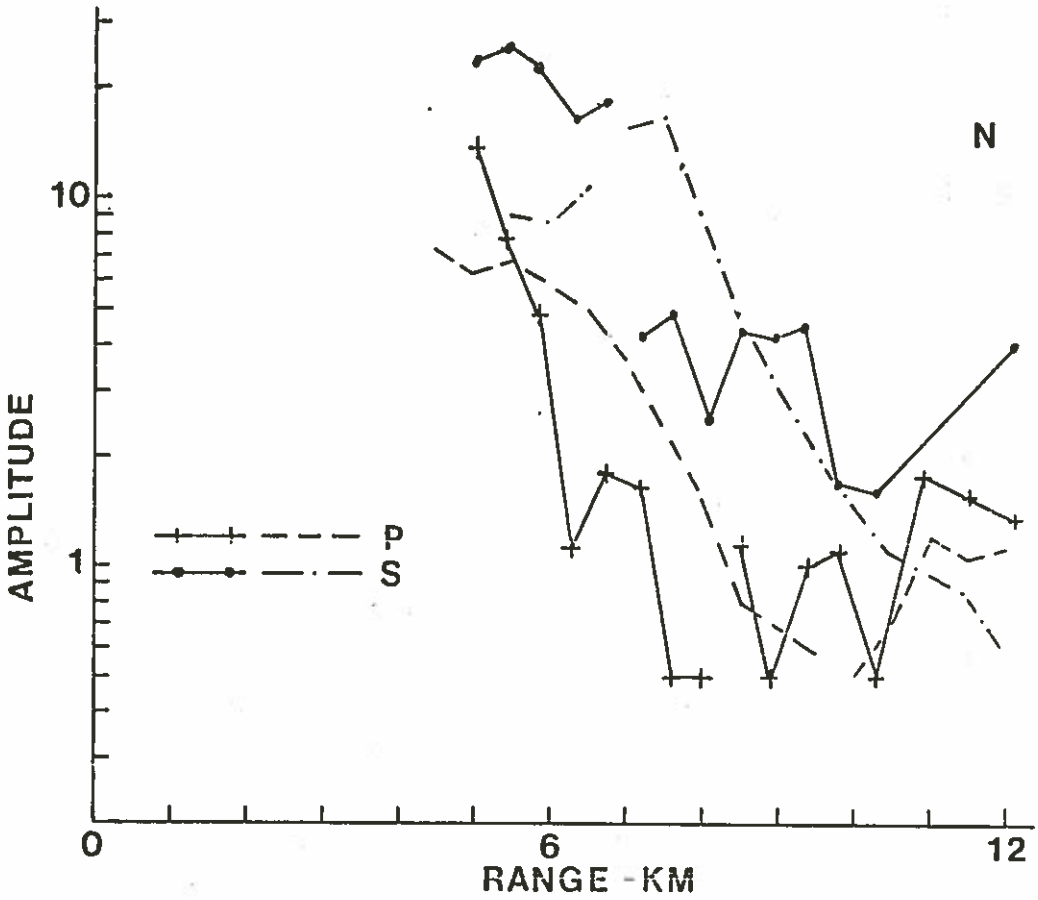

Figure 4-3-14a-d. Amplitude-distance curves for the lines fired at the deep geophone position (North, South, East and West respectively). Amplitudes are the root-mean-square peak-to-peak amplitudes of all three components (two components for synthetics). Solid lines are the curves for the observed data and the dashed lines are curves for the synthetic seismogram of Figure 4-3-4f. The left hand P-wave segment corresponds to refracted P-wave arrivals from layer 3 and the right hand P-wave segment corresponds to interference arrivals. The left hand S-wave segment corresponds to direct S-wave energy and the right hand segment to refracted energy from Layer 3. General trends have been modelled adequately but the observed amplitude data is not consistent or smooth enough to consider more detailed structures or attenuation.

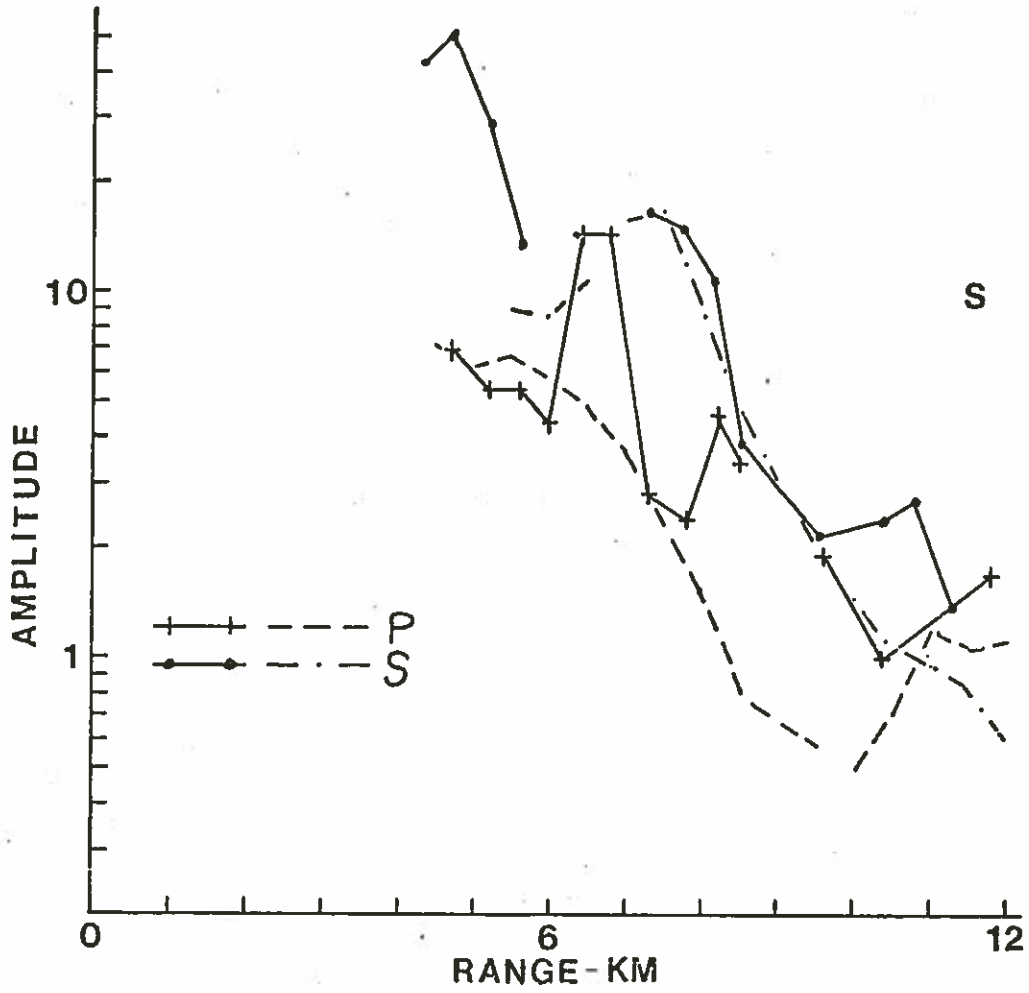

Figure 4-3-14b

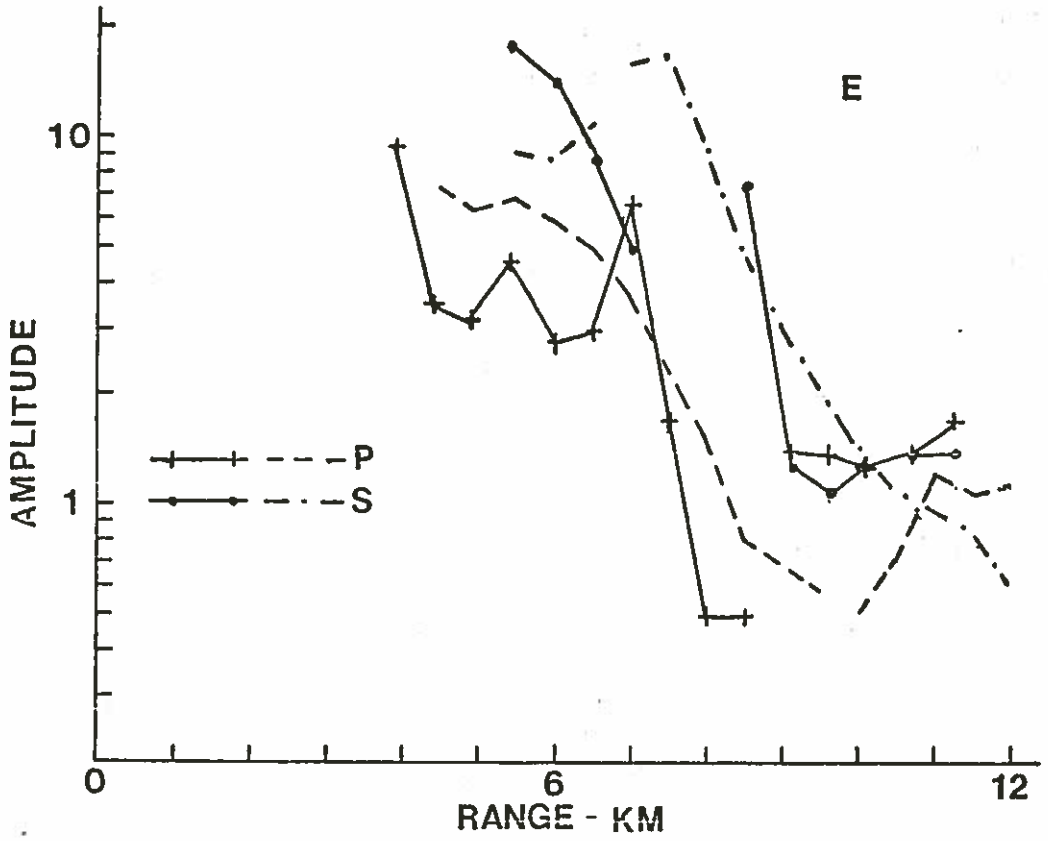

Figure 4-3-14c

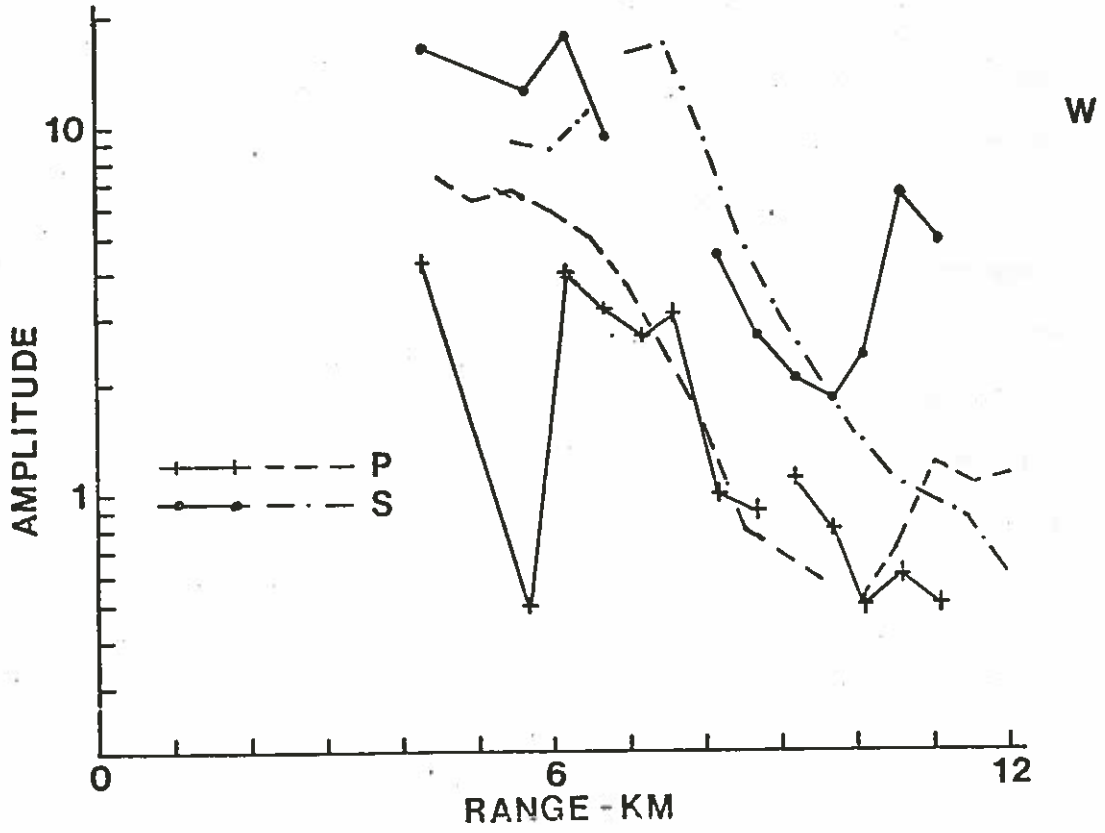

Figure 4-3-14d

Superimposed on the plots is the corresponding curve for the synthetic seismogram based on the single gradient model (Figure 4-3-4f). At ranges less than 5 km it is difficult to differentiate between P-wave and S-wave phases. Consequently this data applies to critically refracted arrivals and apparent arrivals caused by interference effects (Sections 4-2a) and 4-3b)). The compressional wave amplitude curves for real data vary considerably and there are no significant differences between north-south and east-west lines. Shear wave behaviour is more stable. The east and north P-wave amplitudes are similar, the south amplitudes are strongest and the west amplitudes weakest. These trends do not correspond to the velocity trends mentioned in Section 4-2b). Possible causes of this general erratic behaviour are discussed in Section 4-3b). The shallow depth seismograms have not been analysed because they show the same erratic behaviour.

The variations in source signal were checked by looking at the sea bottom reflection on the shallow hydrophone (Appendix C). The reflection coefficient is approximately constant for sub-critical reflections for a water-solid interface (Grant and West, 1965). The amplitudes of the reflected arrivals are generally stable with extrema to about a factor of 2 from the mean. None of these extrema corresponds to the significant peaks and troughs of the geophone amplitude-distance curves.

Considering the large amplitude variations between lines it would be ludicrous to attempt to measure an attenuation effect of the size indicated in Figure 2-3-7.

CHAPTER 5

DISCUSSION AND CONCLUSIONS

5-1. POROSITY DETERMINATIONS FROM THE OSE

Although compressional and shear wave velocity information is insufficient to sort out the effects of porosity and aspect ratio of cracks (as discussed in Section 1-5f)) it is interesting to compare the observed velocities with empirical and theoretical velocity-porosity models. This section applies Wyllie's formula, non-interactive theory, and self-consistent theory to the OSE data.

The time-average formula (Wyllie et al, 1958) can be used to estimate porosity from compressional wave velocity but the limitations outlined in Section 1-5c) must be kept in mind. The porosity (ϕ)-velocity (V_p^*) relation is:

$$\phi = \left(\frac{V_p V_p'}{V_p - V_p'}\right) \frac{1}{V_p^*} - \left(\frac{V_p'}{V_p - V_p'}\right)$$

where primes indicate fluid properties, *'s indicate effective properties and no superscript denotes matrix properties. (The formula is expressed in this form to show clearly the slope and intercepts of a ϕ vs $1/V_p^*$ plot.) Linear regression of 227 laboratory measured velocity-porosity pairs from Holes 417A, 417D and 418 (Hamano, Hobart, Johnson and Salisbury, personal communication) gives $V_p = 6.59$ km/sec and $V_p' = 1.52$ km/sec for measurements at laboratory temperature and pressure. Using these velocities in Wyllie's formula one can calculate porosities in layer 2 which correspond to the single gradient model (Figure 4-3-4f). For the top of layer 2 with a velocity of 4.8 km/sec the porosity is

11%; for the middle of layer 2 with a velocity of 4.8 km/sec the porosity is 5%; and for the bottom of layer 2 with a velocity of 6.4 km/sec the porosity is 1%. These values, of course, assume that rock type in layer 2 is constant. The mean logged velocity in the first 0.123 km of layer 2 was 4.83 km/sec (Francheteau and Salisbury, pers. comm.) and the mean velocity of the laboratory samples was 5.15 km/sec (Hamano et al, pers. comm.), giving an in situ velocity of 5.35 km/sec. (The correction between ship-board velocities and in situ velocities in upper layer 2 is +0.2 km/sec (Hyndman, 1977).) It appears that vugginess contributes to the porosity in the top of layer 2 and that this contribution decreases with depth so that by a quarter of the way into layer 2 only microcracks (as in cores) are present. By the bottom of layer 2 even these cracks seem to be absent.

In the initial study of the short logging run in the basalts (123 m) the sonic log gave porosities between 5 to 10%, the gamma-gamma log gave porosities between 5 to 15% and the neutron log, although not calibrated for basalts, confirmed the trends in the gamma-gamma log (DSDP Leg 51 shipboard party, pers. comm.). A detailed study of the logs is in progress (Salisbury and Francheteau, pers. comm.).

To apply the non-interactive and self-consistent theoretical models to field observations it is necessary to have values for the compressional and shear wave velocities and density of the uncracked rock. The velocities can be estimated by extrapolating the velocity vs porosity curve for laboratory samples to zero porosity. Theory suggests a linear relationship between V_p^* and ϕ (Toksöz et al, 1976) as opposed to a linear relationship between $1/V_p^*$ and ϕ for Wyllie's formula. For the theoretical case, the extrapolation was performed

using the data of Hamano et al (pers. comm.) resulting in a matrix velocity of 6.2 km/sec. This value compares favourably with velocities of basalt cores at 10 kbar pressure (Christensen and Salisbury, 1972 and 1973). An estimate of the matrix shear wave velocity from the V_p^* vs Poisson's ratio relation for Leg 37 basalts of Hyndman et al (1977) is 3.3 $\pm$ 0.25 km/sec. Hamano et al (pers. comm.) gave the matrix density as 2.95 gm/cc for Leg 51, 52 and 53 basalts.

Figure 5-1-1 is a plot of porosity and aspect ratio with respect to normalized effective P and S velocities for the non-interactive theory assuming that the pores are 100% saturated with water. It is obvious that a plot of this type cannot readily distinguish between different combinations of porosity and aspect ratio. The slopes $((V_p^*/V_s^*)/(V_p/V_s))$ for the lines of equal aspect ratio are not sufficiently sensitive to changes in porosity.

In real rocks spectra of aspect ratios must be considered as demostrated by Toksöz et al (1976). It is impossible to know the aspect ratio spectrum for oceanic crust and the problem here is severely under-constrained. It may be, however, that a dominant or mean aspect ratio can be determined.

The point V_p^* = 4.8 km/sec and V_s^* = 2.6 km/sec is plotted in Figure 5-1-1 along with error bars corresponding to $\pm$ 0.2 km/sec. Porosity-aspect ratio pairs ranging from over 30% for spherical pores to ϕ = 2% for α = 0.01 are acceptable. The values corresponding to the mean point are ϕ = 3.5% and α = 0.02. The aspect ratio is reasonable but the porosity is low compared to the 8.4% average of the core samples (Hamano, pers. comm.).

Self-consistent theory is expected to apply to highly fractured rocks. Figure 5-1-2 shows crack density (ε) and saturated crack

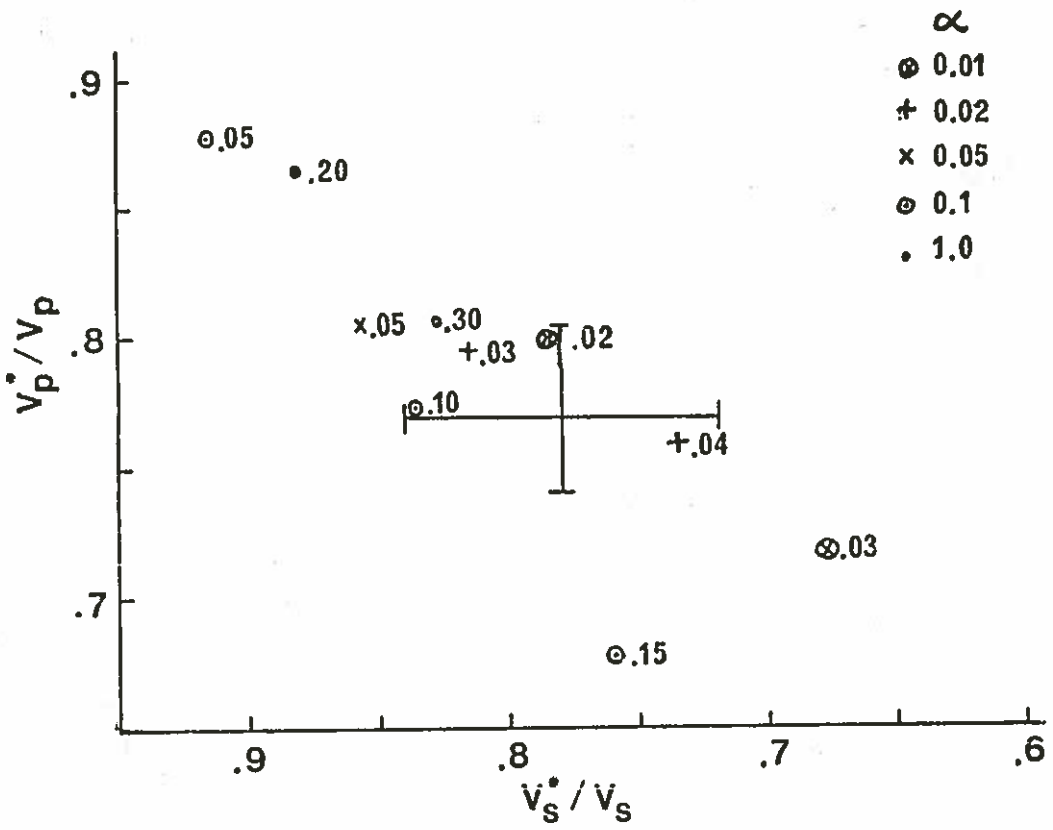

Figure 5-1-1. Porosity (Ø) and aspect ratio (α) points plotted against normalized compressional and shear wave velocities for the non-interactive theory (Kuster and Toksöz, 1974). The calculations were made assuming completely saturated pores in rock with matrix parameters, V_p = 6.2 km/sec, V_s = 3.3 km/sec and ρ = 2.95 gm/cc. Porosities are written beside the points and aspect ratios are indicated using different symbols. For example, • .02 represents a porosity of 2% and an aspect ratio of 1.0. Lines of constant aspect ratio are very close together and have similar slopes. The cross indicates mean velocities of V_p^* = 4.8 $\pm$ 0.2 km/sec and V_s^* = 2.6 $\pm$ 0.2 km/sec.

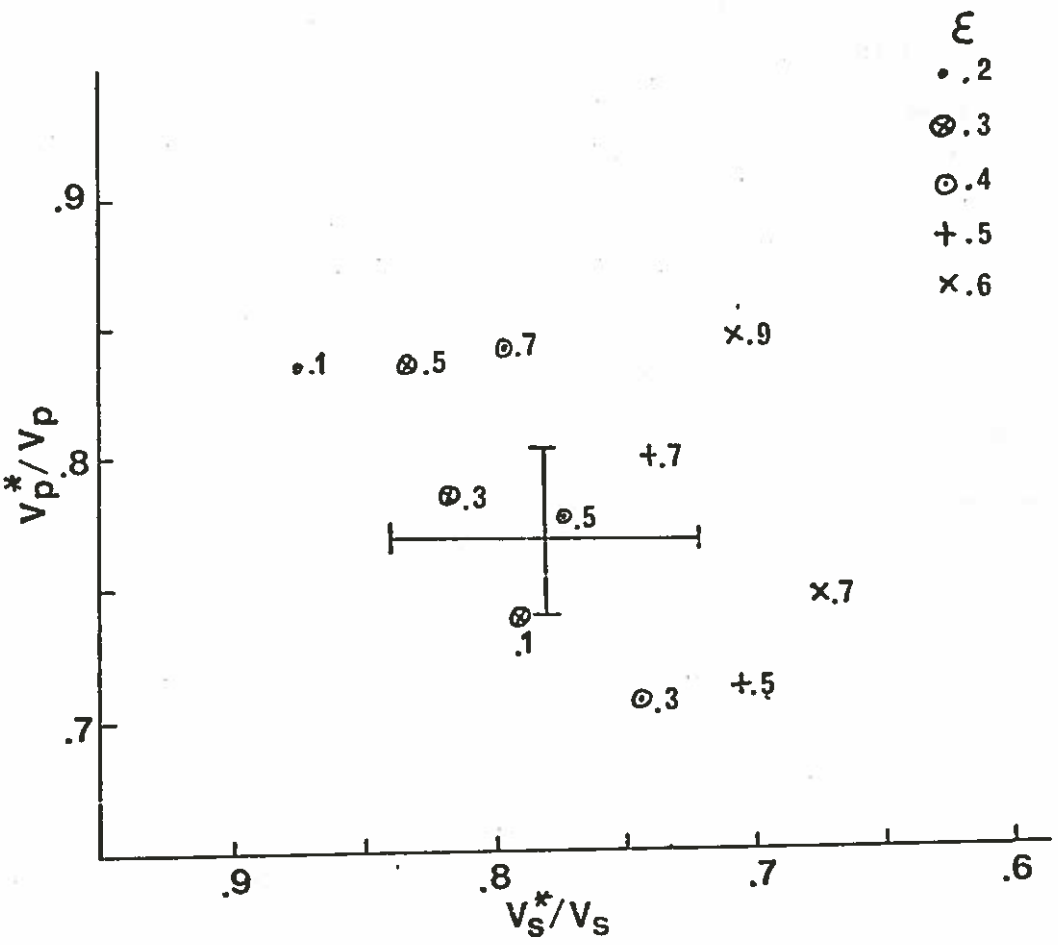

Figure 5-1-2. Saturated fraction (ζ) and crack density (ε) plotted against normalized compressional and shear wave velocities for the self-consistent theory (O'Connell and Budiansky, 1974). The matrix properties and the cross are the same as for Figure 5-1-1. Saturated fraction is written beside points and crack density is indicated by different symbols. The points are more spread out than the porosity-aspect ratio pairs of Figure 5-1-1.

fraction (ζ) plotted against V_p^*/V_p and V_s^*/V_s . The two parameters ε and ζ are well spread out and values can be distinguished. Again the mean point for upper layer 2 velocities is shown with estimated error bars. Crack density ranges from 0.2 to 0.5 with a best estimate of 0.38 and saturated crack fraction ranges from 0.1 to 0.7 with a best estimate of about 0.5 .

If the cracks are assumed to be spheroidal (Section 1-5f)), the crack densities above give an estimated porosity of 16% with limits of 8% and 21% for an aspect ratio of 0.1. Unreasonable results occur for spherical pores and pores with an aspect ratio of 0.01. Assuming that a lower limit for porosity is given by the core samples (8.4%) then a minimum average aspect ratio for cracks in upper layer 2 is 0.04.

Self-consistent theory predicts that about half of the pores in upper layer 2 are unsaturated. Vapour filled cracks may have formed during cooling of the crust as explained by Hyndman (1977). One would expect intuitively that these cracks should be small and evidence for them should be seen in laboratory measurements. Since flat cracks affect velocity more than spherical cracks a relatively few, flat, unsaturated, cracks could cause an exaggerated result in the calculation. Also, only a few per cent of vapour in the pores is sufficient to reduce the bulk modulus and make the cracks appear unsaturated (Toksöz et al, 1976).

In conclusion, self-consistent theory gives more reasonable results for upper layer 2 than non-interactive theory but Wyllie's formula, which does not consider the complication of aspect ratio is as useful as either of the theories. It appears that crack density decreases with depth and vanishes by the bottom of layer 2.

5-2. GEOPHYSICAL RESULTS FROM THE OSE OF MARCH 1977

a). Lateral Velocity Variations (Sections 1-4,2-1,3-2b),4-1g),4-1h),4-2c))

The first objective of the OSE was to look for lateral velocity variations in layer 2. This was to be accomplished by determining how far the structure intersected by the borehole extended laterally from the hole.

In the OSE of March 1977 the hole was only open 260 m into basement and the sonic log was only run for 96 m of this. Consequently, the first requirement for a lateral velocity variation study (ie. that the seismic structure immediately around the hole is known from sonic logging) was not met. Even if the sonic log had been run as deep as possible only about 20% of layer 2 would have been logged. (Layer 2 in the area was 1.34 km thick.) The first objective was not accomplished because the drilling was not as successful as anticipated.

In addition there is little point in looking for lateral velocity variations in layer 2 by travel time analysis unless the basement topography is known in detail. In the area surrounding Site 417 the profiling was inadequate because of the deep water which spoiled resolution and because of the strong mid-sediment reflector which masked deeper energy (Section 4-1g)). These factors are also mentioned in Houtz and Ewing (1976). Certainly in deep water ($>$ 5.0 km) an improved technique for seismic profiling is required before any seismic technique will be useful in studying detailed lateral velocity variations. The masking effect of the diffraction hyperbolae can be reduced by locating the receivers in the profiling system closer to the sea bottom. A deep tow system which tows a low frequency sound source and a hydrophone array just above the sea bed would be ideal.

b). Pores and Cracks (Sections 1-5,4-2a),4-3b),5-1)

The fact that cracks slow down velocities in some way proportional to their densities is undisputed. The single gradient model of Figure 4-3-4f satisfies the OSE data adequately. The P-velocities increase from 4.8 to 6.4 km/sec with depth in layer 2. Since the extrapolated velocity for zero porosity basalt from laboratory measurements is 6.2 km/sec it would appear that the effect of cracks diminishes in layer 2 (assuming that layer 2 is the same material throughout), until by the bottom of layer 2 very few cracks are present. Whitmarsh (1978) arrived at the same conclusions from ocean-bottom-receiver refraction work.

The shear wave velocities from the OSE study behave similarly to the compressional wave velocities. The estimated matrix shear velocity is 3.3 km/sec and the mean shear velocity for cores at atmospheric pressure is 3.1 $\pm$ 0.21 km/sec (Hamano et al, pers. comm.). The in situ velocities increase from 2.60 km/sec to 3.60 km/sec with depth in layer 2.

The confining pressure in layer 2 is generally less than 0.5 kbar (Hyndman, 1977) and is insufficient to close the cracks. Evidence for high velocities in lower layer 2 near the mid-Atlantic ridge (younger than 50 My) is inconclusive (Houtz and Ewing, 1976). That high crack densities are present near the ridge is implied by the high level of hydrothermal circulation needed to explain the heat flow results (Lister, 1972). The scale of these cracks is not known. Why does the crack density decrease with depth? Either hydrothermal or low temperature secondary mineralization seems the most likely answer but why would the cracks start filling at the bottom? An

analysis of the process of secondary mineralization with respect to the typical temperature gradients in oceanic crust is required.

c). Anisotropy (Sections 1-6,4-2b))

No undisputed evidence for preferred crack orientation was found from either velocity or amplitude studies. Rugged basement topography introduces errors into the P-wave travel times on the order of $\pm$ 0.08 sec which make accurate velocity determinations over short ranges impossible.

As discussed in Section 1-6 it is not unreasonable that velocity anisotropy greater than 0.2 km/sec may exist in layer 2. The OSE should be able to detect anisotropy of this magnitude in the direct S arrival which travels in the top of layer 2. The mean north-south velocity (2.56 $\pm$ 0.04 km/sec) however, is not significantly different from the mean east-west velocity (2.66 $\pm$ 0.11 km/sec). The fissures may be associated with layer 2A (Houtz and Ewing, 1976) which gradually thins out at about 40 My. If so, we would not expect to see anisotropy caused by fissures at Site 417 where the age is about 110 My. The OSE results are perfectly consistent with this theory: fissure density decreases with age and the density of small cracks decreases with depth.

It is not clear why the fissure density should decrease with age. Certainly considerable secondary mineralization has occurred in older rocks. Cores from Sites 417 and 418 show that voids and cracks are filled with calcite, smectite, zeolite, quartz, pyrite and other alteration products (Shipboard Parties of Legs 51, 52 and 53, pers. comm.). This mineralization was not as extensive in the younger

crust cored on Leg 37 (Robinson, Hall et al, 1977). Recovery rates in the younger crust were also much lower (20% (Robinson, Hall et al, 1977) vs 70% (Shipboard Parties of Legs 51, 52 and 53, pers. comm.)) indicating either more voids, poorer consolidation, or both. The fissures may fill with cemented breccia while the cracks stay open. Alternatively, fissures may never have formed in the older crust.

Average layer 3 refracted P-wave velocities are 6.71 $\pm$ 0.30 km/sec for north-south lines and 6.61 $\pm$ 0.41 km/sec for east-west lines. The refracted S-wave velocities are 3.77 $\pm$ 0.10 km/sec for north-south lines and 3.60 $\pm$ 0.09 km/sec for east-west lines. These values are not convincing evidence for anisotropy in layer 3. If, however, we assume that most of the spread in errors is caused by small scale topography and accept the mean values then some anisotropy may exist. Since evidence indicates that cracks on all scales are not present at the bottom of layer 3, the anisotropy could be related to crystal orientation or residual fabric (Christensen, 1972 ; Friedman and Bur, 1974).

The OSE should be performed in younger crust where layer 2A exists in an attempt to detect preferred crack orientation and its extent with depth. The anisotropy should be large enough to see above the topographic effects. The OSE is more suitable for this purpose than conventional refraction with either sea-bottom or surface receivers because layer 2A is frequently a poor refractor and when refracted arrivals are present they appear over only a short distance making accurate velocity determinations difficult (Houtz and Ewing, 1976).

d). Attenuation (Sections 1-7,4-3c))

Because of the shallow hole (230 m into basalt) no determination of attenuation from short range (vertical incidence) shots could be made. The effects of attenuation on long range shots are much less than the observed amplitude variations which could be caused by inadequate clamping, undetermined basement topography or lateral inhomogeneities.

5-3. TECHNICAL ASPECTS OF THE OBLIQUE SEISMIC EXPERIMENT

a). The OSE and Conventional Refraction Experiments (Section 1-3)

As outlined in Section 1-3 the OSE has a number of advantages over conventional refraction experiments which use ocean bottom receivers or sonobuoys. In general the OSE is suited to studying detailed structure in upper oceanic crust (Section 1-3, points i-vi, ix and x). Also because a borehole geophone receives strong S-wave arrivals the OSE is better adapted to analysing cracks in oceanic crust (point viii). Attenuation measurements can also be made (point vii). However, since the OSE is a logistically difficult and expensive experiment to carry out, it cannot compete with conventional refraction techniques in the large scale study of oceanic crust.

b). Equipment (Sections 3-1,4-1)

Results confirmed that a 3-component detector is essential for the OSE. A number of improvements, however, can be made on the equipment used in March 1977. The maximum pre-amplifier gain should be increased to 72 db (4,000x) to improve signal-to-noise ratio at

long ranges. Although the feedback circuit which eliminated DC shift in the pre-amplifier was acceptable, it would be more professional to replace it with a design less sensitive to component specifications. The circuit should be built on a printed circuit board rather than a wire wrap system to decrease the chances of bits shaking loose.

Timing accuracy could be improved if an air gun system were used rather than free falling explosives.

c). Synthetic Seismograms (Sections 2-2,4-3)

The reflectivity method synthetic seismogram technique is essential for computing seismograms at ranges greater than 2 km. It ensures that all the conversions and multiples of importance are included. At shorter ranges, where the reflectivity method runs into numerical difficulties, a normal incidence ray tracing technique is sufficient since interconversions are less significant.

d). Logistics (Section 3-2)

From a technical standpoint the experiment is feasible, however, operationally it is an extremely tenuous undertaking. For the 1976 and 1977 experiments, Deep Sea Drilling Project engineers felt that the tool should only be run in a hole after drilling had finished because if the clamping arm failed to retract the hole would be lost. Similar risks are inherent in any downhole logging. Unfortunately drilling frequently stops when the hole is faulty (e.g. re-entry is impossible , there is caving, or pipe is left in the hole). Hence, it is impossible to predict with any degree of certainty where or when a suitable hole will be available and it becomes very difficult to

schedule a second ship. On the 1977 experiment the shooting ship was kept on stand-by for two months. The ship was necessarily inexpensive and consequently so small that weather became a very critical factor. These problems could be alleviated if a boat and explosives were kept on board Glomar Challenger.

An alternative system would be to have the Glomar Challenger and the shooting ship return to a known good hole at a later time. At present, the locating beacons at sites transmit continuously and die after a few months. With new electronic technology it should be simple to build a long term beacon which could be "turned on" by a suitable acoustic signal. Such a beacon could stay in a stand-by mode for years. An interest has recently developed in permanently instrumenting IPOD holes with tilt, heat flow and seismic instruments (Heirtzler, pers. comm.). Installations would be disposable except for the recording package. The OSE could be run as a part of this programme, again having appropriate electronics turned on by an acoustic signal when the shooting ship arrives on site.

The OSE should not be performed again unless some solution is found to the operational difficulties. The three suggestions made here all require that a much higher priority be given to the experiment.

5-4. SUMMARY OF CONCLUSIONS

Based on data from the Oblique Seismic Experiment of March 1977 the conclusions regarding each of the objectives outlined in Section 1-1 are:

i. The lateral extent of the structure intersected by the borehole could not be studied because the hole was not deep enough, the hole was only logged for 90 m into layer 2 and

the basement topography was not known accurately.

ii. Velocity studies from the OSE suggest that layer 2 can be represented by a single velocity gradient. Both P-wave and S-wave velocity models are consistent with the hypothesis that crack density decreases with depth and vanishes by the bottom of layer 2. It would appear that large fissures, as observed in the FAMOUS area, are not as prevalent in old (110 My) crust. The study is consistent with the theory that the density of large fissures decreases with increasing age and that the density of vugs and vesicles decreases with increasing depth.

iii. No significant evidence for anisotropy in layer 2 was found and this is attributed to the absence of large fissures.

iv. The hole was not deep enough to measure attenuation from normal incidence shots. Lateral velocity variations and/or rough basement topography cause significant changes in amplitudes over short (approximately 1.5 km) distances and this makes it impossible to measure attenuation from long range shots.

Appendix A: Cable Specifications

At the time of investigation into cables (October 1975) DSDP had three Schlumberger cables: two on board Glomar Challenger and one at the Edo-Western plant in Salt Lake City. Edo-Western (Grude, pers. comm.) sent the following information on the cable:

Type	7-S52RB
Vector Part #	A20054
# of Conductors	7
Outside Diameter	.520"
Breaking Strength	21,100 lbs
Weight per 1000 feet	462 lbs
Armour	19/20
Temperature Rating	350°F
Voltage rating	1000Vrms at 60 Hz
Resistance	10.9Ω/1000'
Capacitance	45pF/ft

They also did a test for frequency response, using a 50Ω source impedance, a 50Ω load impedance and 21,500 feet of cable. The input was 1 Vrms. The results were:

Amplitude

-3.5 db from 50-500 Hz
-6 db at 3500 Hz
-19.5 db at 8000 Hz

Phase

-1° at 50 Hz
-2° at 100 Hz
-4° at 200 Hz
-11° at 500 Hz
-22° at 1000 Hz
-90° at 4000 Hz

They measured the cable impedance with an impedance bridge and terminated the cable with 600Ω . At 200 Hz the impedance was 800Ω - j400, at 500 Hz it was 500Ω - j600 and at 1 KHz it was 250Ω - j300. They had not been very successful at impedance matching the cable.

They tested crosstalk by putting 440V rms 60 Hz on two leads. Capacitive crosstalk was about 2.5%

DSDP were asked to conduct some tests of ambient noise on the cable while the Glomar Challenger was on an engineering run out of Norfolk, Virginia (Porter, pers. comm.) The results were:

1. With the cable terminated with a resistance of 450Ω there was 2 mV, 60 Hz noise at the open end with 20-25 mV transients due to switching of electrical equipment on the ship.
2. With the configuration of 1) but the open end loaded with a 2K resistance, the transient voltage across 5Ω was 1 mV.

APPENDIX B: GEOPHONE RESPONSE CURVES

The amplitude and phase response curves for the Geo Space HS-1 geophone, with a natural frequency of 4.5 Hz and a coil resistance of 215Ω, are shown in Figures B-1 and B-2 respectively. In the OSE a shunt resistance of 825Ω was used.

The effects of the amplitude and phase responses are discussed in Sections 3-1a) and 4-1i). The amplitude response is sufficiently flat over the frequency range of interest (within 3 db between 5 and 100 Hz) that no allowance for it is necessary. The phase response can cause significant delays (12 msec for 10 Hz signals compared to 5 msec for 50 Hz signals) and for arrivals with the same frequency content introduces a significant systematic error. This should be considered in the interpretation. No allowance for phase response was made in the synthetic seismogram calculations (Sections 2-2 and 4-3) because the source wavelet was chosen empirically and consisted predominantly of a single frequency (approximately 10 Hz).

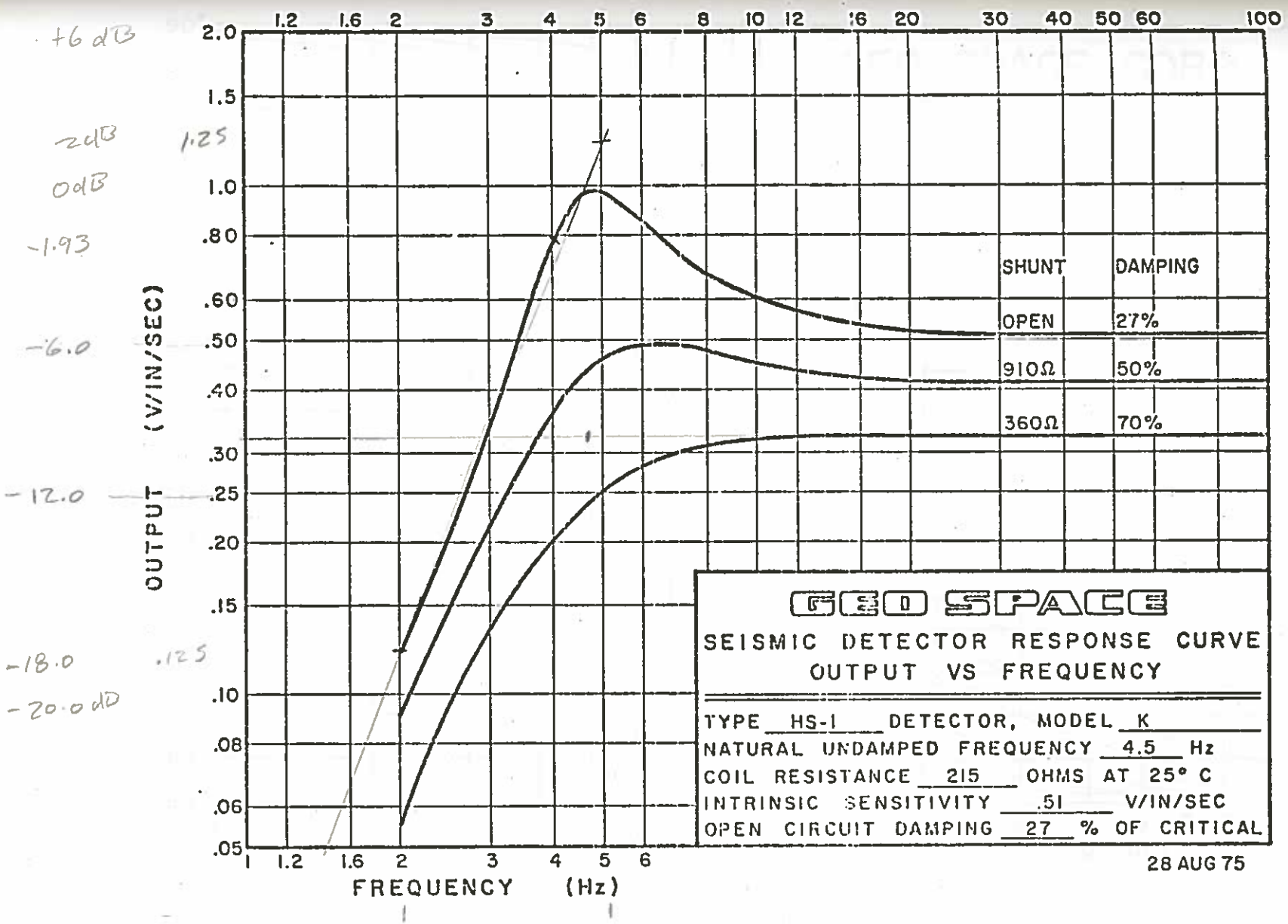

Figure B-1. Amplitude response of the Geo Space HS-1 geophone. (Diagram courtesy of Geo Space, Houston.)

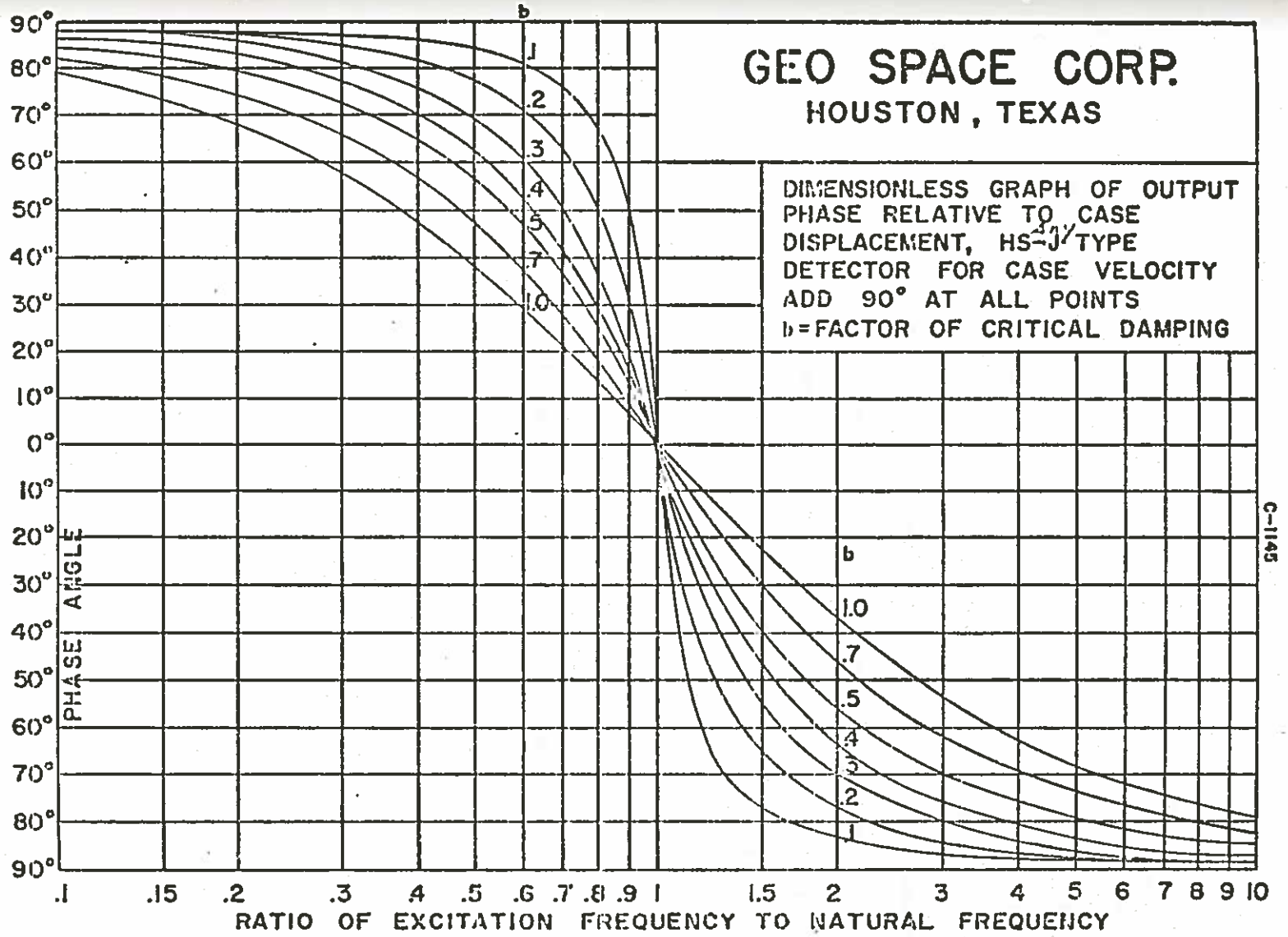

Figure B-2. Phase response of the Geo Space HS-1 geophone. (Diagram courtesy of Geo Space, Houston.)

APPENDIX C

THE OBLIQUE SEISMIC EXPERIMENT DATA

This appendix displays all the data collected on the OSE. Shot locations are shown in Figure 4-1-3. Figures C-1a) to C-6c) are record sections of the three component geophone data for the north, south, east and west lines with the geophone at 6060m BRF and for the north and south lines with geophone at 5840m BRF. Figures C-7a) to C-7f) are the corresponding shallow hydrophone records and Figures C-8a) to C-9c) are geophone records for the azimuthal shots.

All the geophone sections have the same weighting. That is, up to 7 km no weighting has been performed and over 7 km the amplitudes have been multiplied by $(\text{Range}/7.0)^{2.9}$. Direct comparison of amplitudes can be made between sections. Traces on the hydrophone sections have been normalized individually.

No terrain corrections have been made on the sections.

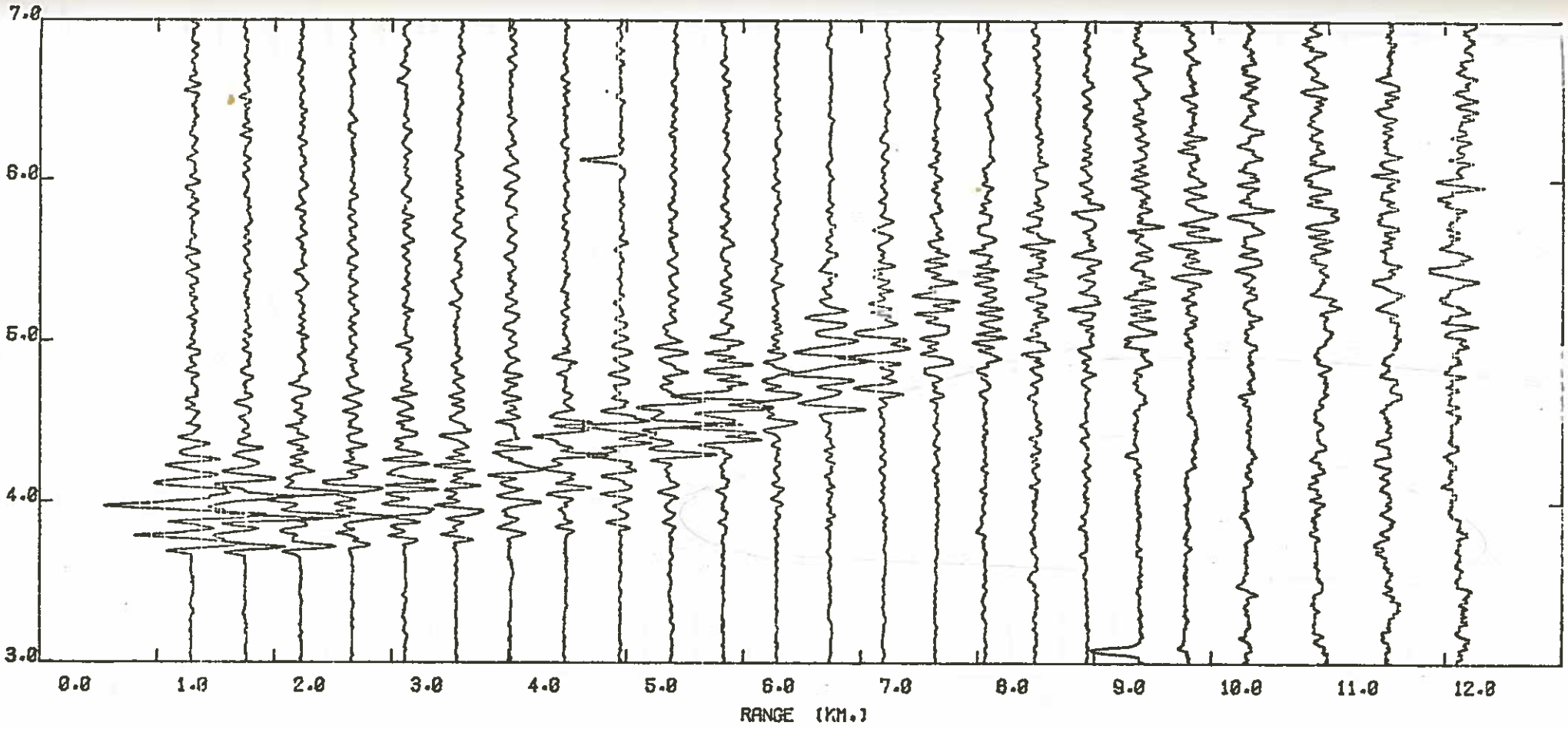

NORTH LINE - VERTICAL COMPONENT - D = 6060 M. BRF

LOW PASS FILTERED AT 30.00 HZ - REDUCTION VELOCITY OF 6.00 KM/SEC
AMPLITUDES WEIGHTED BY (R/7.0)**2.9 FOR R>7.0 KM.

Figure C-1a

Figures C-1a) to C-6c): These figures show the geophone record sections. The numbers 1-6 represent north, south, east and west lines at 6060m BRF (below rig floor) and north and south lines at 5840m respectively. The letters a) - c) represent vertical, horizontal X, and horizontal Y components. The positions of the shots are shown in Figure 4-1-3.

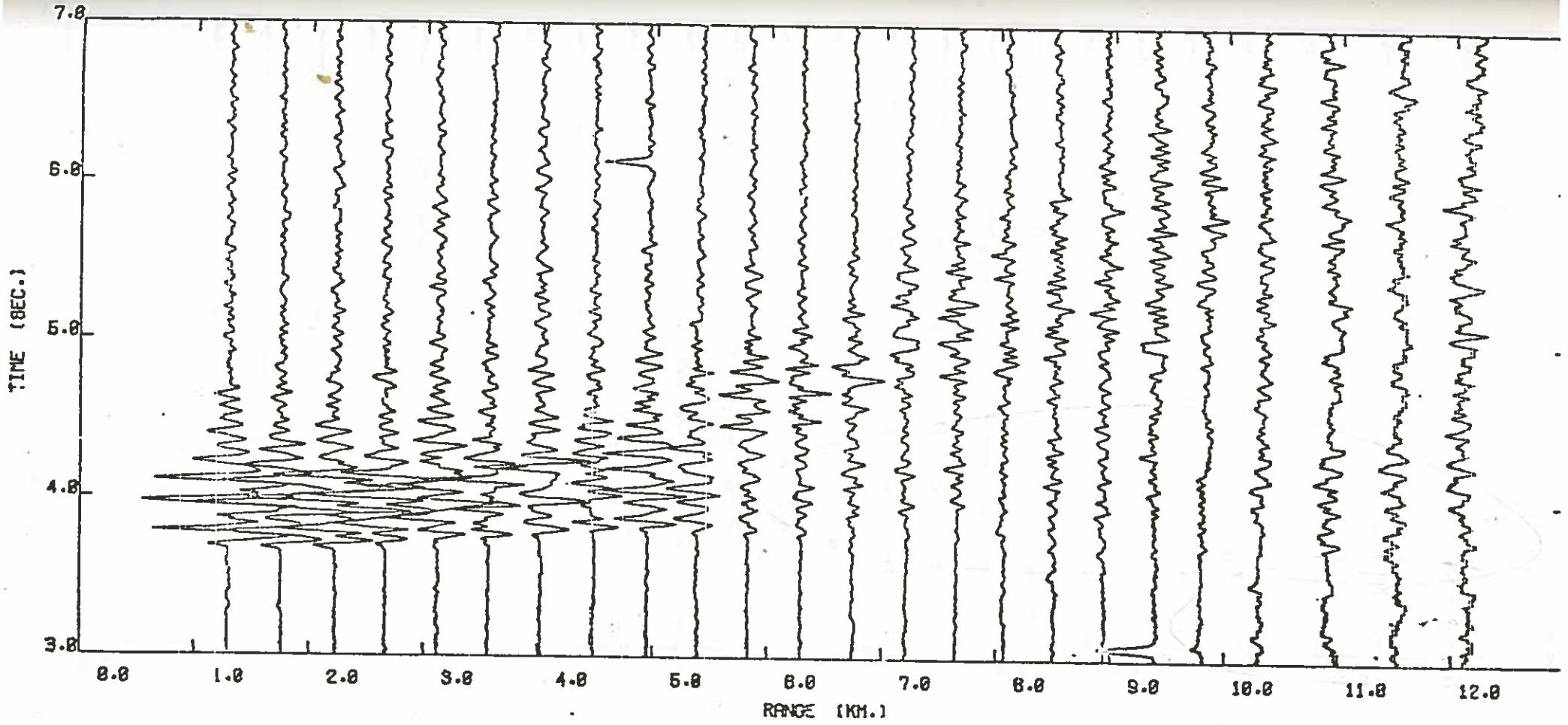

NORTH LINE - HORIZONTAL X COMPONENT - D = 6850 M. BRF

LOW PASS FILTERED AT 30.00 HZ - REDUCTION VELOCITY OF 6.00 KM/SEC
AMPLITUDES WEIGHTED BY (R/7.0)**2.0 FOR R>7.0 KM.

Figure C-1b

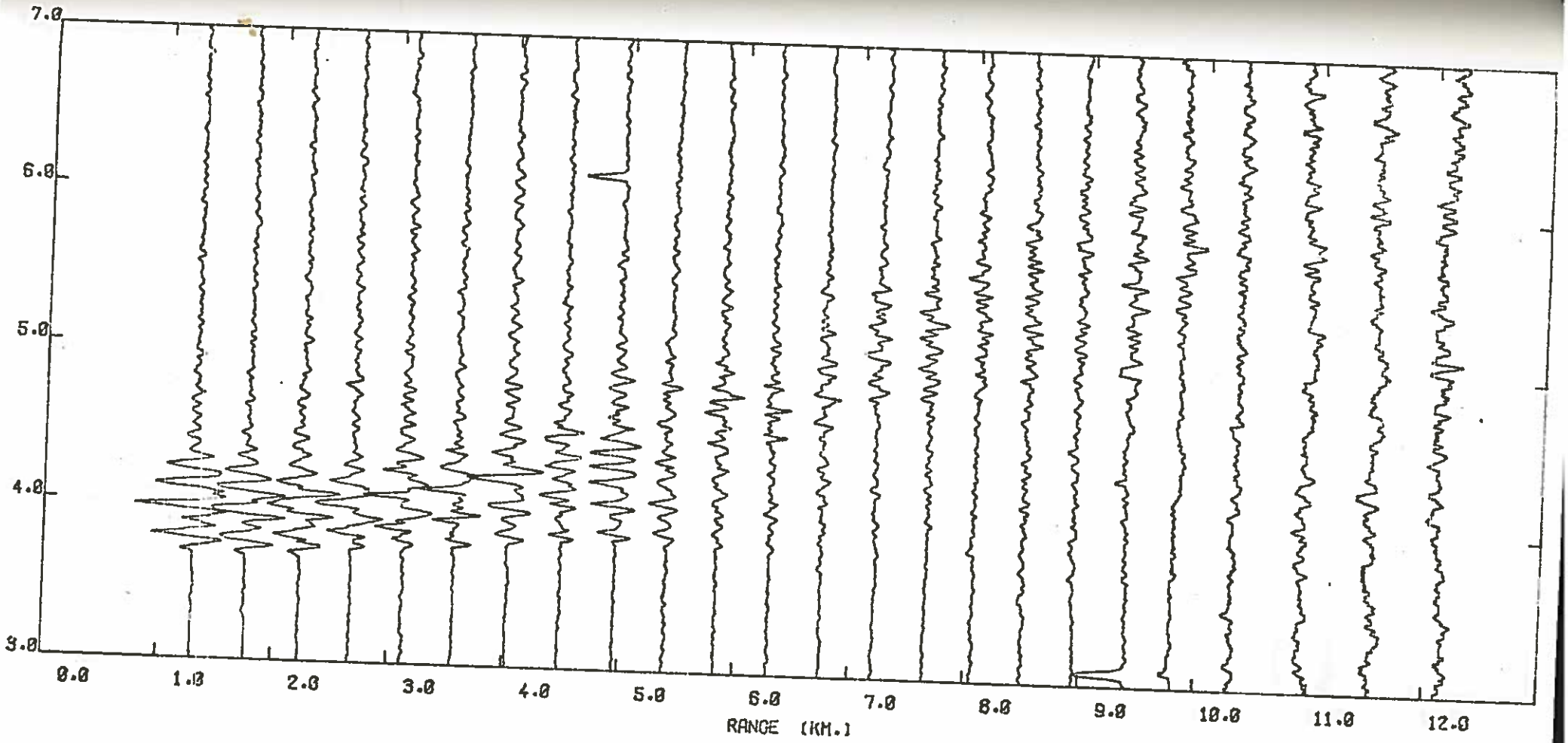

NORTH LINE - HORIZONTAL Y COMPONENT - D = 6060 M. ERF

LOW PASS FILTERED AT 30.00 HZ - REDUCTION VELOCITY OF 6.00 KM/SEC
AMPLITUDES WEIGHTED BY (R/7.0)**2.9 FOR R>7.0 KM.

Figure C-1c

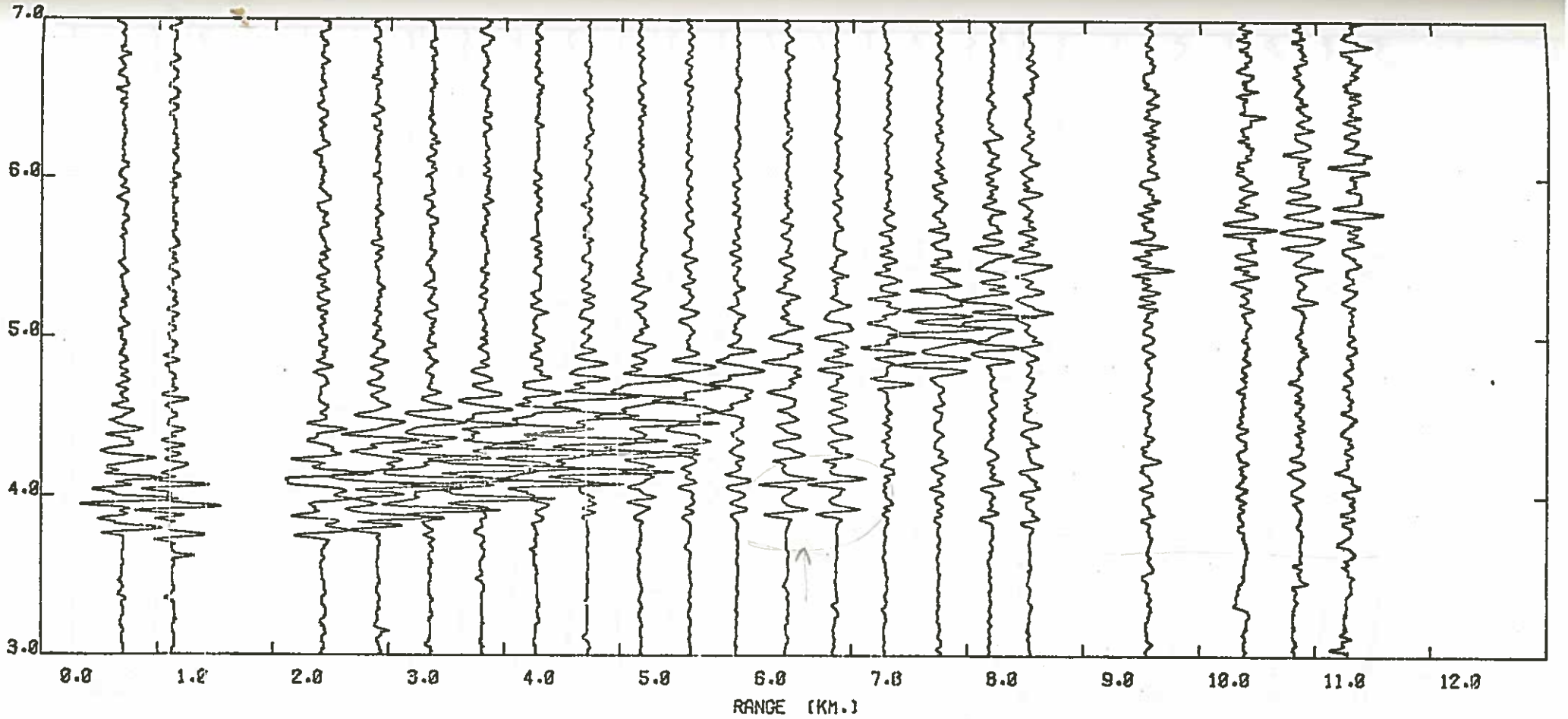

SOUTH LINE -- VERTICAL COMPONENT - D = 6060 M. BRF

LOW PASS FILTERED AT 30.00 HZ - REDUCTION VELOCITY OF 6.00 KM/SEC
AMPLITUDES WEIGHTED BY (R/7.0)**2.9 FOR R>7.0 KM.

Figure C-2a

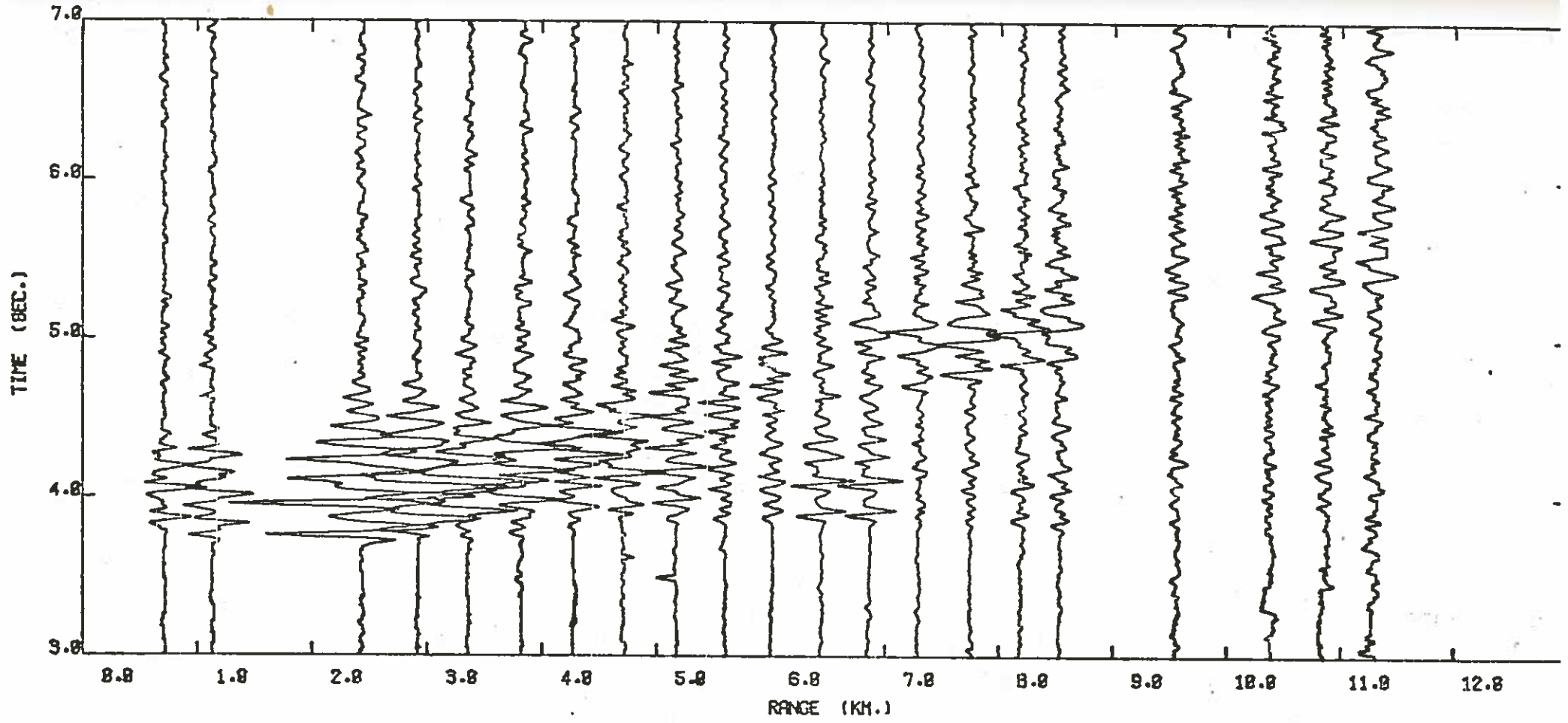

SOUTH LINE - HORIZONTAL X COMPONENT - D = 6360 M. BRF

LOW PASS FILTERED AT 30.00 HZ - REDUCTION VELOCITY OF 6.00 KM/SEC
AMPLITUDES WEIGHTED BY (R/7.0)**2.9 FOR R>7.0 KM.

Figure C-2b

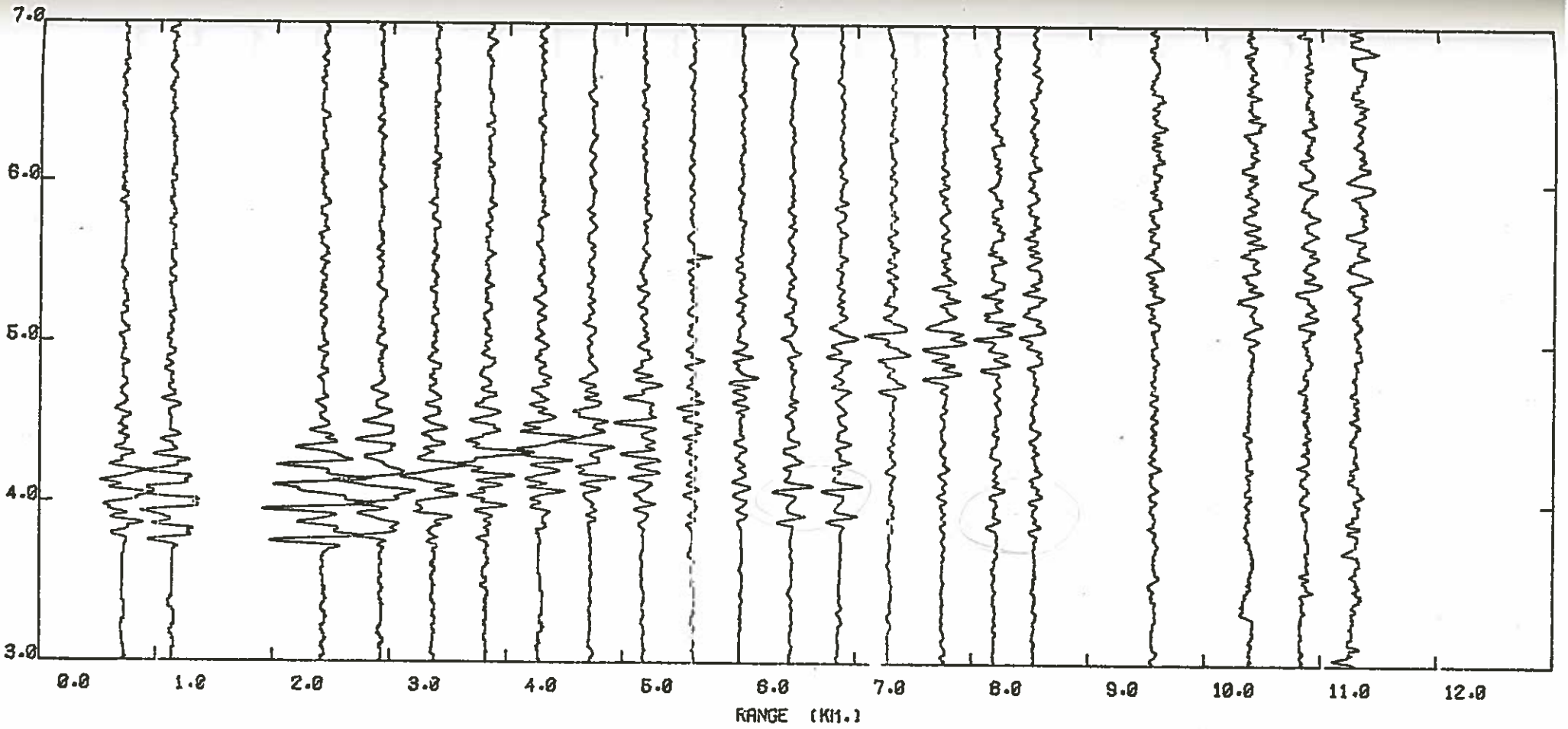

SOUTH LINE - HORIZONTAL Y COMPONENT - D = 6060 M. BRF

LOW PASS FILTERED AT 30.00 HZ - REDUCTION VELOCITY OF 6.00 KM/SEC
AMPLITUDES WEIGHTED BY (R/7.0)**2.9 FOR R>7.0 KM.

Figure C-2:

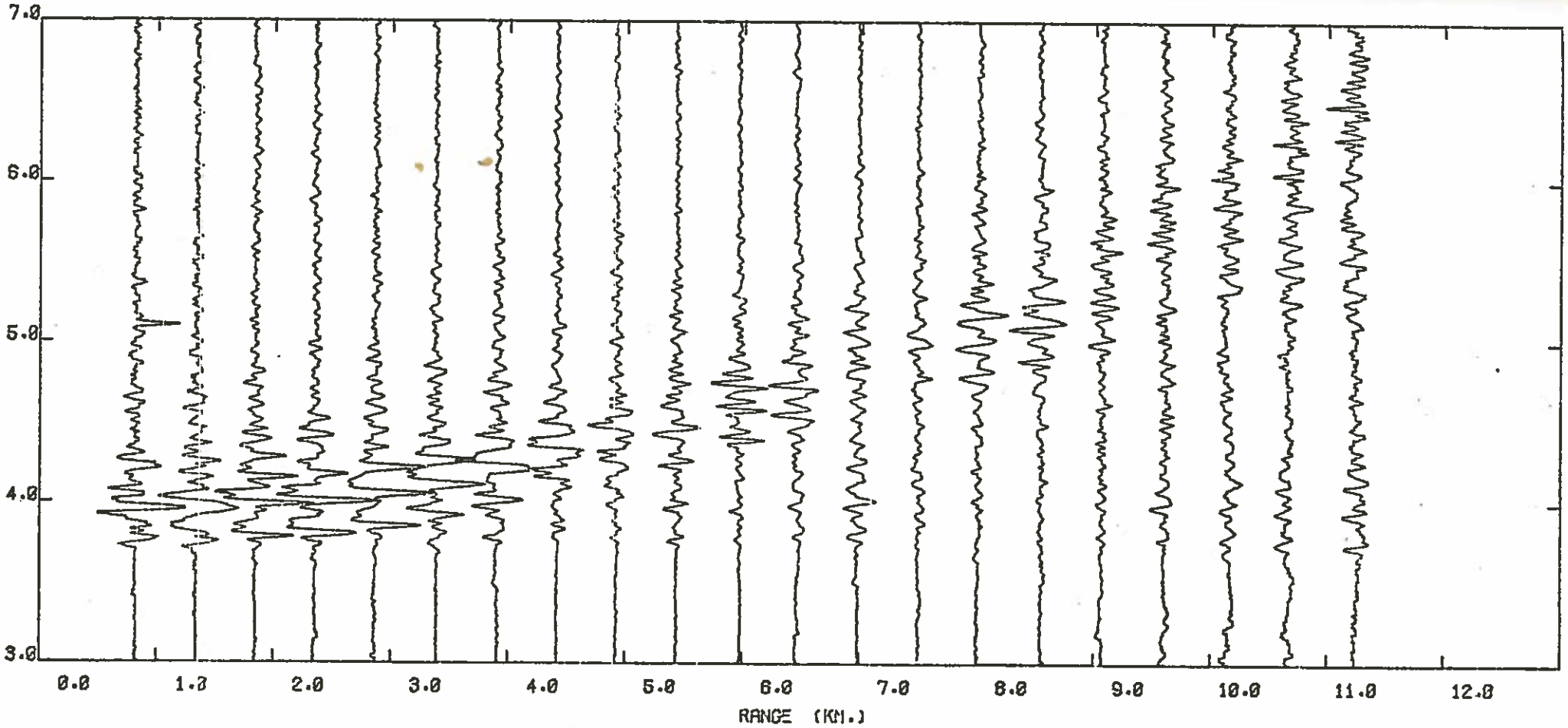

EAST LINE - VERTICAL COMPONENT - D = 6060 M. BRF

LOW PASS FILTERED AT 30.00 HZ - REDUCTION VELOCITY OF 6.00 KM/SEC
AMPLITUDES WEIGHTED BY (R/7.0)**2.8 FOR R>7.0 KM.

Figure C-3a

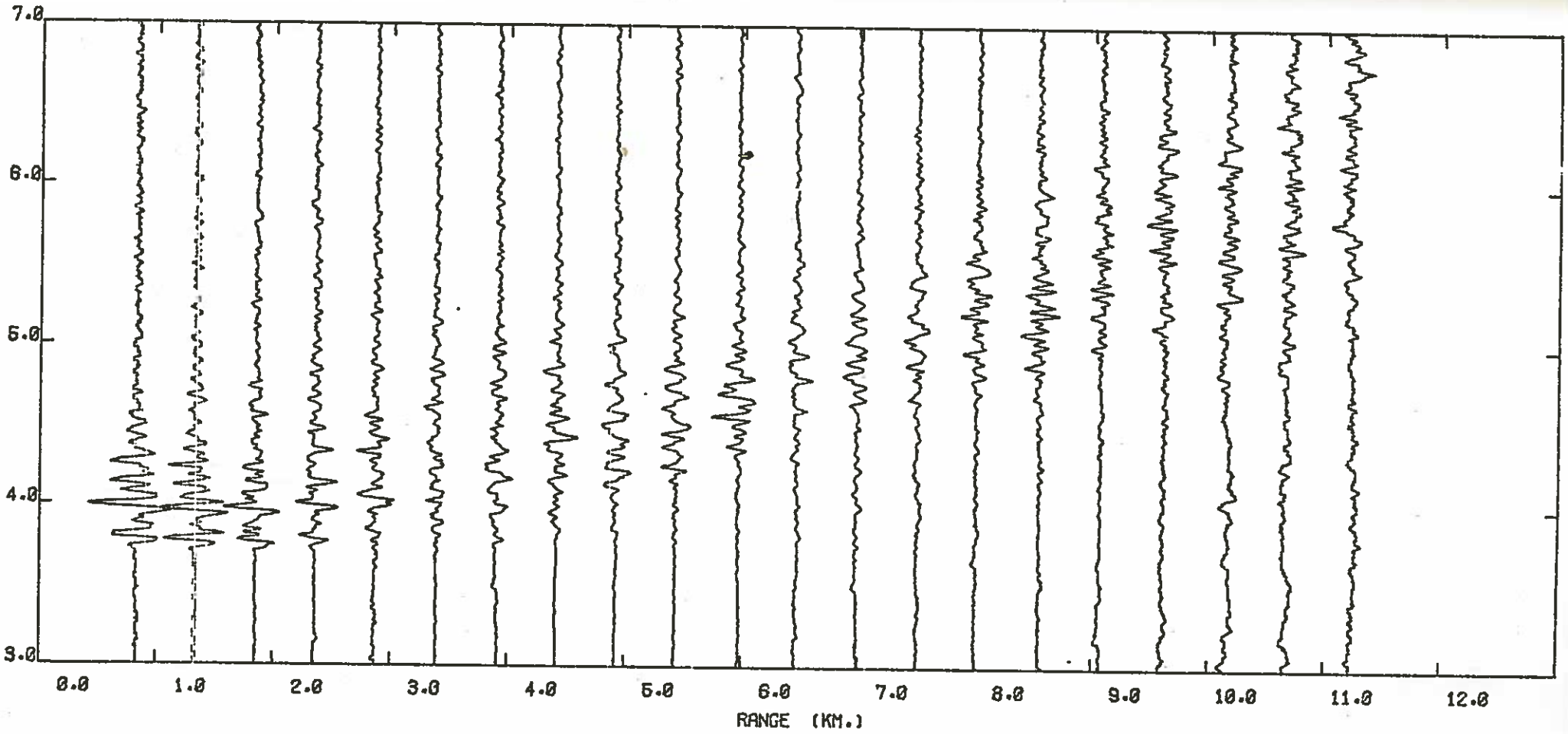

EAST LINE - HORIZONTAL X COMPONENT - D = 6060 M. BRF

LOW PASS FILTERED AT 30.00 HZ - REDUCTION VELOCITY OF 6.00 KM/SEC
AMPLITUDES WEIGHTED BY (R/7.0)**2.9 FOR R>7.0 KM.

Figure C-3b

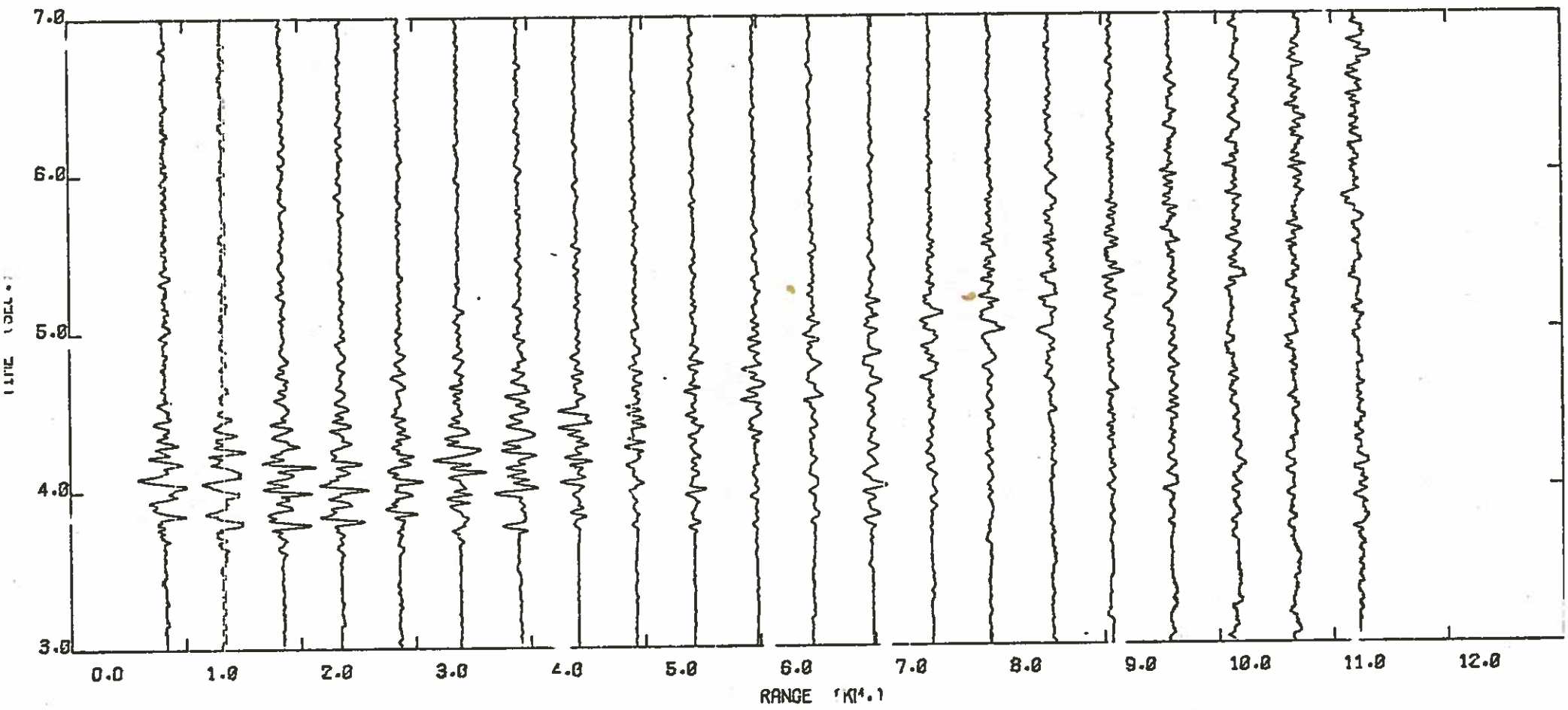

EAST LINE - HORIZONTAL Y COMPONENT - D = 0060 M. BRF

LOW PASS FILTERED AT 30.00 HZ - REDUCTION VELOCITY OF 6.00 KM/SEC
AMPLITUDES WEIGHTED BY (R/7.0)**2.9 FOR R>7.0 KM.

Figure C-3c

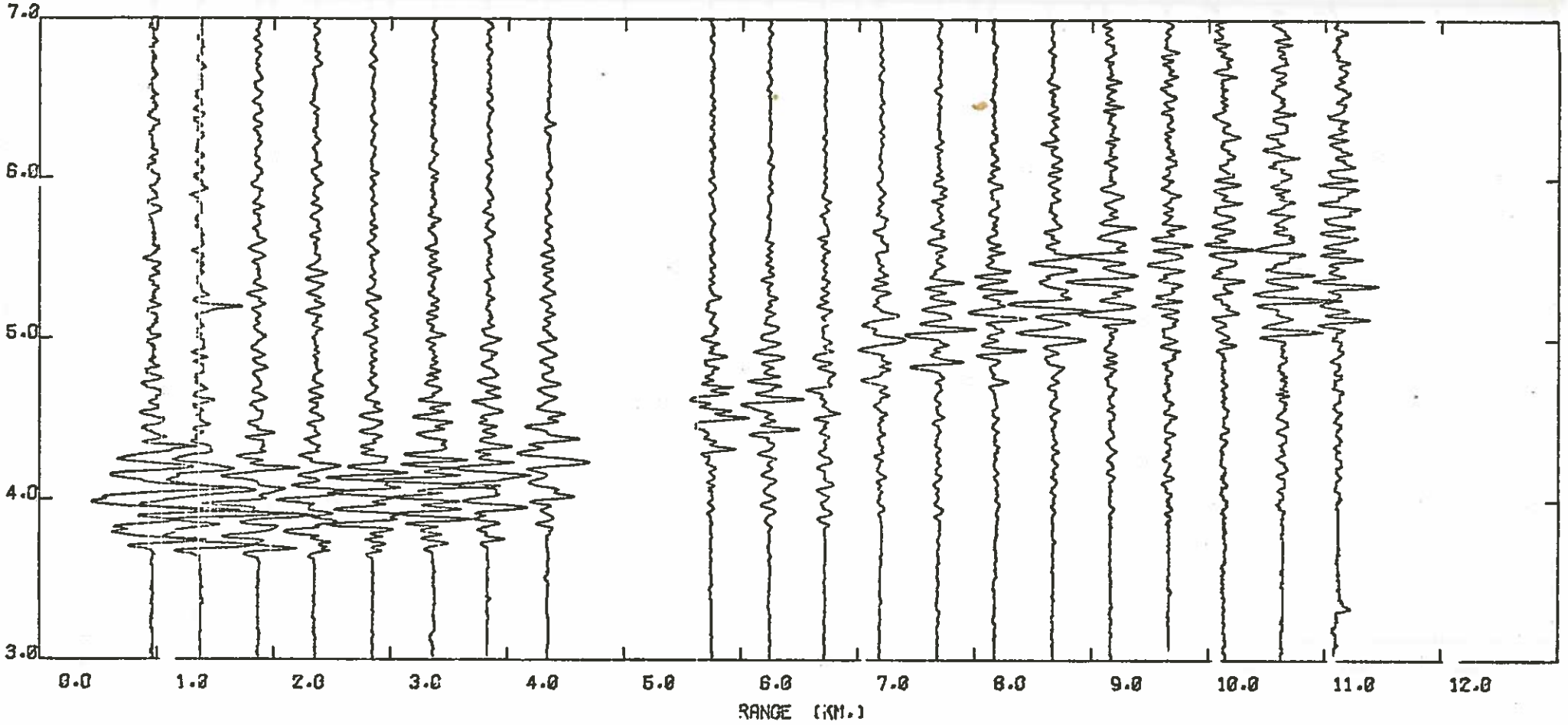

WEST LINE - VERTICAL COMPONENT - D = 6060 M. BRF

LOW PASS FILTERED AT 30.00 HZ - REDUCTION VELOCITY OF 6.00 KM/SEC
AMPLITUDES WEIGHTED BY (R/7.0)**2.9 FOR R> 7.0 KM.

Figure C-4a

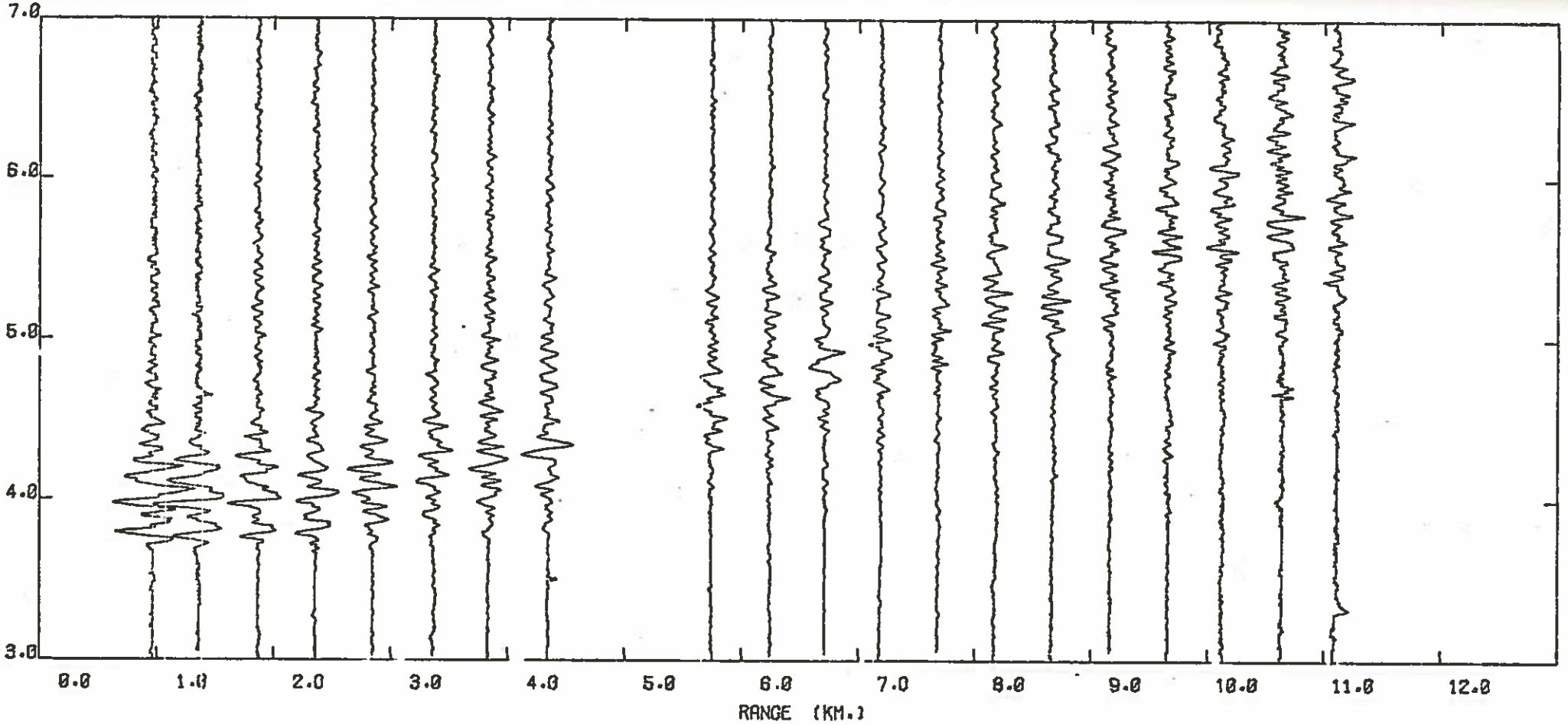

WEST LINE - HORIZONTAL X COMPONENT D = 0000 M. ABF

LOW PASS FILTERED AT 30.00 HZ - REDUCTION VELOCITY OF 6.00 KM/SEC
AMPLITUDES WEIGHTED BY (R/7.0)**2.9 FOR R>7.0 KM.

Figure C-4b

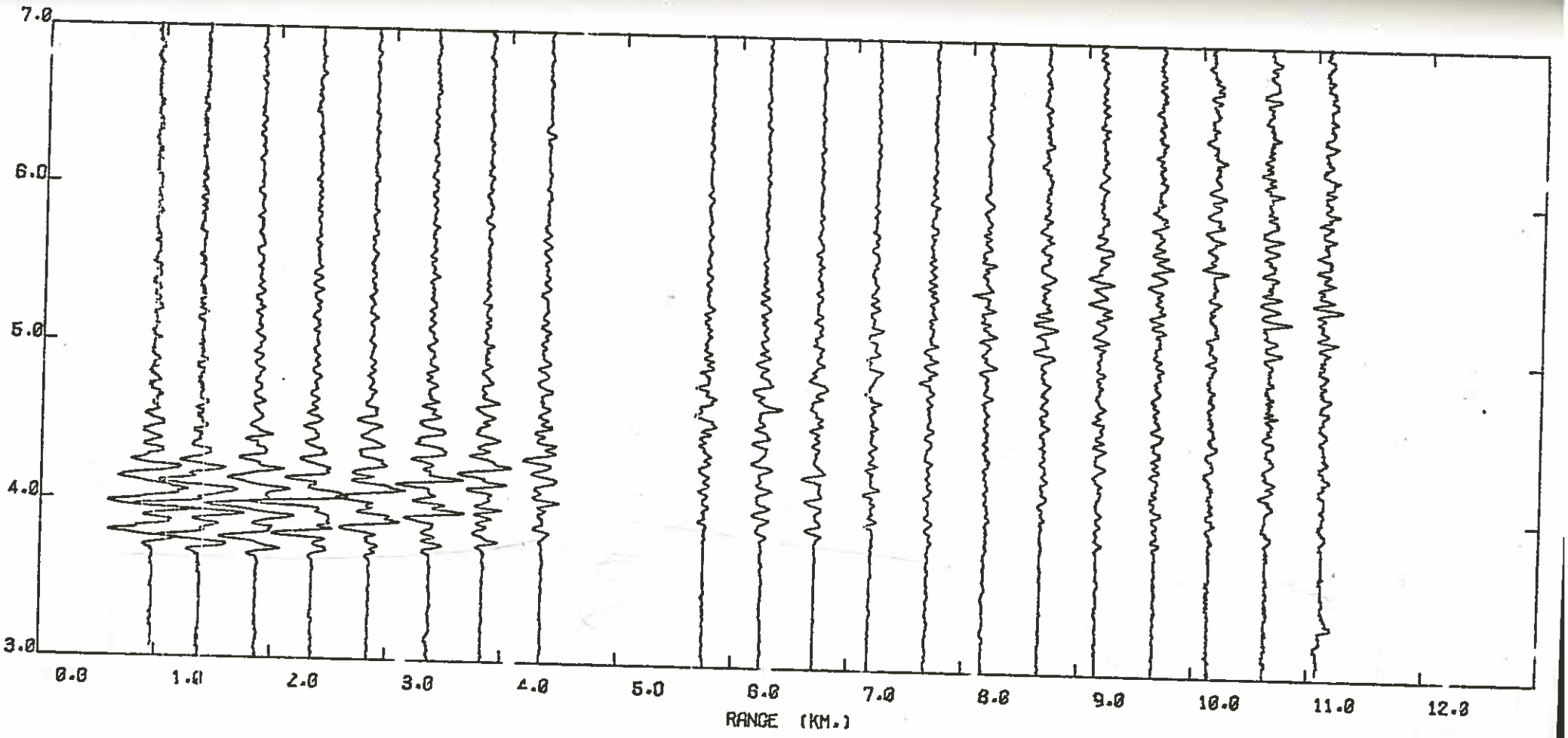

WEST LINE - HORIZONTAL Y COMPONENT - D = 6060 M. BRF

LOW PASS FILTERED AT 30.00 HZ - REDUCTION VELOCITY OF 8.00 KM/SEC
AMPLITUDES WEIGHTED BY (R/7.0)**2.9 FOR R>7.0 KM.

Figure C-4c

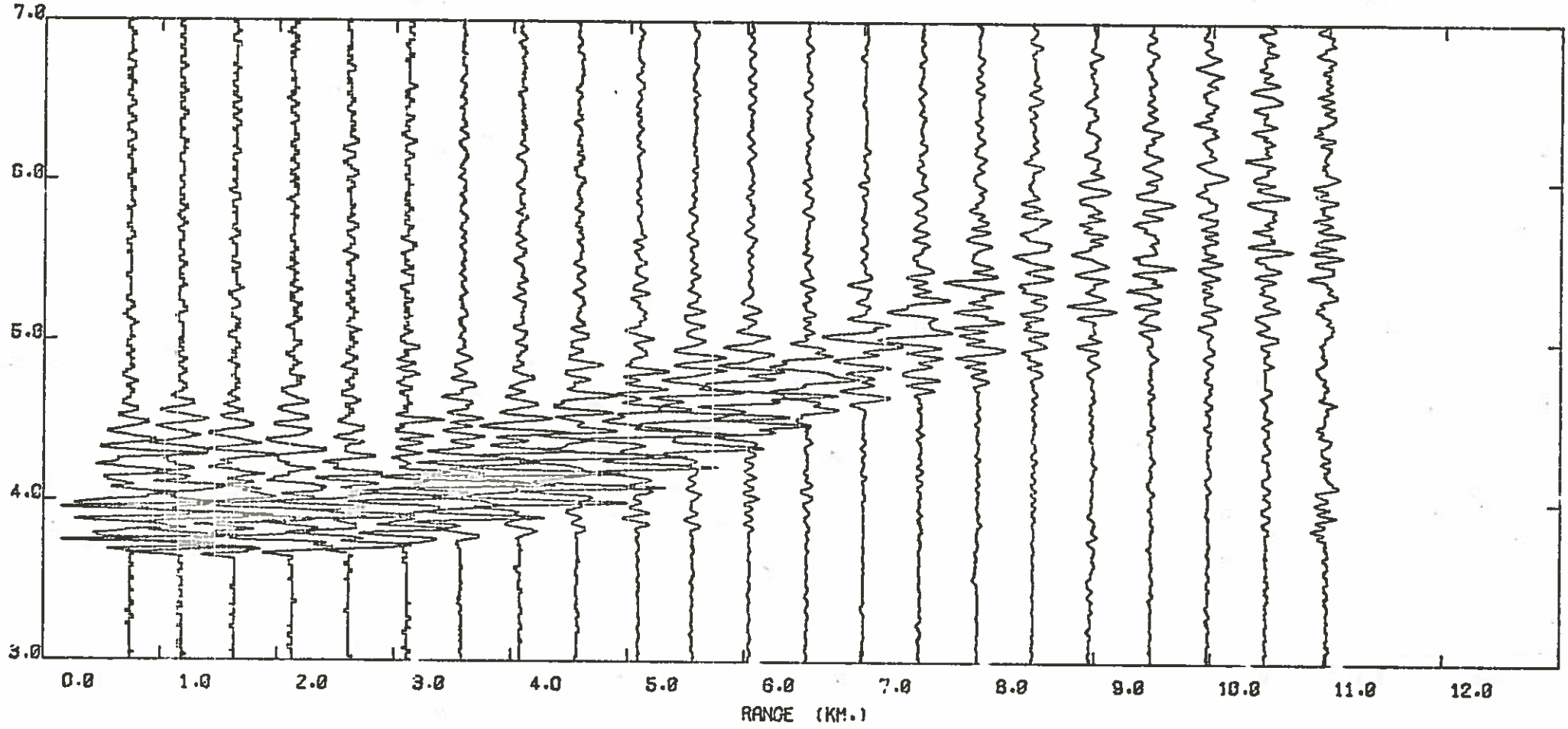

NORTH LINE - VERTICAL COMPONENT - D = 5840 M. BRF

LOW PASS FILTERED AT 30.00 HZ - REDUCTION VELOCITY OF 6.00 KM/SEC
AMPLITUDES WEIGHTED BY (R/7.0)**2.9 FOR R>7.0 KM.

Figure C-5a

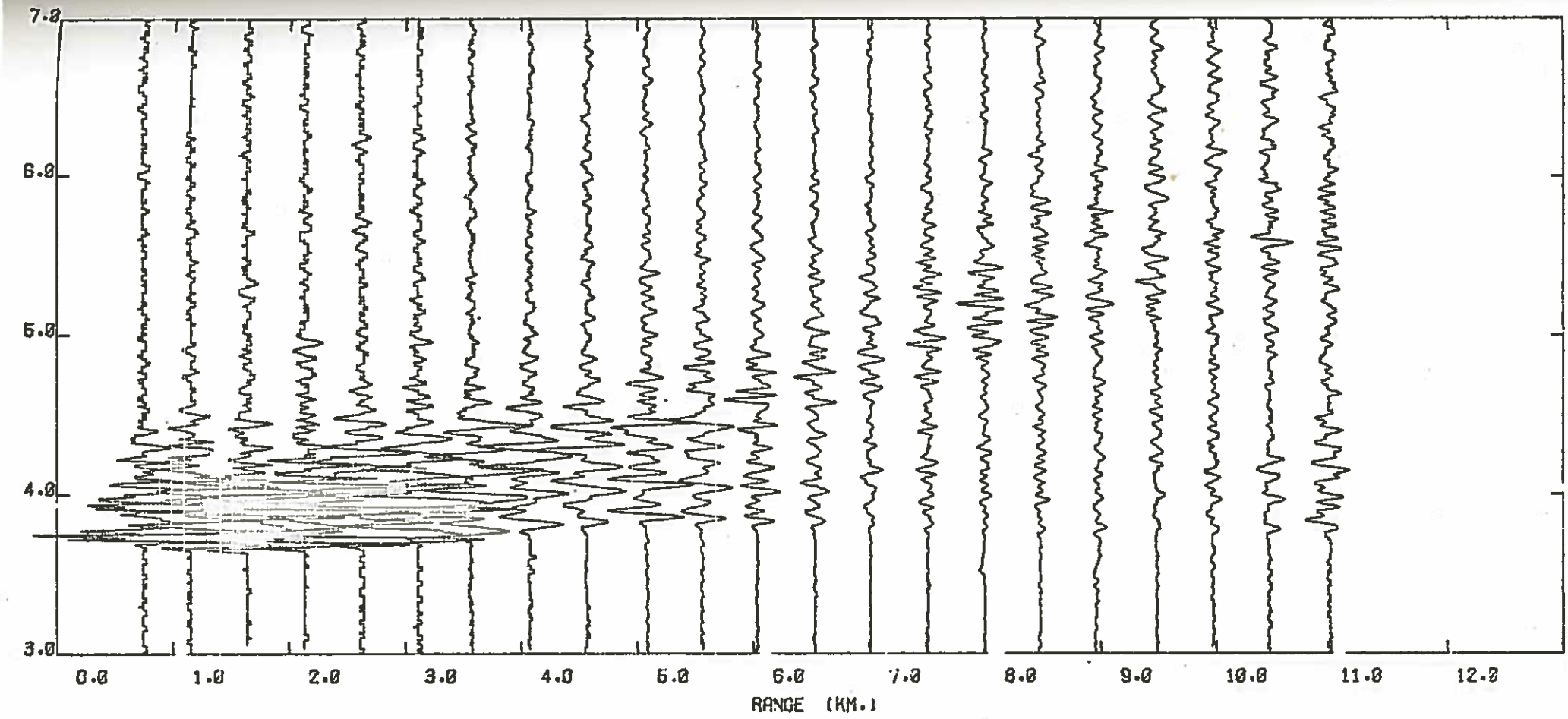

NORTH LINE - HORIZONTAL X COMPONENT - D = 5840 M. BRF

LOW PASS FILTERED AT 30.00 HZ - REDUCTION VELOCITY OF 6.00 KM/SEC
AMPLITUDES WEIGHTED BY (R/7.0)**2.9 FOR R>7.0 KM.

Figure C-5b

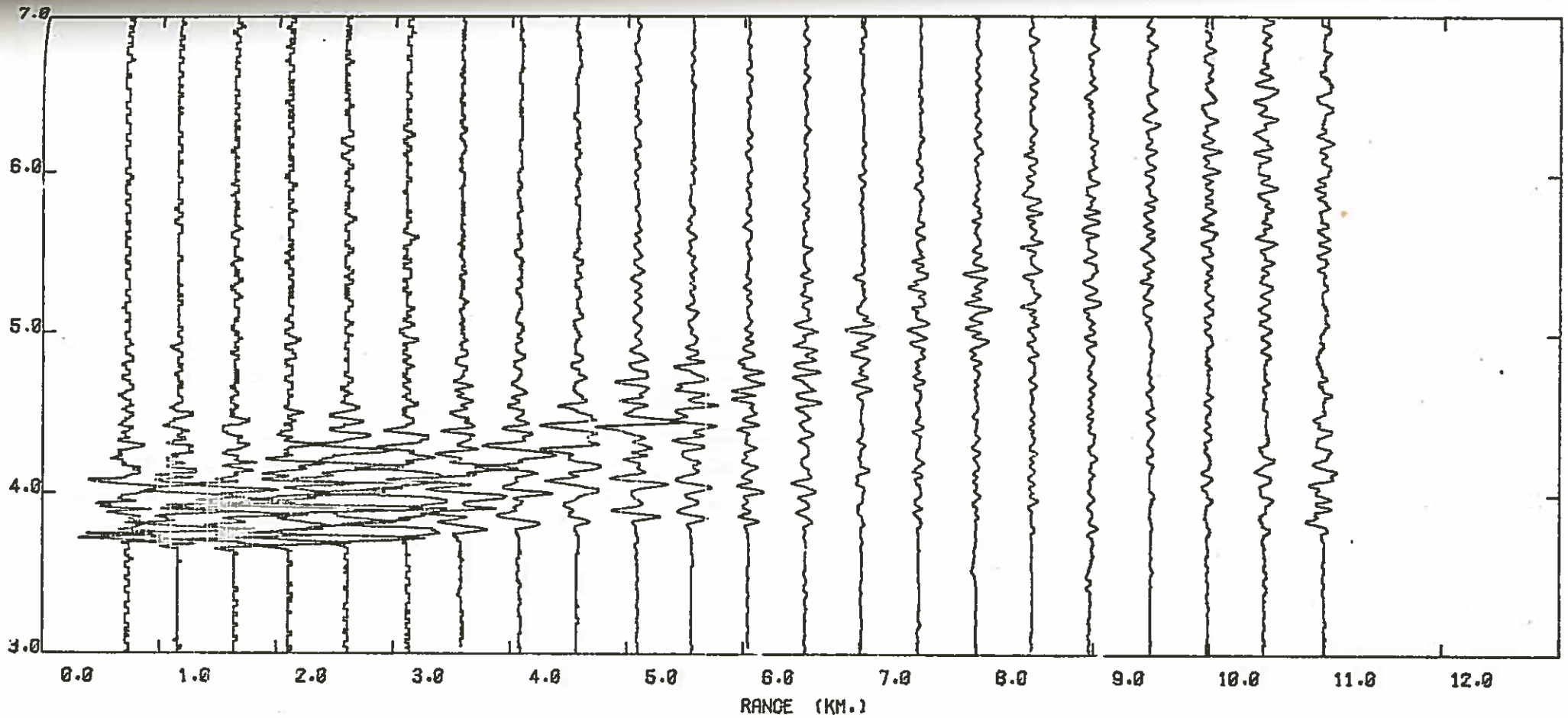

NORTH LINE · HORIZONTAL Y COMPONENT - D = 5840 M. BRF

LOW PASS FILTERED AT 30.00 HZ -- REDUCTION VELOCITY OF 6.00 KM/SEC
AMPLITUDES WEIGHTED BY (R/7.0)**2.9 FOR R>7.0 KM.

Figure C-5c

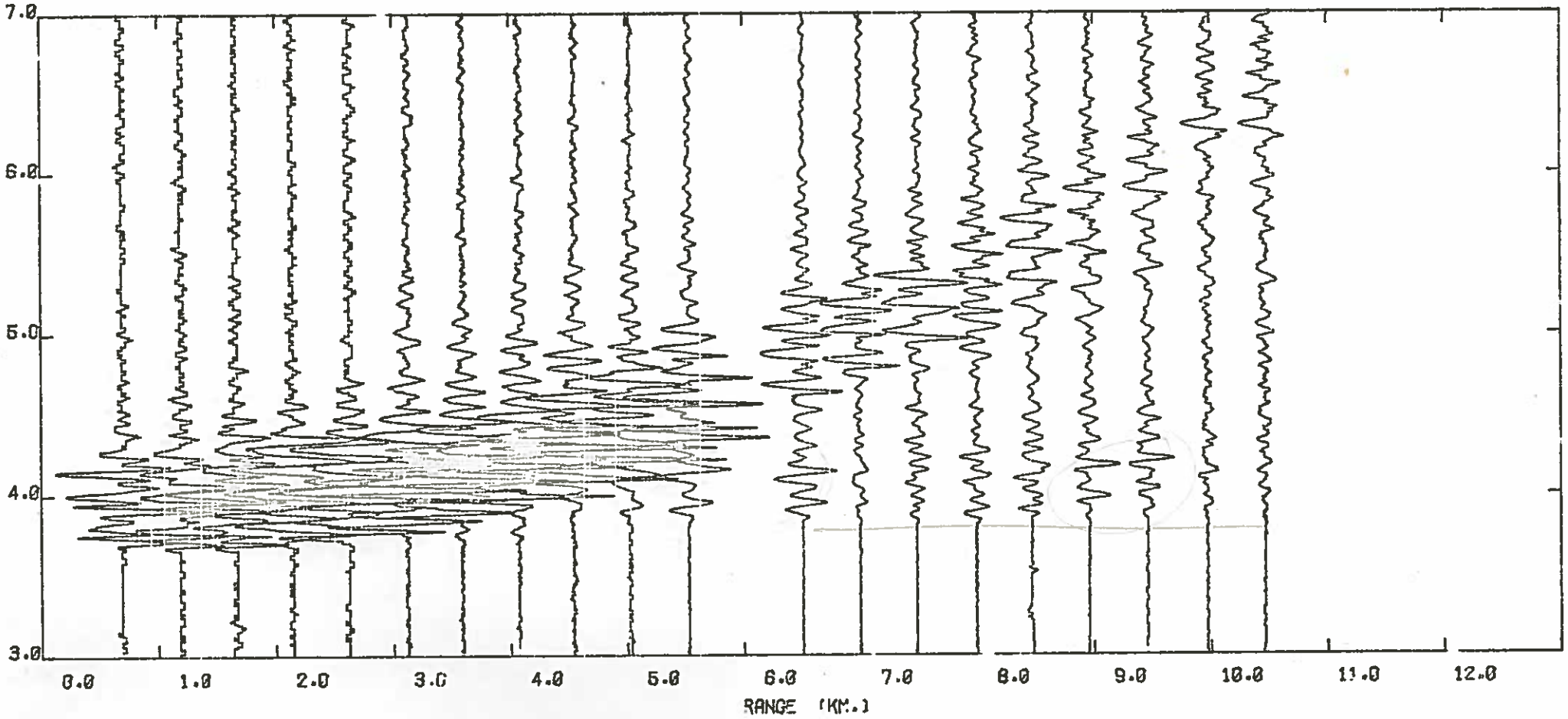

SOUTH LINE - VERTICAL COMPONENT - D = 5840 M. BRF

LOW PASS FILTERED AT 30.00 HZ -- REDUCTION VELOCITY OF 6.00 KM/SEC
AMPLITUDES WEIGHTED BY (R/7.0)**2.9 FOR R>7.0 KM.

Figure C-6a

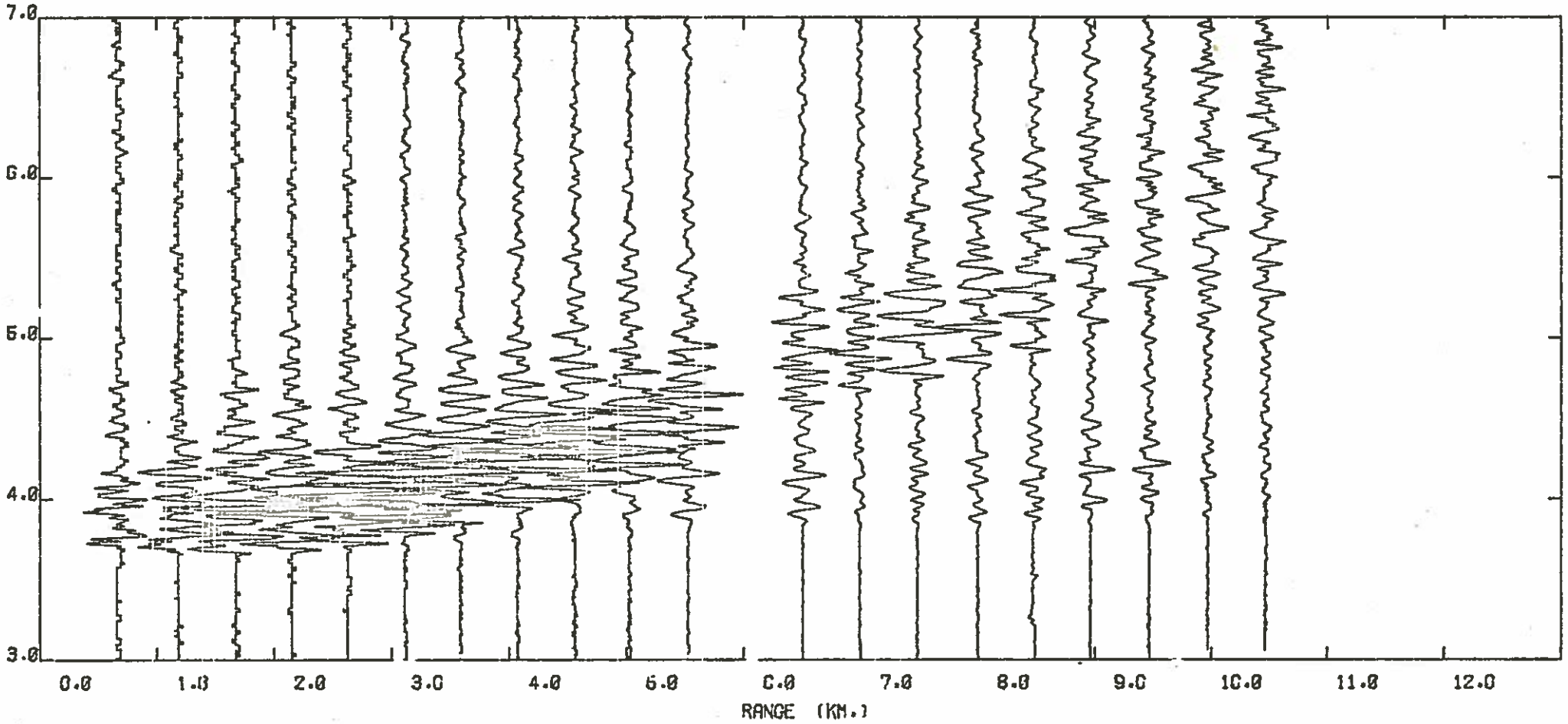

SOUTH LINE - HORIZONTAL X COMPONENT - D = 5840 M. BRF

LOW PASS FILTERED AT 30.00 HZ - REDUCTION VELOCITY OF 6.00 KM/SEC
AMPLITUDES WEIGHTED BY (R/7.0)**2.9 FOR R>7.0 KM.

Figure C-6b

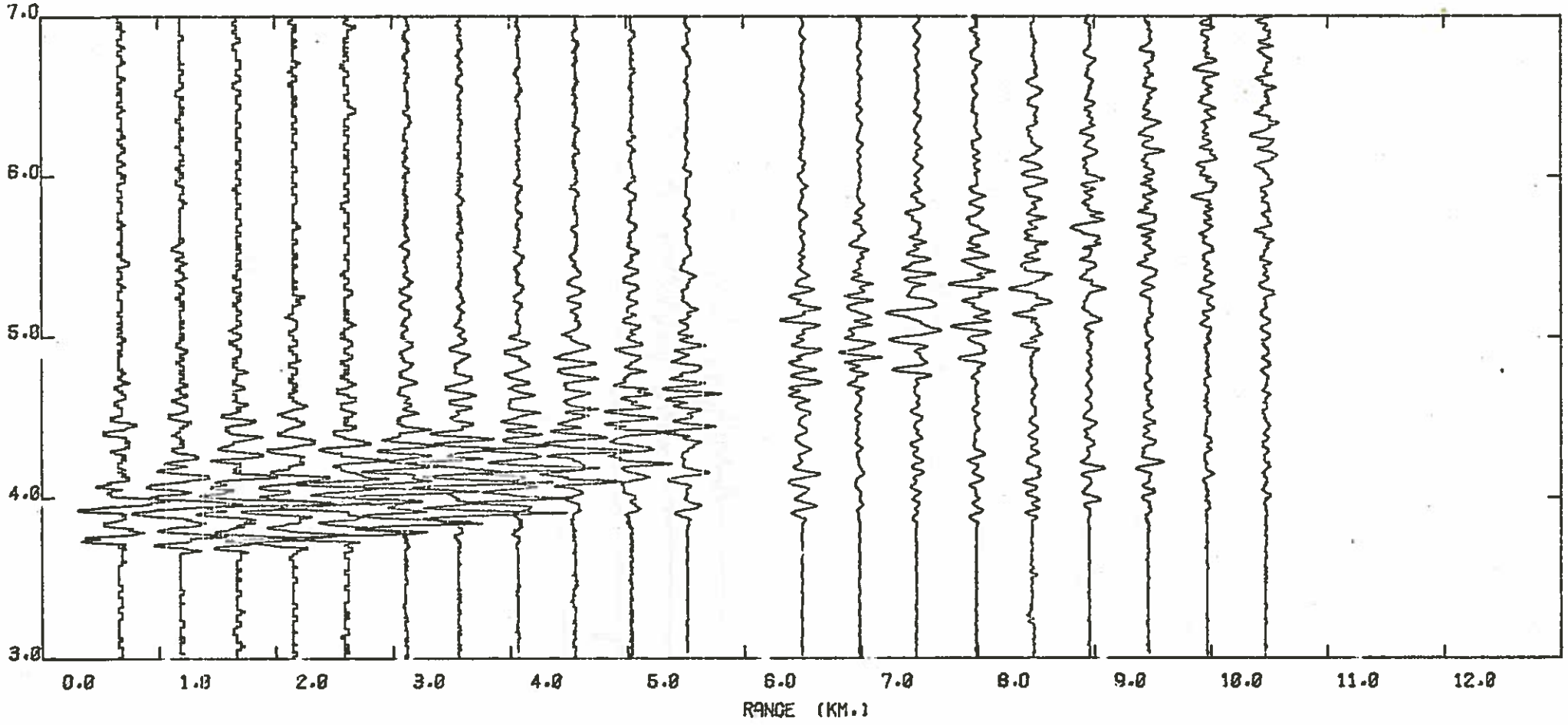

SOUTH LINE - HORIZONTAL Y COMPONENT - D = 5840 M. BRF

LOW PASS FILTERED AT 30.00 HZ - REDUCTION VELOCITY OF 6.00 KM/SEC
AMPLITUDES WEIGHTED BY (R/7.0)**2.9 FOR R>7.0 KM.

Figure C-6c

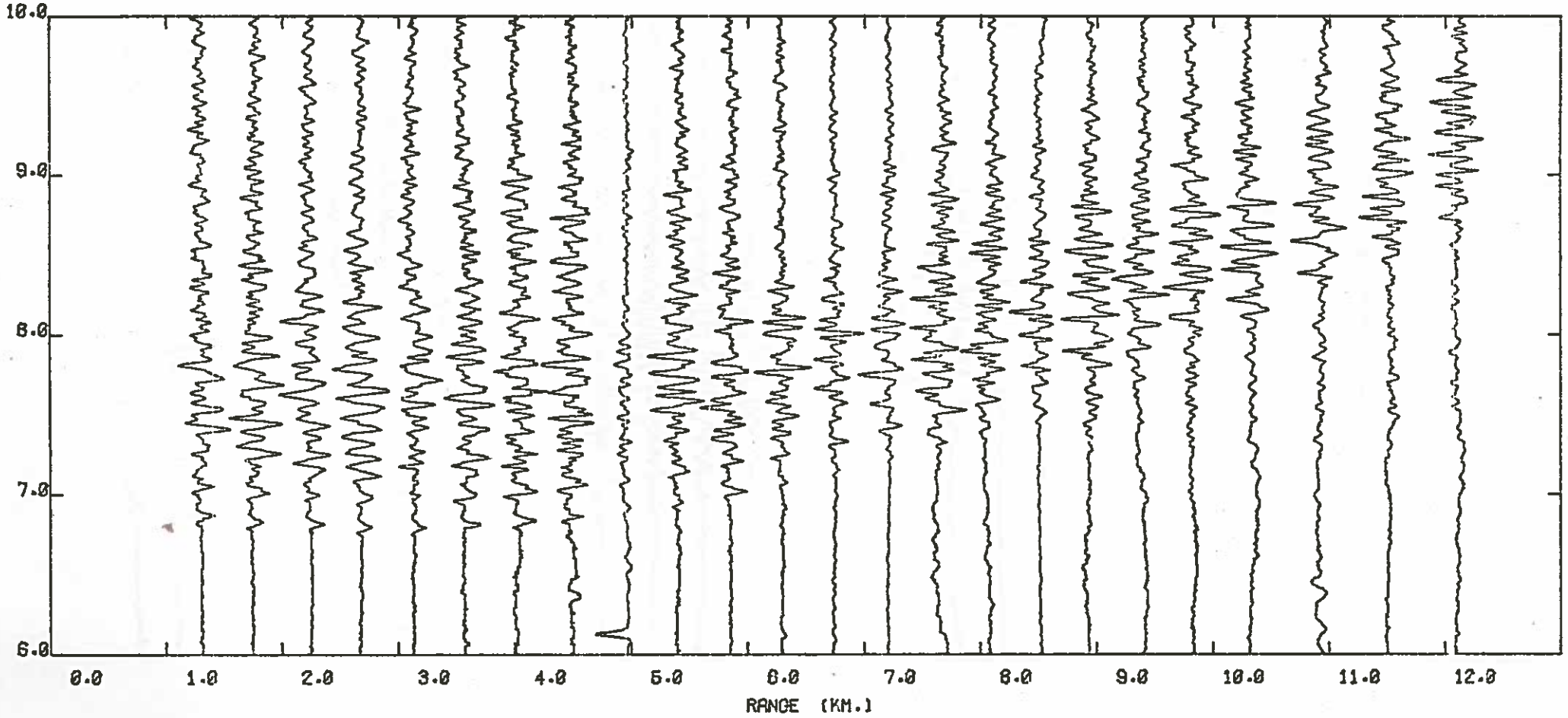

NORTH LINE - HYDROPHONE - D = 6060 M. BRF

LOW PASS FILTERED AT 30.00 HZ - REDUCTION VELOCITY OF 6.00 KM/SEC
INDIVIDUAL TRACES NORMALIZED TO A CONSTANT AMPLITUDE

Figure C-7a

Figures C-7a) to C-7f): These figures show the hydrophone arrivals for the lines in Figures 1-6. The hydrophone records are not used in the interpretation because of the poor quality of the basement arrivals.

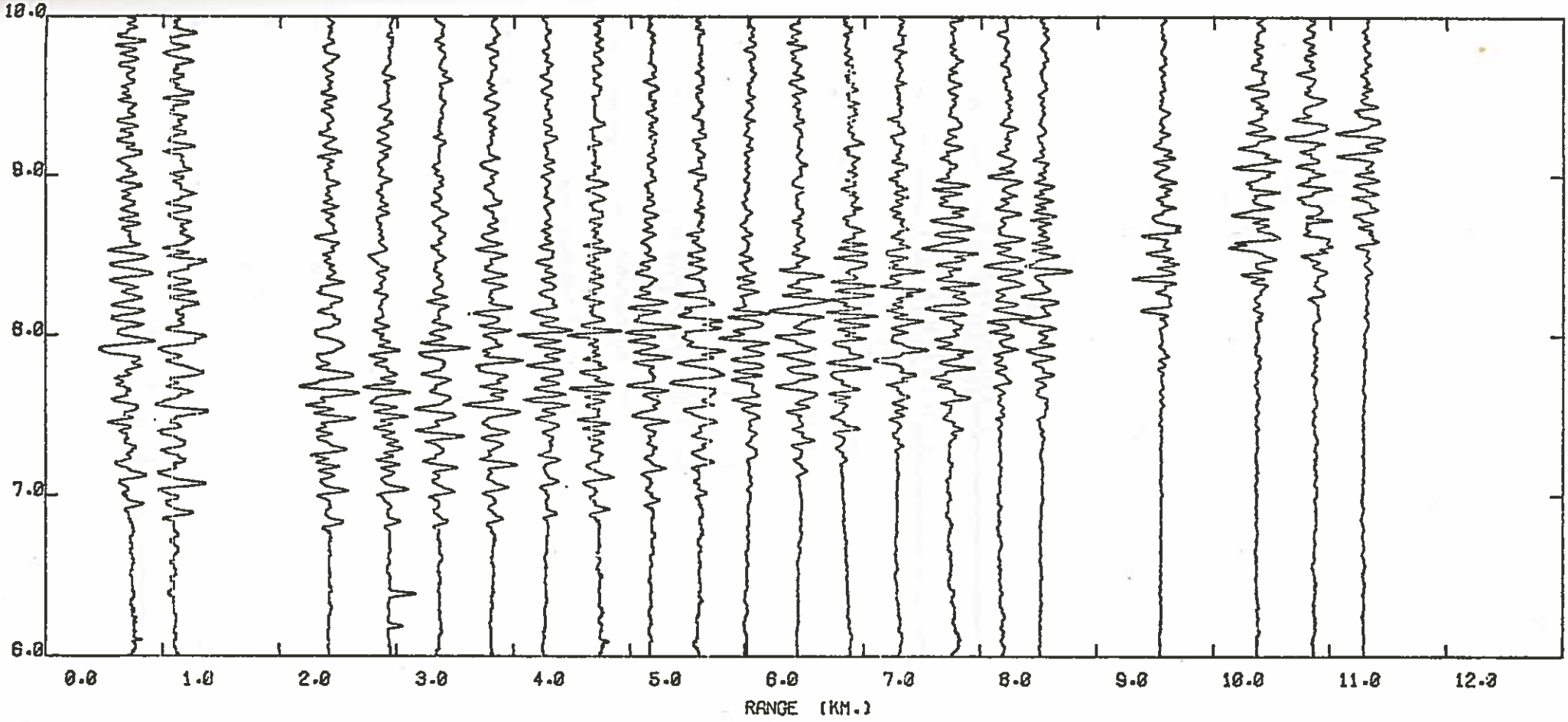

SOUTH LINE - HYDROPHONE - D = 6060 M. BRF

LOW PASS FILTERED AT 30.00 HZ - REDUCTION VELOCITY OF 6.00 KM/SEC
INDIVIDUAL TRACES NORMALIZED TO A CONSTANT AMPLITUDE

Figure C-7b

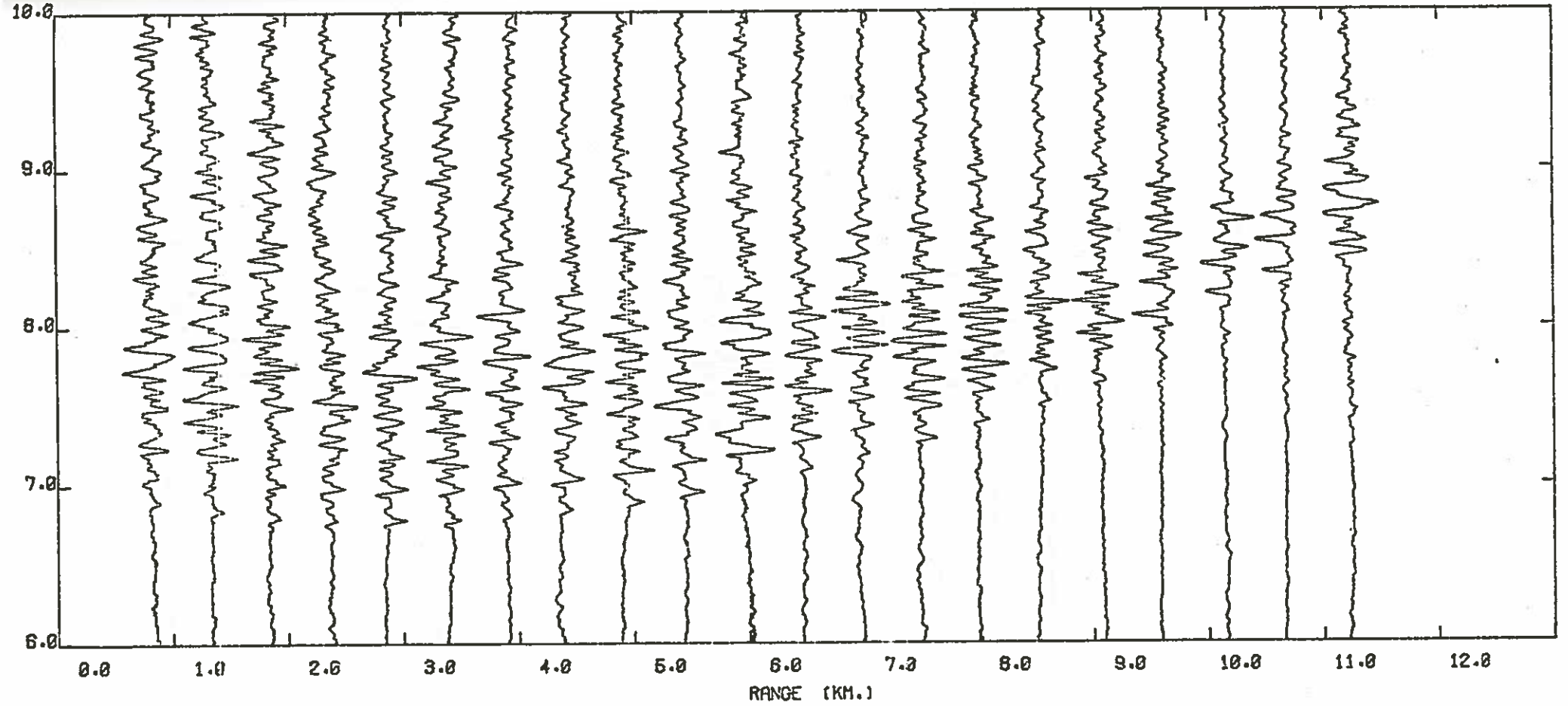

EAST LINE - HYDROPHONE - D = 6060 M. BRF

LOW PASS FILTERED AT 30.00 HZ - REDUCTION VELOCITY OF 8.00 KM/SEC
INDIVIDUAL TRACES NORMALIZED TO A CONSTANT AMPLITUDE

Figure C-7c

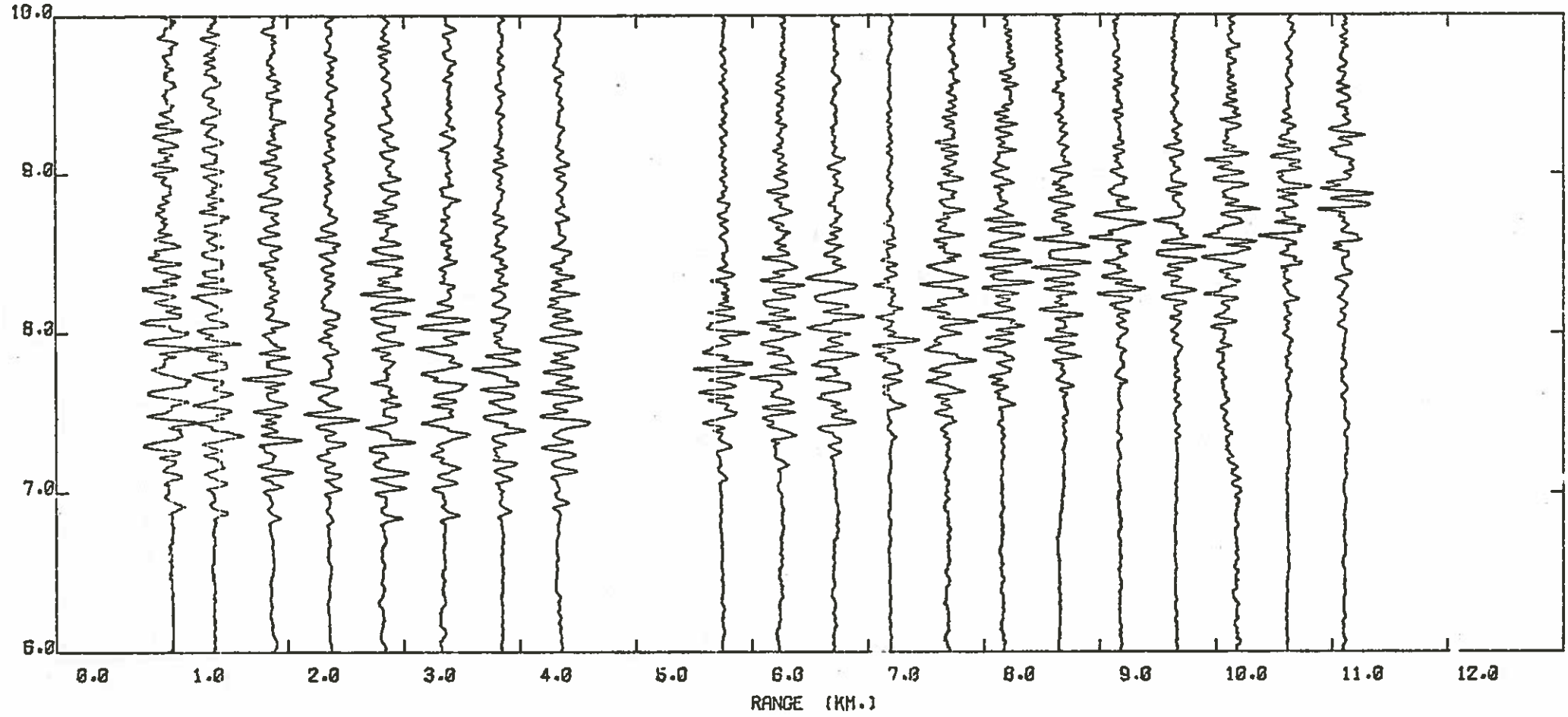

WEST LINE - HYDROPHONE - D = 6060 M. BRF

LOW PASS FILTERED AT 30.00 HZ - REDUCTION VELOCITY OF 6.00 KM/SEC
INDIVIDUAL TRACES NORMALIZED TO A CONSTANT AMPLITUDE

Figure C-7d

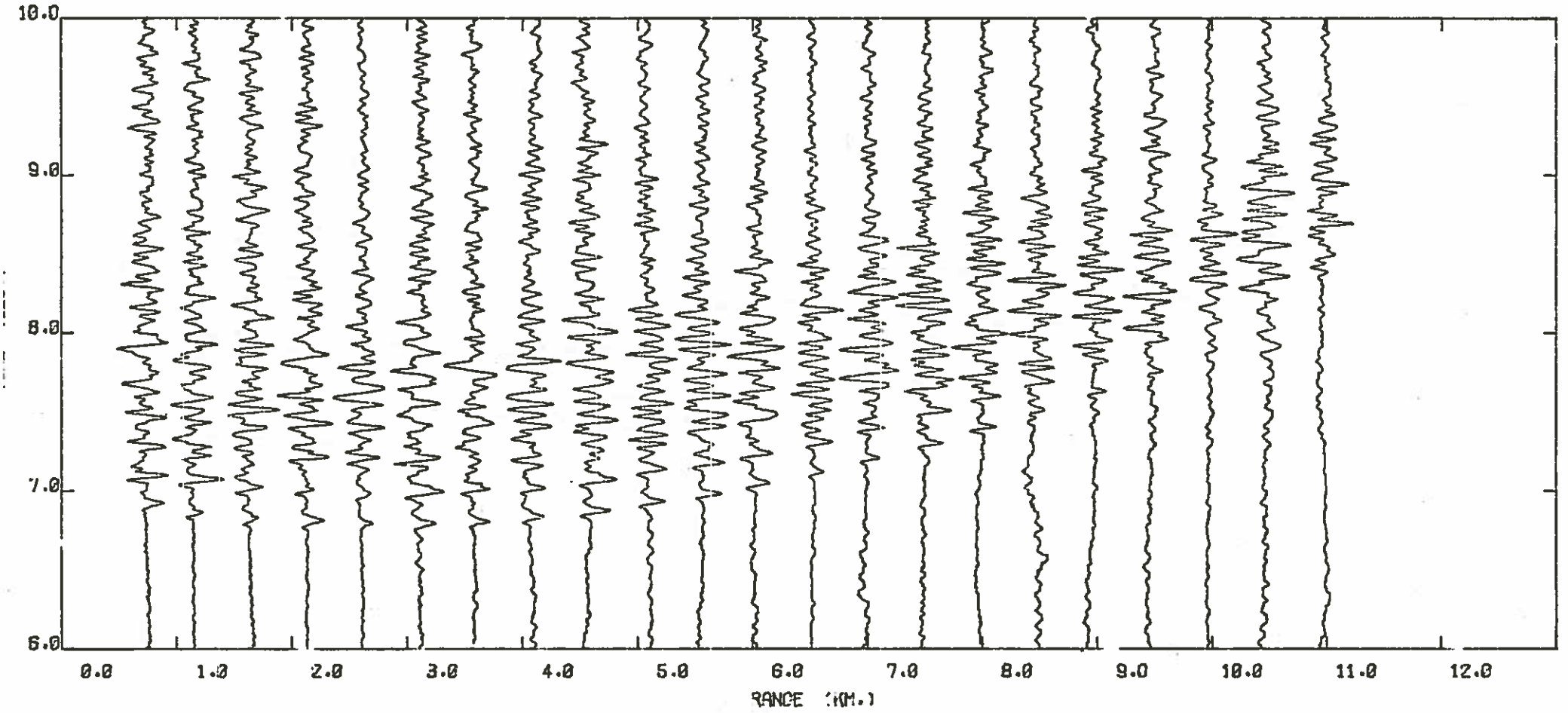

NORTH LINE - HYDROPHONE - D = 5840 M. BRF

LOW PASS FILTERED AT 30.00 HZ - REDUCTION VELOCITY OF 6.00 KM/SEC
INDIVIDUAL TRACES NORMALIZED TO A CONSTANT AMPLITUDE

Figure C-7e

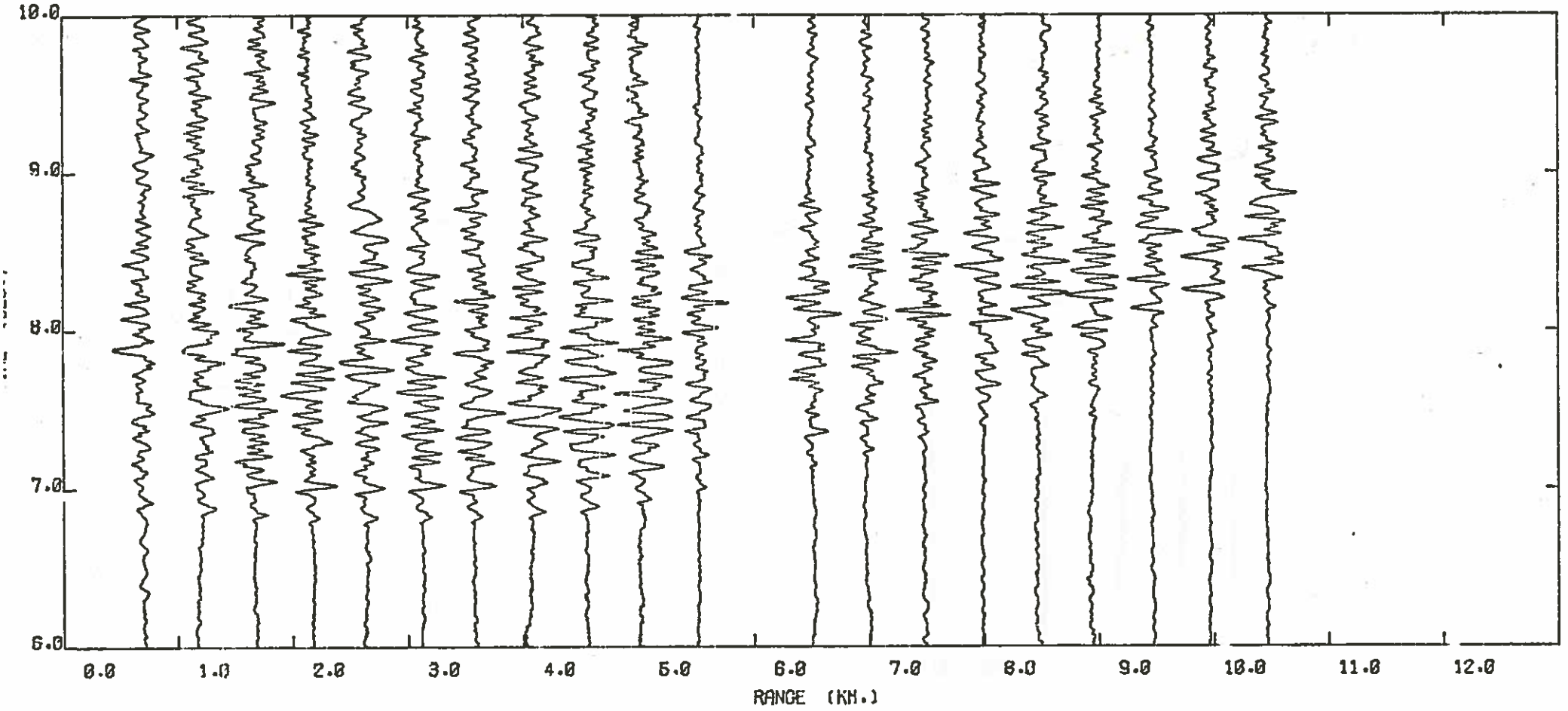

SOUTH LINE - HYDROPHONE - D = 5840 M. BRF

LOW PASS FILTERED AT 30.00 HZ - REDUCTION VELOCITY OF 6.00 KM/SEC
INDIVIDUAL TRACES NORMALIZED TO A CONSTANT AMPLITUDE

Figure C-7f

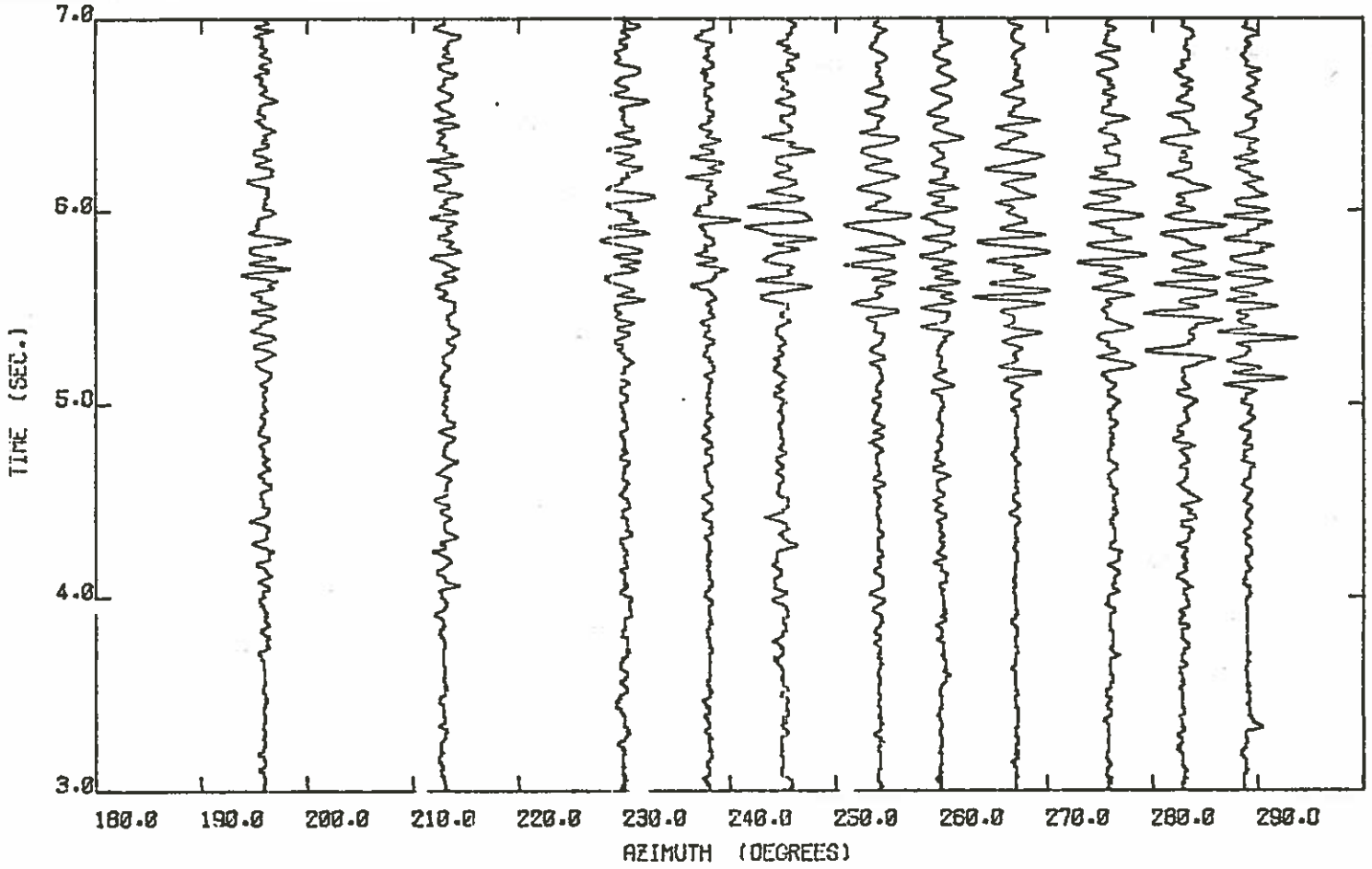

SOUTH-WEST AZIMUTHS - VERTICAL COMPONENT - D = 6060 M. BRF

LOW PASS FILTERED AT 30.00 HZ - REDUCTION VELOCITY OF 3.00 KM/SEC
AMPLITUDES WEIGHTED BY (R/7.0)**2.9 FOR R>7.0 KM.

Figure C-8a

Figures C-8a) to C-9c): These figures are for the azimuthal shots shown in Figures 4-1-3. The signal to noise ratio is too low to pick first arrivals conclusively. Travel times are also not reliable because of uncertainty in the flight time correction (Section 4-1b).

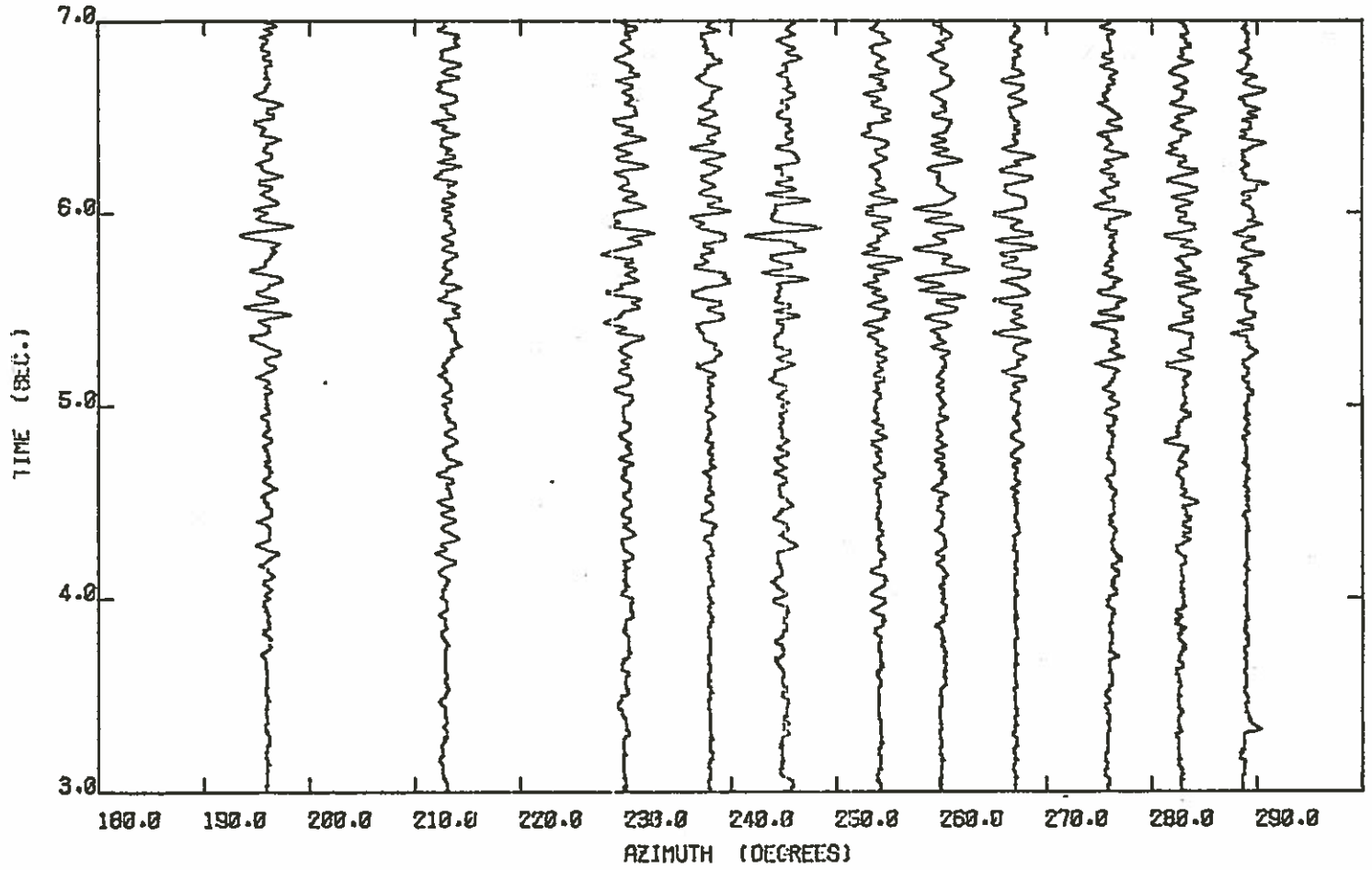

SOUTH-WEST AZIMUTHS - HORIZONTAL X COMPONENT - D = 6060 M. B

LOW PASS FILTERED AT 20.00 HZ - REDUCTION VELOCITY OF 6.00 KM/SEC
AMPLITUDES WEIGHTED BY (R/7.0)**2.9 FOR R>7.0 KM.

Figure C-8b

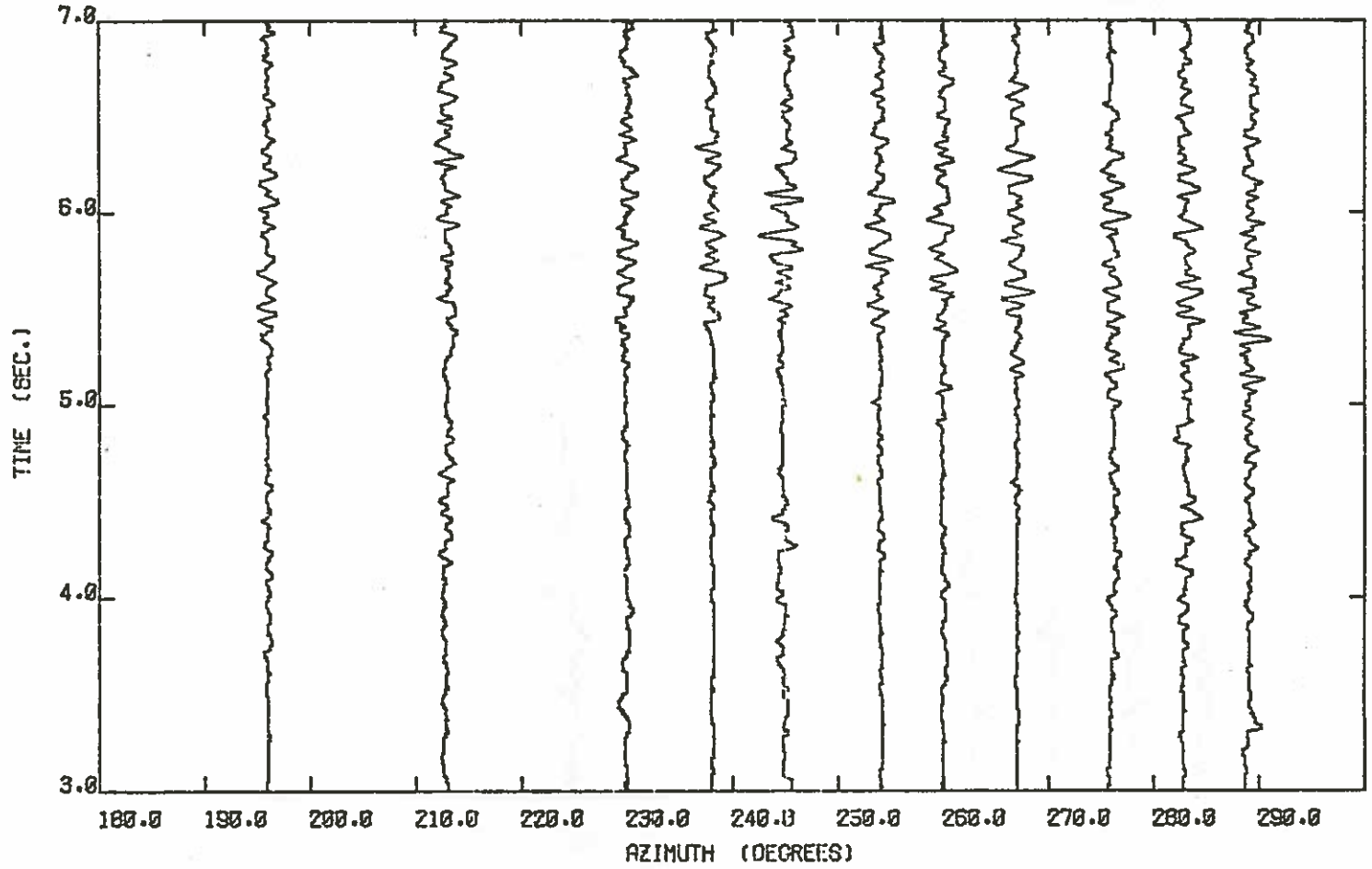

SOUTH-WEST AZIMUTHS - HORIZONTAL Y COMPONENT - D = 6050 M. B

LOW PASS FILTERED AT 30.00 HZ - REDUCTION VELOCITY OF 8.00 KM/SEC
AMPLITUDES WEIGHTED BY (R/7.0)**2.9 FOR R>7.0 KM.

Figure C-8c

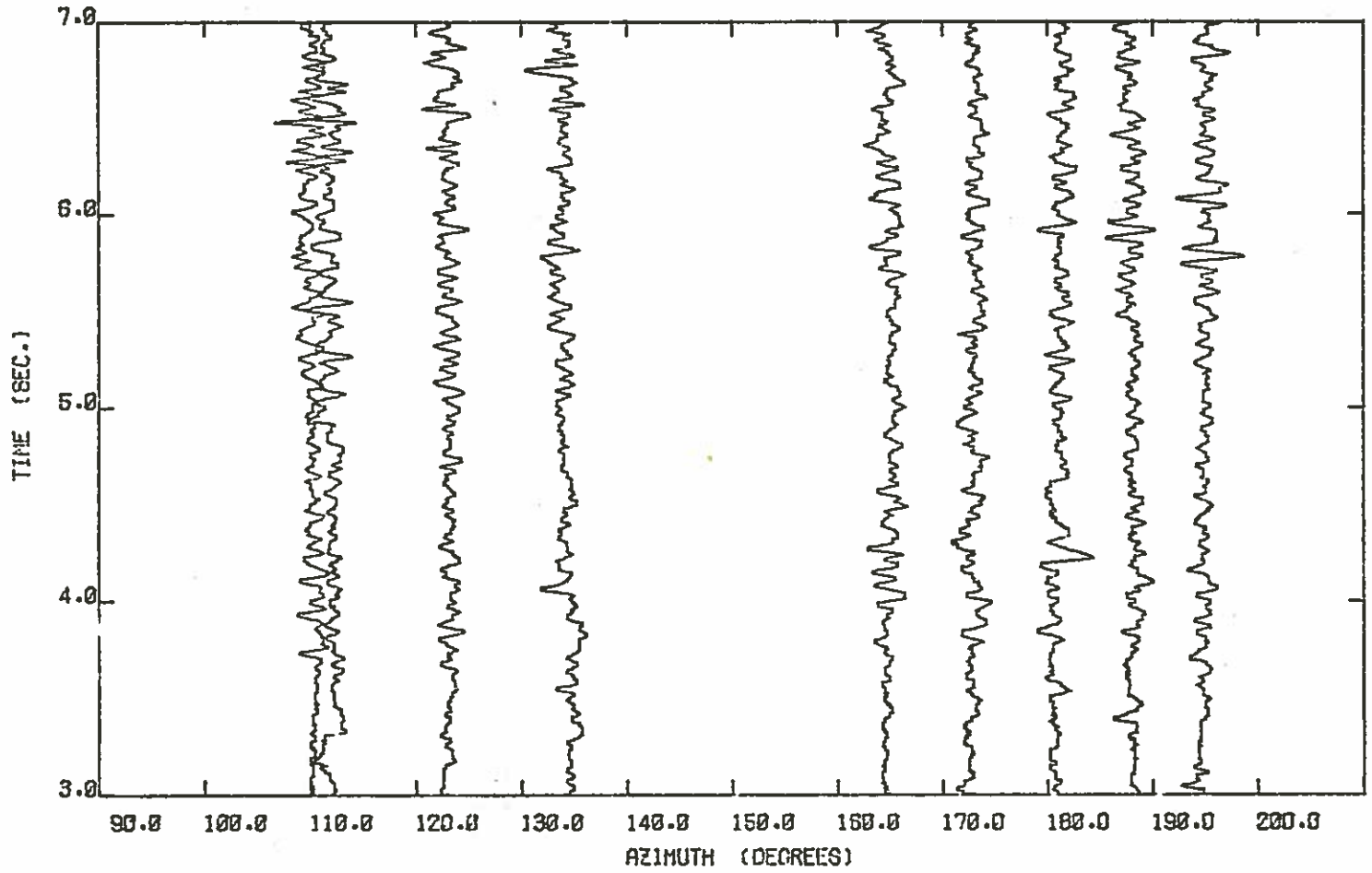

SOUTH-EAST AZIMUTHS - VERTICAL COMPONENT - D = 6060 M. BRF

LOW PASS FILTERED AT 30.00 HZ - REDUCTION VELOCITY OF 5.00 KM/SEC
AMPLITUDES WEIGHTED BY (R/7.0)**2.9 FOR R>7.0 KM.

Figure C-9a

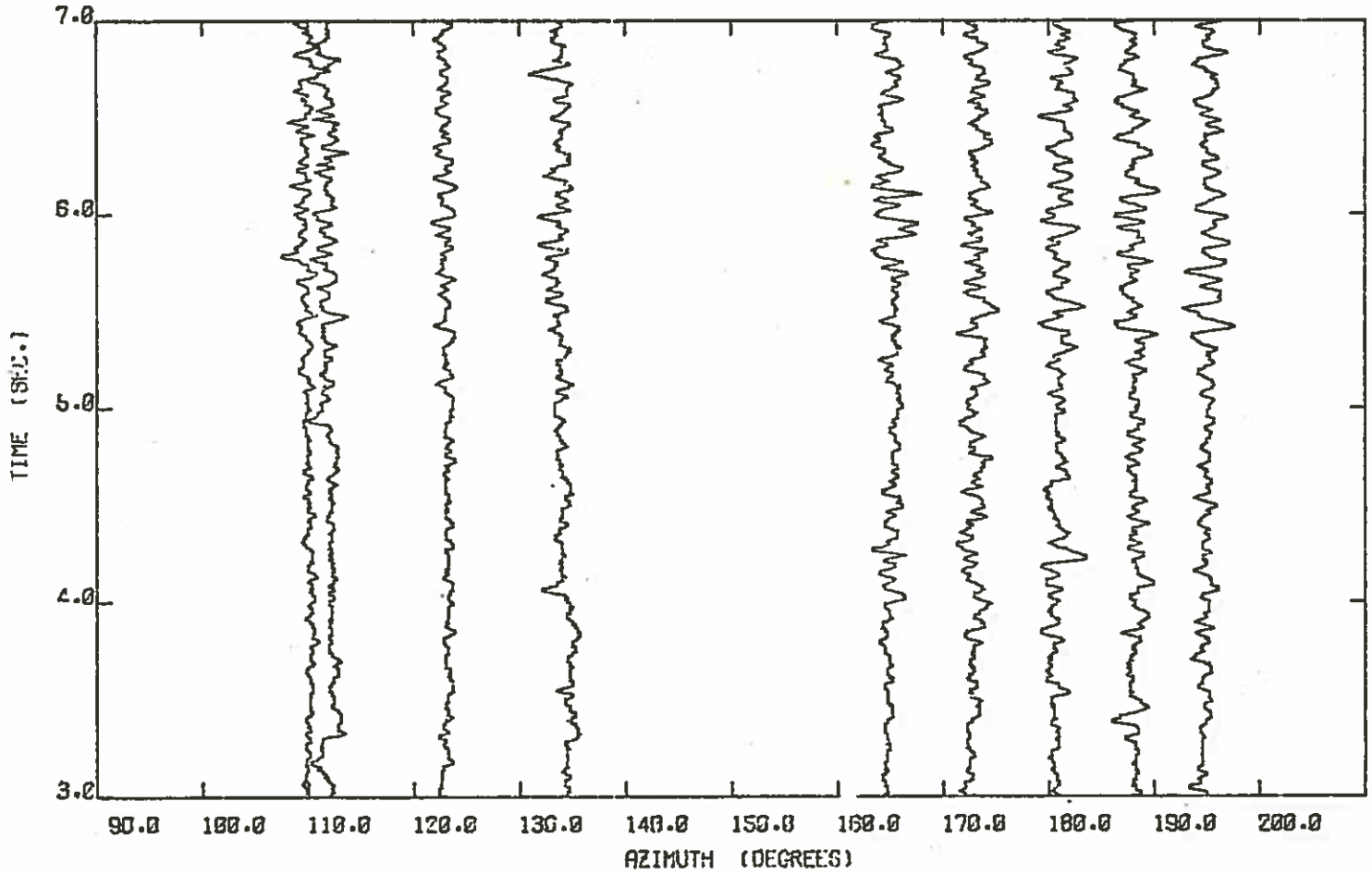

SOUTH-EAST AZIMUTHS - HORIZONTAL X COMPONENT - D = 6030 M. B

LOW PASS FILTERED AT 30.00 HZ - REDUCTION VELOCITY OF 6.00 KM/SEC
AMPLITUDES WEIGHTED BY (R/7.0)**2.9 FOR R>7.0 KM.

Figure C-9b

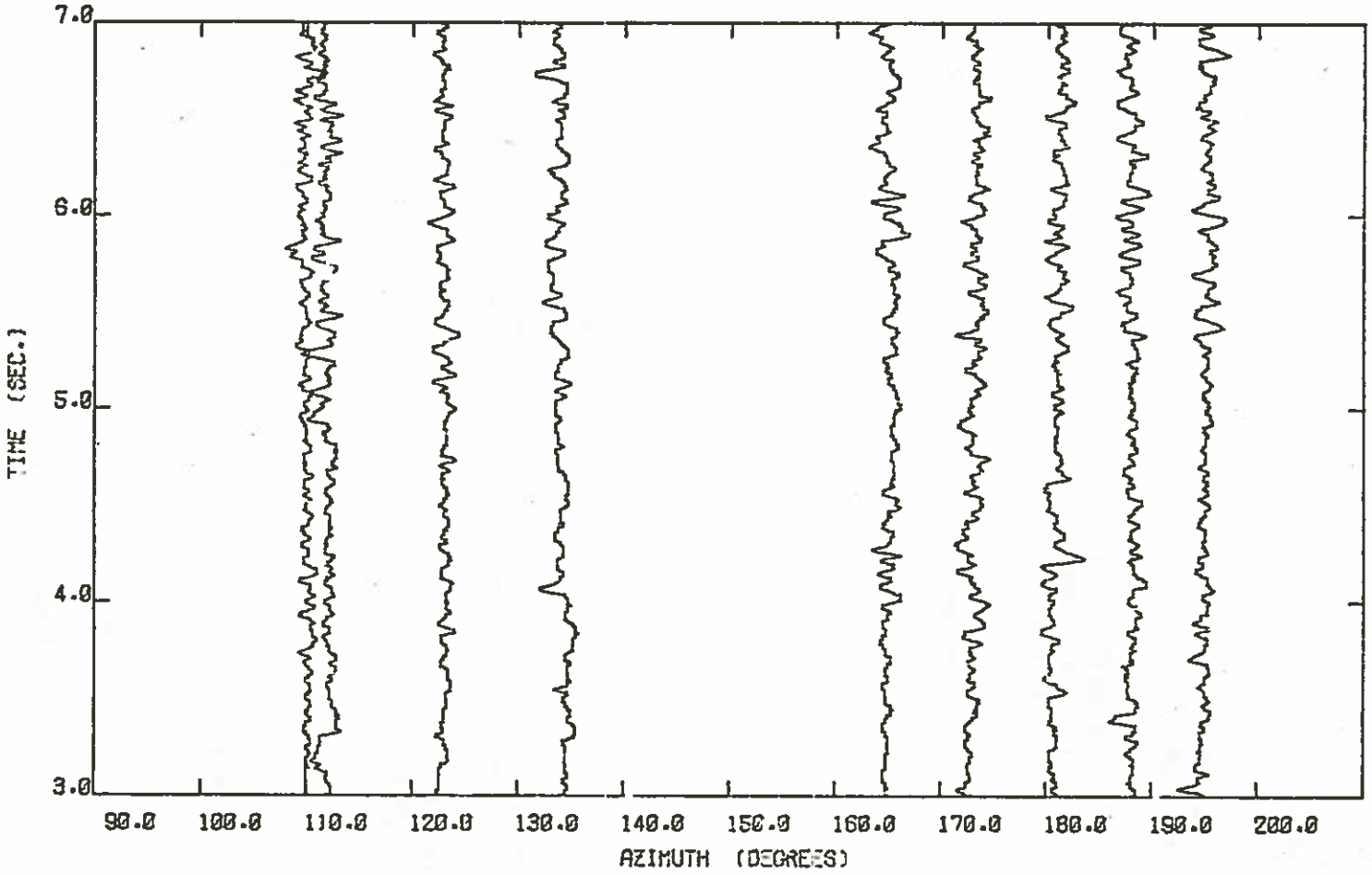

SOUTH-EAST AZIMUTHS - HORIZONTAL Y COMPONENT - D = 6060 M. B

LOW PASS FILTERED AT 30.00 HZ - REDUCTION VELOCITY OF 6.00 KM/SEC
AMPLITUDES WEIGHTED BY (R/7.0)**2.9 FOR R>7.0 KM.

Figure C-9c

REFERENCES

ANDERSON, D.L. 1961. Elastic wave propagation in layered anisotropic media. J. geophys. Res., 66, 2953.

ANDERSON, D.L. and ARCHAMBEAU, C.B. 1964. The anelasticity of the earth. J. geophys. Res., 69, 2071-2084.

ANDERSON, D.L., MINSTER, B and COLE, D. 1974. The effect of oriented cracks on seismic velocities. J. geophys. Res., 79, 4011-4016.

ATTEWELL, P.B. and RAMANA, Y.V. 1966. Wave attenuation and internal friction as functions of frequency in rocks. Geophysics., 31, 1049-1056.

AUMENTO, F., MELSON,W.G. et al. 1977. Site 332. In: AUMENTO, F., MELSON, W.G. et al., Initial Reports of the Deep Sea Drilling Project, Volume 37: (U.S. Government Printing Office) 775-794.

BACKUS, G.E. 1965. Possible forms of seismic anisotropy of the uppermost mantle under oceans. J. geophys. Res., 70, 3429-3439.

BALLARD, R.D., BRYAN, W.B., HEIRTZLER, J.R., KELLER, G., MOORE, J.G. and van ANDEL, T.H. 1975. Manned submersible operations in the Famous area: Mid-Atlantic ridge. Science, 190, 103-108.

BALLARD, R.D. and van ANDEL, T.H. 1977. Morphology and tectonics of the inner rift valley at lat 36°50'N on the Mid Atlantic ridge. Bull. geol. Soc. Am., 88, 507-530.

BARRETT, D.L. and AUMENTO, F. 1970. The Mid-Atlantic Ridge near 45°N, XI. Seismic velocity, density and layering in the crust. Can. J. Earth Sci., 7, 1117.

BAMFORD, D. and CRAMPIN, S. 1977. Seismic anisotropy - the state of the art. Geophys. J.R. astr. Soc., 49, 1-8.

BERRY, M.J. and WEST, G.F. 1966. An interpretation of the first-arrival data of the Lake Superior experiment by the time-term method. Bull. seism. Soc. Am., 56, 141-171.

BIRCH, F., 1960. The velocity of compressional waves in rocks to 10 kb - Part I. J. geophys. Res., 65, 1083-1102.

BIRCH, F., 1961. The velocity of compressional waves in rocks to 10 kb - Part II. J. geophys. Res., 66, 2199- 2224.

BOND, L.O., ALGER, R.P., SCHMIDT, A.W. 1971. Well log applications in coal mining and rock mechanics. Trans. SME of AIME Dec 1971.

BRACE, W.F. 1965. Some new measurements of linear compressibility of rocks. J. geophys. Res., 70, 391-398.

BRACE, W.F., SILVER, E., HADLEY, K. and GOETZE, C. 1972. Cracks and pores: a closer look. Science, 178, 162-163.

BRAILE, L.W. and SMITH, R.B. 1975. Guide to the interpretation of crustal refraction profiles. Geophys. J.R. astr. Soc., 40, 145-176.

BRYAN, W.B., ROBINSON, P.T. et al. 1977. Studying oceanic layers. Geotimes, July/August 1977.

BUNCH, A.W.H. 1977. The Cambridge seismic digital processing system. In-house report, in preparation, Dept. of Geodesy & Geophysics, Cambridge, U.K.

BURKE, J.A., SCHMIDT, A.W. and CAMPBELL, Jr, R.L. 1969. The litho-porosity cross plot. The Log Analyst, November-December, 1969.

CANN, J.R. 1974. A model for oceanic crustal structure developed. Geophys. J.R. astr. Soc., 39, 169-187.

ČERVENÝ, V. 1972. Seismic rays and ray intensities in inhomogeneous anisotropic media. Geophys. J.R. astr. Soc., 29, 1-13.

ČERVENÝ, V., LANGER, J. and PŠENČIK, I. 1974. Computation of geometric spreading of seismic body waves in laterally inhomogeneous media with curved interfaces. Geophys. J.R. astr. Soc., 38, p9.

ČERVENÝ, V. and PŠENČIK, I. 1972. Rays and travel-time curves in inhomogeneous anisotropic media. Z. Geophys., 38, 565-577.

ČERVENÝ, V. and RAVINDRA, R. 1971. Theory of seismic head waves. University of Toronto Press, Toronto, Canada.

CHAPMAN, C.H. 1974. A generalized ray theory for inhomogeneous media. Geophys. J.R. astr. Soc., 36, 673-704.

CHRISTENSEN, N.I. 1970. Composition and evolution of the oceanic crust. Marine Geology, 8, 139-154.

CHRISTENSEN, N.I. 1972. Seismic anisotropy in the lower oceanic crust. Nature, 237, 450-451.

CHRISTENSEN, N.I. 1977. Seismic velocities of Leg 37 rocks and their geophysical implications. In AUMENTO, F., MELSON, W.B. et al., Initial Reports of the Deep Sea Drilling Project, Volume 37: Washington (U.S. Government Printing Office), 389-393.

CHRISTENSEN, N.I. and SALISBURY, M.H. 1972. Sea floor spreading, progressive alteration of layer 2 basalts and associated changes in seismic velocities. Earth Planet. Sci. Lett., 15, 367-375.

CHRISTENSEN, N.I. and SALISBURY, M.H. 1973. Velocities, elastic moduli and weathering age relations for Pacific layer 2 basalts. Earth Planet. Sci. Lett., 19, 461-470.

CHRISTENSEN, N.I. and SALISBURY, M.H. 1975. Structure and constitution of the lower oceanic crust. Rev. Geophys., 13, 57-86.

CHRISTENSEN, N.I. and SHAW, G.H. 1970. Elasticity of mafic rocks from the Mid-Atlantic Ridge. Geophys. J.R. astr. Soc., 20, 271-284.

CRAMPIN, S. 1977. A review of the effects of anisotropic layering on the propagation of seismic waves. Geophys. J.R. astr. Soc., 49, 9-27.

CRAMPIN, S. 1978. Seismic wave propagation through a cracked solid: polarization as a possible dilatancy diagnostic. Geophys. J.R. astr. Soc., in press.

CRAMPIN, S., McGONIGLE, R. and BAMFORD, D. 1978. Estimating crack parameters by inversion of P-wave velocity anisotropy. Geophysics, in press.

CROSSON, R.S. and CHRISTENSEN, N.I. 1969. Transverse isotropy of the upper mantle in the vicinity of a Pacific fracture zone. Bull. seism. Soc. Am., 59, 59-72.

DEFANT, A. 1961. Physical Oceanography, Vol. I. Pergamon Press, New York.

DE WIT, M.J. and STERN, C.R. 1976. A model for ocean-floor metamorphism, seismic layering and magnetism. Nature 264, 615-619.

DIX, C.H. 1939. Interpretation of well-shot data. Geophysics, 4, 24-32.

DOBRIN, M.B. 1976. Introduction to geophysical prospecting. McGraw-Hill Book Company, New York.

DUNKIN, J.W. 1965. Computation of modal solutions in layered media at high frequencies. Bull. seism. Soc. Am., 55, 335-358.

DUNOYER DE SEGONZAC, P.H. and LAHERRER, J. 1959. Applications of the continuous velocity log to anisotropic measurements in the northern Sahara. Geophys. Prosp., 7, 202-217.

ERGIN, K. 1952. Energy ratio of the seismic waves reflected and refracted at a rock-water boundary. Bull. seism. Soc. Am., 42, 349-372.

ESHELBY, J.D. 1957. The determination of the elastic field of an ellipsoidal inclusion and related problems. Proc. Roy. Soc. Ser. A., 241, 376-396.

EWING, J.I. 1963. Elementary theory of seismic refraction and reflection measurements. In: The Sea, Vol. 3, ed. M.N. HILL, John Wiley and Sons, New York.

EWING, W.M., JARDETZKY, W.S., and PRESS, F. 1957. Elastic waves in layered media. McGraw-Hill Book Company Inc., New York.

FACSINAY, L. and SAGHY, G. 1969. Interpretation of refracted-diffracted waves due to dykes. Geophys. Prosp., 17, 392-403.

FOWLER, C.M.R. 1976. Seismic studies of the Mid-Atlantic ridge. Ph.D. thesis, Dept. of Geodesy & Geophysics, University of Cambridge, Cambridge, U.K.

FOX, P.J., SCHREIBER, E. and PETERSON, J.J. 1973. The geology of the oceanic crust: compressional wave velocities of oceanic rocks, J. geophys. Res., 78, 5155-5172.

FRANCIS, T.J.G. 1976. The ratio of compressional to shear velocity and rock porosity on the axis of the Mid-Atlantic Ridge. J. geophys. Res., 81, 4361-4364.

FRANCIS, T.J.G., PORTER, I.T., LANE, R.D., OSBORNE, P.J., POOLEY, J.E., and TOMKINS, P.K. 1975. Ocean Bottom Seismograph. Marine Geophysical Researches, 2, 195-213.

FRANCIS, T.J.G. and PORTER, I.T. 1977. Experience gained with the Blacknest ocean bottom seismograph. Marine Geophysical Researches, 3, 143-150.

FRIEDMAN, M. and BUR, T.R. 1974. Investigations of the relations among residual strain, fabric, fracture, and ultrasonic attenuation and velocity in rocks. Int. J. Rock Mech. Min. Sci. and Geomech., 11, 221-234.

FUCHS, K. 1968a. Das reflexions- und transmissionsvermögen eines geschichteten mediums mit beliebiger tiefen-verteilung der elastischen moduln und der dichte für schrägen einfall ebener wellen. Z. Geophys., 34, 389-413.

FUCHS, K. 1968b. The reflection of spherical waves from transition zones with arbitrary depth-dependent elastic moduli and density. J. Phys. Earth, 16, Special Issue, p 27.

FUCHS, K. 1970. On the determination of velocity depth distributions of elastic waves from the dynamic characteristics of the reflected wave field. Z. Geophys., 36, 531-548.

FUCHS, K. 1971. The method of stationary phase applied to the reflection of spherical waves from transmission zones with arbitrary depth-dependent elastic moduli and density. Z. Geophys., 37, 89-117.

FUCHS, K. and MÜLLER, G. 1971. Computation of synthetic seismograms with the reflectivity method and comparison with observations. Geophys. J.R. astr. Soc., 23, 417-433.

GAL'PERIN, E.I. 1974. Vertical seismic profiling. Society of Exploration Geophysicists (Special Publication No. 12.)

GARDNER, L.W. 1939. An areal plan of mapping subsurface structure by refraction shooting. Geophysics, 4, 247.

GARDNER, G.H.F., GARDNER, L.W. and GREGORY, A.R. 1974. Formation velocity and density - the diagnostic basics for stratigraphic traps. Geophysics, 39, 770-780.

GEERTSMA, J. 1961. Velocity-log interpretation: the effect of rock bulk compressibility. Soc. Pet. Engrs. J. (AIME), 1, 235-246.

GEO SPACE CORPORATION 1972. Technical manual for the wall-lock well geophone. Geo Space Corporation, 5803 Glenmont Drive, Houston, Texas 77036, U.S.A.

GORDON, R.B. and NELSON, C. 1966. Anelastic properties of the earth. Rev. Geophys., 4, 457-477.

GRANT, F.S. and WEST, G.F. 1965. Interpretation theory in applied geophysics. McGraw-Hill Book Company, New York.

GRETNER, P.E.F. 1961. An analysis of the observed time discrepancies between continuous and conventional well velocity surveys. Geophysics, 26, 1-11.

HADLEY, K. 1976. Comparison of observed and calculated crack densities and seismic velocities in Westerly granite. J. geophys. Res., 81, 3484-3494.

HALPERIN, E.I. and FROLOVA, A.V. 1961. Three component seismic observations in boreholes - I & II. Bull. Acad. Sci. USSR, Geophys. Ser., 519-528, 644-653.

HAMILTON, E.L. 1972. Compressional wave attenuation in marine

HAMILTON, E.L. 1976a. Sound attenuation as a function of depth in the sea floor. J. Acoust. Soc. Am., 59, 528-535.

HAMILTON, E.L. 1976b. Attenuation of shear waves in marine sediments. J. Acoust. Soc. Am., 60, 334-338.

HEIRTZLER, J.R. and LE PICHON, X. 1974. A study of the genesis of tectonic plates. Geology, 2, 273.

HEIRTZLER, J.R. and van ANDEL, T.H. 1977. Profect FAMOUS: its origin, program and setting. Geol. Soc. Am. Bull., 88, 481-487.

HELMBERGER, D.V. 1968. The crust-mantle transition in the Bering Sea. Bull. seism. Soc. Am., 58, 179-214.

HELMBERGER, D.V. 1977. Fine structure of an Aleutian crustal section. Geophys. J.R. astr. Soc., 48, 81-90.

HELMBERGER, D.V. and MORRIS, G.B. 1969. A travel time and amplitude interpretation of a marine refraction profile: primary waves. J. geophys. Res., 74, 483-494.

HELMBERGER, D.V. and MORRIS, G.B. 1970. Travel time and amplitude interpretation of a marine refraction profile: transformed shear waves. Bull. seism. Soc. Am., 60, 593-600.

HESS, H. 1964. Seismic anisotropy of the uppermost mantle under oceans. Nature, 203, 629-631.

HILL, M.N. 1963. Single-ship seismic refraction shooting. In: The Sea, Vol. 3., ed. M.N. HILL, John Wiley and Sons, New York.

HOUTZ, R.E. 1976. Seismic properties of layer 2A in the Pacific. J. geophys. Res., 81, 6321-6331.

HOUTZ, R. and EWING, J. 1976. Upper crustal structure as a function of plate age. J. geophys. Res., 81, 2490-2498.

HRON, F. 1972. Numerical methods of ray generation in multilayered media. In: Methods in Computational Physics, Vol 12, ed B.A. Bolt, Academic Press, New York.

HRON, F, KANASEWICH, E.R. and ALPASLAN, T. 1974. Partial ray expansion required to suitably approximate the exact wave solution. Geophys. J.R. astr. Soc., 36, 607-626.

HYNDMAN, R.D. 1974. Seismic velocities of basalts from DSDP Leg 26. In: Davies, T.A., Luyendyk, B.P. et al., Initial Reports of the Deep Sea Drilling Project Volume 26: Washington (U.S. Government Printing Office), 509-512.

HYNDMAN, R.D. 1977. Seismic velocity measurements of basement rocks from DSDP leg 37. In: AUMENTO, F., MELSON, W.G. et al. Initial Reports of the Deep Sea Drilling Project, Volume 37: Washington (U.S. Government Printing Office), 373-387.

HYNDMAN, R.D., VON HERZEN, R.P., ERICKSON, A.J. and JOLIVET, J. 1977. Heat flow measurements DSDP Leg 37. In: AUMENTO, F., MELSON, W.G. et al., Initial Reports of the Deep Sea Drilling Project, Volume 37 Washington (U.S. Government Printing Office), 347-362.

JACKSON, D.D. and ANDERSON, D.L. 1970. Physical mechanisms of seismic attenuation. Rev. Geophys. Space Phys., 8, 1-63.

JOHNSON, J.N. 1974. Inelastic plane-wave propagation in anisotropic rocks. J. geophys. Res., 79, 4900-4907.

JOHNSON, L.R. and WENK, H.R. 1974. Anisotropy of physical properties in metamorphic rocks. Tectonophysics, 23, 79-98.

JOHNSON, R.V.II, LISTER, C.R.B. and LEWIS, B.T.R. 1977. A direct recording ocean bottom seismometer. Marine Geophysical Researches, 3, 65-85.

JOHNSON, S.H., CRANFORD, M.D., BROWN, B.T., BOWERS, J.E., and McALLISTER, R.E. 1977. A free-fall direct-recording ocean bottom seismograph. Marine Geophysical Researches, 3, 103-117.

JOLLY, R.N. 1953. Deep hole geophone study in Garvin County, Oklahoma. Geophysics, 18, 1953.

KANASEWICH, E.R. 1973. Time sequence analysis in geophysics. The University of Alberta Press, Edmonton, Canada.

KANASEWICH, E.R., ALPASLAN, T. and HRON, F. 1973. The importance of S-wave precursors in shear wave studies. Bull. seism. Soc. Am., 63, 2167-2176.

KARUS, E.V. and ZUCKERNIK, V.B. 1958. An ultrasonic apparatus for studying the physical and mechanical properties of rocks intersected by a drill hole. Bull. Acad. Sci. USSR, Geophys Ser. 755-761.

KAYE, G.W.C. and LABY, T.H. 1975. Tables of Physical and Chemical Constants. Longman Group Ltd., London, 14th edition.

KEEN, C. and TRAMONTINI, C. 1970. A seismic refraction survey on the Mid-Atlantic Ridge. Geophys. J.R. astr. Soc., 20, 473-491.

KEITH, C.M. and CRAMPIN, S. 1977a. Seismic body waves in anisotropic media: reflection and refraction at a plane interface. Geophys. J.R. astr. Soc., 49, 181-208.

KEITH, C.M. and CRAMPIN, S. 1977b. Seismic body waves in anisotropic media: propagation through a layer. Geophys. J.R. astr. Soc., 49, 209-223.

KEITH, C.M. and CRAMPIN, S. 1977c. Seismic body waves in anisotropic media: synthetic seismograms. Geophys. J.R. astr. Soc., 49, 225-243.

KENNETT, B.L.N. 1974. Reflections, rays and reverberations. Bull. seism. Soc. Am., 64, 1685-1696.

KENNETT, B.L.N. 1975a. Theoretical seismogram calculation for laterally varying crustal structures. Geophys. J.R. astr. Soc., 42, 579-589.

KENNETT, B.L.N. 1975b. The effect of attenuation on seismograms. Bull. seism. Soc. Am., 65, 1643-1651.

KENNETT, B.L.N. 1977. Towards a more detailed seismic picture of the oceanic crust and mantle. Marine Geophys. Researches, 3, 7-42.

KENNETT, B.L.N. and ORCUTT, J.A. 1976. A comparison of travel time inversions for marine refraction profiles. J. geophys. Res., 81, 4061-4070.

KHALEVIN, N.I. 1958. On the impulse-interval acoustic logging. Bull. Acad. Sci. USSR. Geophys. Ser., 211-216.

KHALEVIN, N.I. and BARYKIN, D.D. 1961. An instrument for acoustical investigation in boreholes. Bull. Acad. Sci. USSR, Geophys. Ser., 41-46.

KOKESH, F.P., SCHWARTZ, R.J., WALL, W.B. and MORRIS, R.L. 1965. A new approach to sonic logging and other acoustic measurements. Jour. Pet. Tech., 17, no 3.

KUSTER, G.T. and TOKSÖZ, M.N. 1974. Velocity and attenuation of seismic waves in two-phase media: Part 1, theoretical formulations. Geophysics, 39, 587-606.

LANGFORD, J.J. and WHITMARSH, R.B. 1977. Pop-up bottom seismic recorder (PUBS) of the Institute of Oceanographic Sciences, U.K. Marine Geophysical Researches, 3, 43-63.

LAUGHTON, A.S. 1963. Microtopography. In: The Sea, Vol. 3, ed. M.N. Hill, John Wiley and Sons, New York.

LAUGHTON, A.S., HILL, M.N. and ALLAN, T.D. 1960. Geophysical investigations of a seamount 150 miles north of Madeira. Deep Sea Research, 7, 117-141.

LE PICHON, X., HOUTZ, R.E., DRAKE, C.L. and NAFE, J.E. 1965. Crustal structure of Mid-Ocean Ridges 1. Seismic refraction measurements. J. geophys. Res. 70, 319-339.

LEVIN, F.K. and LYNN, R.D. 1958. Deep hole geophone studies. Geophysics, 23, 639-664.

LISTER, C.R.B. 1972. On the thermal balance of a mid-ocean ridge. Geophys. J.R. astr. Soc., 26, 515-535.

LISTER, C.R.B. 1974a. Water percolation in the oceanic crust. Trans. Am. Geophy. Union, 55, 740-742.

LISTER, C.R.B. 1974b. On the penetration of water into hot rock. Geophys. J.R. astr. Soc., 39, 465-509.

LORT, J.M. and MATTHEWS, D.H. 1972. Seismic velocities measured in rocks of the Troodos igneous complex. Geophys. J.R. astr. Soc., 27, 383-392.

LOVE, A.E.H. 1934. A treatise on the mathematical theory of elasticity. Cambridge University Press, London.

LUDWIG, W.J., NAFE, J.E. and DRAKE, C.L. 1970. Seismic refraction. In: The Sea. Vol 4 pt 1, ed. A.E. Maxwell, John Wiley and Sons, New York.

LUYENDYK, B.P. 1970. Origin and history of abyssal hills in the north east Pacific ocean. Bull. geol. Soc. Am., 81, 2237-2260.

LUYENDYK, B.P. and MACDONALD, K.C. 1977. Physiography and structure of the inner floor of the FAMOUS rift valley: observations with

MACDONALD, K.C. and LUYENDYK, B.P. 1977. Deep-tow studies of the structure of the Mid-Atlantic Ridge crest near lat. 37°N. Bull. geol. Soc. Am., 88, 621-636.

MARINE INFORMATION AND ADVISORY SERVICE. 1977. Data extracted from USNODC station file of October 1974. Request no 1735 M.I.A.S. Institute of Oceanographic Sciences, Wormley, Godalming, Surrey.

MASON, M. 1975a. Shottone break generator. Internal Report of Dept. of Geodesy and Geophysics, Cambridge, U.K.

MASON, M. 1975b. The Cambridge Sonobuoy Handbook. In-house report, Dept. Geodesy and Geophysics, Cambridge, U.K.

MATTABONI, P.J. and SOLOMON, S.C. 1977. MITOBS; A seismometer system for ocean-bottom earthquake studies. Marine Geophysical Researches, 3, 87-102.

MATTHEWS, D.H. 1976. Notes of Glomar Challenger Leg 46. In-house report, Dept. of Geodesy & Geophysics, Cambridge, U.K.

MATTHEWS, D.H., LORT, J., VERTUE, T., POSTER, C.K. and GASS, I.G. 1971 Seismic velocities at the Cyprus outcrop. Nature Physical Science, 231, 200-201.

McDONALD, W.G., HUBBARD, A.C., BOOKBINDER, R.G. & McCAMY, K. 1977. Design and shipboard operation of a multipupose ocean bottom seismograph. Marine Geophysical Researches, 3, 179-196.

McDONAL , F.J., ANGONA, F.A., MILLS, R.L., SENGBUSH, R.L., VAN NOSTRAND, R.G. and WHITE, J.E. 1958. Attenuation of shear and compressional waves in Pierre shale. Geophys., 23, 421-439.

MEISSNER, R. 1965. P- and SV-waves from uphole shooting. Geophys. Prospect., 13, 433-459.

MELSON, W.J., AUMENTO, F. et al. 1974. The volcanic layer. Geotimes, December, 1974, 16-18.

MOORES, E.M. and JACKSON, E.D. 1974. Ophiolites and oceanic crust. Nature, 250, 136-139.

MORRIS, G.B., RAITT, R.W. and SHOR, Jr, G.G. 1969. Velocity anisotropy and delay-time maps of the mantle near Hawaii. J. geophys. Res., 74, 4300-4316.

MORRIS, R.L., GRINE, D.R., ARKFELD, T.E. 1964. Using compressional and shear acoustic amplitudes forthe location of fractures. J. Pet. Tech., 16, no 6. June.

MÜLLER, G. 1968. Theoretical seismograms for some types of point-sources in layered media I & II. Z. Geophys., 34, 15-35, 147-162.

MÜLLER, G. 1970. Exact ray theory and its application to the reflection of elastic waves from vertically inhomogeneous media. Geophys. J.R. astr. Soc., 21, 261-273.

NEPROCHNOV, YU.P. 1971. Seismic studies of the crustal structure beneath the seas and oceans. Oceanology (English translation), 11, 709-715.

NEPROCHNOV, YU.P., NEPROCHNOVA, A.F., ZVEREV, S.M. and MIRONOVA, V.I. 1967. Deep seismic sounding of the earth,s crust in the central part of the Black Sea depression. In: Problems in Deep Seismic Sounding. ed. S.M. ZVEREV (Eng. Trns. Consu-tants Bureau, New York, 1967), 44-78.

NUR, A. 1972. Dilatancy, pore fluids and premonitory variations of t_s/t_p travel times. Bull. Seism. Soc. Amer., 62, 1217-1222.

NUR, A., and SIMMONS, G. 1969a. The effect of saturation on velocity in low porosity rocks. Earth Planet. Sci. Lett., 7, 183-193.

NUR, A., and SIMMONS, G. 1969b. Stress induced velocity anisotropy in rock: an experimental study. J. geophys. Res., 74, 6667-6674.

O'BRIEN, P.N.S. and LUCAS, A.L. 1971. Velocity dispersion of seismic waves. Geophys. Prosp., 19, 1-26.

O'CONNELL, R.J. and BUDIANSKY, B. 1974. Seismic velocities in dry and saturated cracked solids. J. geophys. Res., 79, 5412-5425.

O'DOHERTY, R.F. and ANSTEY, N.A. 1971. Reflections on amplitudes. Geophys. Prospect., 19, 430-458.

ORCUTT, J.A., KENNETT, B.L.N. and DORMAN, L.M. 1976. Structure of the East Pacific Rise from an ocean bottom seismometer survey. Geophys. J.R. astr. Soc., 45, 305-320.

ORCUTT, J.A., KENNETT, B.L.N., DORMAN, L.M. and PROTHERO, W.A. 1975. Evidence for a low velocity zone underlying a fast spreading ridge crest. Nature, 256, 475-476.

ORDING, J.R. and REDDING, V.L. 1953. Sound waves observed in mud-filled well after surface dynamite charges. J. acoust. Soc. Am., 25, 719-726.

PICKETT, G.R. 1963. Acoustic character logs and their applications in formation evaluations. J. Pet. Tech., 15, no. 6 June.

POSTER, C.K. 1973. Ultrasonic velocities in rocks from the Troodos Massif, Cyprus. Nature Physical Science, 243, 2-3.

POUPON, A., HOYLE, W R., and SCHMIDT, A.W. 1971. Log analysis in formations with complex lithologies. J. Pet. Tech., Aug. 1971.

PROTHERO, W.A., JR. 1977. A digital event-recording ocean bottom seismometer capsule. Marine Geophysical Researches, 3, 119-141.

RABINOWITZ, P.A., MELSON, W.G. et al. 1976. Challenger drills on Leg 45. Geotimes, April, 1976, 20-23.

RACAL THERMIONIC LTD. 1970 Instrumentation Recorders T8000, T8200 and T8300 series. Racal Thermionic Ltd., Hythe, Southampton, U.K.

RAITT, R.W. 1963a. The crustal rocks. In: The Sea, vol 3, ed. M.N. Hill, John Wiley, New York.

RAITT, R.W. 1963b. Seismic refraction studies of the Mendocino fracture zone. MPL-U-23/63, Marine Physical Lab, Scripps Institution of Oceanography, University of California, San Diego.

RAITT, R.W., SHOR, Jr., G.G., FRANCIS, T.J.G., and MORRIS, G.B. 1969. Anisotropy of the Pacific upper mantle. J. geophys. Res., 74, 3095-3109.

RIGGS, E.D. 1955. Seismic wave types in a borehole. Geophysics, 20, 53-67.

ROBINSON, P.T., HALL, J.M. et al. 1977. Leg 37 cruise synthesis: The lithology, structure, petrology and magnetic history of layer 2. In: AUMENTO, F., MELSON, W.G. et al, Initial Reports of the Deep Sea Drilling Project, volume 37, : Washington (U.S. Government Printing Office), 987-997.

ROSENDAHL, B.R. 1976. Evolution of oceanic crust 2. Constraints, implications and inferences. J. geophys. Res., 81, 5305-5314.

ROSENDAHL, B.R., RAITT, R.W., DORMAN, L.M., BIBEE, L.D., HUSSONG, D.M. and SUTTON, G.H. 1976. Evolution of oceanic crust 1. A physical model of the East Pacific Rise crest derived from seismic refraction data. J. geophys. Res., 81, 5294-5304.

SALISBURY, M.H. and CHRISTENSEN, N.I. 1976. Sonic velocities and densities of basalts from the Nazca plate, DSDP leg 34. In: Hart, S.R., Yeats, R.S. et al., Initial Reports of the Deep Sea Drilling Project, Volume 34: Washington (U.S. Government Printing Office), 543-546.

SALISBURY, M.H. and CHRISTENSEN, N.I. 1978. The seismic velocity structure of a traverse through the Bay of Islands Ophiolite Complex, Newfoundland, an exposure of oceanic crust and upper mantle. J. geophys. Res., 83, 805-817.

SCHEIDEGGER, A.E. and WILLMORE, P.L. 1957. The use of least square method for the interpretation of data from seismic surveys. Geophysics, 22, 9-22.

SCHLUMBERGER LIMITED 1972. Log interpretation, Volume 1 - Principles. Schlumberger Limited, 277 Park Avenue, New York 10017, U.S.A.

SCHOENBERGER, M. and LEVIN, F.K. 1974. Apparent attenuation due to intrabed multiples. Geophysics, 39, 278-291.

SCHREIBER, E. and FOX, P.J. 1976. Compressional wave velocities and mineralogy of fresh basalts from the FAMOUS area and the Oceanographer Fracture Zone and the texture of layer 2A of the oceanic crust. J. geophys. Res., 81, 4071-4076.

SCHREIBER, E. and FOX, P.J. 1977. Density and P-wave velocity of rocks from the FAMOUS region and their implication to the structure of the oceanic crust. Bull. geol. Soc. Am., 88, 600-608.

SCLATER, J.G. and FRANCHETEAU, J. 1970. The implications of terrestrial heat flow observations on current tectonic and geochemical models of the crust and upper mantle of the Earth. Geophys. J.R. astr. Soc. 20, 509-542.

SECOR, D.T. and POLLARD, D.D. 1975. On the stability of open hydraulic fractures in the earth's crust. Geophys. Res. Letters, 2, 510-513.

SHIMSHONI, M. and SMITH, S.W. 1964. Seismic signal enhancement with three component detectors. Geophysics, 29, 664-671.

SHOR, Jr. G.G. 1963. Refraction and reflection techniques and procedure. In: The Sea, Vol. 3, ed. M.N. HILL, John Wiley and Sons, New York.

SHOR, Jr. G.G., MENARD, H.W. and RAITT, R.W. 1971. Structure of the Pacific basin. In: The Sea vol 4, pt 2. ed A.E. Maxwell, John Wiley, New York.

SHOR, Jr. G.G. and POLLARD, D. 1964. Mohole site selection studies north of Maui. J. geophys. Res., 69, 1627-1638.

SHORTHOUSE, J.M. 1964. Seismic measurements on the deep sea bed. PhD. thesis, Dept. of Geodesy and Geophysics, University of Cambridge, Cambridge, U.K.

SIMMONS, G. 1964. Velocity of shear waves in rocks to 10 kb. Pt. I. J. geophys. Res., 69, 1123-1130.

SLEEP, N.H. 1975. Formation of oceanic crust: some thermal restraints. J. geophys. Res., 80, 4037-4042.

SMITH, J.T., STEINHART, J.S. and ALDRICH, L.T. 1966. Lake Superior Crustal Structure. J. geophys Res., 71, 1141-1172.

SMITH, P.J. 1975. Crack theory developed. Nature, 253, 593-594.

SMITH, S.G. 1976. The synthesis of seismic reflection profiles. Ph.D. thesis, Dept of Geodesy & Geophysics, Cambridge, U.K.

SMITH, W.A. 1977. The development of a Pull-up Shallow Water Seismometer. Ph.D. Thesis, Dept of Geodesy & Geophysics, Cambridge, U.K.

SNOW, R.B., THROOP, W.H. and WILLIAMS, J.A. 1968. Logging offshore wells in the U.S. Trans. Ninth Ann. Logging Symp. SPWLA, B1-B13.

SPIESS, F.N. and MUDIE, J.D. 1970. Small scale topographic and magnetic features. In: The Sea, Vol. 4, Pt. 1, ed. A.E. Maxwell, John Wiley and Sons, New York.

STEPHEN, R.A. 1975. Travel time curves for O.S.E. Folio, Dept of Geodesy & Geophysics, Cambridge, U.K.

STEPHEN, R.A. 1976. Notes for the Oblique Seismic Experiment - March 1976. In-house Report, Dept of Geodesy & Geophysics, Cambridge, U.K.

STEPHEN, R.A. 1977a. Shooting ship gear for O.S.E. In-house Report, Dept. Geodesy & Geophysics, Cambridge, U.K.

STEPHEN, R.A. 1977b. Synthetic seismograms for the case of the receiver within the reflectivity zone. Geophys. J.R. astr. Soc., 51, 169-181.

STEPHEN, R.A., LOUDEN, K.E. and CLAYDON, A. 1977. Cruise report for Glomar Challenger Leg 52. In-house Report, Dept. of Geodesy & Geophysics, Cambridge, U.K.

STETSON, T.R. and KOELSCH, D.E. 1974. The use of Tovex and Nitamon S explosives aboard research vessels. Internal Report, Woods Hole Oceanographic Institution, Woods Hole, Massachusetts, 02543, U.S.A.

STONELEY, R. 1949. The seismological implications of aleotropy in continental structure. Monthly notices Roy. Astr. Soc. Geophys. Supp., 5, 222-232.

STRICK, E. 1971. An explanation of observed time discrepancies between continuous and conventional well velocity surveys. Geophysics, 36, 285-295.

SUMMERS, G.C. and BRODING, R.A. 1952. Continuous velocity logging. Geophysics, 17, 598-614.

SUTTON, G.H., KASAHARA, J., ICHINOSE, W.N. & BYRNE, D.A. 1977. Ocean bottom seismograph development at Hawaii Institute of Geophysics. Marine Geophysical Researches, 3, 153-177.

TITTMAN, J, SHERMAN, H., NAGEL, W.A. and ALGER, R.P. 1966. The sidewall epithermal neutron porosity log. Jour. Pet. Tech., Oct 1966.

TITTMAN, J., and WAHL, J.S. 1965. The physical foundations of formation density logging. Geophysics, 30, 284-294.

TIXIER, M.P. 1962. Modern Log Analysis. J. Petrol. Tech., 14, 1327-1336.

TIXIER, M.P., ALGER, R.P. and DOH, C.A. 1959. Sonic logging. J. Petrol. Tech., 11, 106-114.

TOKSÖZ, N., CHENG, C.H. and TIMUR, A. 1976. Velocities of seismic waves in porous rocks. Geophysics, 41, 621-645.

UHRIG, L.F. and Van MELLE, F.H. 1955. Velocity anisotropy in stratified media. Geophysics, 20, 774-779.

VANDERSTOEP, D.M. 1966. Velocity anisotropy measurements in wells. Geophysics, 31. 900-916.

VINE, F.J. and MOORES, E.M. 1972. A model for the gross structure of oceanic crust. Geol. Soc. Am. Mem., 132, 195-205.

VOGEL, C.B. 1952. A seismic velocity logging method. Geophysics, 17, 586-597.

WALSH, J.B. 1965. The effect of cracks on the compressibility of rock. J. geophys. Res., 70, 381-389.

WANG, C.Y. and LIN, W. 1974. Velocity ratios for rocks with oriented microcracks. Nature, 248, 579-580.

WHITCOMB, J.H., GARMANY, J.D. and ANDERSON, D.L. 1973. Earthquake prediction: Variation of seismic velocities before the San Francisco earthquake. Science, 180, 632-635.

WHITE, J.E. 1965. Seismic waves: Radiation, transmission, and attenuation (p. 143-211) McGraw-Hill Book Company, New York.

WHITE, J.E. and FROST, H.H. 1956, Unexpected waves observed in fluid-filled boreholes. J. acoust. Soc. Am., 28, 924-927.

WHITMARSH, R.B. 1967. Explosion seismology on the sea bed. Ph.D thesis, Dept. of Geodesy and Geophysics, University of Cambridge, Cambridge, U.K.

WHITMARSH, R.B. 1970. An ocean bottom pop-up seismic recorder. Marine Geophysical Researches, 1, 91-98.

WHITMARSH, R.B. 1975. Axial intrusion zone beneath the median valley of the Mid-Atlantic Ridge at 37°N detected by explosion seismology. Geophys. J.R. astr. Soc., 42, 189-216.

WHITMARSH, R.B. 1978. Seismic refraction studies of the upper igneous crust in the north Atlantic and porosity estimates for layer 2. Earth Planet. Sci. Lett., 37, 451-464.

WILLMORE, P.L. and BANCROFT, A.M. 1960. The time term approach to refraction seismology. Geophys. J.R. astr. Soc., 3, 419-432.

WUENSCHEL, P.C. 1976. The vertical array in reflection seismology - some experimental studies. Geophysics, 41, 219-232.

WYLLIE, M.R., GREGORY, A.R. and GARDNER, G.H.F. 1956. Elastic wave velocities in heterogeneous and porous media. Geophysics, 21, 41-70.

WYLLIE, M.J.R., GREGORY, A.R. and GARDNER, G.H.F. 1958. An experimental investigation of factors affecting elastic wave velocities in porous media. Geophysics, 23, 459-493.

SHIPBOARD PARTIES OF DSDP LEGS 51, 52 AND 53

DSDP Leg 51

Donnelly, T.W.	Co-Chief Scientist
Francheteau, J.	Co-Chief Scientist
Salisbury, M.	Physical Properties
Borella, P.E.	Sedimentologist
Kelts, D.	Sedimentologist
Swift, S.A.	Sedimentologist
Bleil, U.	Paleomagnetist
Smith, B.M.	Paleomagnetist
Juteau, T.	Igneous Petrologist
Rusinov, V.	Igneous Petrologist
Sinton, J.M.	Igneous Petrologist
Ui, T.	Igneous Petrologist
Orr, W.N.	Paleontologist (Forams)
Gartner, S.	Paleontologist (Nannos)

DSDP Leg 52

Bryan, W.B.	Co-Chief Scientist
Robinson, P.T.	Co-Chief Scientist
White, S.	Staff Representative
Byerly, G.	Igneous Petrologist
Swanson, D.A.	Igneous Petrologist
Emmermann, R.	Igneous Petrologist
Ricou, L-E.	Igneous Petrologist
Levi, S.	Paleomagnetist
Pertsev, N.	Igneous Petrologist
Miles, G.A.	Paleontologist (Forams)
Siesser, W.G.	Paleontologist (Nannos)
Hamano, Y.	Physical Properties
Stephen, R.A.	Geophysicist
Bollinger, C.	X-Ray Technician

DSDP Leg 53

Flower, M.F.J.	Co-Chief Scientist
Salisbury, M.	Co-Chief Scientist
Bohrer, D.	Staff Representative
Staudigel, H.	Igneous Petrologist
Mathez, E.	Igneous Petrologist
Mevel, C.	Igneous Petrologist
Pertsev, N.	Igneous Petrologist
Rigotti, P.A.	Paleomagnetist
Hobart, M.	Physical Properties
Johnson, D.	Physical Properties
Pritchard, R.G.	Geochemist
Puchelt, H.	Geochemist